

*Interfacial reactivity and adhesive properties of ternary
transition metal nitride hard coatings in contact with
polymers*

Dissertation

zur Erlangung des Grades

Doktor der Naturwissenschaften (Dr. rer. nat.)

vorgelegt von

M.Sc. Martin Wiesing, geb. 25.03.1990 in Paderborn

Universität Paderborn

Fakultät Naturwissenschaften

Department Chemie

Lehrstuhl für Technische und Makromolekulare Chemie

Prof. Dr.-Ing. Guido Grundmeier

Datum der mündlichen Prüfung: 10.07.2018
Erstgutachter: Prof. Dr.-Ing. Guido Grundmeier
Zweitgutachter: Prof. Dr. Matthias Bauer

Hiermit bestätige ich, dass die vorliegende Arbeit von mir persönlich angefertigt wurde und sämtliche Hilfsmittel, Literaturquellen und anderweitige Hilfestellungen durch Dritte angegeben sind.

Martin Wiesing

Paderborn, den 18.04.2018

Acknowledgement

This work was only possible by the unparalleled support of the beloved and inspiring persons around me. For these reasons, I want hereby to express my deep gratitude and appreciation for their willingness to support me directly or indirectly. It is not my intention to rank or assess these contributions, but I want to highlight exceptional persons, who encouraged and supported me during my work on a daily basis.

Among these, I want to thank Guido Grundmeier and Teresa de los Arcos for providing me an awesome scientific environment. Beside this, it was their clear and logic thinking which guided me how to handle the most stressful situations.

Further, the stimulating discussions and the warm and lively environment provided by my colleagues brightened seemingly pointless days. So I want to thank you Teresa, Markus, Christoph, Ignacio, Markus, Stefan, Chen-Ni, Bastian and all the others of you.

Finally, I also want to stress my deep gratitude for the support I received from my family and thank you Michael, Cornelia and Heinrich.

Abstract

Future plastic products with functional surfaces such as optical components or lab-on-a-chip analytical devices rely on the promising performance of the injection moulding process as a future key technology to produce complex shaped products with finest dimensions at industrial scales. However, a complex interplay of interfacial chemical reactions and adhesive force interactions deteriorates the stability, reproducibility and precision of the injection moulding process and thereby retards this development. In this view, the scope of this thesis is to provide fundamental insights into the reactive and adhesive interactions between polymers and hard coatings, which are used in polymer melt processing to mitigate these technical issues, in order to pave the way for a rational design of tailored hard coatings.

Therefore, the thermal and electrochemical oxidation of the prototypical hard coating $\text{Ti}_{0.5}\text{Al}_{0.5}\text{N}$ was investigated by means of electron and ion spectroscopy and by electrochemical methods. Consequently, microscopic mechanisms of the thermal and of the electrochemical oxidation of $\text{Ti}_{0.5}\text{Al}_{0.5}\text{N}$ were developed and revealed the reactive inward migration of oxygen to be a central motif in both cases to explain the different stages of oxidation observed. These investigations of the reactive interactions were then expanded to study the more complex thermal degradation and interphase formation of molten polycarbonate at $\text{Ti}_{0.5}\text{Al}_{0.5}\text{N}$ and iron surfaces, where the latter mimics the surface of an uncoated steel tool. Among the results, a catalytic degradation of polycarbonate was observed at the iron surface, whereas no accelerated degradation was found in the case of the $\text{Ti}_{0.5}\text{Al}_{0.5}\text{N}$ hard coating. Based on the thorough investigation of the surface chemistry of $\text{Ti}_{0.5}\text{Al}_{0.5}\text{N}$, the interaction forces between $\text{Ti}_{0.5}\text{Al}_{0.5}\text{N}$ and polycarbonate were finally studied by means of force spectroscopy. This analysis was assisted by a novel approach developed to separately quantify the van der Waals force contributions by means of optical data as derived from reflection electron energy loss spectroscopy. The results show that the van der Waals forces are minimized by an enhanced surface oxidation after deposition combined with an enrichment of aluminium ions in the surface oxide layer. The in-depth analysis of the overall adhesion further highlighted that the van der Waals forces are of high relevance even in the case of additional acid-base bonding caused by an increasing degree of oxidation of the interacting surfaces.

In conclusion, the here presented thesis enables a thorough understanding of the functional properties of hard coatings employed in polymer melt processing applications based on a comprehensive understanding of the surface chemistry and the correlated adhesive and reactive interactions.

ACKNOWLEDGEMENT	IV
ABSTRACT	VI
1 MOTIVATION AND OBJECTIVE OF THE THESIS.....	1
2 FUNDAMENTALS.....	3
2.1 TERNARY TRANSITION METAL (OXY-)NITRIDE HARD COATINGS	3
2.1.1 <i>Thin films deposition by High Power Pulsed Magnetron Sputtering</i>	3
2.1.2 <i>Phase properties of TiAlN and TiAl(O,N)</i>	6
2.1.3 <i>Hard coatings for polymer melt processing applications</i>	8
2.1 THEORY OF OXIDATION.....	9
2.1.1 <i>Low-temperature oxidation</i>	9
2.1.2 <i>Electrochemical oxidation</i>	11
2.2 MOLECULAR ADHESION	13
2.2.1 <i>Introduction</i>	13
2.2.2 <i>Experimental approaches</i>	14
2.3 VAN DER WAALS INTERACTIONS.....	19
2.3.1 <i>The Hamaker approach</i>	20
2.3.2 <i>The theory of Lifshitz, Dzyaloshinsky and Pitaevskii</i>	21
2.4 ACID-BASE INTERACTIONS AND COORDINATIVE BONDS	23
2.5 ADSORPTION OF POLYMERS FROM THE MELT	25
3 ADVANCED EXPERIMENTAL METHODS	26
3.1 X-RAY PHOTOELECTRON SPECTROSCOPY (XPS)	26
3.1.1 <i>Basic principles</i>	26
3.1.2 <i>Analysis of chemical effects in XPS</i>	28
3.1.3 <i>Relaxation in d-metal compounds by charge transfer</i>	31
3.1.4 <i>Wagner plots and modified Auger parameters</i>	34
3.1.5 <i>Quantitative XPS</i>	35
3.1.6 <i>Thickness layer determination by XPS</i>	38
3.2 LOW ENERGY ION SCATTERING (LEIS)	39
3.3 DYNAMIC FORCE SPECTROSCOPY (DFS)	41
3.3.1 <i>Introduction</i>	41
3.3.2 <i>Experimental foundations</i>	42
3.3.3 <i>Theoretical foundations</i>	44
4 PUBLICATIONS	47
4.1 THE THERMAL OXIDATION OF TiAlN HIGH POWER PULSED MAGNETRON SPUTTERING HARD COATINGS AS REVEALED BY COMBINED ION AND ELECTRON SPECTROSCOPY.....	49
4.2 COMBINED ELECTROCHEMICAL AND ELECTRON SPECTROSCOPIC INVESTIGATIONS OF THE SURFACE OXIDATION OF TiAlN HPPMS HARD COATINGS	64
4.3 ANALYSIS OF THE INHIBITION OF THERMAL DEGRADATION OF MOLTEN POLYCARBONATE AT TOOL STEEL INTERFACES BY THIN TiAlN COATINGS.....	75
4.4 LIFSHITZ ANALYSIS OF DISPERSION FORCES BASED ON QUANTITATIVE REFLECTION ELECTRON ENERGY LOSS SPECTROSCOPY... ..	90
4.5 ANALYSIS OF DISPERSIVE INTERACTIONS AT POLYMER/TiAlN INTERFACES BY MEANS OF DYNAMIC FORCE SPECTROSCOPY....	105
4.6 UHV AFM BASED COLLOIDAL PROBE STUDIES OF ADHESIVE PROPERTIES OF VALN HARD COATINGS	129
5 OVERALL DISCUSSION	144
5.1 SURFACE CHEMICAL STRUCTURE OF HARD COATINGS	144
5.2 INTERFACIAL ADHESIVE AND REACTIVE INTERACTIONS	146
6 CONCLUSIONS.....	148
7 LIST OF ABBREVIATIONS	150
8 BIBLIOGRAPHY.....	151

1 Motivation and objective of the thesis

Thermal processing of plastics by injection moulding allows the cost-effective mass production of complex shaped products. During the past years this facilitated the development of future technologies such as micro-fluidic and -optical analytical devices (“lab-on-a-chip”) and also resulted into spreading of plastic based products with functional surfaces to increasingly replace glass and other materials.¹⁻³ A key requirement for this development is a high stability, precision and reproducibility of the injection moulding process, which is affected by a variety of interfacial phenomena deteriorating both the quality of the product, but also the functional properties of the tools. To name a few examples, polymers can strongly adhere at mould inserts and extruder screws causing release problems and adhesive wear as illustrated in figure 1.³⁻⁵ For the same reasons, the processed polymer may also accumulate at tool surfaces and form deposits, which after thermal degradation and shear induced release cause discoloured speckles in the surface of the product.^{2,4} Another important mechanism of failure is the electrochemical corrosion of the tool leading not only to erosion but also often to an unwanted, accelerated chemical degradation of the polymer.⁴

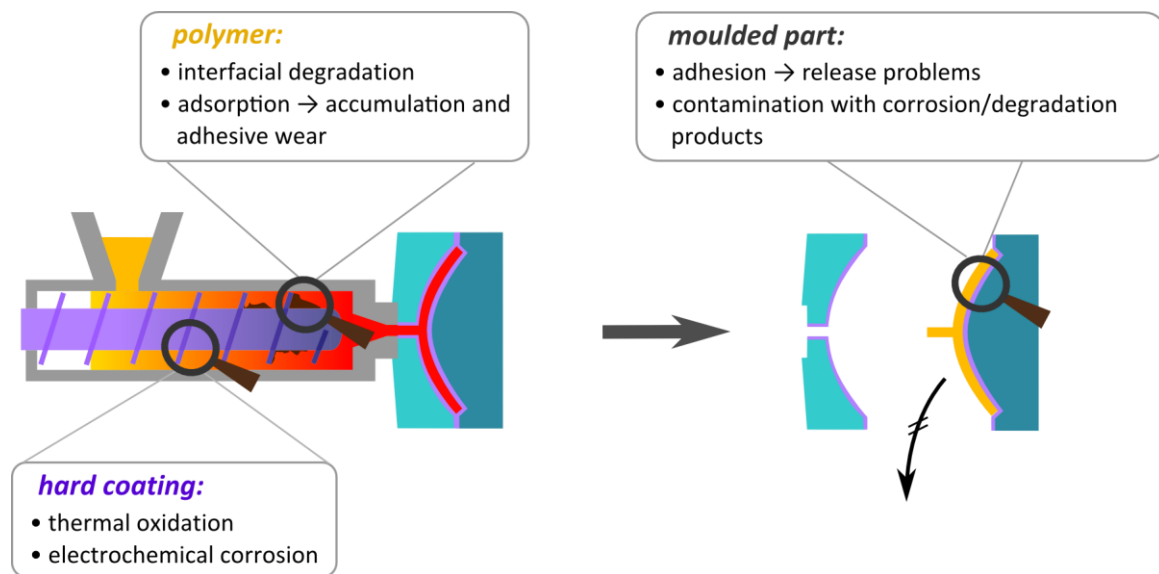


Figure 1: Process instabilities caused by interfacial interactions as encountered during injection moulding.

In conclusion, these observations highlight that especially the reactivity and adhesion of polymers and their degradation products at tool surfaces govern the stability of the injection moulding process and the quality of the products. In order to mitigate these issues, advanced surface coatings such as ternary nitridic hard coatings based on transition metals $M_xAl_{1-x}N$ with M being Ti or Cr are nowadays routinely applied to extruder screws and mould inserts.^{5,6} However, the beneficial functional properties of these coatings have so far been investigated on an empirical basis only (see section 2.1.3). It is consequently the objective of this work to develop a fundamental understanding of the interfacial reactivity and the adhesive interactions of ternary nitridic hard coatings in contact with polymers in order to pave the

way for a rational design of tailored hard coatings for polymer melt processing applications. The main hypothesis followed within this thesis is that the interfacial reactivity and the adhesive interactions between the hard coating and the polymeric phase are defined by the chemical composition and structure of the corresponding interfacial region. In this regards, the surface chemical structure of a hard coating deviates strongly from its bulk composition due to the superficial oxidation encountered after deposition and at polymer melt processing conditions. This raises the following research issues, which are investigated first within this thesis:

- 1) How do the nitridic surfaces of hard coatings oxidize after deposition by exposure to ambient atmosphere or at the elevated operating temperatures?
- 2) Which anodic and cathodic processes occur at hard coating surfaces upon polarization? What reversible and irreversible surface phases are formed?

Based on these results, the reactive and adhesive interfacial interactions between hard coatings and polymers are then investigated and the following fundamental, but hitherto unresolved issues are investigated:

- 3) How does the presence of the hard coating surface influence the bulk thermal degradation and the physical structure of the polymer at the interface?
- 4) What is the total interaction force between a hard coating and a polymer surface? How does the surface chemical structure affect these interactions?
- 5) Is there a method, which allows to predict van der Waals interactions between hard coating and polymer *surfaces* in order to understand the related adhesion force contributions?
- 6) To what extent do van der Waals and acid-base interactions contribute to the overall adhesion and what is the role of the surface chemistry for their relative contributions?

In conclusion, this work correlates the surface chemical structure of hard coatings with their interfacial functional properties and thereby approaches a rational design of tailored hard coatings. Thus, the experimental and theoretical framework of surface science is invoked to study these correlations and $\text{Ti}_{0.5}\text{Al}_{0.5}\text{N}$ as well as additive-free polycarbonate (Makrolon® 3108, $M_w = 31$ kDa) were used as model systems throughout this thesis if not stated otherwise.

2 Fundamentals

2.1 Ternary transition metal (oxy-)nitride hard coatings

Nitridic hard coatings are nowadays widely used functional coatings due to their excellent wear, thermal, chemical and oxidation resistance, low residual stress, high hardness and hot hardness.⁷ The fields of applications of nitridic hard coatings include cutting tools for dry machining, functional optical coatings and diffusion barrier layers in microelectronics as well as tribological coatings in polymer melt processing.^{4,7-10} In the following, an overview about the deposition of hard coatings, the phase properties of the prototypical $Ti_{1-x}Al_xN$ and $Ti_{1-x}Al_x(O,N)$ coatings and the use of hard coatings in polymer melt processing applications is therefore provided.

2.1.1 Thin films deposition by High Power Pulsed Magnetron Sputtering

The technological development of hard coatings was initiated by the Chemical Vapour Deposition (CVD) of TiN, TiC and Al_2O_3 on cemented carbides. A major drawback of the CVD deposition was the high temperature required of around 1000 °C so that only cemented carbides but no steel substrates could be coated.⁸ The advent of advanced physical vapour deposition techniques such as magnetron sputtering alleviated this issues and deposition temperatures below 550 °C allowed to coat steel tools.

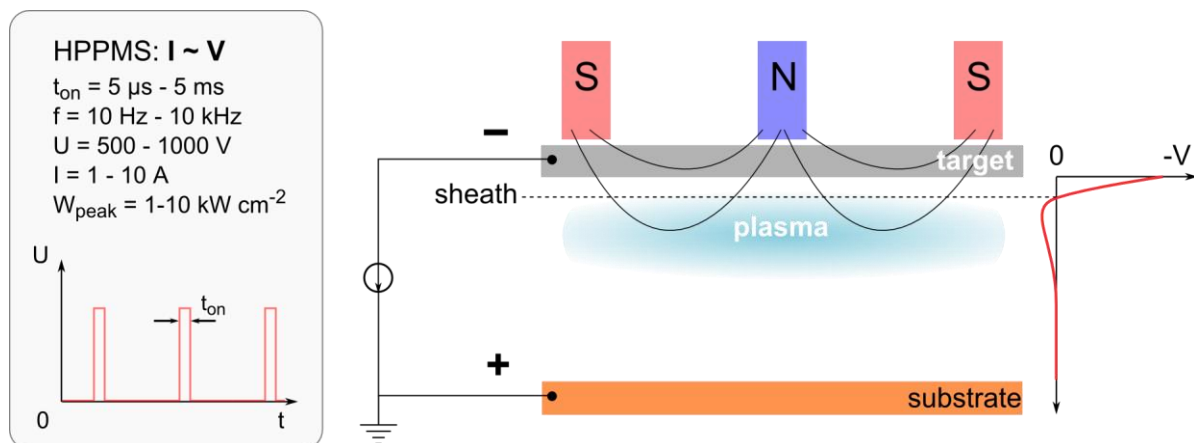


Figure 2: Illustration of a simple balanced magnetron sputtering setup including typical parameters used for HPPMS and a basic sketch of the potential of the plasma region. The plasma is operated at low pressures around 1 Pa.

Nowadays, the deposition of nitridic hard coatings is predominantly performed using the cathodic arc or the magnetron sputtering process.⁷ The advantage of the cathodic arc process is to provide a very high degree of ionization of the particles of up to 100 %, which allows to fill trenches, to provide an excellent adhesion to the substrate and to deposit dense films.¹¹ However, the cathodic arc process suffers from the severe formation of macroscopic defects in the deposited films due to formation of droplets in the gas and filtering of the plasma must be therefore performed to deposit high-quality films.¹²

In contrast, films with very low defect densities can be obtained by magnetron sputtering, but the deposition rate is reduced in the presence of reactive gases such as N₂ and the degree of ionization in conventional direct current magnetron sputtering (dcMS) is below 10 %. Among the shortcomings of dcMS for the deposition of hard coatings, this leads to low density and defective films due to atomic shadowing.^{13,14} In this regards, an increase of the plasma density and thereby also of the degree of ionization (up to 70 % in the case of Cu) can be achieved by using the dcMS experimental setup but by applying short power pulses to the plasma.¹⁵ This sputtering mode is known as High Power Pulsed Magnetron Sputtering (HPPMS or HiPIMS) and extensive reviews about its seminal characteristics are available in literature.^{11,13,16–20} A basic magnetron setup for HPPMS is shown in figure 2. Among the basic vacuum components required to maintain the low pressure of around 1 Pa and the electronics to operate the plasma, the main components are the target (cathode) and the often grounded substrate (anode). However, the key characteristic of a magnetron is its ability to confine the plasma by a magnetic field close to the target. This can be achieved, because the electrical field lines are mainly orthogonal to the magnetic lines in the magnetron configuration so that the electrons undergo gyration due to the Lorentz force and ultimately drift along a circular path in parallel to the targets surface. As a consequence, the residence time of the electrons within the plasma region is increased and more ionizing collisions with the gas become possible. This in turn allows to use lower gas pressures of around 1 Pa instead of 5-10 Pa as in an unconfined glow discharge plasma, which facilitates the transport of the slower ions to the substrate by increasing their mean free path.¹⁸

When considering the sputter deposition process, the first step is the bombardment of the target by ions from the plasma leading to sputtering and secondary electron emission. While the sputtered atoms are mainly neutrals and enter the plasma with low kinetic energies, the electrons become accelerated within the sheath region and feed the plasma with their kinetic energy. When using the HPPMS mode, short power pulses instead of direct current are applied and the maximum plasma density in front of the target can be increased by around 2 orders of magnitude to around 10¹⁸ - 10¹⁹ m⁻³, which decreases the ionization mean free path of a neutral metal atom to around 1 cm.¹⁷ This results into the formation of large fractions of mostly single charged metal ions with energies around 20-30 eV, which bombard the substrate and thereby lead to a beneficial densification of the deposited film and a smoother and more defect-free surface morphology.^{13,17} However, the ions may also be pulled back by the cathode and undergo self-sputtering, which decreases the deposition rate in the HPPMS mode along with the gas rarefaction due to heat expansion and ionization of the gas.

The growth of the deposited thin films occurs at rather low temperatures and high cooling rates in the range of 10¹⁵ K s⁻¹ and is therefore a non-equilibrium process.^{21,22} Tailoring of the thin film properties can be therefore performed by controlling the temperature and by adjusting the energy flux to the substrate as delivered by the ions.²³ This finally enhances the surface and bulk diffusion processes and

thereby affects especially the morphology of the film as described by so-called structure zone diagrams. In this regards, an extended structure zone diagram applicable for the HPPMS process was developed by Anders and is shown in figure 3.²³ The diagram covers typical morphological features observed in thin film deposition, but is not quantitative and neither at scale. In order to construct the diagram, the net thickness t^* is defined, which includes reduction of the thickness due to densification and sputtering or ion etching. Two additional normalized deposition parameters are further used: the generalized temperature T^* represents the film temperature normalized to the melting temperature plus an extra term due to the heating of the film by the loss of potential energy of the incoming particles. The effect of the temperature T^* is to promote surface and bulk diffusion processes. The normalized energy E^* is defined to account for displacement and heating effects due to the momentum of the particles.

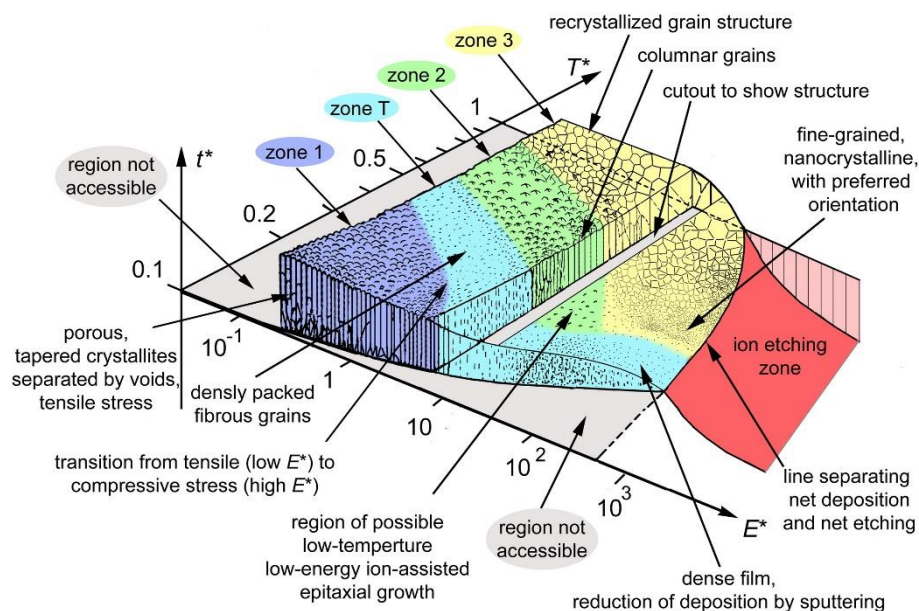


Figure 3: Andersons extended structure zone model.²³ E^* represents the normalized energy due to the displacement and heating of the substrate by the potential of the bombarding particles. T^* is defined as the film temperature normalized to the melting temperature plus the potential energy of the incoming particles. Finally, t^* is the net thickness due to densification but also sputtering or even ion etching. (Reuse license No. 4304120681413, © Elsevier)

The role of the parameters T^* and E^* and their interplay for the structure formation is now outlined using two examples: one special situation can be encountered when the energy of the incoming particles, as reflected by E^* , is along with the temperature T^* sufficiently high to promote surface diffusion but is not sufficient to initiate a bulk collision cascade. In this case even an epitaxial deposition of single-crystalline films can be realized, because the structure of the substrate is conserved.²⁴ In contrast, an extended collision cascade is present at higher energies E^* and the two-fold effect of the particles kinetic energy and its potential becomes prevalent:^{23,25} the first phase of a collision cascade (100 fs) is characterized by ballistic scattering and displacements and results into defect formation and re-nucleation, which is the prerequisite for a dense and fine morphology. Within the subsequent

thermal spike phase (1 ps), a spike volume with a liquid-like behaviour forms and relaxation processes take place, which are further enhanced by the dissipating potential energy of the particle. Within this latter stage, defects are removed again in order to minimize the thermodynamical volume and surface free energy densities.^{23,25}

As a consequence of the joint interplay between the diffusion processes and the collision cascades, different phase morphologies can be accessed by HPPMS, which are summarized in different zones in Anders' structure zone model. In zone 1, tapered crystallites are formed mainly by surface diffusion at low temperatures T^* and energies E^* . These crystallites are only loosely bound to each other so that the film is porous and possesses intrinsic tensile stresses. Increasing T^* results then into a transition region T, where the surface diffusion is largely enhanced and the structure becomes more dense but still remains fibrous (zone T). A further increase of the temperature promotes the relaxation and recrystallization of the structure to form densely packed columnar grains (zone 3) and ultimately a coarse-grained, globular microstructure (zone 4). In contrast, increasing the energy E^* results predominantly into an enhanced rate of nucleation due to collision induced displacements so that at every temperature T^* finer grained and more dense films can be obtained. However, the collisions also cause sputtering, which decreases the deposition rate and thereby the net thickness t^* . Moreover, the collision cascade allows not only for defect nucleation, but also for structural relaxation within the thermal spike phase as outlined above. As a consequence, morphological zones typical for certain temperatures can be entered at lower temperatures by increasing the energy.

For completeness, this section is now concluded by considering specific aspects for the prototypic ternary $Ti_xAl_{1-x}N$ hard coating, which is widely used within this thesis: it could be shown that in this case the adatom mobility decreases with increasing aluminium content so that higher energies or temperatures must be used for deposition in comparison to the synthesis to TiN thin films.²⁶ In contrast, a too high energy flux applied to the surface by the ions induces an usually undesired phase precipitation of wurtzite-type AlN out from the cubic $Ti_{1-x}Al_xN$ phase.¹⁹ This illustrates that the deposition of $Ti_xAl_{1-x}N$ thin films requires a careful optimization of experimental parameters.

2.1.2 Phase properties of TiAlN and TiAl(O,N)

The phase properties of $Ti_{1-x}Al_xN$ and $Ti_{1-x}Al_x(O,N)$ thin films, where oxygen replaces nitrogen located at the non-metal sublattice, were intensively investigated by researchers using theoretical as well as experimental means in order to understand the role of the stoichiometry and the effect of different deposition conditions.²⁷⁻⁴⁷ In this regards, $Ti_{1-x}Al_xN$ is not thermodynamically stable, but forms mixed solid solutions with cubic NaCl structure and randomly distributed metal atoms on the metal sublattice at Al concentrations below $x < 0.7$. Higher Al contents induce then the decomposition into cubic c-TiN and wurtzite w-AlN.^{27,34} This segregation process was investigated more in-depth by joint thermal treatments and phase analysis: it could be shown, that the first step of the thermally induced spinodal

decomposition is characterized by the formation of coherent c-TiN and c-AlN domains with an interconnected network structure, which segregates only gradually into two distinct phases.^{36,37} This initial step is then followed at higher temperatures by the restructuring of the c-AlN grains to w-AlN.³⁵ It follows that the decomposition is not the consequence of a structural mismatch between the c-TiN and c-AlN phases.

The decomposition process not only modifies the structure, but also the chemistry of the single phases and the overall stress in the film. In this regards, molecular nitrogen was detected upon segregation, which was explained by the oxidation of the TiN phase by residual oxygen impurities present in the film.³¹ This interpretation is further corroborated by the finding that upon annealing no oxygen is found in TiN in contrast to the AlN domains.³⁷ Moreover, compressive stresses in the as-deposited film are relaxed within the initial stage of segregation by the enhanced formation of c-AlN as a result of its lower molar volume. In contrast, tensile stresses foster the nucleation of the more voluminous c-TiN domains.³⁹ However, net compressive stresses are finally observed at higher temperatures due to the formation of w-AlN, which also has a higher molar volume than the cubic structured c-AlN.³⁸ This latter aspect has another interesting implication: as shown by Holec et al., the mixing enthalpy becomes highly pressure dependent and the solubility limit of aluminium can be increased by applying compressive stresses.^{27,33} The unwanted formation of w-AlN is therefore thermodynamically suppressed during the service of TiAlN coatings for cutting applications.

When considering further the kinetics of the spinodal decomposition, the investigation of activation energies showed that the segregation is assisted by defects given that the process is triggered by nucleation within the bulk phase.³⁵ In this view, Baben et al. could show that the temperature required for the spinodal decomposition can be increased from around 900 °C to about 1200 °C by using almost defect-free stoichiometric films.⁴³ However, it must be noted that the segregation of $Ti_{1-x}Al_xN$ is not undesirable in applications. The coherent cubic phase obtained in the first stage of the decomposition shows a nanocomposite-like structure with enhanced hardness and enables the beneficial age-hardening mechanism of the films observed at elevated service temperatures.^{8,27} Only the subsequent formation of w-AlN then deteriorates the tools performance due to the related decrease of the hardness.²⁷ Furthermore, it is noted that the c-TiN and c-AlN phases can not only nucleate in the bulk but also at surfaces or at grain boundaries.^{39,48,49}

The metastable phase behaviour of $Ti_{1-x}Al_xN$ contrasts the stability observed for the parent compound c-TiN_x, which is thermodynamically stable within the range of $0.35 < x < 0.5$.⁷ To explain this situation, the bonding situation as well as the mixing enthalpy were studied by ab initio methods.^{42,45-47,50-54} These investigations have shown that the intermixing of Al and TiN to form $Ti_{1-x}Al_xN$ results into a piling up of the non-bonding Ti3d states at the Fermi level and the formation of a p-band, which is composed by a mixture of N2p, Al3p and Ti3d states. As a consequence, the covalent character of the bonding

interactions between the next-nearest titanium atoms (Ti-Ti) and between titanium and nitrogen (Ti-N) are enhanced.⁵³ Furthermore, the Al related bonds become more ionic and therefore weaker with increasing Al content.⁵³ Based on these results, Alling et al. pointed out that the spinodal decomposition is not caused by a structural but rather by an electronic mismatch between the c-AlN and c-TiN phases.^{50,51} The decomposition process is therefore supposed to be triggered by the Ti-Ti covalent interactions, which increase during the process and provide a self-accelerating driving force.⁵¹ The properties and phase behaviour of $Ti_{1-x}Al_x(O,N)$ thin films were much less investigated in literature most probably due to their lower hardness and related less widespread use.⁴⁷ However, the stability of the oxynitridic $Ti_{1-x}Al_xO_yN_{1-y}$ was similarly analysed theoretically by considering oxygen to replace nitrogen in $Ti_{1-x}Al_xN$. It was found that at least within the range of $0 < y < 0.5$ the mixing enthalpy is negative.⁵⁴ The overall phase stability is thereby increased, but when a single nitrogen atom is replaced by an oxygen atom a metal electron must be ejected into the Ti3d band in order to maintain charge neutrality. As a consequence, this leads to a stabilization of point defects such as oxygen interstitials or metal vacancies as demonstrated by Baben and Hans et al.^{46,47}

2.1.3 Hard coatings for polymer melt processing applications

Despite hard coatings are used since the 1970s to prolong the life-time of tools for cutting applications, it was not until 1997 that Bienk and Mikkelsen highlighted their potential use as functional coatings for tools employed in injection moulding and plastic extrusion.⁴ This approach was motivated by the fact that the tools and moulds used in these technical processes are exposed to a complex load including predominantly abrasive and adhesive wear as well as corrosion, which all deteriorate the tools life-time and the quality of the product. It was reported that among several advantages nitridic hard coatings were observed to alleviate many of these issues.^{2,4} As an example, the use of TiAlN coatings drastically reduced abrasive and adhesive wear due to its high hardness and allowed to release tubes made from polypropylene or polyester by simple air blowing, which was not possible in the case of the uncoated steel moulds. Moreover, chromium based coatings such as CrAlN were shown to enhance the corrosion resistance, which is in agreement with their increased anodic and thermal oxidation resistance.⁵⁵

Investigations about the precise origin of the functional properties of hard coatings are still scarce in literature. However, recent investigations have shown that the improved release behaviour of polycarbonate based plastics from CrAlN surfaces can be explained by the lower surface energies of the coatings in comparison with the tool steel.⁵⁶ Similarly, a lower amount of shear energy required to tear off solidified polycarbonate or poly(methyl methacrylate) from $Cr_{0.5}Al_{0.3}N_{0.2}$ surfaces was demonstrated to correlate well with a lower wettability of these surfaces with the corresponding polymer melt.⁵⁷ These investigations show that obviously the performance of hard coatings is determined by their interfacial interactions with the polymer melt. In this regards, more fundamental

studies were performed by Music et al. by means of ab initio simulations to investigate the interactions of hard coating surfaces with model molecules. The authors showed that the nitridic $\text{Ti}_{0.5}\text{Al}_{0.5}\text{N}$ and $\text{Cr}_{0.5}\text{Al}_{0.5}\text{N}$ surfaces develop only weak interactions to propylene independent of their precise surface chemistry, but are highly reactive towards aliphatic radicals, which bind strongly to these surfaces.⁵⁸ In conclusion, the present literature about hard coatings in polymer melt processing well recognizes their technological advantages, but a thorough understanding of the interfacial structures and interaction forces is approached only recently.

2.1 Theory of oxidation

2.1.1 Low-temperature oxidation

Surfaces of clean metals and semiconductors have high surface energies in the range of 1000 mJ m^{-2} as a consequence of the presence of unsaturated dangling bonds.⁵⁹ The surfaces oxidize therefore already at low oxygen partial pressures ($<0.01 \text{ Pa}$) near room temperature and form surface oxide films with a thickness of around 1- 20 nm, which define their surface chemistry.⁶⁰ Thus, basic principles of this low-temperature oxidation process are therefore outlined in the following.⁶⁰⁻⁶⁸

The first initial step of oxidation is the chemisorption of oxygen, which is an activation-free process leading to dissociation and at least partial ionization of the O_2 molecule.⁶³ The resulting structures of the chemisorption layers are usually complex and largely affected by the conditions of oxygen exposure. As an example, four different metastable configurations exist in the case of the oxygen chemisorption on $\text{Ag}(110)$: physisorbed, molecularly chemisorbed, dissociatively chemisorbed oxygen and a dissolved, subsurface state can be observed.⁶⁸ Moreover, the surface oxygen species are often unstable and oxygen atoms are incorporated into subsurface layers by place-exchange reactions with metal cations, which are triggered by the heat of the chemisorption or by the image potential set up by the ionized oxygen atoms.^{62,63} The place-exchange process not necessarily decreases the surface energy instantaneously, but often continues until a surface oxide with a thickness of several monolayers is being formed and the image potential becomes negligible. When assuming that the image forces activate the initial fast oxidation, Fehlner and Mott pointed out that the resulting rate law is linear.⁶² In contrast, manifold rate laws are experimentally and theoretically observed when nucleation and recrystallization are present.⁶³ This teaches the general rule that the sole investigation of the kinetics for the analysis of oxidation mechanisms is not sufficient and complementary experimental means must be invoked.⁶⁵

Following the initial fast oxidation, a homogeneous electrical field is built up across the oxide by the surface oxygen ions. This adsorption induced Mott potential V then activates ionic transfer processes required for further surface oxide growth. A first model to describe this relatively slow oxidation process was developed by Cabrera and Mott.⁶¹ Within their theory, it is assumed that the rate-limiting

step of oxide growth is the injection of cations into the oxide and that the Mott potential is constant during film growth. The effect of the Mott potential V on the activation energy required to inject the cation with charge q into the oxide with the lattice constant a is illustrated in figure 4.

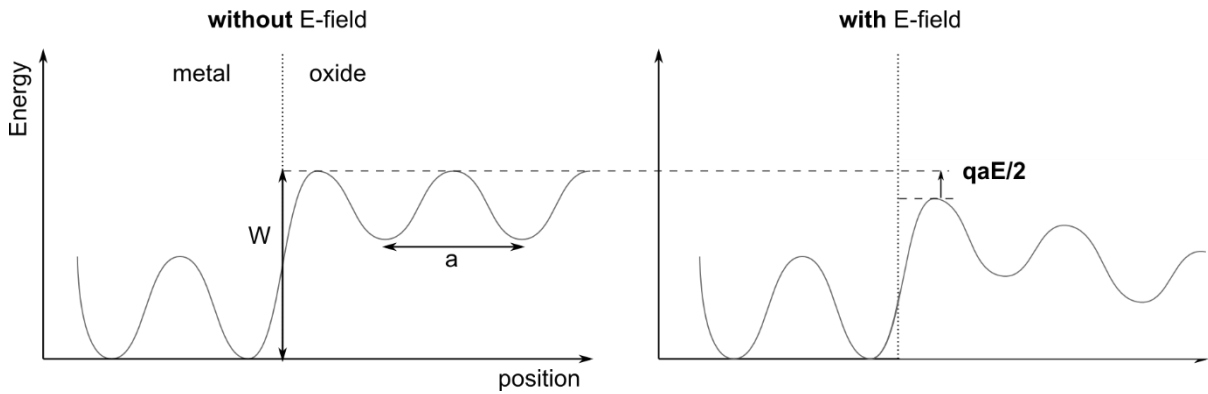


Figure 4: Illustration of the effect of the Mott potential on the activation energy required for injecting a cation into the oxide.

The idea is that the cation experiences a different lattice potential in the metal than in the oxide. Consequently, the interface is characterized by a steep potential rise W , which equals the activation energy for injection in the absence of an external potential. In this regards, the injection step can be assumed to be rate determining, because the activation energy for hopping of the cation within the oxide phase is smaller than W . The effect of the Mott potential is now that the lattice potential is pulled down so that the activation energy for injection is reduced. As depicted in figure 4, the decrease of the activation energy equals the electrostatic energy E to bring the cation to the maximum, which is $qaE/2$. By assuming further simple Arrhenius kinetics, the growth rate can be described by

$$\frac{dX}{dt} = av \exp\left(-\frac{W}{kT} + \frac{qaV}{2X}\right) \quad (1)$$

where X is the thickness of the film and v the frequency factor, which corresponds to the lattice vibration frequency. Equation (1) ultimately leads to an inverse logarithmic growth rate and to self-limited oxidation as the thickness increases the activation energy again. However, the assumption of rate-limiting charge injection into the oxide is a limiting case for high fields and thin films in the range of below 10 nm.⁶⁵ At larger film thicknesses, the migration of ions and defects within the oxide film becomes more relevant and above around 1 μm rate-limiting. This regime can be described by the phenomenological theory by Wagner, which is based on the consideration of mass transport by coupled diffusion so that a parabolic rate-law can be derived.⁶⁵

However, several refinements of the Cabrera-Mott theory were made and Fromhold introduced the concept of coupled currents, which allowed to include the charge neutrality condition.⁶⁴ An even more comprehensive theory was developed by Fromm to further account for the role of intermediate surface species.⁶⁰ The advantage of this model is that it considers up to three different rate-determining steps: the high-field assisted injection of ions, the flux of electrons from the metal to the surface and the coupled migration of ions and defects in a low electric field. Simulations based on the

Fromm model can thereby give realistic predictions of the effect of different physical parameters and chemical surface reactions. This approach thereby supports the analysis of low-temperature oxidation mechanism and is much more informative than fitting experimental kinetic data, because again rate laws do not allow to unambiguously conclude on the physical mechanism.

2.1.2 Electrochemical oxidation

As discussed in the foregoing section, the thermal oxidation of metal surfaces is driven by a potential set up by the chemisorption of oxygen. This picture can be directly transferred to the case of the electrochemical oxidation, where also an interfacial potential develops due to the redox-active particles in the electrolyte and the polarization of the metal. Thus, the high-field models of the thermal oxidation were directly used or expanded to describe the electrochemical oxidation as well.^{69,70} As an example, the Cabrera-Mott theory covers both oxidation mechanisms and also provides the basis for the advanced model of Kirchheim, which describes the passive film formation on iron.^{61,71} However, electrochemically formed surface oxide films are highly complex and thus no universal theory has emerged yet. Nowadays, two theories, namely the high field model (HFM) and the interface model (IFM), are therefore commonly employed for modelling experimental data.^{69,70,72–75} The scope of these models is largely restricted to simple homogeneous surface oxides of the so-called valve metals (Al, Ti, Zr, Hf, Nb, Ta). These metals are characterized by their ability to form homogeneous and thin surface oxides films with low electronic conductivities so that the potential drops mainly across the oxide film.⁷⁶

In this context, the oxide growth is explained by the HFM in terms of rate-limiting ion migration within the film.⁶⁹ The growth rate thereby increases linearly with the field strength at fields below 10^5 V cm^{-1} , but exponentially above a critical field strength of around 10^6 V cm^{-1} . When assuming that the current solely originates from the oxidation process, the growth rate becomes in the latter case

$$\frac{dX}{dt} = A \exp\left(-\beta \frac{V}{X(t)}\right) \quad (2)$$

where A and β are constants.^{69,72} Thus, the resulting growth law is self-limiting due to the continuously decreasing field strength and is usually approximated by an inverse logarithmic function of the form

$$\frac{1}{X} = A - B \log(t) \quad (3)$$

where B is another constant. It is noted that the HFM model in this form predicts endless oxide growth though oxidic barrier layers are commonly observed to reach a steady-state thickness as a consequence of the counteracting dissolution of the films. In order to take this aspect into account, a corresponding term can be therefore added to the growth rate in equation (2).

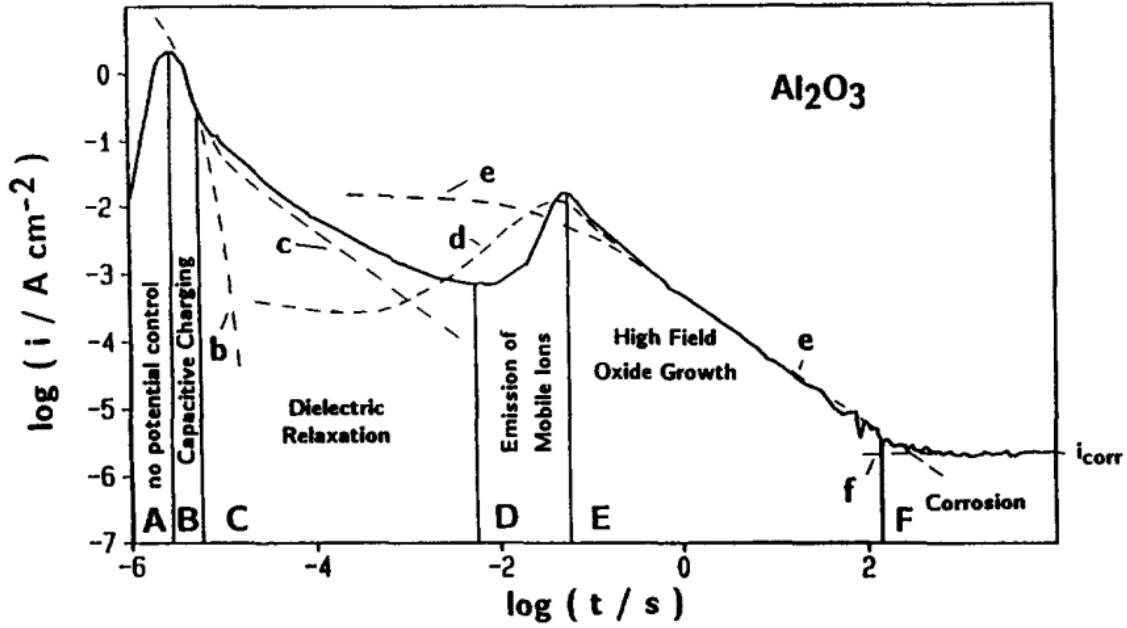


Figure 5: Current transient of an anodic Al|Al₂O₃ surface oxide film with a thickness of 10.9 nm after stepping the voltage from 0 to 6 V.⁶⁹ The dashed curves correspond to model calculations: the non-faradaic currents, which dominate in regions B and C, are derived from impedance measurements. The non-stationary emission of mobile ions in region D and the oxide growth in region E were simulated based on an extended HFM. (Reuse license No. 4322510765702, © Elsevier)

Despite the HFM in this basic form rationalizes the oxidation kinetics rather well, several short-comings and limitations require a refinement of the theory. Among these issues, the Tafel behaviour of the current and its temperature dependence as predicted by equation (2) is often not observed and especially the overshooting of the current as encountered during potentiodynamic polarization cannot be explained. Researchers have thereby focused on the investigation of current transients as obtained by potentiostatic pulsing in order to extend the HFM as thoroughly described in Lohrengel's review.⁶⁹ Such an experiment and its interpretation in terms of an extended HFM is shown in figure 5. The key idea of the extended HFM is that the oxide growth is anticipated by the injection of mobile ions at the interfaces into the oxide, which results into a regime with non-stationary fields and defect concentrations. This in turn explains the rapidly increasing current during the overshooting and shows that high defect concentrations in the range of a few percent of the lattice atoms are present during oxide growth. Based on this concept also the apparent Tafel anomalies could be resolved by temperature dependent measurements and were rationalised by counteracting corrosion and hydration of the oxide films.

In contrast to the HFM, the IFM assumes interface controlled kinetics and explains the self-limiting behaviour by the idea that the activation energy W required for film growth increases with the thickness X .⁷² This allows to derive rate equations of the form

$$\frac{dX}{dt} = A \exp\left(-\frac{W_0 + \mu X}{kT}\right) \quad (4)$$

where μ is a constant.⁷²

Logarithmic growth laws are then observed

$$X = K + L \log(1 + Mt) \quad (5)$$

where again K, L and M are constants. An example of the IFM is the Point Defect Model (PDM), which covers the steady-state only and considers different interfacial reactions to govern the state of the surface oxide.⁷³⁻⁷⁵ The PDM predicts several steady-state properties, which can be used as diagnostic criteria:⁷⁷ based on the assumptions that n-type semiconductors are doped due to oxygen vacancies and/or cation interstitials, the steady-state current is predicted to be independent on the applied voltage. In contrast, p-semiconductors are assumed to be characterized by cation vacancies and therefore show an exponential increase of the steady-state current with the potential. Moreover, the concentration of the metal vacancies is supposed to be unaffected by the pH value, while the other defects are. This for example rationalizes the pH induced transition of the semiconductor type of certain alloys.⁷⁸ An interesting prospect of the PDM is further its ability to define kinetic stability diagrams in analogy to the widely used thermodynamic Pourbaix diagrams.

Within the context of the practical analysis of anodic oxide films it is finally noted that the validation of the applicability of either the HFM or the IFM is not possible by simple comparison of the experimental kinetic data with the respective growth laws due to their similar lineshapes. Instead, Olsson et al. suggested to measure current transients within a two potential step sequence within the passive region. This allows to determine the oxidation current for a thin and a thick surface oxide layer. Since the HFM depends on the film thickness and the IFM not, these mechanisms can be distinguished. Moreover, another diagnostic criterion developed by Zhang et al. was refuted by Wu et al.^{79,80}

In conclusion, these models allow to describe the oxide formation in the simple case of the rather homogeneous oxide formation of the valve metals, but become impractical or fail when it comes to multi-layer formation, significant hydration or impurity incorporation of the oxide, high degrees of lateral heterogeneity or recrystallization.^{69,70}

2.2 Molecular Adhesion

2.2.1 Introduction

Complex adhesion mechanisms, as encountered at the macroscale, are the result of the superposition of different interactions acting at multiple length- and timescales.⁸¹ A comprehensive understanding of adhesion therefore requires the separate assessment of these contributions and is founded on a thorough investigation of the physical and chemical binding forces at the nanoscale, which ultimately cause adhesion. Basic concepts and approaches, which enable such a molecular understanding of adhesion, are therefore outlined in the following.

The formation of a surface of area A from the bulk is accompanied by thermodynamic work required to introduce the dangling bonds into the surface. This work is given by the corresponding change of the Gibbs free energy G and is termed surface energy γ

$$\gamma := \left(\frac{\partial G}{\partial A} \right)_{p,T} \quad (6)$$

where p and T are the pressure and temperature.⁸² In the case of an interface, these dangling bonds are only in parts compensated and an interface energy arises, which is also termed as γ and is similarly defined by equation (6). As an example, the creation of a surface in the case of a metal leads to the spilling of conduction band electrons out from the lattice into the vacuum due to their kinetic energy. As a consequence, a surface dipole structure is formed (Friedel oscillations) and all energy contributions (kinetic, electrostatic, exchange and correlation) are changed.^{83,84} Obviously, the surface energy of even such a fundamental model system is highly complex and it is consequentially practically impossible to understand or even to predict surface and interface energies in detail. However, it turned out that when it comes to the formation of an interface, also a single contribution only may dominate: the interactions between a non-reactive metal surface with an insulator in contact are for example governed by the exchange and correlation contributions, i.e. by the van der Waals forces.^{59,85} This illustrates that adhesion forces originate in general from manifold interactions but may also in specific cases be determined by a single contribution. The objective of a molecular understanding of adhesion is therefore to identify the atomic or molecular interaction forces and to assess their relevance in order to rationalize macroscale adhesion phenomena.⁸¹ In view of equation (13), this translates into an investigation of the partitioning of the thermodynamic interfacial energy into individual contributions related to specific molecular structures or types of forces.⁸⁶ This conceptual leap in understanding adhesion was already coined in the 1920s by Langmuir, who introduced the concept of the principle of Independent Surface Action (ISA): the ISA states that local surface energies can be assigned to molecular subunits.^{87,88} As an example, the surface energies of hexane and 1-hexanol are basically identical due to the fact that in both cases the aliphatic hexyl units point outwards and terminate the surface.

2.2.2 Experimental approaches

2.2.2.1 Contact angle

Several techniques enable the analysis of interfacial energies and among them, an instructive example and convenient method is the investigation of contact angles.^{89,90} Though the contact angle experiment is not used within this thesis, many concepts and thermodynamic principles with general validity were developed in this context and the method may be recognized as a link between the macro- and the nanoscale. A survey of the contact angle approach is therefore provided in the following.

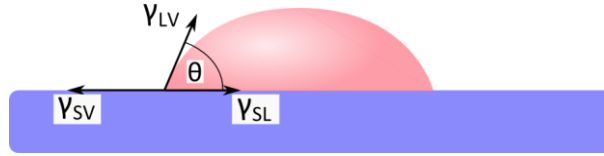


Figure 6: Illustration of the force equilibrium at the three phase boundary during a contact angle experiment.

As shown in figure 6, the equilibrium contact angle θ is measured at the three-phase boundary, which is defined by the balance of the solid-vapour (γ_{SV}), solid-liquid (γ_{SL}) and liquid-vapour (γ_{LV}) interfacial energies. This energy balance is expressed by the Young equation:

$$\gamma_{SV} = \gamma_{SL} + \gamma_{LV} \cos \theta \quad (7)$$

In order to complement the analysis, the thermodynamic adhesion energy W_{ad} is further considered and can according to Dupré generally be defined by a Born-Haber cycle:

$$W_{ad} = \gamma_{LV} + \gamma_{SV} - \gamma_{SL} \quad (8)$$

The combination of the latter two relations yield the Young-Dupré equation:

$$W_{ad} = \gamma_{LV}(1 + \cos \theta) \quad (9)$$

In this regards, the spreading pressure, which describes the interactions of the free solid surface with the gas atoms of the atmosphere, is neglected in the above equations, but this assumption is valid in the case of low-energy surfaces.⁹¹

In order to evaluate the Young equation, it must be first recognized that three variables are used. Among these, the surface energy of the liquid γ_{LV} can be precisely determined by other means (e.g. Wilhelmy plate).⁹² Moreover, the unknown variables are further reduced to a single one under the condition of the Dupré equation. The equations can then be solved easily for the specific case that the interfacial solid-liquid interactions originate from van der Waals forces only. This situation can be realized in the experiment by using a non-polar test liquid such as hexadecane, which only compensates the van der Waals forces at the interface.⁸² In this limit, the adhesion energy can be expressed as the geometric mean of the corresponding surface energies according to the Good and Girifalco mixing rule:^{93,94}

$$W_{ad}^d = \gamma_{LV}^d(1 + \cos \theta) = 2\sqrt{\gamma_{SV}^d \gamma_{LV}^d} \quad (10)$$

Here, the index d indicates that only van der Waals interaction energies are covered. In the case of a non-polar test liquid the liquids surface energy γ_{LV} is of course the same as γ_{LV}^d . Solving equation (10) then gives γ_{SV}^d and the Young equation yields γ_{SL}^d . The analysis can be completed by measuring also the contact angles of polar test liquids, which cause acid-base bonding and determine the corresponding adhesion energies. In these cases it was shown by Fowkes and later on by van Oss, Chaudhury and Good that the adhesion energy as well as the single surface or interface energies can be subdivided into individual contributions related to the van der Waals and acid-base interactions.^{86,95,96}

$$W_{ad} = W_{ad}^d + W_{ad}^{ab} \quad (11a)$$

$$\gamma = \gamma^d + \gamma^{ab} \quad (11b)$$

These relations can be regarded as the manifestation of the principle of independent surface action and is therefore of general validity. However, the van der Waals components of test liquids γ_{LV}^d can be separately determined so that the van der Waals component of the adhesion energies W_{ad}^d can be calculated.⁹¹ The comparison with the total adhesion energy then yields W_{ad}^{ab} according to equation (11a). For completeness, it is also noted that the analysis of contact angles is commonly extended by using purely empirical mixing rules for the acid-base adhesion energy based on the form of the Good and Girifalco mixing rule.^{86,97} As has been pointed out by Fowkes, this procedure is physically incorrect, but good consistency is found within the experiment and the benefit of this method is that also the adhesion energy between two solids can be estimated and related to acid-base and van der Waals components.^{90,91} Concluding, the analysis of contact angles can reveal the principal force contributions and their relevance for adhesion within a thermodynamic theoretical framework. However, the contact angle approach is rather restricted to the macroscale, but the use of model surfaces with well-defined properties allows the indirect investigation of adhesion and other processes at the molecular scale. Such model surfaces can be obtained by the self-assembled adsorption of bi-functional molecules: the head group of these molecules causes chemical bonding and adsorption to the substrate, whereas the tail group induces van der Waals attraction between the adsorbed molecules leading to two-dimensional crystallization into a highly ordered array.⁹⁸ Also molecules with terminal functional groups may be used so that the surface chemistry of the self-assembled monolayers (SAMs) can be controlled. In this regards, Bain and Whitesides investigated the wettability of SAMs either with terminal ether groups, which are in direct contact with the liquid, or with the ether groups placed into increasingly deeper sublayers.⁹⁹ The result was that the contact angle is sensitive to subsurface functional groups due to the penetration of probe molecules into sub layers. However, it could be shown that especially large molecules such as hexadecane or glycerol do less penetrate the interface due to their molecular size. Moreover, the same authors investigated SAMs with terminal acid groups and observed the reactive spreading of test liquid out from the drop, which leads to the formation of a molecular pre-wetting film.¹⁰⁰ Chaudhury et al. studied the effect of terminal polar or non-polar functional groups on their free surface energies by using well defined functionalized polymer surfaces.⁸⁸ Their contact angle experiments revealed a decreased surface energy of methyl terminated surfaces in comparison to surfaces with exposed methylene groups. This finding was unexpected due to the higher polarizability of the methyl group and it was proposed that the more efficient shielding of the carbon atom by the hydrogen atoms in the methyl group may explain the situation. The authors also showed that a terminal hydroxyl group increases the surface energy from 20 to around 55 mJ m⁻². This illustrates the high relevance of the surface chemistry for adhesion.

2.2.2.2 Atomic Force Microscopy

A true molecular approach to adhesion can be realized by using the Atomic Force Microscope (AFM) due its capability of measuring forces with pN sensitivity at even atomic resolution.¹⁰¹ The principle setup of this experiment is shown in figure 7. A cantilever with a sharp tip is brought into contact with a surface, while the deflection of a laser beam reflected by the cantilever is measured. As a result of the interaction forces between tip and surface, the cantilever is bend and the position of the laser spot on the detector is changed in proportion to the interaction forces. A calibration of the cantilever allows then to measure the force profile during the approach and retraction from the surface.¹⁰² This not only allows to investigate the adhesion force, but also to analyse the contact and non-contact regime.

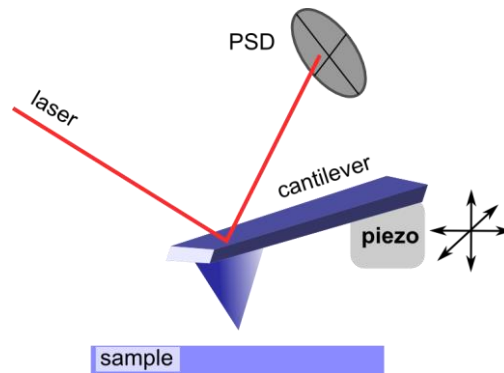


Figure 7: Setup of for basic Atomic Force Microscopy.

Several AFM techniques exist for investigating interactions at an interface as summarized in figure 8. Common to all these method is their ability to measure under specific conditions the binding forces of single bonds, which allows to estimate single binding energies ΔG^{ab} and thereby to predict the acid-base work of adhesion as a macroscale parameter

$$W_{ad}^{ab} = -N^{ab} \Delta G^{ab} \quad (12)$$

where N^{ab} is the number of bonds.⁸² As an example, Chemical Force Microscopy (CFM) was employed to determine adhesion energies for comparison with values derived from contact angle experiments. In CFM, the cantilevers tip is chemically modified with SAMs to control the surface chemistry.¹⁰³ Within the studies of Clear et al. and Tormoen, CFM was therefore used to measure adhesion forces on SAMs for studying the mutual interactions between NH_2 , COOH , COH and CH_3 groups.^{104,105} By using basic mechanical models, the authors were able to convert the adhesion forces to energies and to estimate the number of interacting chemical groups. Moreover, they found a good agreement between CFM and contact angle derived adhesion energies. Another approach to determine single binding forces was introduced by Skulason and Frisbie, which have shown that histograms of the adhesion force can show a periodic structure due to the rupture of individual bonds if the liquids surface energy is not too high, the tip sharp is enough and the probability of bond formation is close to unity.^{106,107}

However, these single bond forces must be interpreted carefully, because adhesion forces measured by the AFM are always related to the cantilever stiffness and loading rate due to the combination of the spring potential of the cantilever with the tip-sample interaction potential.^{108–110} This very important aspect was neglected in these early studies, but its relevance was highlighted by Merkel et al., who investigated the loading rate dependence of the biotin-streptavidin interactions and observed single bond strengths ranging from 5-170 pN.¹¹¹ In this regards, the theoretical modelling of the Atomic Force Spectroscopy experiment with soft levers is complex and still continues.^{108–110} However, Noy pointed out that thermodynamic bond energies can be determined at low loading rates in the range of around 1 nN s^{-1} .¹¹² In this regime, Friddle et al. measured adhesion force distributions and could estimate the single bond energy between COOH groups in ethanol to around 5.7 kJ mol^{-1} .¹¹³

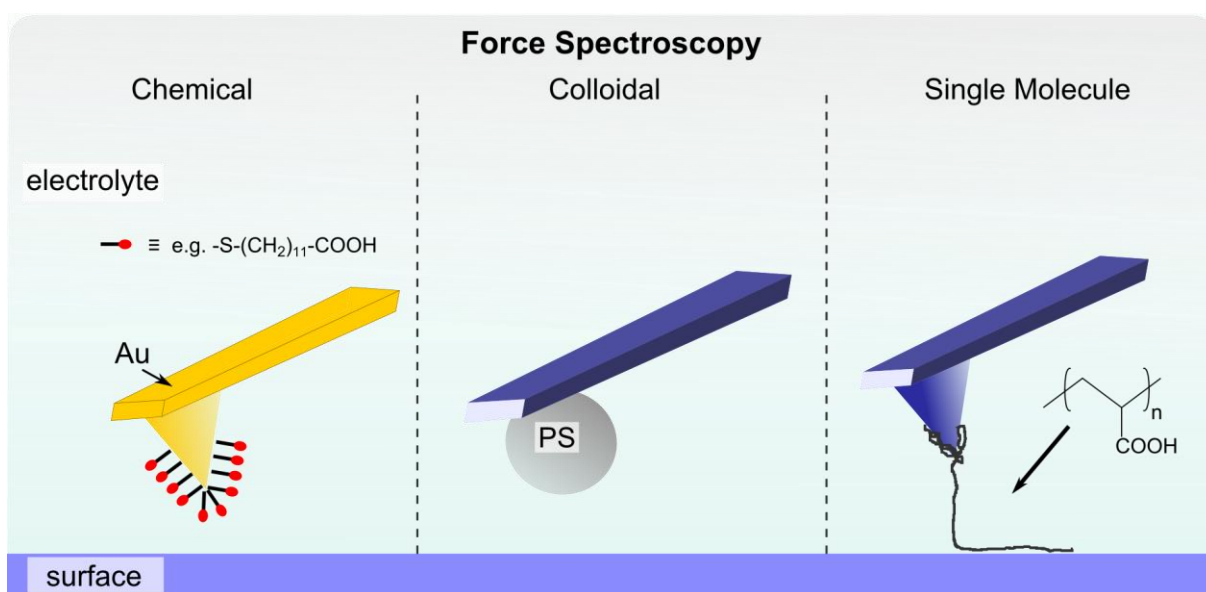


Figure 8: Illustration of the basic setups of Chemical, Colloidal and Single Molecule Force Spectroscopy.

A similar technique is the Single Molecule Atomic Force Spectroscopy (SMFS), where a polymeric linker is used to attach a probe molecule to the AFM tip.^{114,115} Alternatively, also the polymer of interest may be directly bound to the cantilever. The benefit of this configuration is that rebinding events are suppressed and also the interacting functionality of the tip can be precisely controlled. Using this technique, the interaction forces between single amine and ether groups with the single-crystalline $\text{Al}_2\text{O}_3(11-20)$ surface were investigated in water.¹¹⁶ The adhesive interactions could be therefore ascribed to coordination of the nitrogen and oxygen atoms to the Al ions in the oxides surface via the non-bonding O2p electrons. Moreover, SMFS is ideally suited to investigate unfolding forces of polymers.¹¹⁷ A rigorous theoretical description of this experiment was developed by Szabo and Hummer and allowed to quantitatively recover the free energy landscape of the polymers intramolecular interactions as demonstrated by Gupta et al. in the case of DNA hairpins.^{118,119}

Another technique is the Colloidal Force Spectroscopy, where a particle attached to the cantilever beam is used to probe the force interactions.^{120,121} Obviously, the direct measurement of surface-particle or particle-particle interactions becomes possible, which is of high relevance for understanding the behaviour of powders. As an example, Rabinovich et al. investigated the adhesion between a silica microsphere and a silica surface under control of the humidity.^{122,123} It could be shown, that the adhesion force is governed by the formation of a water meniscus, which forms within a few 10 s at a humidity level of above 30 %. Based on the well-defined geometry of the experiment, the authors could further developed a kinetic model of the meniscus formation for rationalizing their experimental data. Besides a more facile theoretical modelling of the experiment, another advantage of the experimental geometry of the colloidal probe is that the stress within the contact region can be kept relatively low in comparison to the stress developed by sharp probes on surfaces with tip radii of around 10 nm. The interactions of polymers with solid surfaces can be therefore investigated more carefully. In this regards, Biggs et al. analysed the role of viscoelasticity for adhesion and could show that the adhesion force of a polystyrene bead on mica is governed at low loads by its elastic behaviour, while at high loads visco-elastic and plastic deformation affect the adhesion in agreement with the Maugis-Pollock theory.¹²⁴

Besides force spectroscopic experiments, also topographic studies have aided the molecular understanding of interaction forces: the strong attractive interactions observed between hydrophobic surfaces within a polar liquid (“hydrophobic forces”) have raised an intense debate about their origin.¹⁰¹ Though the situation does not seem to be finally settled, it turned out that a cavity can form upon retraction explaining the long-range attractive forces.^{125,126} However, strong attraction is also observed upon approach and this could be rationalized by incomplete wetting of the hydrophobic surfaces due to the presence of nanobubbles, which were visualized by topographic measurements.¹²⁷

2.3 Van der Waals interactions

Van der Waals interactions are fundamental forces and act between two bodies irrespective of their composition and size. These interaction forces were first noticed by Johannes Diderik van der Waals within his investigations about the state of gases at elevated temperatures. The effect of the van der Waals forces was in this context the mutual attraction of neutral gas particles, which leads to a self-compression of the gas. Van der Waals interactions are also highly relevant when understanding forces between low energy surfaces such as polymers and are therefore particularly considered within this thesis.⁸⁸ In the following, basic principles and fundamental aspects of van der Waals forces are therefore revisited.

2.3.1 The Hamaker approach

The classic approach introduced by Hamaker for describing van der Waals forces between two macroscopic bodies is to consider first the interaction between particles and then to apply pairwise summation to describe the behaviour of condensed materials.¹²⁸ At the particle level, three different interaction mechanisms can be distinguished as shown in figure 9: firstly, the Keesom force is caused by the interactions of two static dipoles. The force between a static and an induced dipole is called the Debye force and the London dispersion force acts between induced dipoles. It is important to note, that all these individual contributions scale with d^{-6} and can thereby not be differentiated by the form of an experimental force/potential curve.

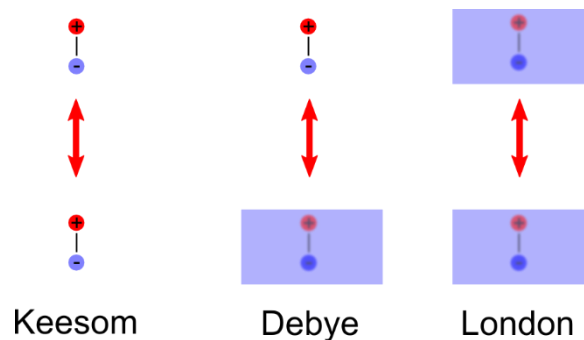


Figure 9: Illustration of the physical origin of the Keesom, Debye and London van der Waals force contributions.

However, Hamaker described the total force between two bodies by assuming that the mutual particle interactions do not affect each other within a condensed material. By making further use of the Derjaguin transformation, simple power-laws can then be derived for specific geometries as shown in figure 10.¹²⁹

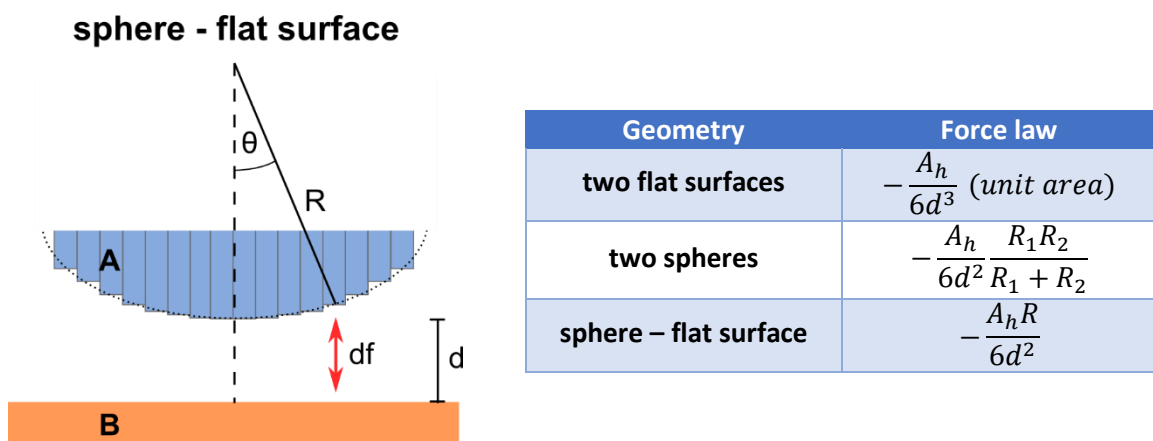


Figure 10: Derjaguin approximation of the sphere – flat surface case and resulting force laws also for two flat surfaces and two spheres.

The basic concept of the Derjaguin approximation is that the geometry of a complex shaped body can be divided into building blocks with simple geometries. In the case of a sphere interacting with a flat surface, the sphere can therefore be represented by an assembly of infinitesimal concentric rings as

shown (see figure 10). Though this approach is intuitive and mathematically relatively straightforward, the Derjaguin transformation requires that such infinitesimal homogeneous portions can be defined. This is only possible if the curvature is low and the nanoscale graininess of the surfaces due to the atoms can be neglected. The approximation therefore fails at molecular distances but also at large separations, where the influence of steep edges raises. The most striking result of the Hamaker approach is that the force laws show a simple structuring and are composed of a geometric factor and the so called Hamaker coefficient A_h only. The Hamaker coefficient in turn accounts for the complete interaction forces and is defined by the single-particle interaction constant and the particle densities of the materials. Concluding, adhesive phenomena by van der Waals forces can be thus seamlessly separated into material and geometric effects for their analysis.

2.3.2 The theory of Lifshitz, Dzyaloshinsky and Pitaevskii

The origin of van der Waals forces are the collective fluctuations of electromagnetic fields between two bodies or particles. These fluctuations emerge due to the uncertainty of the energy of electromagnetic fields so that the van der Waals forces are a true quantum dynamical phenomenon.¹³⁰ Thus, Lifshitz, Dzyaloshinsky and Pitaevskii developed a quantum dynamical framework for a quantitative description of van der Waals forces and for simplicity, this theory is called Lifshitz theory further on.¹³⁰ Interestingly, the Lifshitz theory allows to calculate Hamaker coefficients and force laws directly from the optical properties of the materials in form of the complex dielectric function ϵ . In the following, central equations of the Lifshitz theory are reviewed in order to illustrate different physical and practical aspects of this approach.

The Lifshitz approach to derive the van der Waals force laws from the optical behaviour of materials can be rationalized when considering that the collective oscillations can only occur at their natural oscillation frequencies, which can be determined from optical experiments. Obviously, all frequencies contribute to the overall force, but the quantum dynamical nature of the van der Waals forces is also reflected in the Lifshitz formalism and obscures this aspect: the evaluation of the dielectric function $\epsilon(\omega)$ is performed by first converting the frequency axis ω to imaginary frequencies $i\omega$ and considering then only specific values at the so-called Matsubara frequencies ξ . The Kramers-Kronig type transformation and the Matsubara frequencies are described by¹³¹

$$\epsilon(i\xi) = 1 + \frac{2}{\pi} \int_0^{\infty} \frac{\omega \epsilon''(0, \omega)}{\omega^2 + \xi^2} d\omega \quad (13a)$$

$$\xi_n = \frac{2\pi kT}{\hbar} n \quad (13b)$$

where ϵ'' is the imaginary part of the dielectric function, ξ_n the n th Matsubara frequency, k the Boltzmann constant, \hbar the Planck constant divided by 2π and T the temperature. When inspecting these equations, it becomes clear that the Matsubara frequency is equidistant and starts around

1200 nm. Nevertheless, this does not mean that only portions of the dielectric function are required, because the transform in equation (13a) covers the whole spectrum in agreement with the aforementioned. The Lifshitz theory is therefore scarcely used in practical surface analysis yet, because the dielectric function is usually not available and only very few techniques can measure it up into the important high energy range of 30 eV or more.

Based on the dielectric function, the interaction forces are then determined by evaluating *differences* in the “polarizabilities”, as reflected by $\epsilon(i\omega)$, as shown by the following approximate expression for the limit of distances approaching contact:¹³¹

$$A_h = \frac{3}{2} kT \sum_{n=0}^{\infty} ' \sum_{q=1}^{\infty} \frac{(\Delta_{Am} \Delta_{Bm})^q}{q^3} \quad (13c)$$

$$\Delta_{jm} = \frac{\epsilon_j - \epsilon_m}{\epsilon_j + \epsilon_m} \quad (13d)$$

In these equations, the index m represents the medium and A and B the respective materials of the two bodies. The stroke of the first sum indicates, that the static term has to be multiplied by 0.5. These relations illustrate that the intervening medium screens the interactions except for vacuum, which behaves neutral. This screening can result not only into decreased forces but can also lead to a net repulsion given that the polarizability of the medium is in between that of A and B. The consequence is that the system then tries to relocate the less polarizable phase in between. Another interesting aspect is the temperature dependence of equation (13c), which suggests a linear behaviour. In contrast, the Matsubara frequencies similarly shift and the net effect is in fact that the temperature has no significance, which means that the mechanism of the collective fluctuations in itself is unaffected by the temperature. Instead, the temperature dependence of the van der Waals forces is determined by the influence of the temperature on the optical behaviour of the materials, i. e. on the electronic structure.¹³²

The picture of collective electromagnetic fluctuations has also another crucial implication: with increasing distances, the oscillators become out of step and are therefore more loosely coupled to each other resulting into decreased interaction forces.¹³³ As a consequence of this so called retardation effect, the Hamaker coefficient becomes a function of the distance and is at large distances determined by the static contribution of $\epsilon(i\omega)$ only, where the Matsubara frequency is zero. However, the Hamaker coefficient also becomes a function of the specific geometry, because at increasing distances all parts of the interacting bodies become of similar relevance for the total interactions and the effective geometry changes.¹³¹

Finally, it must be noted that even the Lifshitz theory does not allow to directly calculate van der Waals contributions to experimental adhesion forces for several reasons: First, the Lifshitz and Hamaker approach are continuum models, which fail at close distances. This becomes clear even from a practical

point of view: the equilibrium distance d_0 is usually not known though being sometimes successfully assumed to be 0.165 nm.¹³⁴ Furthermore, roughness becomes of increasing relevance at short distances and affects the magnitude of the Hamaker coefficient as well as it brings the continuum approach to its limits for obvious reasons.¹³⁵ Physically, also non-local effects must be considered at close distances, which are caused by the coupling of the environment to local optical excitations and result into decreased interactions.^{136–138} Moreover, the continuum theories do not cover the dipole present at the surface, which is essentially a result of uncompensated electromagnetic fields.

2.4 Acid-Base interactions and coordinative bonds

Coordinative bonds formed by Lewis acid-base interactions at an interface can be an important contributor to the overall interfacial energy and govern molecular interfacial processes. Especially in cases where the van der Waals interactions are almost completely screened by the intervening medium, the acid-base interactions often determine the interfacial forces as for example in the case of polymer adsorption.¹³⁹ Consequently, fundamental aspects of interfacial acid-base interactions are presented in the following.^{140–142}

The energy of the interaction between a nucleophile and an electrophile ΔE has been derived from perturbation theory by Klopman and Hudson and can be described by

$$\Delta E = -\frac{Q_{nu}Q_{el}}{\epsilon R} + \frac{2(\beta C_{nu}C_{el})^2}{E_{HOMO} - E_{LUMO}} \quad (14)$$

where Q_{nu} and Q_{el} are the charges of the donor and acceptor, ϵ the static permittivity, R the distance, C_{nu} and C_{el} coefficients of the atomic orbitals, β the resonance integral and E_{HOMO} and E_{LUMO} the energies of the highest and lowest unoccupied molecular orbitals.¹⁴³ The first term in this equation corresponds to the Coulomb interactions between the molecules or atoms and the second to the binding interactions of the frontier orbitals. This description of binding energies could provide a first quantitative framework for Pearson's Hard-Soft Acid-Base (HSAB) principle used for explaining molecular acid-base interactions.¹⁴⁴ The HSAB can therefore be explained as follows:

- 1) Hard-hard interactions, as observed between molecules with low polarizability are governed by electrostatic interactions.
- 2) Soft-soft interactions, as observed between molecules with high polarizability are governed by the binding interactions caused by their frontier orbital overlap.

Though acid-base interactions are well rationalized the HSAB principle, the interactions between surfaces are not directly covered by this model. In this regards, Rose et al. investigated in 1981 the metal-metal interface by ab initio methods and found a universal scaling behaviour of the interaction potential (which they termed as adhesion energy).¹⁴⁵ The scaled potential curve was found to depend only on the equilibrium binding energy and the interstitial electron density. Most importantly, it turned

out that their scaling law shows a universal behaviour and covers not only bimetallic interfaces, but also the energy of the interactions between diatomic-molecules, cohesion in solids, chemisorption and interactions within nuclear matter.¹⁴⁶ This coined the term Universal Binding Energy Relation (UBER), which can be expressed as

$$E(d) = -E_0(1 + d^*) \exp(-d^*) \quad (15a)$$

$$d^* = \frac{d - d_0}{l} \quad (15b)$$

where E is the total energy, d the distance, E₀ the equilibrium energy, d₀ the equilibrium distance and l a scaling constant, which is in the range of the Thomas-Fermi length (around 50 pm).^{142,147} As pointed out by Banerjea et al., the surprising universality of the scaling law originates from the key role of the electron density, which is also scalable and decays as a good approximation always exponentially into vacuum or defect sites.¹⁴⁶ The UBER equation could also be expanded to cover additional electrostatic interactions in molecules or across interfaces due to charge transfer (e.g. alkali halides):

$$E(d) = -CE_0(1 + d^*) \exp(-d^*) - (\delta Z)^2/d \quad (16)$$

Here, C in the first overlap term is a measure of the magnitude of covalent interactions and δZ in the second Coloumbic term is the effective charge transferred.¹⁴² Smith also highlighted that the overlap usually dominates, because electrostatic interactions are only relevant at increasing distances due to their higher decay length.¹⁴² It is interesting to compare the Klopman and Hudsons expression for coordinative bonding in equation (13) and the UBER equation: the physical meaning of the single terms directly translate into each other.

A convenient description of acid-base interaction enthalpies was given by Drago.¹⁴⁸ The enthalpy of the bond ΔH^{ab} can be therefore described by

$$-\Delta H^{ab} = C_A C_B + E_A E_B \quad (17)$$

where C and E are the covalent and electrostatic parts of the interactions by the molecules A and B.¹⁴⁸ Again it is noted that the similar physical meaning of the terms in this equation is in agreement with the latter relations. The E and C parameters of Drago's relation can be determined by microcalorimetry or by spectroscopic means.^{88,149} For example the infrared band of the stretching frequency of the C=O bond of ethyl acetate in hexane was shown to shift linearly with the enthalpy of the bond ΔH^{ab} of the acid-base complex.¹⁴⁹ Thus, simple infrared spectra of at least two complexation experiments allows to determine unknown E and C parameters. The accuracy of this approach is within 5 %, but is limited by the assumption that a molecule is considered to have either acidic or basic character. Amphoteric surfaces are thereby not directly covered and the C and E parameters of the interfaces under investigation are therefore usually not available in practical adhesion analysis. The estimation of binding energies by the Bolger-Michaels method is therefore more useful in practical situations.⁸⁸ The binding energy ΔG^{ab} is in this model given by

$$\text{acid: } \Delta G^{ab} = -RT (IEPS - pK_a) \quad (18a)$$

$$\text{base: } \Delta G^{ab} = -RT (pK_a - IEPS) \quad (18b)$$

where IEPS is the isoelectric point of the surface, R the universal gas constant, T the temperature and the pK_a the negative logarithm of the acids or bases dissociation constant. This estimation is especially valuable, because in the case of high bonding energies, the surface is going to be corroded and possibly forms a conversion layer.

2.5 Adsorption of polymers from the melt

The structure and physical properties of polymers in the vicinity (< 10-20 nm) of a wettable surface are strongly perturbed due to the interfacial forces and deviate therefore significantly from the bulk properties. This is manifested by changed glass transition temperatures, decreased static polarizabilities and chain mobility, increased densities and the irreversible formation of the adsorbed layers.^{150,151} In contrast to the adsorption of polymers from solution, which is today theoretically as well as experimentally rather well understood, the adsorption from the melt is poorly investigated though being of major relevance for the thermal processing of polymers.^{152–154} In the following, an overview about basic principles and the current state of research is therefore provided.

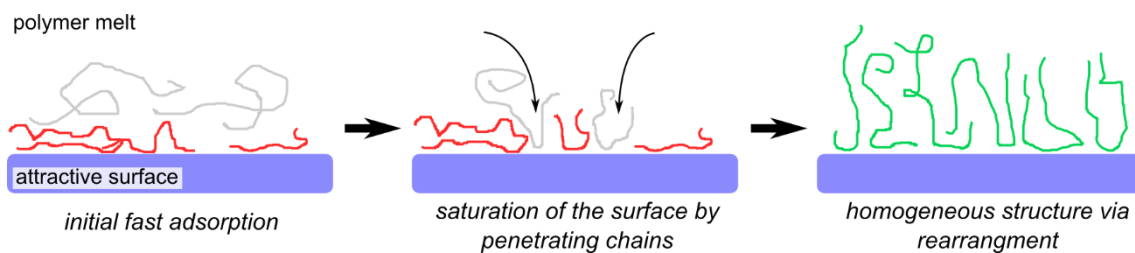


Figure 11: Illustration of the different steps and processes of the adsorption of polymers to surfaces out from the melt.

The interface between a polymer melt and a wettable surface is stabilized by van der Waals and acid base interactions. Whereas the van der Waals interactions are maximized quasi instantaneously as the interface forms, the localized acid-base interactions develop at very slow timescales possibly even exceeding the timescale of the experiment.^{155,156} As discussed within the publications of Napolitano et al, the adsorption is a multi-step process as depicted in figure 11.^{150,156,157} the first step of interface formation is the diffusion of chains to the surface to adsorb at free surface sites. The polymers adopt in this initial fast step flat conformations with many trains pinned to the surface so that the chain mobility decreases.^{158,159} Due to the dynamic binding and unbinding of monomers, the polymer optimizes its conformations to even more increase the number of intimate monomer-surface contacts. This process is accompanied by the penetration of the adsorbed layer by unbound polymer coils to adsorb on the few left free surface sites. These polymer chains must therefore stretch and adapt their conformations to fit into the constrained space between the flat adsorbed chains and therefore lose high-rate mobility modes as revealed by broadband dielectric spectroscopy.¹⁵⁶ The bimodal

distribution of the polymer chains is then removed within the last stage of the adsorption by the continued dynamical un- and rebinding of the monomers. As a consequence, the fraction of adsorbed trains decreases in favour of the formation of loops and tails and the low-rate mobility modes related to the trains are reduced. This process is also reflected in the thickness of the adsorbed layer h_{ads} , which develops with time t by

$$h_{ads}(t) = \begin{cases} h_{t=0} + vt & t \ll t_{cross} \\ h_{cross} + \Pi \log t & t \gg t_{cross} \end{cases} \quad (19)$$

where v and Π are the rate constants of the linear and the logarithmic regime, h_{cross} and t_{cross} the thickness and time at the cross-over point of the kinetics.^{150,157} In this view, the linear regime corresponds to the initial fast adsorption of polymers with flat chain configurations. The logarithmic rate law in turn describes the adsorption of penetrating chains with stretched configurations kinetically limited by the formation of loops out of trains to reveal free surface sites.¹⁶⁰ Since the chains obey the model of random walk reflected at a wall, the height h_{ads} scales at all times with the polymerization number N as $N^{1/2}$.^{157,161} This also means that the cross-over height h_{cross} scales with $N^{1/2}$, whereas the cross-over time t_{cross} scales with N^0 . In this regards, the insensitivity of t_{cross} can be explained by the scaling of v with $N^{1/2}$. These results including the rate laws in equation (20) were recently corroborated by simulations.¹⁶⁰

The role of the energy of the acid-base interactions for the adsorption of polymers is in the view of the aforementioned obscured. Basically, the interfacial energy increases the amount of adsorbed monomers at the surface.¹⁵⁰ Moreover, it was shown that the maximum attainably thickness h_{max} increases with increasing interaction energy between the polymer and the surface, but the formation of this quasi-equilibrium state also requires longer annealing times.¹⁵⁹

3 Advanced experimental methods

3.1 X-Ray Photoelectron Spectroscopy (XPS)

3.1.1 Basic principles

The experimental principles of XPS are illustrated in figure 12a. In a simple XPS experiment, a surface is irradiated in vacuum ($< 10^{-3}$ Pa) with light having energies in the X-ray regime (typically 1200-1500 eV). This provokes the photoemission of electrons of which the intensity and the kinetic energy distribution are detected by an electron spectrometer.¹⁶² The kinetic energies of the photoelectrons are rather low and efficient stopping of the electrons occurs due to inelastic optical transitions in the matrix and elastic backscattering.¹⁶³⁻¹⁶⁵ The path travelled by the electrons before being detected is therefore low and XPS shows a very high surface sensitivity. In this regard, the inelastic mean free paths (IMFP) describes the path length travelled before an electron undergoes an inelastic collision and is in the range of 1-3 nm. Based on the IMFP, the depth of information can be approximated to

around $3 \cdot \text{IMFP}$, i.e. 5-10 nm.¹⁶⁶ However, the depth of information also depends on the angle of emission θ due to the geometry of the experiment as shown in figure 12b. For these reasons, the angle of emission θ is also typically controlled in XPS experiments and angle-resolved spectra can be investigated to conclude on concentration depth profiles.¹⁶⁷

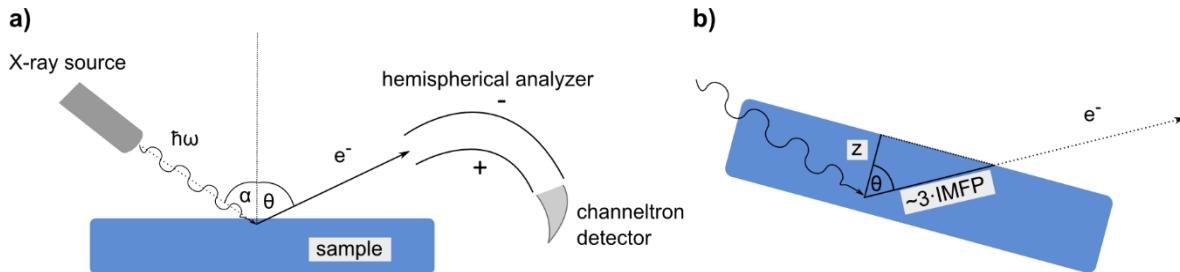


Figure 12: **a)** Typical experimental setup used for XPS including an X-ray source, a hemispherical electron analyser and a channeltron detector.¹⁶² **b)** Geometry of the path travelled by the photoelectron in an angle-resolved experiment.

An energetic description of the photoemission process is depicted in figure 13. As an approximation, the photoemission can be considered to be a three step process:¹⁶⁸ in the first step, core level and valence band electronic states of the solid are ionized due to the high energy of the X-rays. The so formed photoelectrons show a spectrum of kinetic energies due to the individual potentials of the orbitals they originate from. Then, the photoelectrons are transported to the surface, which is accompanied by energy losses and the formation of secondary electrons.

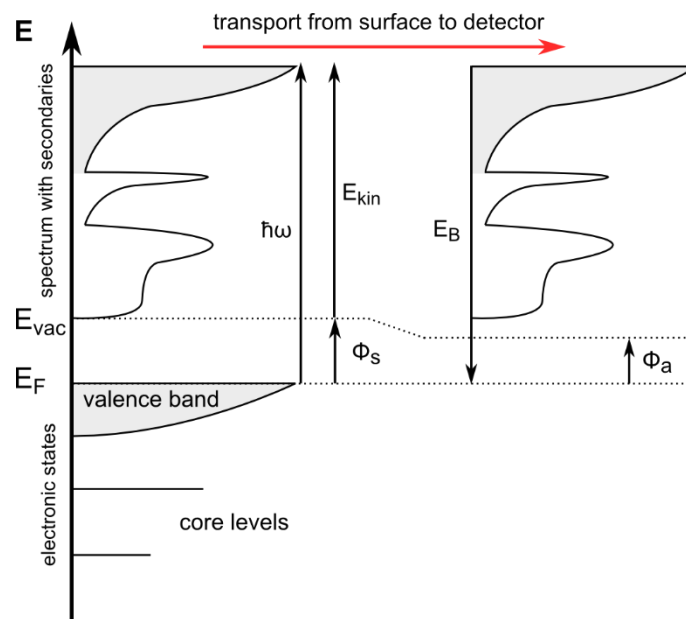


Figure 13: Energy diagram of the photoemission of electrons from a solid sample with the work function Φ_s due to incoming light with an energy of $\hbar\omega$. The photoelectrons are post-accelerated when travelling to the detector due to the alignment of the Fermi level of detector and sample by grounding.

In the third step, the electrons must penetrate the surface and as a consequence the slowest electrons with kinetic energies being lower than the work function of the sample Φ_s are removed from the kinetic energy spectrum. This picture explains qualitatively the typical form of an XPS spectrum, which

resembles the electronic structure of the sample overlaid by an inelastic background and a cut-off at low kinetic energies.

However, the detection of the electrons requires them to travel to the detector and this transport across vacuum is accompanied by an additional electrical work caused by the contact potential between the sample and the detector. Since the Fermi levels of the sample and the detector are both aligned due to grounding, the additional electrical work is then given by $-\Phi_s + \Phi_a$. According to the principle of the conservation of energy, the kinetic energy spectrum is therefore given by

$$E_{kin} = \hbar\omega - E_B - \Phi_s - (-\Phi_s + \Phi_a) = \hbar\omega - E_B - \Phi_a \quad (20)$$

where E_B is the binding energy of the electron in the solid and Φ_a the work function of the detector.¹⁶⁶ This shows, that the experimental binding energies are independent of the work function of the individual sample, but are referenced to the calibrated work function of the analyser.¹⁶⁹ Instead, the samples work function Φ_s is reflected by the total width of the XPS spectrum.

It is important to note that the photoemission process is not adiabatic and the core hole created during the photoemission process can also relax by many-body interactions which results into increased kinetic energies of the photoelectron (corresponding to decreased binding energies). Relaxation can even cause the occurrence of multiple core level signals if the time scale of relaxation is at the time scale of the photoemission.¹⁶⁸ For these reasons, the binding energy E_B of the photoelectrons is not defined by equation (20), but rather by the difference between the initial ground state energy of the n -electron system and the final energy of the relaxed $(n-1)$ -electron system, which further includes the reorganisation of the electronic structure of the system due to the presence of the core hole:^{166,170}

$$E_B := E_{n-1}(final) - E_n(initial) \quad (21)$$

In this view, an XPS experiment allows the determination of the binding energies of electrons, which are specifically related to their orbital energies and therefore to the nature of the elements they originate from. For these reasons, a wide energy-range XPS spectrum as schematically shown in figure 13 allows to determine the elemental composition of the sample.

3.1.2 Analysis of chemical effects in XPS

The chemical structure of a material has a significant influence on the whole XPS spectrum. Particularly, core level binding energies are affected by chemical effects and shifts are usually observed between different chemical compounds.¹⁷¹ These binding energy shift ΔE_B can be analysed to conclude on the chemical properties of the materials, but this procedure is hampered by superimposed physical effects as described in several reviews.^{166,168,170,172-175} In this view, the binding energy shift must be regarded as a complex observable, which is not only influenced by chemical effects, but also by environmental (charging¹⁷⁶, local electric fields^{177,178}), intra-atomic (e.g. configuration interactions¹⁷⁹, intrinsic plasmons¹⁸⁰) and by other initial and final state effects as well as by their interplay.^{170,173} The scope of

this chapter is therefore to rationalize the effect of the materials chemistry on XPS core level binding energies and to introduce strategies for its analysis.

As a first attempt to explain core level binding energy shifts, a qualitative correlation between the partial charge residing on an atom and the binding energies of core levels was established within the original work of Siegbahn et al.¹⁷¹ In this approach, the orbitals were assumed to be represented by concentric spheres having a uniform charge distribution. The binding energy of a core electron increases in this picture linearly with the oxidation number so that the chemical shift is additive. These principles were developed within the potential model using simple electrostatics and later on by means of quantum mechanics, which allowed to relate the chemical shifts observed for different sets of various organic and inorganic compounds to the net charges residing on the atoms.^{181–186} The binding energy shift between a core level of a free atom and that of a chemical compound is within the potential model given by

$$\Delta E_B = kq_i + V_i + l \quad (22a)$$

$$V_i = \sum_j \frac{q_j}{R_{ij}} \quad (22b)$$

where k is an element specific constant, q_i the (fractional) charge of atom i , V_i the molecular potential at nucleus i , R_{ij} the distance between nuclei i and j and l a constant depending on the choice of the reference level.^{184,185} The first term reflects the electrostatic potential caused by the valence charge at the core level so that k can be approximated by the reciprocal of the valence radius.^{173,187} The second term resembles the potential induced by the surrounding atoms at the core level, which corresponds for ionic compounds to the Madelung potential.¹⁸⁷ It is therefore highlighted that the intuitive purely chemical interpretation of XPS core level binding energy shifts of solids totally in terms of valence charges is therefore inaccurate and only valid for single gaseous atoms. In solids, the binding energy shift is according to the simple potential model further influenced by an additional environmental potential. The high relevance of this effect is illustrated by the chemical shifts observed for the alkaline earth oxides: the metal oxides show lower binding energies than the corresponding metals due to an overcompensation of the positive shift induced by the cations valence charges by the intense Madelung potential in the oxidic compounds.^{188,189}

The potential model in the form of equation (22) covers not only a few ionic systems, but particularly also covalently bound molecules due to the use of partial charges. Binding energy shifts can be thereby estimated by calculating these charges or electronegativities based on valence band electron distributions in the initial ground state.¹⁸³ The numerical effort to evaluate equation (22) by the calculation of charges can be relatively low and even semi-empirical quantum chemical calculations involving valence electrons only may be used.¹⁸⁴ Consequently, this procedure can in simple cases also be inverted to calculate charges from experimental chemical shifts as noted earlier.¹⁸⁵

However, though the potential model successfully explains the trends of the chemical shifts observed in sets of molecular closed-shell compounds, several simplifications prevent its universal use.^{172,190,170} To clarify this aspect, it is highlighted that the potential model relies on the sudden approximation and the related Koopman's theorem.¹⁹¹ The sudden approximation, which is accurate for photon energies with energies being ~100-200 eV above the photoionization threshold, assumes that the final state wavefunction can be described by a one electron continuum wavefunction in combination with the wavefunction of the (N-1) electron bound state.¹⁹² Moreover, the (N-1) wavefunction is assumed to be simply determined by removing an electron from the emitting orbital with the other orbitals left unchanged. This wavefunction is therefore called the frozen orbital wavefunction, because the surrounding orbitals are "frozen" and unaffected by the photoemission process. The potential model therefore only accounts for the initial state effects and neglects any relaxation. On the basis of the sudden approximation, Koopman's theorem states that for a closed-shell system the binding energy of the photoelectron is given by the negative Hartree-Fock ground state energy ϵ_i^{HF} of the frozen orbital i .¹⁷³ This principle is not restricted to closed-shell compounds, but could also be extended to open-shell systems.¹⁹³ In this view, it is assumed within the potential model that the binding energy shift ΔE_B can be approximated by the change of the Koopman's binding energy $-\Delta\epsilon_i^{HF}$ while changes of the relativistic ΔE_i^{rel} , the electron-electron correlation ΔE_i^{corr} and of the reorganization energy ΔE_i^{reorg} can be neglected as shown in equation (23).¹⁷²

$$\Delta E_B = -\Delta\epsilon_i^{HF} + \Delta E_i^{reorg} + \Delta^2 E_i^{corr} + \Delta^2 E_i^{rel} \cong -\Delta\epsilon_i^{HF} \quad (23)$$

As a consequence, observed chemical shifts are assumed to be solely determined by the initial ground state properties of the wavefunctions without relaxation taking effect after the generation of the core hole, which is obviously a main inherent inaccuracy. Furthermore, the potential model treats charge distributions within a point model and as a consequence neglects the influence of interpenetrating orbitals and the possible formation of bonding levels with covalent character.¹⁷³ Such hybridization can either result into decreased binding energies due to the relocation of electrons in covalent bonds closer to the core level or into increased binding energies due to the overcompensation of this effect by the elevation of valence electrons into more diffuse hybridized orbitals.¹⁹⁴ Concluding, hybridization must be considered in order to rationalize the subtle chemical shifts observed e.g. for aromatic organic molecules or chemisorbed particles at surfaces.^{170,195,196}

The effect of hybridization and covalent bonding as well as final state reorganization cannot be described mathematically by simple relations and as the more rigorous analytical approach accurate wave functions for the initial and final states can be calculated for solving the complete equation (23) basically directly.¹⁷⁰ An advantage of this method is the possibility to analyse chemical bonding mechanisms and therefore to develop a sharpened understanding of the chemical effects in core level binding energy shifts.¹⁹⁷ However, especially highly correlated open-shell systems such as high-spin

transition metal oxides require large computational effort and are therefore difficult to investigate. Instead, simplified semi-empirical quantum physical models or model extensions were developed for describing relaxation effects in complex systems, but care must be taken not to explain lineshapes and binding energy shifts due to incorrect physical reasons.^{187,190,196,198–201} For completeness, it is finally noted that a practical form of the more comprehensive extended potential model, which accounts properly for relaxation and is applicable for closed-shell compounds, can be found in the reviews of Moretti or Grosvenor.^{202,203}

3.1.3 Relaxation in d-metal compounds by charge transfer

Semi-empirical models for well understood classes of compounds aid the interpretation of XPS spectra and are carefully used for the discussion of spectroscopic data within this. In the following, the charge transfer screening model for d-metal compounds is therefore outlined, which explicitly considers the relaxation of the core hole by interactions with the valence band.

The basic concept of the charge transfer model is shown in figure 14.^{168,201,204} In the case of a metallic compound, the created core hole locally pulls down the energy levels of the atom due to its positive potential. As a consequence, also hitherto unoccupied d-states can reach energies below the Fermi level and become filled by conduction band electrons, which are scattered due to their interaction with the positive core hole. The time required for this charge transfer depends on the degree of hybridization of the local state with the conduction band and the conduction bands electron density and can be relatively slow for the narrow d- or f-bands when compared with the photoemission process.²⁰⁵ Two spectral components can then be observed in a core level spectrum of which the higher binding energy component is related to the situation where the local state remains empty (poorly screened peak) and the lower binding energy component corresponds to the filled state (well screened peak). This screening mechanism can also be transferred to insulators, which are characterized by completely filled valence bands with localized character (see figure 14). In this view, the core hole polarizes the valence band of the ligand (e.g. O2p) and an electron can be scattered into either the more diffuse sp band (poorly screened) or into the local d state (well screened). Due to the local nature of the ligands valence electrons, the electron transfer occurs usually due to interactions with the nearest neighbour ligand (local screening), but also next-nearest neighbour ligand interactions (non-local screening) can be relevant as discussed for NiO.^{206,207}

The theoretical development of the charge transfer model is founded on the work of Mahan, Nozières and DeDominicis, who investigated the response of a free electron continuum on the sudden creation of a deep lying hole.^{208–210} It was observed that the electrostatic interactions between the core hole and the conduction band leads to the creation of electron-hole pairs with possible excitation energies ΔE starting from 0 eV up to the whole bandwidth of the metal. The probability for these transitions to occur develop with $1/\Delta E$ and the derived lineshapes could be used to discuss threshold singularities

observed in X-ray absorption and emission experiments.²⁰⁹ The same model was also used in XPS for the development of the famous Doniach-Sunjić lineshape, which allowed to quantify core level spectra of simple sp-metals with great accuracy.^{211–213}

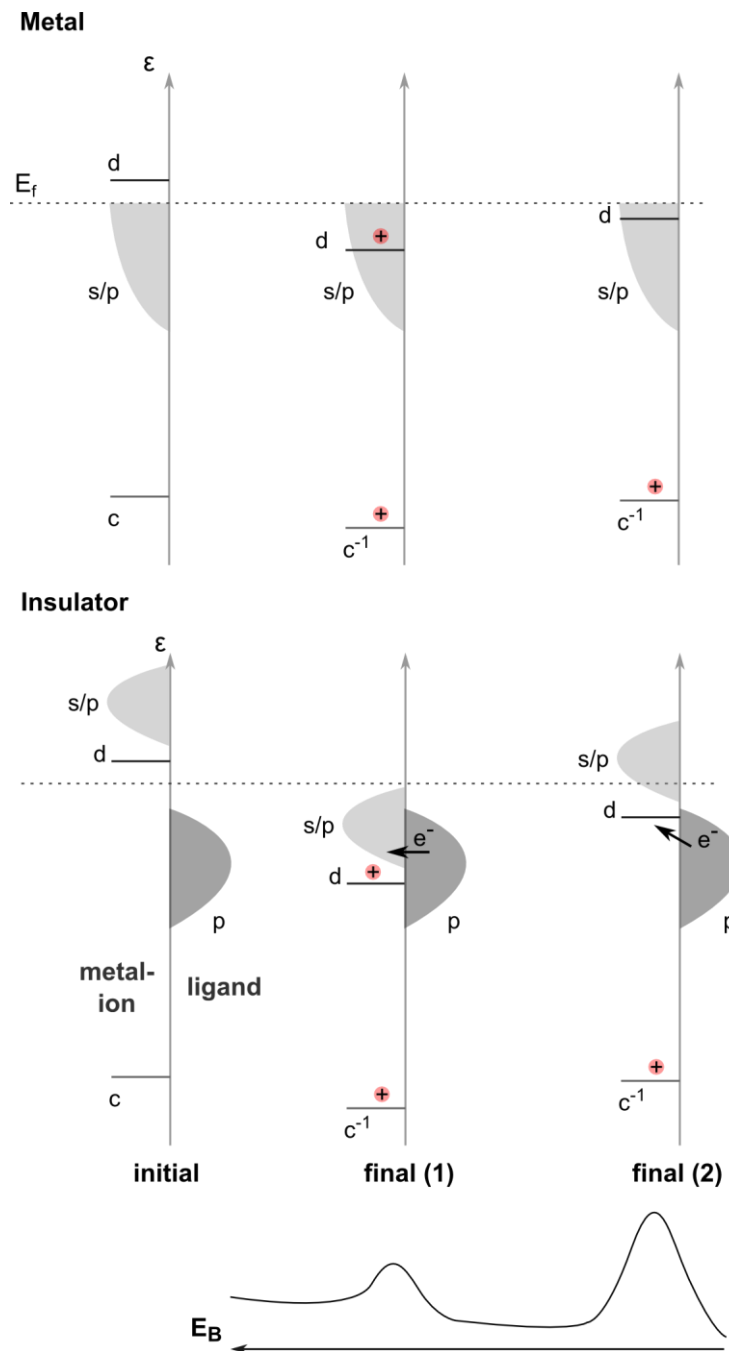


Figure 14: Illustration of charge transfer processes in d-metals and their insulating compounds upon relaxation of a core hole in the final state according to the Kotani-Toyozawa model (adapted).^{168,204}

However, electron-electron correlation interactions are key for the charge transfer model, but are uncovered in a free electron model. Thus, Kotani and Toyozawa extended the Mahan-Nozières-DeDominicis model by considering the electrostatic interactions of the core hole with a d-state, which is localized at the same atom and coupled to an s-type conduction band.^{204,214,215} This modified electronic system allowed to observe the scattering of conduction band electrons into the local d-state

when the d-state is pulled-down to below the Fermi level (see figure 14) and enabled thereby a qualitative understanding of photoemission spectra.²¹⁵

More elaborate calculations based on an Anderson impurity model were presented by Gunnarsson and Schönhammer and allowed finally to quantitatively explain the satellite structures observed in XPS spectra of d- and f-metal compounds by charge transfer.^{201,205,216,217} Beside the assignment of XPS core level satellites to related final state configurations, the Gunnarsson-Schönhammer theory (GS) also allowed to determine the hybridization energy Δ of the f-level with the conduction band and its initial state occupancy n_f . The quantification of these parameters has led to a reinterpretation of the XPS spectra and ground state electronic structures of f-metal compounds. As an example, the occupancy of the f-level of CeRu₂ could be determined to around 0.8, whereas an occupancy of zero was expected.²⁰⁵ The GS theory does also not specify the nature of the band from which the charge is removed from and can be therefore transferred to insulators with filled valence bands as well. However, recent investigations of doped transition metal oxides and Cu-based high-temperature superconductors have raised a discussion about the comprehensiveness of the GS theory.^{218,219} In this regards, Taguchi et al. extended the GS theory by considering that the charge transferred must not necessarily originate from a sole conduction or valence band only, but can stem in addition to that from further states close to the Fermi level.^{218,220} This approach was challenged by van Veenendal, who showed by using the GS theory that a thorough consideration of competing local and non-local screening effects may also explain the spectra of transition metal compounds.²¹⁹ Today, the question about the validity of these both methods or whether they are equivalent remains unresolved.²²⁰

It must be noted that even in the case that the charge transfer model may provide simulated core level spectra, which show a high degree of consistency with experimental data, the correctness of its use is not guaranteed and the physical origin of the satellite structure may thereby be misinterpreted. In this regards, the interpretation of the Ni 2p spectra of metallic Ni and related compounds has frequently been revised: within the extensive review of Hüfner, the satellite around 6 eV may be explained by charge transfer relaxation.¹⁶⁸ Conversely, based on Electron Energy Loss experiments Grosvenor et al. assigned that satellite rather to the energy loss by surface plasmon excitation.¹⁷⁹ This interpretation was then questioned again by Karis et al., who observed a shifted satellite structure in the Ni 1s spectrum, which is incompatible with the plasmon loss assignment.^{179,221} Instead, the shift of the satellites was explained by considering that the core-valence electron correlations are different for the Ni 1s and Ni 2p levels. This in turn indicates that relaxation by charge transfer may represent the main mechanism causing the occurrence of the satellites.

However, several researchers followed experimental approaches to corroborate the charge transfer model: it could be shown that the probability of charge transfer screening increases with the amount of electrons located in the conduction/valence band.^{222,223} In this context, the role of the nitrogen

stoichiometry in TiN_x hard coatings was tested and the occurrence of a poorly screened peak was observed as x approaches 1 due to the removal of electrons from the Ti3d conduction band.²²³ In other experiments, also the bandwidth of the local screening orbital, which increases with its degree of hybridization and coupling to the conduction/valence band, was found to correlate well with core level lineshapes.²²⁴ Finally, the non-local screening by next-neighbour ligands was also tested by investigating the effect of diluting the transition metal ion as in the case of Ni doped MgO.²⁰⁶ Concluding, it is important to consider relaxation as described by the charge transfer model when discussing the satellite structure of transition metal compounds. However, other mechanisms must also be considered in order to clarify the nature of satellites: photoelectrons may lose defined amounts of energy by exciting plasmons when being emitted (intrinsic plasmon loss) or while travelling through the material (extrinsic plasmons).²²⁵ Also other losses due to optical excitation of the matrix are possible and especially intra- and interband transitions can result into distinct peaks or bands at lower binding energies.²²⁶ Finally, the core hole may also interact with the spins of the ions valence electrons leading to multiplet structures.^{227,228}

3.1.4 Wagner plots and modified Auger parameters

As discussed above, the binding energy is affected by relaxation of the matrix upon the creation of the core hole and is thus not only determined by initial, but also by final state effects. Relaxation energies are therefore not only key for understanding binding energies, but also sensitively resemble the phase properties of the surrounding matrix. In this regards, XPS allows also to separately investigate relaxation by the analysis of the modified Auger parameter α' and fundamental as well practical aspects of this approach are therefore outlined in the following.^{202,229,230}

The modified Auger parameter α' is determined within an XPS experiment from the binding energy of a core level Z and the kinetic energy of the related X-ray excited Auger electron involving the core levels W, X and Y of the same atom:^{175,202,229}

$$\alpha' = E_k(W, X, Y) + E_B(Z) \quad (24)$$

In the view of equation (24), the modified Auger parameter benefits from not being influenced by the analysers work function or charging effects and can show shifts among different compounds even when no shift is observable in the core levels binding energy. The sensitivity of the modified Auger parameter towards the relaxation energy can be discussed based on an extended potential model, which gives²⁰²

$$\alpha' \cong K_{WXYZ} + 2 R_W \quad (25)$$

where K_{WXYZ} is a purely atomic constant and R_W the complete relaxation energy of the core hole in the level W including both intra- and extra-atomic relaxation energies. It follows that shifts of the modified Auger parameter $\Delta\alpha'$ between different compounds correspond to changes of the relaxation energy. However, intra-atomic contributions to the overall relaxation energy do not depend on the matrix as

long the valence charge of the ion is always the same (same oxidation number and no charge transfer by relaxation).²⁰² The shift of the modified Auger parameter $\Delta\alpha'$ then becomes

$$\Delta\alpha' \cong 2 \Delta R^{ea} \quad (26)$$

where R^{ea} is the extra-atomic relaxation energy.^{175,202}

The modified Auger parameter is typically evaluated for a set of compounds within the so-called Wagner plot, where the Auger kinetic energy is plotted against the core level binding energy and the slope is analysed. According to equation (25), a slope of 1 is observed when the total relaxation energy in a given set of compounds is the same. It could be also shown that a slope of 3 corresponds to the situation where the compounds show the same initial state properties.²⁰² However, often deviations from this simple rule are observed as a result of the assumptions made. Among these, it is assumed in equation (25) that the core levels are closely located to the nucleus, which is in the case of e.g. the P2p and S2p signals used for phosphorus and sulphur not true.²⁰² Moreover, the chemical shift does often not affect all core levels involved in the Auger transitions to the same extent due to different shielding and other slopes are then observed.¹⁶⁶ Nevertheless, the Wagner plot is a widely used phase sensitive surface analytical approach and as an example the transition of a shallow aluminium oxide thin film from the amorphous to crystalline state during growth could be characterized.²³¹

3.1.5 Quantitative XPS

As outlined in section 3.1.1, a wide range XPS spectrum includes core level lines of the atoms in the near-surface region. This allows not only to qualitatively conclude on the presence of elements, but also enables their quantification as outlined in the following.

The first step in this quantification procedure is the identification of the core levels by using database binding energies. Then, backgrounds are applied to the main peaks to separate the primary photoelectrons from the inelastic background. Different backgrounds are usually used for this procedure: the linear background gives good results for closed shell compounds like organic molecules or insulators, where the background is scarcely affected by the core level signal. If the core level signal significantly increases the background, the Shirley background is most commonly used. The Shirley method assumes that the background within a core line is simply proportional to the intensity of the primary photoemission signal.²³² However, the specific optical properties of the material are thereby neglected and the Shirley background is of limited use as the structure of the background becomes more complex. For these reasons, Tougaard developed a background model, which explicitly accounts for the optical properties of the material and the related inelastic scattering of the electrons.²³³ In this model, the optical response of the material is considered by a parameterized model. However, the individual optical properties are usually not available for unknown samples and for practical purposes universal coefficients are thus in use.²³⁴ Another drawback of this approach is that the background is defined across a spectral range of 50 eV or more and long acquisition times are required. Another

approach, which accounts for the specific optical properties of the sample, is the deconvolution of the core level signals with rescaled REELS spectra measured on the same sample.²³⁵ Obviously, this method is not well suited for routine analysis due to its high effort, but it also suffers from the fact that the effect of the core hole is not taken in account. Moreover, also the backscattering angle and energy used in the REELS experiment can be decisive and errors may be induced when using inadequate REELS spectra. Finally, it must be considered that the electron beam passes the sample twice within the REELS experiment, whereas the electrons in XPS pass the sample only once. Therefore, bulk and surface plasmon losses are also not properly taken into. The most accurate background subtraction method is therefore the determination of the dielectric function of the material by quantitative REELS and the separate simulation of the background, but again the effort is still high.^{236,237}

After background subtraction (often a Shirley type background), the intensity of the peak A I_A is quantified to calculate atomic concentrations in the sample surface. When assuming a laterally homogeneous sample surface and unpolarised X-ray irradiation, the detected peak intensity I_A is given by¹⁶⁶

$$I_A = \sigma_A W_A (\beta_{eff}, \psi) G(E_A) \frac{I_{hv}}{\cos \alpha} \frac{\Delta\Omega}{4\pi} \int_0^\infty N_A(z) \exp \left[-\frac{z}{\lambda_{m,E(A)} \cos \theta} \right] dz \quad (27)$$

where σ_A is the ionization cross section of the shell A, W_A the Reilmann asymmetry factor at the angle ψ between source and analyser, β_{eff} the effective asymmetry factor, $G(E_A)$ the analyser efficiency at the energy E_A , I_{hv} the intensity of the X-rays at the angle of incidence α , $\Delta\Omega$ the acceptance angle of the analyser, $N_A(z)$ the density of atoms of type A, $\lambda_{m,E(A)}$ the effective electron attenuation length (EAL) of the surface at the photoelectrons kinetic energy and θ the angle of emission.²³⁸⁻²⁴⁰ In this view, the intensity of photoelectrons from shell A is determined by a combination of experimental (I_{hv} , $\Delta\Omega$, θ) and fundamental physical parameters (W_A , β_{eff} , $\lambda_{m,E(A)}$) and the atomic concentration profile $N_A(z)$ of the sample.

It is noted, that the asymmetry factor W_A accounts for the angular intensity distribution of the photoelectrons caused by the conservation of their angular momentum. This effect can be neglected in XPS systems, where the angle between the source and the analyser is at the magic angle of 54.74°. In contrast, the XPS system used within this thesis has an angle of 102° and the asymmetry of the photoemission must be therefore considered for quantification.²³⁹ The EAL is a complex parameter, which accounts for the attenuation of the electrons by the matrix and is based on the inelastic mean free path (IMFP). The latter describes the stopping of the electrons by inelastic losses and resembles the related exponential depth-dependence. The IMFP shows therefore a similar behaviour between different materials and simple semi-empirical equations exist for its estimation.¹⁶³ However, the EAL also includes the effect of elastic collisions of the photoelectrons, which further decreases their range travelled and shows a complex non-exponential behaviour. The estimation of the EAL for practical

purposes is therefore complicated and beside available database values, a simple semi-empirical equation for the estimation of the EAL has emerged only recently (S3).^{164,240}

Equation (27) can be easily integrated when assuming that the sample is homogeneous and shows a constant atom density profile N_A :

$$I_A = \sigma_A W_A (\beta_{eff}, \psi) G(E_A) \frac{I_{hv} \Delta\Omega}{\cos \alpha 4\pi} \lambda_{m,E(A)} \cos \theta N_A \quad (28)$$

For practical surface analysis, a homogeneous sample is often assumed and equation (28) is therefore the fundamental relation for quantification. When using identical experimental parameters, the atom density N_A of an unknown sample can be determined by measuring a reference with $I_A^0(\lambda_{A,E(A)}, N_A^0)$. It is highlighted that the EAL is mainly influenced by the atom density and therefore differs between reference and sample. N_A is then given by

$$N_A = \frac{I_A \lambda_{A,E(A)}}{I_A^0 \lambda_{m,E(A)}} N_A^0 \quad (29)$$

The atomic concentration X_A can be finally calculated based on the atom density of the sample N_m by

$$X_A = \frac{N_A}{N_m} = \frac{I_A \lambda_{A,E(A)} \rho_A^0 M_m}{I_A^0 \lambda_{m,E(A)} \rho_m M_A^0} = \frac{I_A}{I_A^0} F_{A,m} \quad (30)$$

where the atom densities N are expressed in terms of the densities ρ and the (mean) molar masses M and $F_{A,m}$ is the matrix correction factor. It is standard in practical XPS quantification to neglect matrix effects in XPS, because the atom densities are usually not known. In this case, the atom density of the sample N_m can be approximated by the density of the reference N_A^0 . In this limit, also the EALs of sample and reference are then identical and equation (30) simplifies to

$$X_A \cong \frac{N_A}{N_A^0} = \frac{I_A}{I_A^0} \quad (31)$$

Consequently, the atomic concentration of an element can in the limit of negligible matrix effects be determined by measuring the core level intensities of the sample and a reference with known atom density. The quantification procedure can be even simplified by using the Palmberg equation²⁴¹

$$X_A \cong \frac{I_A / I_A^0}{\sum_i I_i / I_i^0} = \frac{I_A / S_A^{rel}}{\sum_i I_i / S_i^{rel}} \quad (32)$$

where S_i^{rel} is the relative sensitivity factor of element i (E-RSF), which corresponds to the intensity of the reference of that element I_i^0 normalized to another reference intensity I_{ref}^0 (often C1s or F1s):

$$S_i^{rel} = \frac{I_i^0}{I_{ref}^0} \quad (33)$$

The benefit of the Palmberg equation is that tabulated E-RSF values can be used. Nevertheless, it must be emphasized that tabulated E-RSF values are usually defined for XPS systems in magic angle configuration and thereby do not cover the effect of asymmetry. Consequently, the Palmberg equation

in form of equation (32) must be corrected. In this regards, equations (29)-(33) and especially the Palmberg equation require that the asymmetry factor $W(\beta_{\text{eff}}, \psi)$ drops out (same emission angle θ) or is one as in the magic angle situation.¹⁶⁶ This can be realized by adjusting the E-RSF values according to

$$S_i^{\text{rel}} \rightarrow S_i^{\text{rel}} \frac{W_A(\theta, \psi)}{W_{\text{ref}}(\theta, \psi)} \quad (34)$$

where the asymmetry factors $W_i(\theta, \psi)$ are calculated for the emission and source/analyser angles of the experiment and at the energies corresponding to the photoelectrons of the respective core lines.¹⁶⁶ It is clear, that inaccuracies in the quantification arise due to the assumption of negligible matrix effects. In the case of nanostructured surfaces showing lateral or in-depth heterogeneities also inaccurate concentrations may be calculated with errors exceeding 100 % when not taking the heterogeneities properly into account.²⁴² Finally, the evaluation of measured intensities for quantification relies on an accurate background subtraction of not only the sample under investigation, but also of the reference. Since it is usually not clear how the background was removed in the case of tabulated E-RSF values and the background removal by the commonly used methods such as the Shirley background are estimates at best, this can also cause significant errors in praxis. However, advanced quantification procedures can reduce these errors: the first issue can be encountered by using matrix corrected sensitivity factors.¹⁷⁵ Moreover, the routine analysis of heterogeneous surface has become possible by the development of the QUASES software facility by Tougaard and finally accurate references can be obtained by measuring reference materials with the same XPS system.^{243,244}

3.1.6 Thickness layer determination by XPS

XPS can also be used to determine the concentration depth profile $N(z)$ of a sample by depth profiling or angle-resolved measurements.²⁴⁵⁻²⁴⁷ However, passivating films formed on top of reactive materials such as nitridic hard coatings often show a multi-layered structure. When each layer causes the occurrence of a corresponding signal within a core level spectrum, the principal ordering of the layers can be easily identified by recording angle-resolved spectra of the core level and tracking the development of the relative intensities. Also the thickness of these layers can be readily calculated when assuming sharp interfacial boundaries.²⁴⁸ For the simple situation of a homogeneous overlayer L with a sharp boundary and thickness t located on a homogeneous substrate S equation (27) becomes

$$I_L = I_L^\infty \left[1 - \exp\left(-\frac{t}{\lambda_{L,E} \cos \theta}\right) \right] \quad (35a)$$

$$I_S = I_S^\infty \exp\left(-\frac{t}{\lambda_{L,E} \cos \theta}\right) \quad (35b)$$

The thickness can be therefore calculated by evaluating the fraction of the substrate or overlayer component to the overall core level spectrum I_i/I_i^∞ and by using a database EAL. When using different

core level signals, the different kinetic energies and therefore different EALs and asymmetry factors must be considered.

3.2 Low Energy Ion Scattering (LEIS)

LEIS is performed by bombarding a surface typically with noble gas ions at energies of around 0.5-10 keV and by measuring the resulting energy spectra of the reflected ions at a backscattering angle θ (see figure 15). Under these experimental conditions most ions are reflected from the surface after experiencing a single binary collision with a surface atom. As a consequence they lose defined amounts of energy determined by the masses of the target atoms present in the surface. This results into element specific peaks in the spectrum at kinetic energies E_f , which can be calculated from the initial energy E_0 using the principles of momentum and mass conservation.²⁴⁹⁻²⁵¹

$$E_f = k E_0 = \left(\frac{\cos\theta \pm \sqrt{\left(\frac{m_2}{m_1}\right)^2 - \sin^2\theta}}{1 + \frac{m_2}{m_1}} \right)^2 E_0 \quad (36)$$

within equation (36) the kinematic factor is represented by k , m_1 is the mass of the projectile and m_2 the mass of the target atom in the surface. For completeness it is noted that binary collision peaks may also be accompanied by low-energy shoulders as a result of additional discrete inelastic loss processes (e.g. exciton formation) or by peaks at higher energies related to double or multiple scattering events.²⁵¹ Since the energy shift of peaks originating from discrete loss processes do not depend on the initial energy of the projectile, the consideration of spectra measured at different primary energies may in such cases clarify the situation. Furthermore, the investigation of surfaces at different backscattering angles can assist the interpretation of the spectra, because double or multiple scattering is favoured at low backscattering angles. This highlights that LEIS spectra require a careful interpretation in the case of completely unknown samples.

Besides undergoing a binary collision, an ion may also penetrate the surface and enter subsurface layers. As the ion approaches the surface, different neutralization, but also reionization processes can occur and result into a dynamic state of charge of the projectile while moving in the bulk.²⁵² In this regards, the commonly used noble gas ions mostly neutralize when entering subsurface layers.²⁵² Such neutral projectiles can also reach the surface again, become reionized and detected. However, the reionized projectiles do not contribute to the main elastic peaks due to the additional stopping experienced in the subsurface volume. Instead, reionized ions scattered in sub layers almost exclusively cause an inelastic background, which rationalizes the low-energy tails, but also the slight asymmetric lineshapes of the elastic peaks (see figure 15b).²⁵¹ Concluding, the high electron affinity of the noble gas ions paired with the efficient stopping of projectiles in the subsurface volume explains the excellent surface sensitivity of LEIS when using noble gas ions.

As a consequence, LEIS can not only be used to identify, but also to quantify the surface atomic concentration of atomic species.^{249,251,253–259} The quantification is based on the evaluation of the elastic peak intensities, but suffers from matrix effects, an inaccurate background removal and the lack of appropriate standards and must therefore be critically appraised.²⁵⁷ Within the herein reported studies, the quantification was not found to be successful and the reader is for a more thorough description of this procedure referred to literature.^{249,251,253–259}

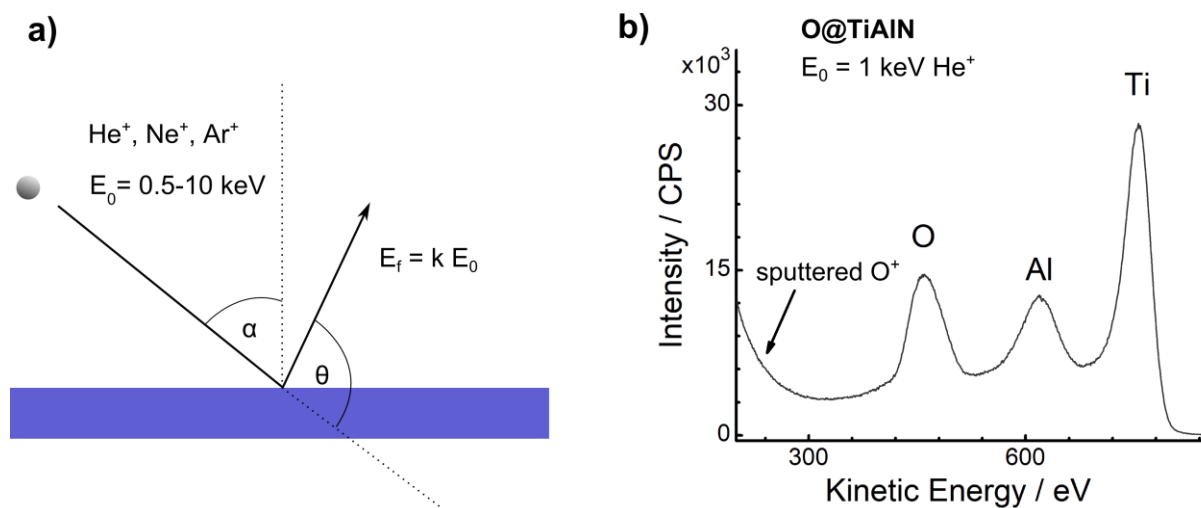


Figure 15: a) Illustration of the experimental setup used for LEIS. b) LEIS spectrum of a sputter cleaned TiAlN surface after oxygen chemisorption (O@TiAlN) measured using 1 keV He^+ ions.²⁶⁰

For a more in-depth understanding of the shape of He^+ LEIS spectra also reionization and sputtering effects must be considered: when a He^+ or He projectile approaches a target atom, the increasing overlap of the valence orbitals during the collision causes the formation of an intermediary mixed state of the $\text{He}1s$ and the valence orbital of the target atom. Due to the anti-bonding nature of this state the energy of the state is increased with increasing overlap, i.e. with increasing kinetic energy of the projectile projected into the direction of the surface atom. When the projectile is in this intermediary mixed state, it can undergo a collision induced neutralization or reionization if its energy and angle of incidence are such that a threshold energy is exceeded.²⁶¹ These threshold energies are determined by the atomic numbers of the target atoms and can be even higher than the energy provided by the primary He^+ ion beam. Consequently, spectra can be obtained even without any background (e.g. Cu, Ag, Ni, Zn, Pb).^{251,262}

However, most surfaces including the herein investigated Ar^+ sputter cleansed and oxidized $\text{Ti}_{0.5}\text{Al}_{0.5}\text{N}$ surfaces consist of elements such as oxygen (or aluminium in the case of sputter cleansed $\text{Ti}_{0.5}\text{Al}_{0.5}\text{N}$), which show threshold energies as low as 300 eV.^{251,261} This rationalizes the presence of backgrounds by the reionization of neutrals as a result of collisions with atoms like oxygen located in the outermost surface.^{251,262} Following these arguments, also no signal should be detectable at energies below 300 eV, whereas instead a steeply increasing background can be typically observed when investigating

oxygen-bearing surfaces (see figure 15b). As pointed out earlier, the intensity measured in this range is rather explained by preferential sputtering and ionization of surface oxygen atoms.^{251,263}

LEIS experiments can be non-destructive (static) when using sensitive instrumentation to keep the ion dose to below 10^{13} ions cm^{-2} .²⁵¹ The continuous sputtering however also allows to measure LEIS dynamically and thereby to profile the surface with very high surface sensitivity. This can be used to investigate interdiffusion layers as in the case of thermally grown SiO_2 , where an excess of around 20 % Si could be found within an Si| SiO_2 interfacial region of around 15-20 Å thickness.²⁶⁴ It is noted, that LEIS experiments for the investigation of the surface chemistries of hard coatings are scarcely reported in literature. Within the only publication found, Aguzzoli et al. investigated TiN films after exposure to atmosphere and observed that the surface nitrogen was completely exchanged by oxygen due to oxidation.²⁶⁵ These examples show, that LEIS represents a promising means for the investigation of the surface oxidation of hard coatings.

3.3 Dynamic Force Spectroscopy (DFS)

3.3.1 Introduction

DFS has been developed during the past decade and emerged as a routine method for the analysis of interaction forces.^{266–269} Most remarkably, this technique allows to determine the complete height dependent interaction potential $U(z)$ and thereby also the force $F(z)$ between a surface and the tip of an AFM cantilever with high sensitivity and without being limited to UHV conditions. In this regard, a recent publication of Herruzo et al. demonstrates the high sensitivity attainable by DFS.²⁷⁰ Within that study, the authors determined the whole potential volume above the surfaces of muscovite mica and of the GroEL protein in water with a resolution of 10 pN, 2 Å and with an acquisition time of only 40 s for the whole volume (It is noted that a minimum force resolution of 10 pN is usually considered to be required for atomic resolution.²⁷¹). The high time resolution allowed to reveal dynamic instabilities in the structure of the hydration layer close to the GroEL surface, which are proposed to relate to topographical corrugations or to elastic deformation of the protein. Moreover, the possibility to probe the whole potential volume by DFS not only allows to analyse adhesion forces, but also to investigate friction within the same experiment.²⁶⁹ Based on the different decay lengths of forces, the continuously determined force profile $f(z)$ by DFS also allows to differentiate between individual force contributions as reported earlier.²⁷² However, so far only the applicability of DFS for the investigation of polymeric surfaces has been demonstrated yet.²⁷³ The DFS experiments shown in this thesis therefore represent a first approach to harness the capabilities of DFS for the analysis of interaction forces between complex material systems. As a consequence, performing the DFS experiment with hard coating and polymer surfaces was found to be challenging and not only the fundamental theoretical and

experimental aspects of DFS are thus outlined in the following, but also specific obstacles occurring when investigating polymer surfaces are discussed.

3.3.2 Experimental foundations

Basically, DFS is performed by exciting an AFM cantilever at its resonance frequency f and measuring the frequency shift Δf when approaching a surface (see figure 16). This resonance frequency shift is caused by tip-sample interaction forces F_{ts} , which can then be quantitatively recovered by deconvoluting the experimental $\Delta f(z)$ curve.

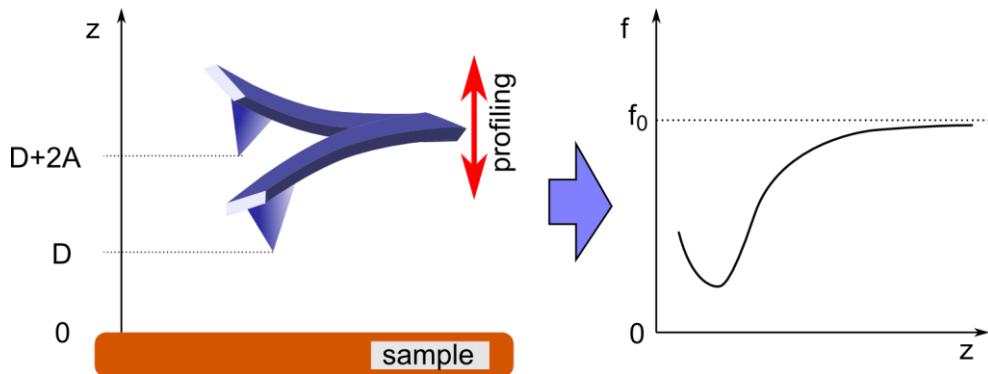


Figure 16: Experimental principle of DFS.

The interaction forces also affect the amplitude A of the oscillation, which can be measured and provides information about the dissipated energy. The oscillation amplitude can also be kept constant by a control loop (AGC), which allows to measure the amplitude A_{exc} required for exciting the cantilever instead as realized in the herein reported DFS experiments.

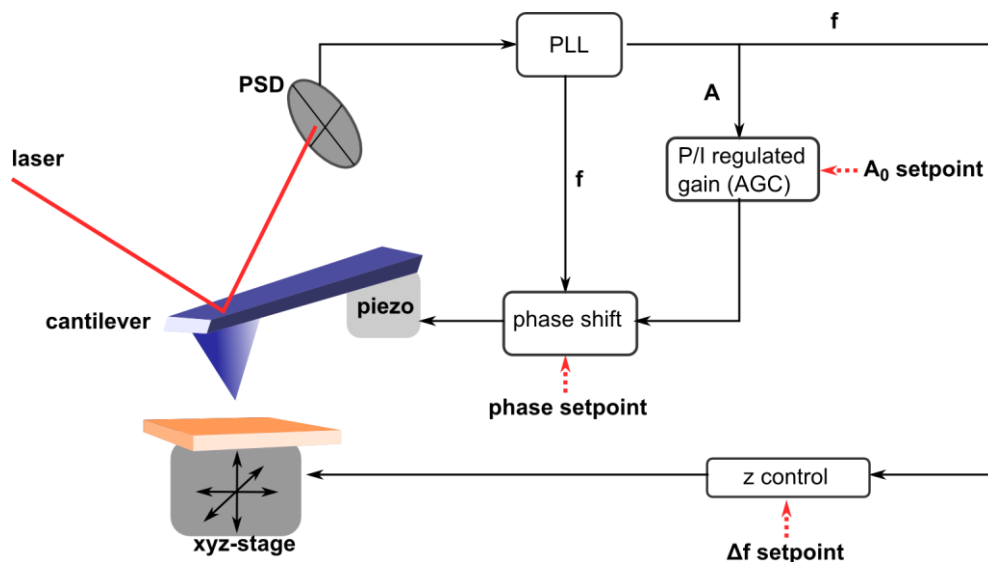


Figure 17: Functional diagram of a typical frequency modulated AFM setup for performing DFS at constant amplitude.

It is noted that for DFS an excited cantilever is used, because the oscillatory energy stored in the beam (around 10-15 keV) prevents instabilities, i.e. the cantilever does not suddenly snap onto the surface when a certain force gradient is exceeded, but remains stable in a nearly sinusoidal motion. In this

view, DFS is a frequency modulated AFM technique (FM-AFM) and a functional diagram of a typical setup using the optical beam deflection method is shown in figure 17.²⁷⁴

In DFS, a laser is focused onto the apex of the AFM cantilever beam and the reflected light is measured with a four segment position sensitive detector (PSD). The signal generated by the PSD is then demodulated using a PLL in order to accurately measure the frequency, amplitude and phase shift (with reference to the internal clock of the PLL) of the cantilever oscillation. The PLL also feeds an input signal back to excite the cantilever, which is phase shifted such that a minimal gain is required. Under these conditions the oscillation of the cantilever is unperturbed and occurs at the resonance frequency.²⁷⁵ The gain of the excitation signal is further controlled by the automatic gain control (AGC) for maintaining a constant amplitude during operation. This grants that the two experimental channels frequency shift and excitation amplitude are physically independent from each other and do not carry intermingled information about the dissipated energy and the tip-sample force.^{276,277} Furthermore, the strongly repulsive regime can be probed, which is without an AGC not possible.²⁷⁶ Concluding, the here described FM control scheme provides a stable oscillation of the cantilever even in the presence of frequency shifts caused by interaction forces.

The microscope can now be operated in two ways: as depicted in figure 17, the measured frequency shift Δf can be used to adjust the sample height (or more commonly the cantilever height) until a constant frequency shift setpoint is reached. In this configuration, the sample topography can be recorded by rastering the surface and measuring the height required for maintaining the setpoint at each pixel. In contrast, during DFS the frequency shift and excitation amplitude are simply recorded at a certain position while approaching the sample with the cantilever.

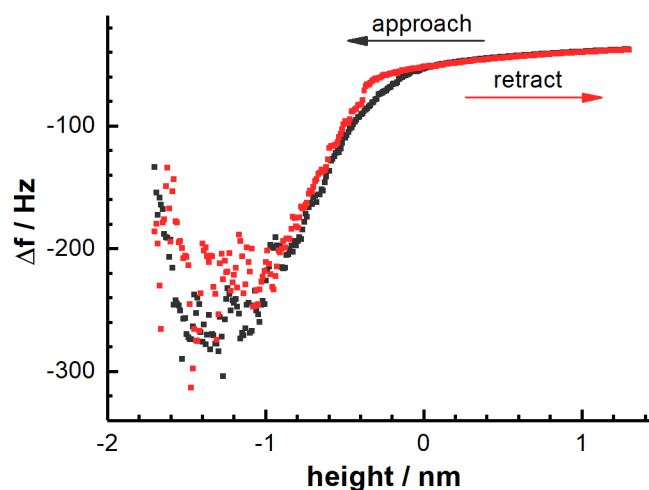


Figure 18: Frequency shift curve measured between a TiAlN coated cantilever and a PS surface at a speed of 1.25 nm s^{-1} .

However, the measurement of frequency shift curves $\Delta f(z)$ by DFS was found to be intricate on polymeric surfaces and specific aspects must be considered. To exemplify this, figure 18 shows the frequency shift $\Delta f(z)$ measured with a TiAlN coated cantilever while approaching and retracting from

a polystyrene surface. Whereas the noise in the frequency shift is typically very low in the true non-contact region (above a height of 0 nm), a strong noise is observed when being in contact with the surface. This can be in parts rationalized when considering the thermal noise limit of cantilevers for FM detection: the minimal detectable force F_{\min} is approximated by

$$F_{\min} = \sqrt{\frac{4kk_BTB}{\pi f_0 Q}} \quad (37)$$

when assuming that the experimental noise is solely determined by the finite cantilever vibration caused by Brownian motion.²⁷⁴ In equation (37) k represents the force constant of the cantilever, k_B the Boltzmann constant, T the temperature, B the bandwidth of the demodulator (here: the PLL), f_0 the free resonance frequency and Q the quality factor of the oscillation, which is the ratio between energy stored in the oscillator and the energy dissipated within one cycle. When assuming typical experimental parameters ($k = 40 \text{ N m}^{-1}$, $B = 500 \text{ Hz}$, $f_0 = 350 \text{ kHz}$, $Q = 4000$), a minimum detectable force of around 0.3 pN can be achieved. In contrast, this high force sensitivity is severely affected by the mechanical coupling of the vibrating cantilever to the surface and high energy dissipation rates of several hundreds of eV per oscillation cycle are observed.²⁷⁸ When estimating the force sensitivity for this case by using equation (37) and a Q factor of around 40 (calculated using a dissipation rate of 300 eV per cycle and an internal energy of 12.5 keV) a minimum detectable force F_{\min} of 3 pN is obtained. Thus, the force sensitivity is decreased by around one order of magnitude when a mechanical contact is established. In this view, the use of increased acquisition times (lower speeds) for decreasing the experimental noise is generally restricted by drift of the z-scanner and several curves are therefore averaged for the determination of the interaction forces.

3.3.3 Theoretical foundations

When assuming a nearly sinusoidal motion of the cantilever, the resonance frequency shift due to the interaction forces F_{ts} can be described by

$$\Delta f = -\frac{f_0^2}{Ak} \int_0^{1/f_0} F_{ts}(D + A(1 + u)) \frac{u}{\sqrt{1 - u^2}} du \quad (38)$$

where t is the time and D the height of the tip at closest approach during a cycle.^{269,279} The interaction forces F_{ts} can then be determined by simulating equation (38) using a parametric description of F_{ts} and comparing the results with the experimental $\Delta f(D)$ curve or more conveniently by inverting equation (38).^{280,281} In this regards, an accurate inversion was derived by Sader and Jarvis and relates the interaction potential $U(D)$ (from which the interaction force F_{ts} can be calculated by differentiation) with the frequency shift.²⁸¹

$$U(D) = 2k \int_z^\infty \frac{\Delta f}{f_0} \left((t - D) + \frac{A^{0.5}}{4} \sqrt{\frac{t - D}{\pi}} + \frac{A^{1.5}}{\sqrt{2(t - D)}} \right) dt \quad (39)$$

Equation (39) can be easily implemented if one changes the integration variable $t \rightarrow D + u^2$ in order to avoid the singularity caused by the square-root in the denominator of equation (39) at the lower integration boundary.^{269,282} It is also highlighted, that equations (38) and (39) are not only valid for the constant amplitude, but also for the constant excitation FM mode where the AGC is turned off and the amplitude is allowed to change accordingly during the interactions.²⁶⁷ The constant excitation mode is for DFS measurements therefore more practical, because the very slow AGC is not required any more. The energy dissipation ΔE can be calculated according to the approximation^{278,283}

$$\Delta E(D) \cong \pi k \left(AA_{exc}(D) - \frac{A^2}{Q} \right) \quad (40)$$

It is noted that in the case of constant excitation equation (40) is also valid and the amplitude becomes $A(D)$.²⁶⁷

When inspecting equations (38) and (40) it becomes clear that the evaluation of the measured frequency shift curves and of the excitation voltages requires the calibration of the oscillation amplitude A and the excitation amplitude A_{exc} . This can be accomplished within the same setup as used for DFS and is usually performed at large amplitudes (around 10-20 nm). Equation (38) then simplifies in this limit to²⁷⁹

$$\Delta f \cong \frac{f_0}{\sqrt{2\pi k A^{1.5}}} \int_D^{D+2A} \frac{F_{ts}(u)}{\sqrt{u - D}} du \quad (41)$$

A normalized frequency shift $\Delta \gamma$ can be therefore defined, which only depends on the distance of closest approach D :²⁷⁹

$$\Delta \gamma := \frac{\Delta f k A^{1.5}}{f_0} \cong \frac{1}{\sqrt{2\pi}} \int_D^{D+2A} \frac{F_{ts}(u)}{\sqrt{u - D}} du \quad (42)$$

Based on this relation, the voltage signal of the oscillation amplitude A is calibrated as follows:²⁸⁴ first the amplitude is changed resulting into a change of the frequency shift. Afterwards, the height of the cantilever z is regulated in order to maintain a constant normalized frequency shift. According to equation (42) this is equivalent to maintaining a constant distance D . Since the height of the cantilever z is furthermore the sum of the distance D and the amplitude A (see figure 16), the change of the cantilever height z corresponds directly to the change of the amplitude. Consequently, the voltage signal of the oscillation amplitude is calibrated to the height scale.

In comparison, the calibration of the excitation amplitude A_{exc} is straightforward. By tuning the free cantilever the Q factor can be determined from the FWHM of the resonance curve. Due to the absence

of external forces, the oscillation amplitude is then solely determined by the internal energy dissipation of the cantilever which yields:²⁷⁸

$$A = QA_{exc} \quad (43)$$

4 Publications

The following six main author publications published in peer-reviewed journals were selected for this thesis:

- I. **Wiesing, M.**, de los Arcos, T., Grundmeier, G.
The Thermal Oxidation of TiAlN High Power Pulsed Magnetron Sputtering Hard Coatings as Revealed by Combined Ion and Electron Spectroscopy.
Adv. Mater. Interfaces 1600861 (2017), doi: 10.1002/admi.201600861
- II. **Wiesing, M.**, to Baben, M., Schneider, J. M., de los Arcos, T., Grundmeier, G.
Combined Electrochemical and Electron Spectroscopic Investigations of the Surface Oxidation of TiAlN HPPMS Hard Coatings.
Electrochimica Acta 208, 120–128 (2016), doi: 10.1016/j.electacta.2016.05.011
- III. **Wiesing, M.**, de los Arcos, T., to Baben, M., Rueß, H., Schneider, J. M., Grundmeier, G.
Analysis of the inhibition of thermal degradation of molten polycarbonate at tool steel interfaces by thin TiAlN coatings.
Polym. Degrad. Stab. 143, 196–206 (2017), doi: 10.1016/j.polymdegradstab.2017.07.013
- IV. **Wiesing, M.**, Grundmeier, G.
Lifshitz analysis of dispersion forces based on quantitative Reflection Electron Energy Loss Spectroscopy.
J. Colloid Interface Sci., 514, 625-633 (2018), doi: 10.1016/j.jcis.2017.12.069
- V. **Wiesing, M.**, Arcos, T. de los, Gebhard, M., Devi, A., Grundmeier, G.
Analysis of dispersive interactions at polymer/TiAlN interfaces by means of dynamic force spectroscopy.
Phys. Chem. Chem. Phys. 20, 180–190 (2018), doi: 10.1039/C7CP05373H
- VI. **Wiesing, M.**, de los Arcos, T., Grundmeier, G.
UHV AFM based colloidal probe studies of adhesive properties of VAlN hard coatings.
Appl. Surf. Sci. 428, 767–774 (2018), doi: 10.1016/j.apsusc.2017.09.208

The consistent context of these publications can be rationalized as follows: among the selected publications, the surface chemical as well as structural properties of the shallow oxide layers formed on $\text{Ti}_{0.5}\text{Al}_{0.5}\text{N}$ by thermal oxidation were investigated in **publication I**. Consequently, a microscopic mechanism of the multi-step oxidation process could be developed.

This model was then adapted in **publication II** at ambient conditions for understanding the electrochemical surface oxide formation and corrosion behaviour of $\text{Ti}_{0.5}\text{Al}_{0.5}\text{N}$ in aqueous electrolytes.

Publication III then transfers these insights about the surface chemistry of hard coatings in order to explain their reactivity as investigated by exposing $\text{Ti}_{0.5}\text{Al}_{0.5}\text{N}$ to molten polycarbonate at typical operating temperatures.

For understanding the interaction forces and their relation to the interfacial chemistry, a new approach was introduced in **publication IV** for quantifying and predicting van der Waals forces based on optical data with unprecedented accuracy and surface sensitivity.

This method was therefore used within **publication V** in combination with dynamic force spectroscopy and the structural, chemical and electronic origin of the adhesive van der Waals interactions at the $\text{Ti}_{0.5}\text{Al}_{0.5}\text{N}$ |polycarbonate interface could be revealed. Complementary, the objective of **publication VI** was to understand the influence of the oxidation states of the interacting surfaces and thereby the effect of interfacial acid-base bonding on adhesion.

In conclusion, these studies enable a thorough understanding of the surface chemistry and surface oxidation behaviour of hard coatings, which is then transferred to explain the related surface reactivity and adhesive force interactions in contact with polymers.

4.1 The Thermal Oxidation of TiAlN High Power Pulsed Magnetron Sputtering Hard Coatings as Revealed by Combined Ion and Electron Spectroscopy

The manuscript was reproduced from the following publication:

The Thermal Oxidation of TiAlN High Power Pulsed Magnetron Sputtering Hard Coatings as Revealed by Combined Ion and Electron Spectroscopy

Wiesing, M., de los Arcos, T., Grundmeier, G., *Advanced Materials Interfaces*, 1600861, 2017,
doi:10.1002/admi.201600861

Copyright © 2016, WILEY-VCH Verlag GmbH & Co. KGaA, Weinheim

Author contributions:

- Planning/experimental work/interpretation/manuscript preparation **MW**
- Proof reading/content check **TA** and **GG**

Placement:

Hard coatings form after their deposition thin surface oxide layers with a thickness of a few nanometres due to exposure to atmosphere and oxidize even further in polymer melt processing applications as a result of the elevated operating temperatures of around 600 K. The thermal oxidation process of $Ti_{0.5}Al_{0.5}N$ and the resulting chemical as well as structural properties of the surface oxide were therefore fundamentally investigated within this publication using a combined electron and ion spectroscopic approach. As a consequence, a microscopic mechanism of the surface oxidation could be developed for a wide range of temperatures and pressures. This not only allows for a comprehensive understanding of the surface chemistry and thereby of the interfacial interactions of hard coatings after their deposition, but also rationalizes their thermal oxidation behaviour under polymer processing conditions.

The Thermal Oxidation of TiAlN High Power Pulsed Magnetron Sputtering Hard Coatings as Revealed by Combined Ion and Electron Spectroscopy

Martin Wiesing, Teresa de los Arcos, and Guido Grundmeier*

The thermal oxidation of TiAlN hard coatings deposited by High Power Pulsed Magnetron Sputtering (HPPMS) is investigated at room temperature and 800 K at oxygen pressures ranging from 10^{-6} to 10^{-2} Pa by means of in situ X-ray and Ultraviolet Photoelectron Spectroscopy as well as Low Energy Ion Scattering. The spectra reveal that oxygen binds selectively to titanium during the initial chemisorption step and simultaneously some oxygen is dissolved into subsurface layers, which stay metallic. Enhanced oxidation results into continuous formation of a multilayered oxide film including oxynitride TiAl(O,N) as a metastable reaction product buried below an oxidic top layer. This top layer is either composed of mixed TiAlO after oxidation at 800 K or of segregated TiO₂ and Al₂O₃ when oxidizing at 293 K. Additionally, evaluation of UV-valence bands reveals nitrogen doping of the surface oxide films. The results are of high relevance for tailoring of the surface characteristics of TiAlN after deposition, for the design of TiAlN multilayers and for an improved understanding of the interactions of gas particles with these coatings.

injection molding.^[5] In this case the TiAlN coating is in contact with an oxygen containing polymer melt at a temperature of 500–700 K. Among the plethora of parameters that govern the development of specific surface-near multilayer structures upon oxidation the stoichiometry and internal structure of the coating previous to oxidation is of central importance. These latter aspects can be tailored up to a certain point through control of the deposition process. In particular, high power pulsed magnetron sputtering (HPPMS) has gained much attraction recently for the deposition of hard coatings with high density and improved properties in terms of adhesion, hardness, and low surface roughness.^[6–9] The reason for the increased quality of HPPMS-deposited films lies in the highly increased fraction of ionized species during deposition,

1. Introduction

Ternary hard coatings such as TiAlN have found widespread use for cutting tools due to their high hardness and resistance against wear and thermal oxidation.^[1,2]

Early studies of high temperature oxidation of TiAlN revealed the surface enrichment of aluminum and thus the formation of a protective Al₂O₃ cover layer on top of titanium nitride and oxynitride.^[2] This near surface structure clarified the improved oxidation resistance of TiAlN when compared to the prototypic TiN. Notably, investigations on the effect of the aluminum content on the oxidation resistance revealed that the formation of a closed Al₂O₃ cover layer was deteriorated at higher aluminum concentrations due to the formation of a mixed Al–Ti oxide and decomposition of the metastable cubic phase of TiAlN.^[3,4] Recently, such hard coatings have attracted additional interest due to the observed low wettability of polymers on surfaces of TiAlN and TiAl(O,N), which makes these coatings promising candidates as functional coatings of tools used in polymer

which allows for a higher degree control on the growing film structure.^[9]

However, independently of the degree of control achievable during the deposition process, a final issue critical for the establishment of a top oxide layer is the way samples react to different ambient conditions once the deposition process is finished. This aspect has been explored both theoretically and experimentally. Music et al., for example, used ab initio molecular dynamics to investigate the interaction of TiAlN surfaces with residual and environmental gases, namely O₂, H₂O, and CO₂.^[10] Greczynski et al. showed experimentally how the surface composition of TiN films dramatically changed as function of the conditions in which the venting procedure is performed.^[11] In short, in order to achieve specific oxide-terminated surfaces, the basic mechanisms by which thermal oxidation proceeds in the medium temperature range need to be better understood.

Preliminary experimental investigations of the oxygen chemisorption layer of HPPMS-deposited TiAlN have been already performed, showing that the oxygen chemisorption is self-limited and results into a surface segregated Ti₂O₃ layer.^[12] However, the present work is intended to provide a more accurate microscopic model of the chemisorption layer by using combined in situ X-ray Photoelectron Spectroscopy (XPS) and Low Energy Ion Scattering (LEIS). Based on the results obtained, a microscopic model of the oxidation of TiAlN at medium temperatures which are relevant for polymer processing will be developed.

M. Wiesing, Dr. T. de los Arcos, Prof. G. Grundmeier
Technical and Macromolecular Chemistry
University of Paderborn
Warburger Straße 100, 33098 Paderborn, Germany
E-mail: guido.grundmeier@tc.uni-paderborn.de



DOI: 10.1002/admi.201600861

2. Results and Discussion

2.1. Oxidation at 1×10^{-6} Pa O_2 and Room Temperature

Before surface oxidation, the TiAlN sample was cleaned from organic contaminations and its native oxide by means of Ar^+ sputter cleaning. The sputtering process is well known to affect structure and composition of the near-surface region due to preferential sputtering, atomic mixing and implantation of Ar, just to name a few.^[13] It must be thereby noted, that care has to be taken when comparing the results presented with the oxidation process of hard coatings as encountered directly after deposition.

However, the samples were exposed to oxygen at a pressure of 1×10^{-6} Pa after sputter cleaning. The exposure time was

10 min, thus ensuring that the surface concentration of chemisorbed oxygen reached a steady value. According to Kunze et al. it is expected that the first monolayer of chemisorbed oxygen hampers the 3D growth of the oxide film at these values of oxygen pressure and substrate temperature.^[12] The layer of chemisorbed oxygen was subsequently investigated in situ by XPS and LEIS.

Figure 1 shows the high resolution XPS spectra of the Ti2p, O1s, N1s, and Al2p core levels after (a) sputtering, (b) chemisorption, and (c) after LEIS characterization.

After Ar^+ sputtering (Figure 1a), the Ti2p line shape can be roughly described by two major components at binding energies of 455.0 and 456.6 eV, which are accompanied by a weaker satellite structure at 458.2 eV. The spin-orbit splitting of the

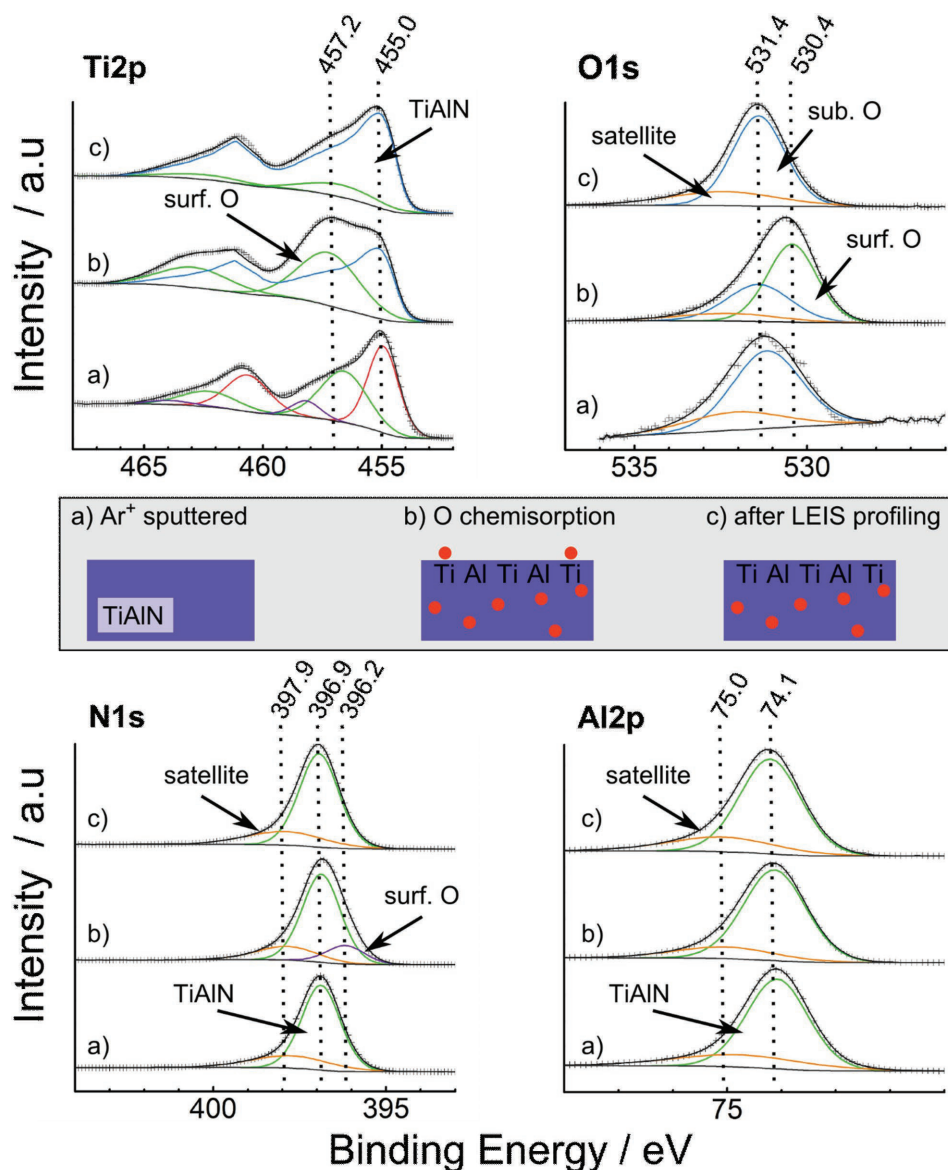


Figure 1. High-resolution XPS spectra of the Ti2p, O1s, N1s, and Al2p core levels a) after Ar^+ sputter cleaning, b) after oxygen chemisorption (10^{-6} Pa oxygen) at room temperature, and c) after measuring LEIS depth profiles of the state described in panel (b). The spectra have been normalized and shifted vertically for better visualization and the raw data are represented by symbols (+). The sketch illustrates the corresponding surface layer model for each experimental condition.

components was set to 5.7 eV for the peak fitting procedure.^[14] The component at 455.0 eV was included in order to account for the presence of a well screened peak in the spectrum of TiAlN, where relaxation occurs due to transfer of a d-band electron into a locally pulled-down d-state during the photoemission process.^[15–17] Complementary, the component at 456.6 eV was included for the case where no such relaxation proceeds (poorly screened peak). The satellite structure at 458.2 eV was motivated by EELS measurements of TiAlN, which show a Ti3d t_{1g} - t_{2g} intraband shake-up at 1.55 eV relative to the main signal with a relative intensity of 0.19. The satellite component in the Ti2p spectrum was set accordingly relative to the poorly screened peak at 456.6 eV. For illustration of the quality of the data and the fitting procedure, the reader is referred to Figure S1 (Supporting Information), which shows the data, fits, and residuals of Figure 1a in more detail and is representative for the XPS spectra discussed in the following.

The Ti2p line shape in TiN and TiAlN compounds is complex and has been the subject of several studies, which attribute the different components to different effects, such as an shake-up event due to Ti3d intraband transitions, changes in the screening ability of the conduction electrons associated with an increasing nitrogen content or structural effects.^[15–17] A good overview about different aspects of Ti2p line shape interpretation can be found elsewhere.^[18] Given the low concentration of oxygen detected after Ar⁺ sputtering (below 2.5 at%; see **Table 1**) we assume that the contribution of possible oxides or oxynitrides to the Ti2p line shape can be considered as negligible and thus that the Ti2p line as measured after the sputter cleaning treatment represents the state of an essentially oxygen-free TiAlN surface. The measured Ti2p line shape directly after Ar⁺ sputtering will be used as reference in all following mathematical decompositions as a whole in order to determine the additional components appearing as a consequence of oxygen exposure. This procedure is an empirical approach and neglects that the lineshape of the TiAlN substrate layers could change due to oxide overlayers, which is to some extent expected because the intraband transition represents an extrinsic energy loss mechanism. All components assigned in this publication using this empirical approach are thus primarily discussed based on qualitative arguments and reinforced by the use of complementing techniques such as LEIS and Wagner plot analysis. Where appropriate, quantitative stoichiometric calculations are discussed.

The corresponding N1s and Al2p core levels were located at 396.9 and 74.1 eV respectively, which is typical for TiAlN.^[18–20] However, both signals showed a distinct tailing to the higher

binding energy site, which was taken into account by fitting an additional satellite component shifted by 0.9 eV relative to the main signal. This tailing is common for several nitridic hard coatings but is scarcely discussed in literature.^[21] Some authors assign this component to the appearance of N–O species.^[22,23] However, tailing was also observed in essentially oxygen-free (4 at% oxygen) in situ XPS spectra of single crystalline Ti₂AlN and there are also indications that structural defects could be responsible for this spectral feature.^[17,24] The weak O1s contribution left after the sputtering was fitted using a linear background and two components: one at 531.2 eV related to oxygen impurities and another component at 532.1 eV ascribed to the satellite as in the case of the N1s and Al2p spectra.

The Ti2p, N1s, Al2p, and O1s core level lines after exposure of the sample to oxygen for 10 min can be seen in Figure 1b. The changes induced in the Ti2p line shape were described by the appearance of an additional broad component at 457.2 eV, which was related to the formation of Ti–O bonds. The Al2p peak however was unaffected by chemisorption. The N1s lineshape was described by using the components of TiAlN and fixing their positions and the FWHM of the main signal. Further, a lower binding energy component at 396.2 eV was included and assigned to the presence of surface oxygen. This latter component was scarcely resolved and the position was thereby fixed relative to the main nitride component. This peak model was validated by the spectra of the more oxidized samples discussed below. The O1s line is decomposed into three components at 530.4, 531.4, and 532.3 eV. The component at 530.4 eV is assigned to the formation of Ti–O bonds of surface oxygen, while the component at 531.4 eV is associated with subsurface oxygen. The third component at 532.3 eV is as before ascribed to the satellite. The binding energies of the latter two components were taken from the O1s signal after LEIS profiling as discussed below and fixed for deconvolution. These assignments are justified by the LEIS characterization of the surface, as described in the following paragraphs.

After first performing XPS measurements of the chemisorbed layer, the sample was investigated in situ by LEIS and the results are shown in **Figure 2** (Supporting Information). The bombardment of the sample by He⁺ ions during the measurement lead to a progressive sputtering of sample material with the corresponding changes in the LEIS spectrum as can be seen in the figure. Three main components can be identified in the LEIS spectrum at 756, 622, and 459 eV kinetic energy and are assigned to titanium, aluminum and oxygen respectively.^[25] Trace amounts of nitrogen were observed in the form of a shoulder appearing at about 400 eV at the lower kinetic energy side of the oxygen signal. During LEIS “profiling,” the titanium signal increased at the expense of the oxygen signal, whereas the aluminum signal remained constant. Since LEIS is almost entirely sensitive to the outermost atomic layer, this analysis shows that aluminum and titanium atoms are both present at the very surface. However, it was found that no aluminum oxide cover layer was formed during chemisorption, and that the chemisorbed O atoms preferentially bind to titanium. This interpretation is supported when considering the density of states of TiAlN and TiAl(O,N):^[26] according to the stoichiometry of Ti_{0.2}Al_{0.3}N_{0.5} (see **Table 1**), ≈1 electron is located in the Ti3d valence band, which is separated from the largely mixed

Table 1. Stoichiometry of the investigated samples in atomic percent as derived from XPS survey spectra measured at 60°.

Sample	X _{Al} [at%]	X _N [at%]	X _{Ti} [at%]	X _O [at%]	Al/Ti
Ar ⁺ sputtered	32.8	43.6	21.3	2.4	1.54
10 ⁻⁶ Pa, 10 min, 293 K	30.2	37.3	19.3	13.2	1.56
LEIS profiling	32.1	40.5	20.5	7.0	1.56
5 × 10 ⁻² Pa, 24 h, 293 K	25.4	26.6	17.3	30.7	1.47
5 × 10 ⁻² Pa, 24 h, 800 K	26.9	19.6	15.1	38.4	1.78

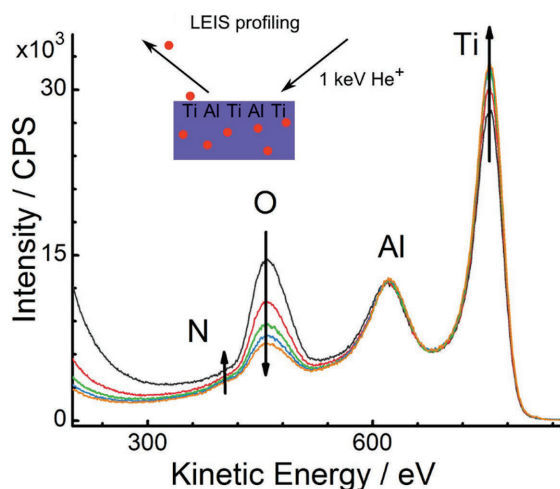


Figure 2. LEIS depth profile measured with 1 keV He⁺ of the oxygen chemisorption layer on TiAlN as obtained after sputter cleaning and exposure to 10⁻⁶ Pa oxygen at 293 K for 10 min. Each spectrum corresponds to one scan, and all scans were performed consecutively. The arrows indicate the evolution with time.

N2p, Al3p, and O2p band by a pseudo band gap. Thus, spill-over Ti3d electrons are transferred into localized oxygen states during oxygen adsorption resulting into oxygen to bind selectively to titanium atoms at the surface. This preferential interaction of oxygen with titanium was also found within simulations of the gas/solid interactions for a TiAlN(001) surface.^[10]

The LEIS characterization allows to refine the interpretation of XPS data, especially when comparing the XPS characterization of the chemisorbed layer done before (Figure 1b) and after LEIS (Figure 1c). The main effect of the LEIS measurement is the preferential sputtering of oxygen. The stoichiometry of the samples as determined from the XPS data showed that the oxygen concentration decreased to 53% of its original value, from about 13 at% after chemisorption to about 7 at% after LEIS profiling. In comparison with the oxygen LEIS signal, a larger decrease to 31% of the initial oxygen value was observed. Since the LEIS oxygen signal reflects surface oxygen atoms only, this shows that oxygen is also present in subsurface layers and is thereby measured by XPS. When comparing Figure 1b,c, the sputter removal of surface oxygen is further associated with the disappearance of the O1s component at 530.4 eV, which reinforces the interpretation that this component represents the surface oxygen atoms. In turn, the other component at 531.4 eV is consequently related to subsurface oxygen species. These assignments are qualitatively in good agreement with chemical shifts of chemisorbed oxygen on α_2 -TiAl, where dissociated surface oxygen was found at 530.7 and subsurface oxygen at 532.0 eV.^[27] The results show that the oxygen chemisorption on TiAlN is accompanied by inward migration of oxygen.

The oxygen behavior is also reflected in the Ti2p and N1s peaks. In the case of Ti2p, the Ti–O component at 457.2 eV diminished also to 31% of its original intensity after LEIS profiling. This matches the decrease of the LEIS oxygen signal and thus allows to assign this Ti2p component similarly to titanium binding to surface oxygen. This further implicates that one oxygen atom is bound to one titanium atom at the surface.

Accordingly, the component of N1s at 396.2 eV also decreased concomitantly with the surface oxygen component of the Ti2p spectrum and is thereby similarly related to the presence of surface oxygen. This finding is in agreement with earlier observations of oxynitride at this binding energy, which show that the binding energy of nitride is affected by the presence of oxygen.^[17]

The 1:1 stoichiometry of the surface oxygen layer can be supported by means of cross-peak self-consistency calculations: the amount of oxygen related only to surface oxygen (Ti–O) was calculated from both Ti2p (component at 457.2 eV) and O1s (component at 530.4 eV) spectra assuming a stoichiometry of 1:1 for the Ti–O structure.^[28] The surface oxygen concentration of the sample as calculated from the Ti2p and O1s core levels is 9.6% and 8.9 at% respectively thus validating the 1:1 stoichiometry assumption. This allows now to estimate the oxygen content related to the N1s surface oxygen component at 396.2 eV by subtracting the amount of surface adsorbed oxygen from the total oxygen content of the surface. It follows that around 4 at% oxygen relate to the N1s surface oxygen component, which corresponds to 5.6 at% nitrogen, and that the N/O ratio is therefore ≈ 1.4 .

To conclude this section, the combined XPS and LEIS data showed that oxygen preferentially interacts with the Ti3d spill-over electrons during chemisorption, which results into selective binding of oxygen to titanium on the surface. Further, self-limited inward migration of oxygen occurs resulting into a stable situation, where some oxygen is dissolved in subsurface layers.

2.2. Oxidation at 5×10^{-2} Pa O₂ and 800 K

The thermal oxidation of TiAlN was studied at an oxygen pressure of 5×10^{-2} Pa and at temperatures of 293 and 800 K. In this set of experiments, performed in a second ultrahigh vacuum (UHV) chamber attached to the XPS chamber, the surface after oxygen chemisorption (1×10^{-5} Pa oxygen for 5 min) served as starting point for enhanced oxidation in order to mitigate adsorption of organic contaminations during transfer. The amount of adventitious carbon was generally below 2 at% and neglected in the following analysis. The corresponding XPS core level spectra are shown in Figure 3.

Following oxidation at 293 K for 3 h (Figure 3a), the appearance of a broad Ti2p component centered at 457.4 eV was clearly visible. This component can be, as in the chemisorption case, assigned to surface oxygen. However, since the Ti2p peak for oxynitrides is also expected in the range of 455.5–457.7 eV, we assign this component to a mixture of oxynitridic TiAl(O,N) and surface oxygen.^[17] This is supported by the N1s component at 396.2 eV, which was clearly more intense than in the chemisorption experiment and is typical for TiAl(O,N).^[17] The joined behavior of Ti2p and N1s peaks was thus interpreted in terms of the inset of enhanced surface oxide growth via an oxynitridic TiAl(O,N) growth region.^[2] The O1s peak was decomposed into two components located at 531.8 and 530.3 eV. The precise chemical nature of both components could not be entirely resolved. This is because the components used for the chemisorption of oxygen (Figure 1a) overlap with the oxygen signal

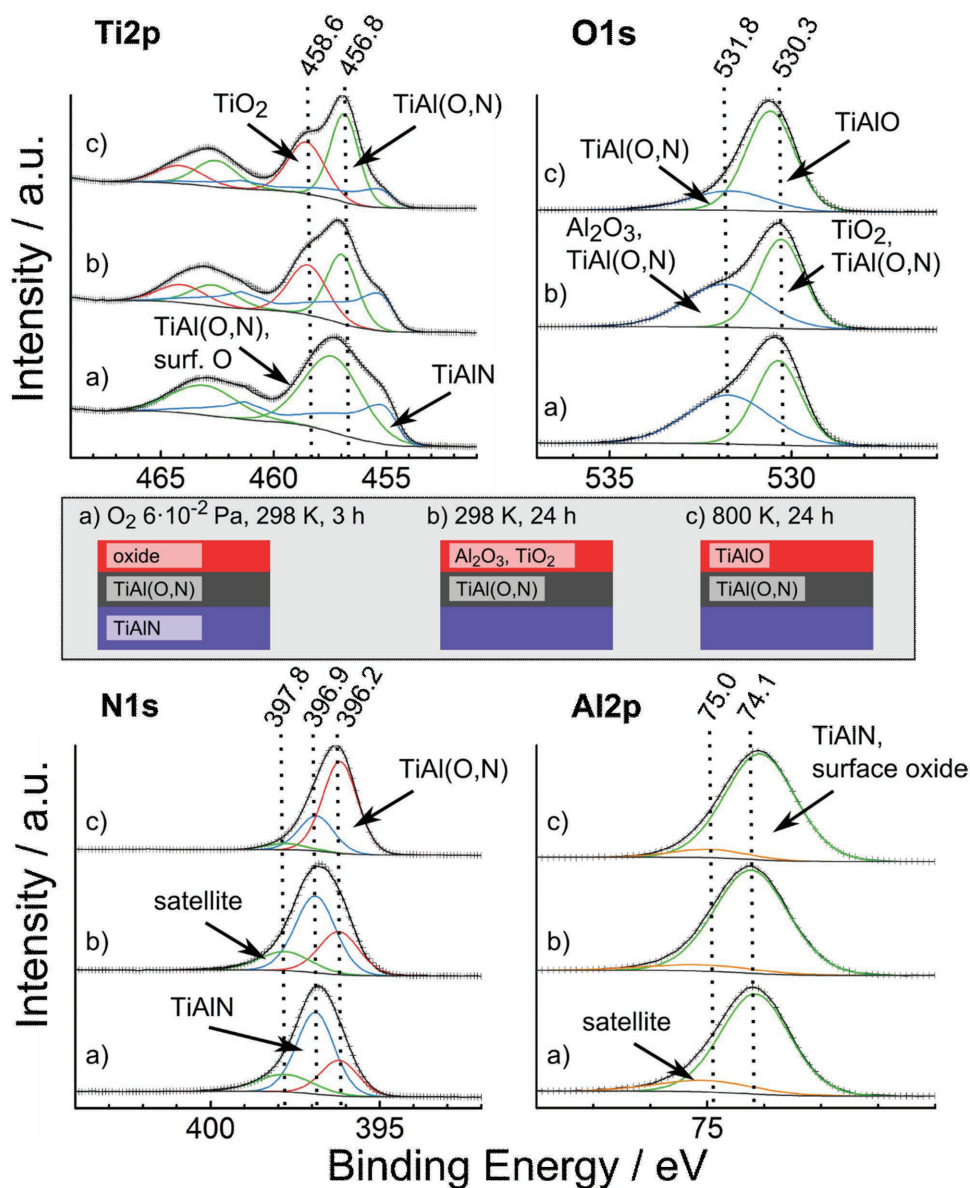


Figure 3. High-resolution XPS spectra of the Ti2p, O1s, N1s, and Al2p core levels of TiAlN after Ar^+ sputtering and a) exposure to 5×10^{-2} Pa O_2 for 3 h at 293 K, b) exposure to 5×10^{-2} Pa O_2 for 24 h at 293 K, and c) exposure to 5×10^{-2} Pa O_2 for 24 h at 800 K. The spectra have been normalized and shifted vertically for better visualization and the raw data are represented by symbols (+). The sketch illustrates the corresponding surface layer model for each experimental condition.

of the TiAl(O,N) growth region. Further, it is shown below that segregation into Al_2O_3 and TiO_2 sets in during oxidation at room temperature, which additionally impedes a precise chemical assignment. The Al2p peak showed as in the chemisorbed case no relevant variation of the lineshape and binding energy with respect to the clean, oxide-free TiAlN surface.

Longer oxygen exposures for 24 h at different substrate temperatures were also investigated. The corresponding XPS spectra are shown in Figure 3b (substrate temperature 273 K) and c (substrate temperature 800 K). The most notable effect in both cases was seen in the Ti2p component, for which two well separated components appear at 456.8 and 458.6 eV. The complete lineshape was described by fixing the shift of the

spin-orbit split components to 5.7 eV and the intensities to 0.44 of the related $Ti2p_{3/2}$ components. This intensity value contrasts the expected value of 0.5 but was the experimentally observed ratio when using a Shirley background. The component at 458.6 eV is assigned to Ti in its highest oxidation state, which could correspond to either TiO_2 or TiAlO and is for the moment simply described as “Ti(IV).”^[14] The component at 456.8 eV describes the contribution from TiAl(O,N). The oxynitride component is also clearly identified in the N1s peak at 392.2 eV by its increase in intensity.

The decomposition of the Ti2p into two clearly separated components makes the question arise whether they correspond to phases separated in a multilayer structure. Additional angle

Table 2. Surface layer thicknesses of the different surface oxide layers as obtained after exposure to oxygen at 5×10^{-2} Pa (see the Supporting Information for details of the calculation).

Temperature [K]	Duration [h]	$d\{\text{TiAl(O,N)}\}$ [nm]	$d\{\text{Ti(IV)}\}$ [nm]
293	3	1.96	–
293	24	1.26	0.66
800	24	2.18	0.75

resolved measurements (see Figure S2, Supporting Information) done in this case showed that the Ti(IV) component was closer to the surface than the TiAl(O,N) component, which indicates the formation of a fully oxidized layer onto a TiAl(O,N) sublayer.

Assuming a clear separation of these two layers, it is possible to use the relative ratios of the Ti2p components to estimate their thickness, which are shown in Table 2 (see supporting information for details about the calculation). A comparison of the two experiments performed at room temperature and different times shows that after 3 h a TiAl(O,N) layer of about 2 nm thickness is formed. Longer exposure times at the same temperature show that this layer separates with time into a fully oxidized Ti(IV) top layer of about 0.7 nm thickness and an underlying 1.3 nm thick TiAl(O,N) layer. In comparison, oxygen exposure for 24 h at 800 K resulted into a clear increase of the underlying TiAl(O,N) thickness to 2.2 nm, while the Ti(IV) layer at 0.7 nm showed only a negligible increase in thickness with respect to the low temperature case.

Assuming a model of perfectly separated layers, the observed behavior can be explained as a stepwise formation of first a TiAl(O,N) growth region due to inward migration of oxygen and then the establishment of a top layer of fully oxidized Ti(IV). This interpretation is also supported by recent investigation on the electrochemical oxidation of TiAlN, where the electrochemical oxidation of TiAlN could be described by a reactive migration mechanism as well.^[29] The relevance of the oxygen inward migration for the oxidation is further highlighted by the Al/Ti ratios reported in Table 1: though preponderant aluminum outward migration is expected in the case of the high temperature TiAlN oxidation, the Al/Ti ratios remained rather constant and only slight enrichment of aluminum was observed at 800 K.^[2]

Additional information about the nature of this rather generically described Ti(IV) layer can be obtained by a careful analysis of the O1s peak after the exposure for 24 h. In Figure 3, the O1s peaks were decomposed into two components: after oxidation at room temperature (case b) the binding energies and relative ratios of these components were 530.2 (54%) and 531.7 eV (46%) and after oxidation at 800 K (case c) the binding energies and relative ratios were 530.3 (76%) and 531.4 eV (24%). In both cases, the lower binding energy position component at about 530.3 eV can be assigned to either mixed TiAlO (see film 3 of Cremer et al.^[30]) or TiO₂.^[3,17,27,31] The other component at 531.7 eV could relate to oxynitride or Al₂O₃ according to its binding energy.^[3,32–34] In this regards, it must be noted that the partial pressure of water during the long-term 24 h oxidations was 1.2×10^{-6} Pa due to the purity of the gas and was thus not negligible. The presence of water might eventually result into

hydroxylation, and could easily account for the higher binding energy components.^[35–37] However, the angle-resolved O1s spectra shown in Figure S2 (Supporting Information) show surface depletion of the higher binding energy components, which allows to exclude the presence of surface hydroxylation or the adsorption of water.

The question is now open whether the topmost layer is composed by a segregated two-phase mixture of TiO₂ and Al₂O₃ or by a homogenous TiAlO layer. This problem was addressed by an analysis of the O1s modified Auger parameter of the samples. The corresponding Wagner plot is shown in Figure 4.

It was found that the modified Auger parameter dropped after oxidation at 800 K, whereas at 293 K only a small decrease was observed. Since the modified Auger parameter is a measure for the extra-atomic relaxation energy of the core hole, this indicates a decrease of the polarizability of surface oxides, which depends on the temperature of oxidation.^[38,39] In this regard, it is noted that due to the small depth of information the modified Auger parameter dominantly reflects the polarizability of the so-called Ti(IV) outer layer. This allows for a comparison with values for metastable mixed TiAlO, which was earlier investigated by Cremer et al., who identified two separated regimes that were ascribed to segregated Al₂O₃ and TiO₂ at 1042 eV and mixed TiAlO between 1037 and 1041 eV.^[30] In our case, the Auger parameter of the surface oxide formed at 293 K indicates the inset of segregation, whereas at 800 K a mixed TiAlO apparently grows.

These results can be corroborated by cross-peak self-consistent stoichiometric calculations.^[28] Following these principles, the oxygen concentrations related to TiO₂ and TiAlO formed after 24 h at 293 and 800 K were calculated from the

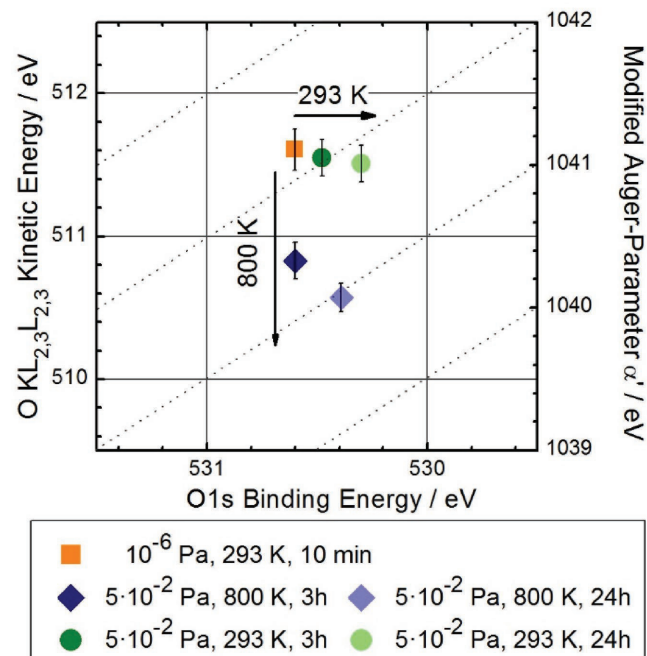


Figure 4. Wagner plot of the O1s modified Auger parameter of the surface oxide layer formed on the samples investigated in this work. The uncertainty of the O1s binding energy was below 65 meV.

Table 3. Cross-peak self-consistent calculations of the assignments of the Ti(IV) component of the Ti2p and O1s peaks in the case of oxidation for 24 h at 293 and 800 K based on the sample stoichiometries from Table 1.

Temperature [K]	Transition	Components BE [eV]	Proposed assignment	X _o [at%]
293	O1s	468.6	TiO ₂	10.7
		530.2	TiO ₂	14.7
		531.7	Al ₂ O ₃	12.5
800	Ti2p	468.6	TiAlO	25.7 ^{a)}
		530.3	TiAlO	23.8
		531.4	TiAl(O,N)	10.7

^{a)}The concentration of oxygen bound to Al(III) in TiAlO was calculated by assuming that the Al2p component associated with TiAlO (not resolved in the Al2p peak) had the same fraction as that of the corresponding Ti2p component.

respective Ti2p and O1s components. The results are shown in **Table 3**. For the oxidation at 800 K it was assumed that the fraction of Al2p related to TiAlO is the same as for Ti2p, because the Al2p lineshape was unaffected by oxidation and no TiAlO-related Al2p component could be resolved. With this assumption, the surface oxygen concentration due to TiAlO is either 25.7 or 23.8 at% when calculated from either the O1s or the Ti2p spectra. Since these values are essentially identical, the assignments of the TiAlO components in the O1s and Ti2p spectra are in mutual agreement and thereby corroborated. Further, the calculation shows that the lower binding energy O1s component at 531.4 eV corresponds to TiAl(O,N) in the case of oxidation at 800 K.

After oxidation at 293 K no spectral components could be assigned unambiguously due to uncertainties of the peak position of the TiAl(O,N) component, which depends on the oxidation temperature.^[28]

In conclusion, Wagner plot analysis in combination with cross-peak self-consistent calculations indicates that the oxidation at 800 K results into mixed TiAlO whereas at 293 K segregation into Al₂O₃ and TiO₂ occurs. An illustration of this surface layer model is shown in **Figure 5**

2.3. Electronic Properties of the Surface Near Regions

A more thorough characterization of the electronic properties of the surface oxides during the different stages of oxidation was done by Ultraviolet Photoelectron Spectroscopy (UPS)

measurements of the valence band region. The results for the sample oxidized at 800 K during 24 h are shown in **Figure 6** and are representative for the oxidation at both temperatures (see **Figure S3** (Supporting Information) for the spectra of the sample oxidized at 293 K).

Following Ar⁺ sputter cleaning (**Figure 6a**), a Fermi cutoff was observed and attributed to Ti3d electrons present at 0 eV binding energy, which reflects the metallic behavior of the hard coating. The broad band around 5 eV is ascribed to mixed N2p/Al3p states (p-band).^[15] After chemisorption of oxygen (**Figure 6b**) a decrease of the Ti3d electron density and relative increase of the p-band intensity was observed. This is explained by the capture of Ti3d electrons by oxygen and the incorporation of O2p states into the p-band.^[26] The fact that Ti3d states are still present at the Fermi level shows that the near-surface region is not completely oxidized and that the oxygen incorporation does not reduce the metallic character significantly in the chemisorbed case. By contrast, the Ti3d component disappeared in the thermally oxidized case (**Figure 6c**).

The quasi-metallic character of the oxygen chemisorption layer was also reflected by the corresponding Ti2p spectrum in **Figure 1b**, where only surface oxygen but not the subsurface oxygen affected the Ti2p lineshape. Considering that strong interactions between O2p and Ti3d states occur, it is supposed that the oxygen concentrations in buried layers are diluted. This interpretation is in accordance with the initial stages of the oxidation of α₂-TiAl, where similarly adsorption and incorporation of oxygen into the metallic alloy was observed.^[27]

Apart from the decrease of intensity at the Fermi level, another effect of the progressive incorporation of oxygen into the surface is the appearance of a shoulder at about 3 eV during chemisorption that shifts toward an approximate position of 2 eV after thermal oxidation. Based on the partial density of states of TiAl(O,N) we attribute this shift to changes in the p-band: preferential binding of oxygen to aluminum substitutes the nitrogen–aluminum bonds and pushes the N2p band to lower binding energies.^[26] The nitrogen can thus be regarded to act essentially as a deep trap. This explanation is corroborated by nitrogen doping studies of TiO₂, where a similar electronic structure is observed and nitrogen dopants present on lattice sites are also forming the oxynitridic O–Ti–N structure with a similar N1s binding energy of 397 eV.^[40,41] Considering further the low depth of information of UPS, this further implicates that the oxidized top layers formed after oxidation are nitrogen-doped.

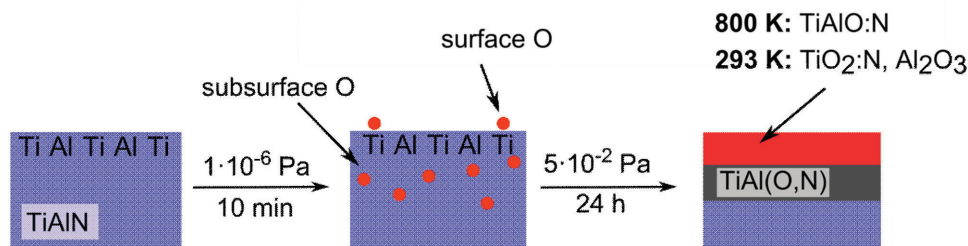


Figure 5. Schematic of different stages of surface oxide growth on TiAlN assuming a model of sharp separation between layers. Note that the illustration is not at scale.

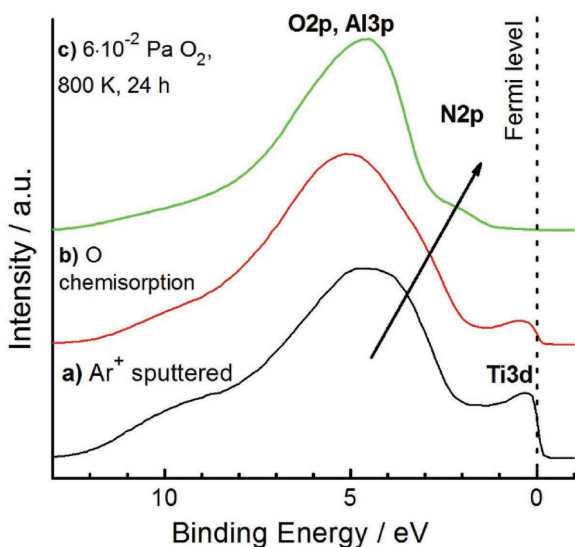


Figure 6. UPS (21.2 eV) valence band measurement of TiAlN after a) Ar⁺ sputter cleaning, b) chemisorption at $p(\text{O}_2) = 1 \times 10^{-6}$ Pa and 293 K for 10 min, c) oxidation at $p(\text{O}_2) = 5 \times 10^{-2}$ Pa and 800 K for 24 h. The spectra were normalized and shifted vertically for better visualization.

3. Conclusion

The transition from oxygen chemisorption to surface oxidation of TiAlN was investigated by means XPS, UPS, and LEIS. The results show that the nonoxidized Ar⁺ sputter cleaned surface is essentially metallic, and terminated by titanium and aluminum. Subsequent oxygen chemisorption at 5×10^{-6} Pa leads to selective binding of oxygen to titanium sites and a concomitant inward migration of oxygen. This process does not result into a 3D surface oxide, but is restricted to the incorporation of oxygen without substantially changing the metallic character of the subsurface layers.

During oxidation at oxygen partial pressure of 5×10^{-2} Pa, a multilayered surface oxide formed on top of an oxynitridic growth region due to reactive inward migration of oxygen. The nitrogen within that region was found to be destabilized due to reactive exchange of Al–N bonds by Al–O bonds. The structure of the formed surface oxides was determined by the temperature: detailed chemical analysis using the Wagner plot indicated the formation of a mixed TiAlO top layer at 800 K, whereas the oxide segregated at 293 K into TiO₂ and Al₂O₃. These results are of high relevance for postprocessing of TiAlN directly after deposition and its reactivity in contact with polymer melts.

4. Experimental Section

Thin Film Deposition: The HPPMS deposition process was chosen due to the superior quality of the coatings. As described elsewhere, TiAlN thin films with a thickness of 1.2 μm were deposited on boron-doped (100) Si wafer (1–5 Ω cm).^[29] The deposition chamber (CemeCon CC-800/9) was equipped with a rectangular magnetron (500 × 88 mm²) and a Ti/Al compound target, which provided a Ti/Al ratio of nearly 1 and was located 80 mm away from the substrates. The substrates were held at floating potential and heated to 550 K. Sputter deposition was performed at 800 Hz with an on-time of 50 μs, which gives a

time-averaged power density of 6.8 W cm⁻² and a peak power density of 0.4 kW cm⁻². The gas pressure inside the chamber was 0.46 Pa and the Ar:N₂ ratio was set to 4:1. The structure of the samples was characterized by X-Ray Diffraction and a random structure was found.^[29] The density of the TiAlN was around 4.8 g cm⁻³ and the stoichiometry was Ti_{0.2}Al_{0.3}N_{0.5} as determined by an Ar⁺ sputtered sample measured by XPS. Minor bulk oxygen contaminations were also found by XPS and are neglected in the following discussion (2.4 at%).

Sample Preparation: The as-deposited samples were sonicated in analytical grade ethanol for 5 min before introduction into the UHV environment of the characterization chamber. In situ cleaning of the specimens was performed by Ar⁺ sputtering using the Figure 5 from PHI Physical Instruments (3 kV, 8 μA cm⁻², 20 min, 30° angle of incidence) until the residual O content of the near-surface layer decreased to a constant value below 2.5 at% as determined by XPS. After this cleaning step the samples were exposed to different oxygen pressures (99.998%, <2 ppm H₂O, Air Liquide) at different substrate temperatures and exposure times. The room temperature (293 K)-low pressure (1×10^{-6} Pa) experiments were performed directly in the analytical chamber of the XPS. Enhanced oxidation at 800 or 293 K and higher oxygen pressures (1×10^{-6} and 5×10^{-2} Pa) was performed in a second UHV-preparation chamber directly attached to the XPS, so that the samples were transferred between the different chambers without breaking the vacuum.

Surface Chemical Analysis: The UHV facility is composed of two interconnected chambers, one for oxidation experiments, and a second one dedicated to sample characterization by XPS, UPS, and LEIS. The spectrometer was an ESCA+ system (Oxford Instruments, Omicron Nanotechnology). For XPS, monochromated Al Kα irradiation (1486.7 eV) was used, with a source to analyzer angle of 102°. The spectral resolution was 0.77 eV as determined from the silver metal Ag3d_{5/2} lineshape. Similarly, the binding energy was referenced to the Ag3d_{5/2} line at 368.0 eV and no charge neutralizer was used. Unless otherwise stated, XPS spectra were measured at an emission angle of 15° relative to the surface normal, resulting into an information depth of the measured core level spectra (O1s, Ti2p, N1s, Al2p) of ≈5.5 nm.^[42] For the construction of Wagner plots the X-ray excited O KLL spectra were measured at 15°, while the O1s spectra were taken at 60°. This was done in order to match a similar value of the information depth of 2.7 nm, taking into account the different attenuation lengths of the emitted electrons due to their different kinetic energies.^[42] The modified Auger parameter was then calculated by adding the value of the O1s binding energy to the kinetic energy of the oxygen KLL signal.^[39] The acquired XPS data were evaluated with CasaXPS (2.3.15 Casa Software Ltd.) using asymmetry corrected elemental sensitivity factors and GL(30) lineshapes. Peak fitting was performed without any constraints and using a Shirley background unless otherwise stated. A Monte Carlo procedure for estimating uncertainties of fit parameters was used as implemented in CasaXPS. Generally, the uncertainty of XPS components was better than 0.07 eV and is thereby neglected. The error of the oxygen KLL signals for the construction of the Wagner plots was estimated by empirically fitting the KLL peak by three GL(30) peaks and making similarly use of the Monte Carlo method. The He I line at 21.2 eV was used for UPS measurements (HIS 13 VUV Source, Omicron Nanotechnology). The geometry of the He⁺ LEIS comprised an incidence angle and an emission angle of 30° and 60° with respect to the surface normal resulting into a scattering angle of 115°. The flux of the primary He⁺-ions generated by the Figure 5 sputter gun with an energy of 1 kV was ≈ 1×10^{13} ions cm⁻² s⁻¹ and can be thus regarded as destructive.^[25] The beam was rastered across an area of 1 mm² in order to increase the sensitivity. The acquisition time of a single spectrum was 75 s with an energy resolution of 2.2 eV.

Supporting Information

Supporting Information is available from the Wiley Online Library or from the author.

Acknowledgements

The authors gratefully thank M. to Baben and J. M. Schneider for the synthesis of the hard coating. Further, the authors acknowledge the German Research Foundation (DFG) for financial support within the Transregional Collaborative Research Center SFB TR 87.

Received: September 6, 2016

Revised: October 20, 2016

Published online:

-
- [1] T. Leyendecker, O. Lemmer, S. Esser, J. Ebberink, *Surf. Coat. Technol.* **1991**, *48*, 175.
- [2] S. Hofmann, *Thin Solid Films* **1990**, *193–194*, 648.
- [3] F. Esaka, K. Furuya, H. Shimada, M. Imamura, N. Matsubayashi, T. Kikuchi, H. Ichimura, A. Kawana, *Surf. Interface Anal.* **1999**, *27*, 1098.
- [4] J.-L. Huang, B.-Y. Shew, *J. Am. Ceram. Soc.* **1999**, *82*, 696.
- [5] K. Bobzin, R. Nickel, N. Bagcivan, F. D. Manz, *Plasma Process. Polym.* **2007**, *4*, S144.
- [6] V. Kouznetsov, K. Macák, J. M. Schneider, U. Helmersson, I. Petrov, *Surf. Coat. Technol.* **1999**, *122*, 290.
- [7] K. Sarakinos, J. Alami, S. Konstantinidis, *Surf. Coat. Technol.* **2010**, *204*, 1661.
- [8] D. Lundin, K. Sarakinos, *J. Mater. Res.* **2012**, *27*, 780.
- [9] J. T. Gudmundsson, N. Brenning, D. Lundin, U. Helmersson, *J. Vac. Sci. Technol., A* **2012**, *30*, 030801.
- [10] D. Music, J. M. Schneider, *New J. Phys.* **2013**, *15*, 073004.
- [11] G. Greczynski, S. Mráz, L. Hultman, J. M. Schneider, *Appl. Phys. Lett.* **2016**, *108*, 041603.
- [12] C. Kunze, D. Music, M. to Baben, J. M. Schneider, G. Grundmeier, *Appl. Surf. Sci.* **2014**, *290*, 504.
- [13] S. Hofmann, *Philos. Trans. R. Soc., A* **2004**, *362*, 55.
- [14] *NIST X-Ray Photoelectron Spectroscopy Database*; Version 4.1, National Institute of Standards and Technology, Gaithersburg, MD **2012**.
- [15] I. leR. Strydom, S. Hofmann, *Vacuum* **1990**, *41*, 1619.
- [16] L. Porte, L. Roux, J. Hanus, *Phys. Rev. B* **1983**, *28*, 3214.
- [17] P. Prieto, R. E. Kirby, *J. Vac. Sci. Technol., A* **1995**, *13*, 2819.
- [18] A. Arranz, C. Palacio, *Surf. Sci.* **2006**, *600*, 2510.
- [19] G. Greczynski, J. Jensen, J. E. Greene, I. Petrov, L. Hultman, *Surf. Sci. Spectra* **2014**, *21*, 35.
- [20] A. Schüler, P. Oelhafen, *Phys. Rev. B* **2001**, *63*, 115413.
- [21] A. J. Perry, *J. Vac. Sci. Technol., A* **1988**, *6*, 2140.
- [22] D. Jaeger, J. Patscheider, *J. Electron Spectrosc. Relat. Phenom.* **2012**, *185*, 523.
- [23] I. Milošv, H.-H. Strehblow, B. Navinšek, M. Metikoš-Huković, *Surf. Interface Anal.* **1995**, *23*, 529.
- [24] Z. Zhang, Y. Nie, L. Shen, J. Chai, J. Pan, L. M. Wong, M. B. Sullivan, H. Jin, S. J. Wang, *J. Phys. Chem. C* **2013**, *117*, 11656.
- [25] H. H. Brongersma, M. Draxler, M. de Ridder, P. Bauer, *Surf. Sci. Rep.* **2007**, *62*, 63.
- [26] M. to Baben, L. Raumann, J. M. Schneider, *J. Phys. Appl. Phys.* **2013**, *46*, 084002.
- [27] V. Maurice, G. Despert, S. Zanna, P. Josso, M.-P. Bacos, P. Marcus, *Acta Mater.* **2007**, *55*, 3315.
- [28] G. Greczynski, L. Hultman, *Appl. Surf. Sci.* **2016**, *387*, 294.
- [29] M. Wiesing, M. to Baben, J. M. Schneider, T. de los Arcos, G. Grundmeier, *Electrochim. Acta* **2016**, *208*, 120.
- [30] R. Cremer, M. Witthaut, D. Neuschütz, *Fresenius' J. Anal. Chem.* **1999**, *365*, 28.
- [31] I. Bertóti, M. Mohai, J. L. Sullivan, S. O. Saied, *Appl. Surf. Sci.* **1995**, *84*, 357.
- [32] H. C. Barshilia, N. Selvakumar, K. S. Rajam, D. V. Sridhara Rao, K. Muraleedharan, *Thin Solid Films* **2008**, *516*, 6071.
- [33] V. Maurice, H.-H. Strehblow, P. Marcus, *Surf. Sci.* **2000**, *458*, 185.
- [34] L. P. H. Jeurgens, W. G. Sloof, F. D. Tichelaar, E. J. Mittemeijer, *Surf. Sci.* **2002**, *506*, 313.
- [35] E. McCafferty, J. P. Wightman, *Surf. Interface Anal.* **1998**, *26*, 549.
- [36] G. Ketteler, S. Yamamoto, H. Bluhm, K. Andersson, D. E. Starr, D. F. Ogletree, H. Ogasawara, A. Nilsson, M. Salmeron, *J. Phys. Chem. C* **2007**, *111*, 8278.
- [37] X. Deng, T. Herranz, C. Weis, H. Bluhm, M. Salmeron, *J. Phys. Chem. C* **2008**, *112*, 9668.
- [38] C. D. Wagner, *Faraday Discuss. Chem. Soc.* **1975**, *60*, 291.
- [39] G. Moretti, *Surf. Sci.* **2013**, *618*, 3.
- [40] C. Gnoth, C. Kunze, M. Hans, M. to Baben, J. Emmerlich, J. M. Schneider, G. Grundmeier, *J. Phys. Appl. Phys.* **2013**, *46*, 084003.
- [41] C. Di Valentin, A. Tilocca, A. Selloni, T. J. Beck, A. Klust, M. Batzill, Y. Losovyj, U. Diebold, *J. Am. Chem. Soc.* **2005**, *127*, 9895.
- [42] C. Di Valentin, G. Pacchioni, A. Selloni, *J. Phys. Chem. C* **2009**, *113*, 20543.
-

**ADVANCED
MATERIALS**
INTERFACES

Supporting Information

for *Adv. Mater. Interfaces*, DOI: 10.1002/admi.201600861

The Thermal Oxidation of TiAlN High Power Pulsed
Magnetron Sputtering Hard Coatings as Revealed by
Combined Ion and Electron Spectroscopy

*Martin Wiesing, Teresa de los Arcos, and Guido Grundmeier**

Supporting Information

Title

The thermal oxidation of TiAlN High Power Pulsed Magnetron Sputtering hard coatings as revealed by combined ion and electron spectroscopy

*Martin Wiesing, Teresa de los Arcos, Guido Grundmeier**

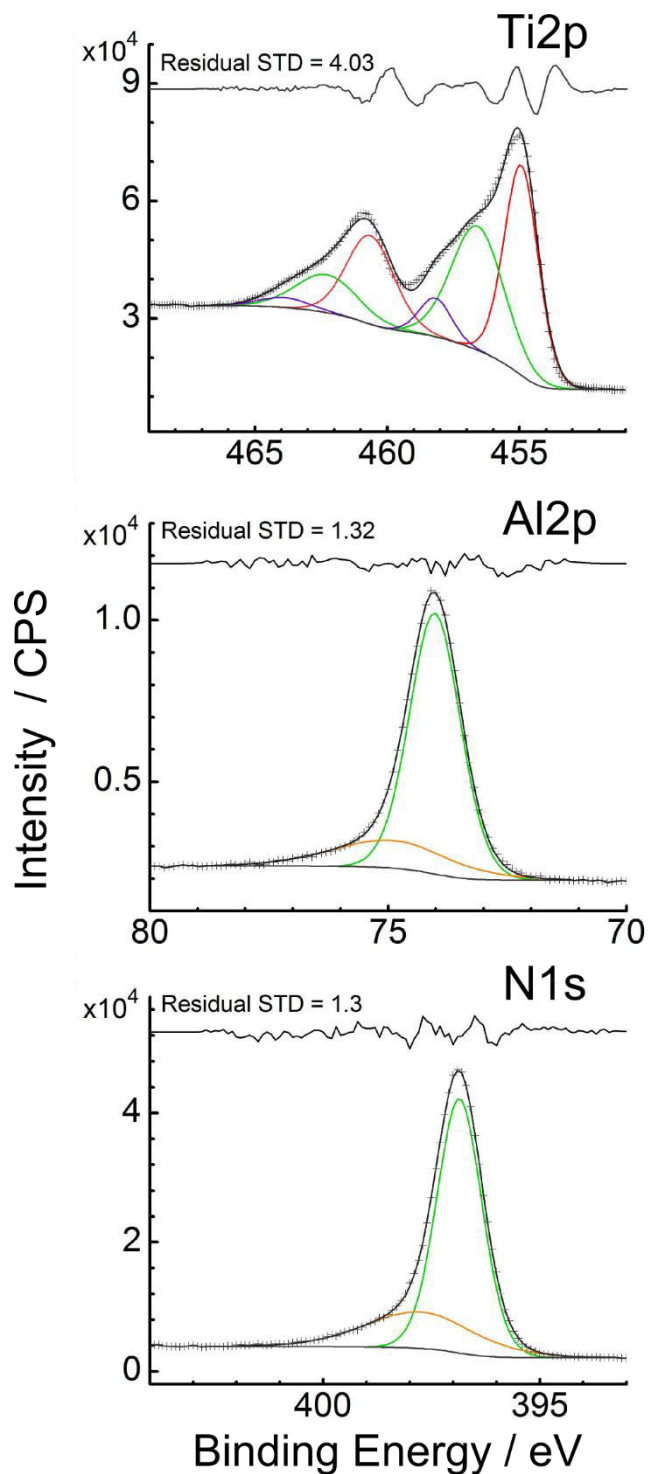


Figure S1. High-resolution XPS spectra of TiAlN after Ar⁺ sputter cleaning. The data is identical with figure 1a. For better visualization of the data and fit quality, the raw data is presented by symbols (+) and the synthesized components by lines. The corresponding residuals are provided on top of each diagram.

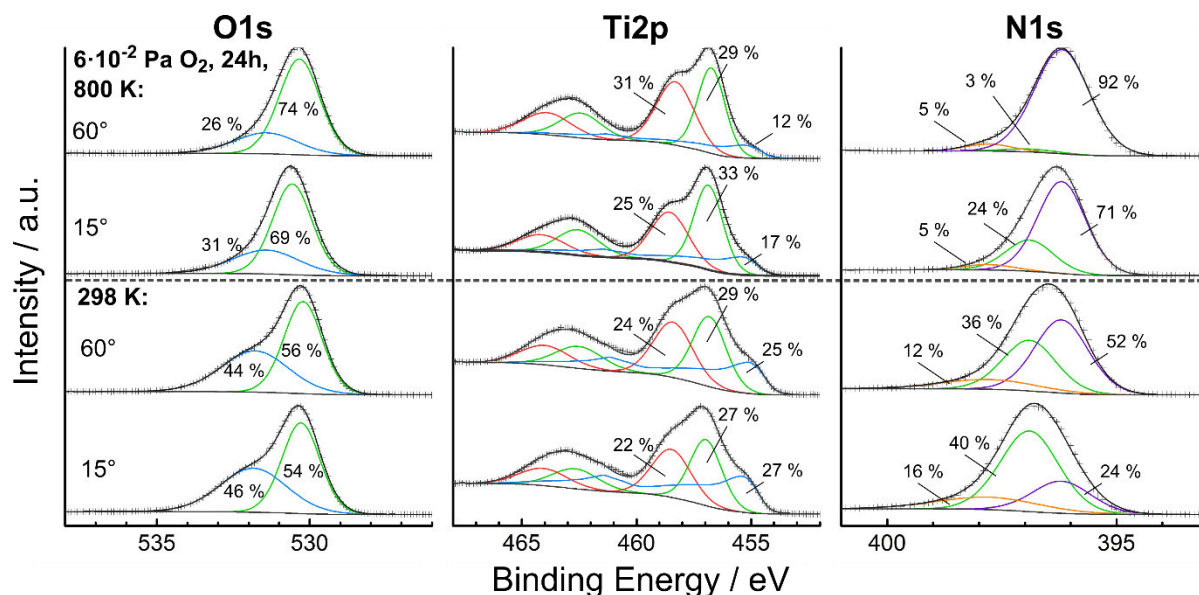


Figure S2. Angle-resolved Ti2p core level XPS spectra of TiAlN oxidized at an oxygen pressure of $5 \cdot 10^{-2}$ Pa for 24 h at a temperature of 293 K measured at an emission angle of **a)** 15° and **b)** 60° and oxidized at 800 K and measured at an emission angle of **c)** 15° and **d)** 60°. The spectra were normalized and shifted vertically for clarity. The raw spectral data is represented by a symbol (+).

1. Thickness calculations of multilayered surface oxides

For quantitative XPS and layer thickness determination of the surface oxide films, a layered structure with sharp interface boundaries and homogeneous phases was assumed. The densities were assumed to be equal, which is justified by the low differences between TiAlN (4.8 g cm^{-3}) and the oxides (Al_2O_3 : 3.95 g cm^{-3} , TiO_2 : 4.25 g cm^{-3}) and the lack of significant surface enrichment of metals. Further, the Ti2p core level spectrum was evaluated for all layered systems and thus allows to restrict the formalism to a single electron kinetic energy.

In the case of a single cover layer C on a substrate B, which is the case for the oxynitridic growth region on TiAlN, the Hill equation was simplified accordingly:^[1]

$$d_c = \lambda \cos(\theta) \ln\left(\frac{I_{tot}}{I_B}\right) \quad (1)$$

Where I_B is the intensity of the substrate component and I_{tot} is the total intensity of the same core level. Note that the usually present reference intensities cancel due to the assumptions made. The intensity ratio corresponds then to the relative fraction of the corresponding component to the total core level signal, which is directly measured in a single detail spectrum and was evaluated with an average practical effective attenuation length λ of 1.8 nm for Ti2p.^[2]

The calculations for a double layered surface oxide on a substrate B with a cover layer C and an interlayer A was extensively discussed recently.^[3] The effect of the presence of another layer on top was described by a weakening factor affecting the usual equations for the single cover layer system. However, when accounting for the assumptions made the following equations are obtained:

$$\frac{I_A}{I_{tot}} = \exp\left(-\frac{d_c}{\lambda \cos(\theta)}\right) \left\{1 - \exp\left(-\frac{d_A}{\lambda \cos(\theta)}\right)\right\} \quad (2)$$

$$\frac{I_B}{I_{tot}} = \exp\left(-\frac{d_A}{\lambda \cos(\theta)}\right) \exp\left(-\frac{d_c}{\lambda \cos(\theta)}\right) = \exp\left(-\frac{d_{tot}}{\lambda \cos(\theta)}\right) \quad (3)$$

$$\frac{I_C}{I_{tot}} = 1 - \exp\left(-\frac{d_c}{\lambda \cos(\theta)}\right) \quad (4)$$

Thus, the calculation of the surface layer thicknesses of the double layered oxides with an oxynitride interlayer A covered by a Ti(IV) containing top layer C on the TiAlN substrate B was performed by calculation of the total oxide thickness by mean of equation (3) and subtracting the cover layer thickness as given by equation (4). The intensity ratios used for generating table 1 are documented in **Table S1**.

Table S1. Intensity ratios used for the calculation of surface oxide layer thicknesses.

Temperature / K	Duration / h	I[TiAlN]/I[Ti2p]	I[TiAl(O,N)]/I[Ti2p]	I[Ti(IV)]/I[Ti2p]
293	3	0.32	0.68	-
293	24	0.33	0.35	0.32

800	24	0.18	0.47	0.35
-----	----	------	------	------

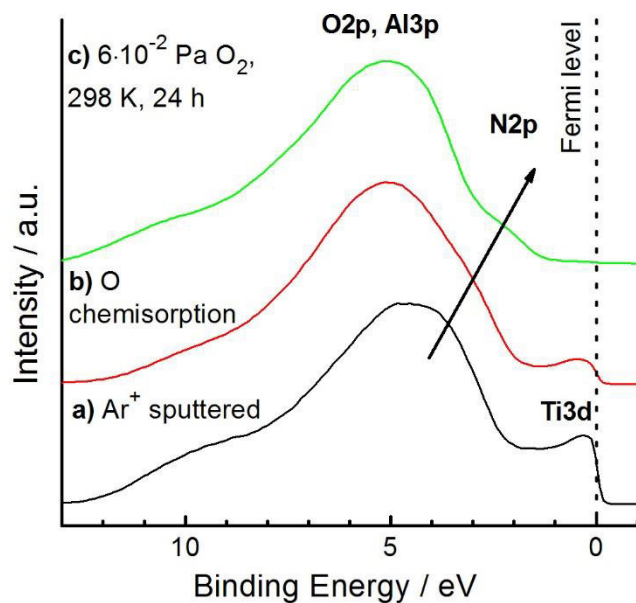


Figure S3. UPS valence band measurement of TiAlN after **a)** Ar⁺ sputter cleaning, **b)** formation of the oxygen chemisorption layer, **c)** oxidation at 293 K for 24 h.

References

- [1] J. M. Hill, D. G. Royce, C. S. Fadley, L. F. Wagner, F. J. Grunthaner, *Chem. Phys. Lett.* **1976**, *44*, 225.
- [2] C. J. Powell, A. Jablonski, *NIST Electron Effective-Absorption-Length Database*; Version 1.3; National Institute of Standards and Technology, Gaithersburg, MD, **2011**.
- [3] S. Hofmann, *Auger- and X-Ray Photoelectron Spectroscopy in Materials Science*; Springer, Berlin-Heidelberg, **2013**.

4.2 Combined Electrochemical and Electron Spectroscopic Investigations of the Surface Oxidation of TiAlN HPPMS Hard Coatings

The manuscript was reproduced from the following publication:

Combined Electrochemical and Electron Spectroscopic Investigations of the Surface Oxidation of TiAlN HPPMS Hard Coatings

Wiesing, M., to Baben, M., Schneider, J. M., de los Arcos, T., Grundmeier, G.

Electrochimica Acta, 208, 120–128, 2016, doi:10.1016/j.electacta.2016.05.011

Copyright © 2016, Elsevier Ltd.

Author contributions:

- Planning/experimental work/interpretation/manuscript preparation **MW**
- Hard coating deposition/Proof reading **MB**
- Proof reading/content check **GG**
- Proof reading **TA** and **JMS**

Placement:

The surface chemistry of hard coatings is affected by electrochemical corrosion under polymer processing conditions as a consequence of their metallic properties and the presence of residual amounts of water in the polymer melt. Moreover, practical experience show that corrosion enhances the interfacial degradation and accumulation of polymer during injection moulding. Thus, the fundamental anodic and cathodic behaviour of $Ti_{0.5}Al_{0.5}N$ electrodes was investigated in aqueous electrolyte with particular focus on the anodic surface oxidation processes using joint electrochemical and electron spectroscopic means. This allowed to develop a microscopic model of the electrochemical oxidation and showed that $Ti_{0.5}Al_{0.5}N$ electrodes do not undergo a passivation process but rather form a still highly reactive and electrically conductive surface oxide film. These results provide the basis for a rational understanding of the interfacial chemical and adhesive interactions encountered under polymer processing conditions and also explain the corrosion resistance of these coatings.



Combined Electrochemical and Electron Spectroscopic Investigations of the Surface Oxidation of TiAlN HPPMS Hard Coatings



Martin Wiesing^a, Moritz to Baben^b, Jochen M. Schneider^b, Teresa de los Arcos^a, Guido Grundmeier^{a,*}

^a Technical and Macromolecular Chemistry, University of Paderborn, Warburger Str. 100, 33098 Paderborn, Germany

^b Materials Chemistry, RWTH Aachen University, Kopernikusstr. 10, 52074 Aachen, Germany

ARTICLE INFO

Article history:

Received 9 December 2015
Received in revised form 2 May 2016
Accepted 2 May 2016
Available online 3 May 2016

Keywords:

Oxidation
TiAlN
coating
HiPIMS
Cyclic Voltammetry

ABSTRACT

The surface oxidation of TiAlN High Power Pulsed Magnetron Sputtering (HPPMS) hard coatings was investigated using a combined electrochemical and electron spectroscopic approach. The reversible and irreversible surface redox reactions as well as the resulting surface electronic properties were investigated by means of Cyclic Voltammetry (CV) and Electrochemical Impedance Analysis (EIS). X-ray Photoelectron Spectroscopy (XPS) of the TiAlN near-surface region as oxidised in air after deposition revealed a duplex surface film consisting of oxynitridic TiAl(O,N) covered by a shallow Al rich oxide layer. Complementary EIS revealed metallic conductivity of this TiAl(O,N) phase. A detailed microscopic model of the electrochemical oxidation process highlighting the importance of O interstitials for the oxidation process is presented. The electrochemical oxidation induced by CV resulted into a transition from metallic to n-type semiconducting properties of the surface oxide film. As disclosed by XPS and XPS sputter profiling, a complex multi-layered film was formed comprising segregated $a\text{-(TiO}_2)_x(\text{Al(OH)}_3)_y$ located on top of a more ordered electrochemically inactive oxide film. Further, an intermediary nitrogen doped but segregated $a\text{-(TiO}_2)_x(\text{Al(OH)}_3)_y\text{:N}$ phase was also observed. The results are of high importance for understanding the electrochemical oxidation and corrosion resistance of these hard coatings.

© 2016 Elsevier Ltd. All rights reserved.

1. Introduction

Ternary hard coatings based on Ti, Al and N have found widespread use for cutting and forming tools due to their high hardness and low wear [1–3]. Recently, several works related to the structure-property relationship of these films [4–9] have been published, reflecting the increased interest in corrosion resistant TiAlN hard coatings. Systematic variations of the Al content in a wide range revealed an enhanced resistance against corrosion of cubic TiAlN at intermediate Al concentrations, as evidenced by reduced exchange current densities [6]. At higher Al concentrations, however, precipitation of wurtzite-AlN resulted into an increased corrosion current [6]. Characterisation of the anti-corrosion properties of TiAlN was also performed at different pH values [4], in simulated proton exchange membrane fuel cell environment [9], simulated body fluid [5], and chloride-containing

electrolytes [7,8] illustrating the excellent inert behaviour of TiAlN. Especially the effect of microstructure was of pivotal interest in research: impedance and potentiodynamic analysis disclosed grain boundaries and growth defects to facilitate electrolyte transport and thus corrosion of the underlying substrate especially for arc-evaporated coatings containing droplets [10–12].

Fundamental research on the electrochemical properties of TiAlN or the prototypic TiN is scarce on literature. The processes of thermal and electrochemical oxidation of TiN, CrN, and ZrN were compared using X-ray photoelectron spectroscopy (XPS) [13]. The electrochemical oxidation of TiN was found to proceed within a two-step reaction pathway: (i) a slow oxidation at low potentials leading to preferential formation of oxynitride and (ii) full oxidation at higher potentials. The oxidation behaviour of CrN was found to exhibit differences due to formation of Cr(VI) species in the transpassive regime. Fundamental aspects of anodic passivation of TiN were further investigated by means of XPS and Mott-Schottky analysis [14]. The formed TiO₂ top layer was found to be highly defective and n-type.

* Corresponding author.

E-mail address: guido.grundmeier@tc.uni-paderborn.de (G. Grundmeier).

Recently, a kinetic study of the electrochemical oxidation of TiN_x revealed N vacancy oxidation and formation of Ti oxynitride in the lower potential oxidation regime [15]. Due to the lack of complementing spectroscopic and electrochemical analysis, no microscopic model of the oxidation process could be developed, which represents a prerequisite for a thorough understanding of the transport-controlled electrochemical processes and reactions.

In general, reported research on the electrochemistry of TiAlN does not include a thorough analysis of the as deposited surface and the bonding in the electrochemically formed oxidation product. Recently, it was shown that the as deposited surface of TiAlN is enriched with oxygen and aluminium [16]. It was suggested that the surface oxidation is due to reaction with residual gas [17] during cooling in the deposition chamber and/or due to reaction with ambient air after removing the samples from the deposition system [16]. In this regard, it was recently shown within a combined theoretical and experimental study that at room temperature oxygen chemisorption on a clean TiAlN surface mainly happens via formation of Ti-O bonds leading to Ti_2O_3 -like bonding [18,19]. Concluding, a detailed microscopic model of the surface processes involved during potentiodynamic polarization and oxide film formation is developed within this work based on the data obtained by a combination of electron spectroscopy and electrochemical techniques.

2. Experimental

2.1. Chemicals and Materials

All chemicals (Aldrich) and organic solvents (VWR International Germany) were of analytical grade and used without further purification. For deposition, p-Si(100):B (1-5 W cm) substrates were used (Si-Mat, Kaufering, Germany).

2.2. Deposition parameters

TiAlN thin films with a thickness of 1.2 μm were deposited onto Si substrates by means of High Power Pulsed Magnetron Sputtering (HPPMS) on p-Si:B (1-5 Ωcm) using a commercial CemeCon CC-800/9 deposition chamber. The rectangular magnetron (500 \times 88 mm^2) was capped with a $\text{Ti}_{0.5}\text{Al}_{0.5}$ compound target, providing a Ti/Al ratio close to 1. The substrate was electrically at floating potential and heated to 280 °C. The discharge conditions were set at 770 V target voltage and 800 Hz pulsing frequency, with an “on” time of 50 μs , corresponding to a time-averaged power density of 6.8 W cm^{-2} and a peak power density of 0.4 kW cm^{-2} normalized to the whole target surface. These conditions place the plasma at the edge of the HPPMS regime [20] and within the stochastic plasma regime (not within the regime where stable rotating spokes are typically observed in HPPMS plasmas). The distance between target and substrate was 80 mm and the total pressure was 0.46 Pa before deposition. For synthesis of TiAlN, the flow ratio of Ar: N_2 was set to 4:1. The deposited samples were removed from the deposition chamber after cooling in vacuum for 2.5 h down to 80 °C, stored in laboratory air and sonicated in tetrahydrofuran and then in ethanol for 5 minutes each before further analysis.

The surface topography of the samples was investigated by means of AFM (Nanowizard 3, JPK Instruments) operated in AC-AFM mode and using non-contact cantilevers (325 kHz, NSC15, Mikromasch). The root-mean squared surface roughness of these samples was 4.3 nm and the ratio between measured and projected surface amounted 1.05.

X-Ray Diffraction of these samples was performed using an AXS D8 Discover General Area Detection Diffraction System (Bruker) with

Cu-K α radiation under an incidence angle of 15°. Fig. 1 illustrates the diffraction pattern of the TiAlN film of which the peaks are located in between the corresponding peaks of cubic-TiN and cubic-AlN as expected for a solid solution. Thus, TiAlN is present in the cubic structure without the presence of wurtzite-AlN.

2.3. Electrochemical analysis

Cyclic voltammetry (CV) and Electrochemical Impedance Spectroscopy (EIS) were performed in aerated borate buffer solution (250 mM, pH 8.3) in the dark. A three-electrode arrangement was used throughout the experiments equipped with an Ag/AgCl reference electrode (DriRef, WPI) and an Au counter electrode (2.3 cm^2). In the following, the potential is quoted against the standard hydrogen electrode (SHE). Polarisation was done using a Reference 600 potentiostat (Gamry Instruments). The sweep rate during CV was set to 50 mV/s if not stated otherwise. Excitation for EIS was done potentiostatically within the linear regime with an rms amplitude of 10 mV. Impedance spectra were evaluated by means of equivalent circuit analysis implemented in EchemAnalyst (Gamry Instruments).

2.4. Surface chemical analysis

Surface chemical characterization was performed by means of XPS implemented in an ESCA+ facility (Oxford Instruments, Taunusstein, Germany) at a base pressure $<2.0 \times 10^{-10}$ mbar using monochromated Al K α irradiation (1486.7 eV). Calibration was performed using the C 1s signal (at 284.8 eV) of adventitious carbon as internal reference. Take-off angles are referenced in the following with respect to the surface normal.

The information depth depends on the take-off angle and the attenuation length of the escaping photoelectrons, which depends in turn on the kinetic energy [21]. In our case, the information depth at 10° for the O 1s, N 1s and Ti 2p signals, whose kinetic energies lie within a narrow energy range between 950 and 1100 eV, is around 5.3 nm. In the case of Al 2p, the depth of information is 7 nm due to the higher kinetic energy of Al 2p photoelectrons (~1410 eV). The quantification thus includes a matrix correction procedure in order to avoid an overestimation of the Al signal. Assuming a homogeneous film composition, the additional correction factor for the Al 2p peak when compared with the Ti 2p peak is approximately given by $(E_{\text{Al}}/E_{\text{Ti}})^{0.75} = 1.27$ [22]. The inherent adventitious carbon overlayer increased the O

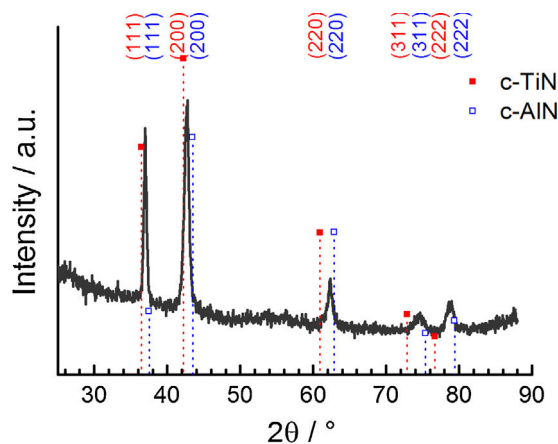


Fig. 1. X-ray diffraction pattern of the as deposited TiAlN. Peaks of cubic TiN and AlN are marked for comparison.

content by <10 at% as calculated from survey and C 1s high resolution spectra. The O concentrations were corrected accordingly in each case. Peak analysis and Shirley background removal were performed using CasaXPS (V 2.3 Casa Software Ltd.) and Gauss-Lorentzian (70:30) lineshapes.

The compositional depth distribution was profiled using Ar⁺ bombardment with Zalar rotation (3 kV, 1 μA, 2Hz) and analysing X-ray excited Auger photoelectrons of O KLL and N KLL.

3. Results and Discussion

3.1. Spectroscopic analysis of TiAlN before electrochemical oxidation

TiAlN samples after deposition (“as deposited”) were characterized using X-ray Photoelectron Spectroscopy (XPS) and Electrochemical Impedance Spectroscopy (EIS). The sample surfaces were exposed firstly to the residual gas [17] in the deposition chamber immediately after deposition at high temperature and secondly to ambient air during the transfer from the deposition chamber to the spectrometer [16]. It is noted that the solvent-cleaning of the samples by sonication did not affect the surface chemical composition, as observed by XPS.

The elemental stoichiometry and relevant atomic ratios of as deposited TiAlN and of an Ar⁺-sputtered sample (“bulk” composition) are shown in Table 1. A significant enrichment of Al within the near-surface region of as deposited TiAlN compared to the bulk stoichiometry was found. A similar surface enrichment of Al was observed by Gnoth et al. in the passive layer formed on similar HPPMS coatings due to reaction with residual gas during cooling in the deposition chamber and/or due to reaction with ambient air after removing the samples from the deposition system [16]. According to literature, such an Al-enrichment in the near-surface region can be explained by the high mobility of Al³⁺ in the

Table 1

Atomic concentrations and relevant ratios of electrochemically oxidised samples as determined from XPS survey spectra. The C content due to adventitious carbon was omitted for clarity.

X _{Ti} /at.%	X _{Al} /at.%	X _O /at.%	X _N /at.%	(O + N)/ (Ti + Al)	Al/Ti
exposed to air (“as deposited”)					
14	26	22	38	1.52	1.9
Ar ⁺ etched (“bulk” composition)					
24	23	7	46	1.12	0.98
3 sweeps CV					
13	18	63	6	2.24	1.40
20 sweeps CV					
13	18	68	1	2.19	1.41

oxynitride and oxide phases of TiAlN [23]. Moreover, Al₂O₃ is thermodynamically more stable than TiO₂. However, it is interesting to note at this point that an exposure of TiAlN samples to low oxygen doses under ultra-high vacuum conditions at room temperature did not lead to surface enrichment of Al, whereas selective chemisorption of O to Ti-sites was observed instead [18]. By comparing experimental and *ab initio* molecular dynamic simulation [19] the authors proposed that the initial stages of the oxidation of TiAlN at room temperature are governed by the formation of Ti₂O₃ like bonding which in turn results in the formation of Ti vacancies, while the oxidation of Al played a subordinated role [18].

The Ti 2p core level spectra of as deposited TiAlN are shown in Fig. 2. The peak was separated into three components located at

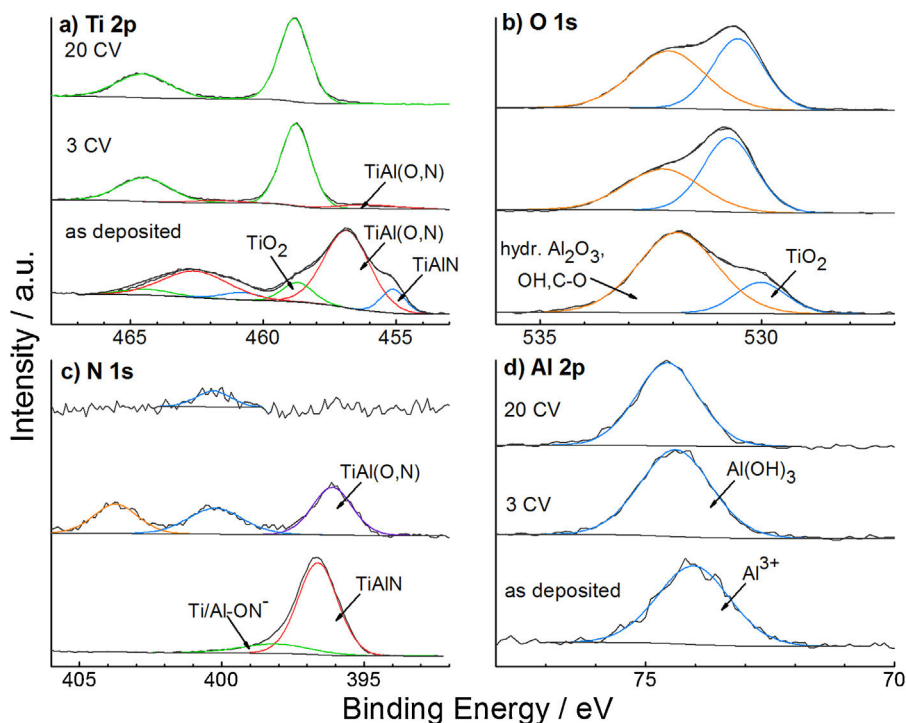


Fig. 2. (a–d) High resolution XPS spectra of the Ti 2p, O 1s, N 1s and Al 2p core levels of electrochemically oxidised samples. Residual oxynitride present in these films as low energy shoulders of the Ti 2p signals is marked and correlates with the low binding energy component of the N 1s signal.

455.1, 456.9 and 458.7 eV, which were assigned to TiAlN (455.1 eV) and TiO₂ (458.7 eV) by comparison with binding energies from literature [16,24]. The intense component at 456.9 eV could not be precisely assigned based on its binding energy due to overlap of Ti₂O₃-like and TiAl(O,N) species [16,24]. In this regard, an oxynitridic TiAl(O,N) growth region was found following thermal oxidation at elevated temperatures in air located beneath an Al rich top-layer and is thus equally claimed in this case [23,25]. This assignment is further supported by the observed low O content. The mathematical decomposition of the Ti 2p showed that the oxynitridic phase was dominant, with only small amounts of TiO₂ present. As a consequence of the oxidation process, both O containing phases are assumed to be located on top with the TiO₂ phase terminating the surface, which allows to estimate the thickness of the total O containing film to 3.2 nm and the thickness of the TiO₂ containing surface film to around 0.3 nm using the local attenuation length [21,22].

The O 1s core level peak depicted in Fig. 2 was fitted with two components at 530.0 and 531.9 eV corresponding to TiO₂ and hydrated Al₂O₃ [26–28]. It is noted, that this last component could also contain contributions from hydroxyl groups and carbon-bound O, which appear at 531.5 eV [14] and 531.1–531.6 eV [29] respectively. The N 1s line-shape was described by two components: the main component at 396.7 eV was associated with TiAlN [30,16] while the higher binding energy component located at 398.1 eV could be related to Al-NO⁻ or Ti-NO⁻ surface species [31]. The Al 2p peak showed a single signal at 74.0 eV related to Al³⁺. A more accurate assignment was not attempted due to the strong overlap of nitridic and oxidic Al components [16].

The as deposited TiAlN was further investigated using EIS at open circuit potential (OCP) of which the results are depicted in Fig. 3. Equivalent circuit analysis allowed to describe the data using a single time constant using a constant phase element (CPE) with an exponent of $\alpha = 0.927$.

The frequency dispersion reflected by a CPE was recently discussed from a fundamental point of view [32–34]. Briefly, a CPE originates from a homogeneous distribution of time constants, which are either in series or in parallel to each other. Physically this is realized e.g. by a homogeneous surface distribution of activation or adsorption energies [35,36]. In the case of TiAlN, the observed blocking behaviour allows unambiguously to exclude a depth distribution of time constants and to calculate the effective capacitance $C_{\text{eff}} = 15.2 \mu\text{F cm}^{-2}$ [32] including the AFM derived roughness factor of 1.05. For comparison it is noted that the correction of the effective capacitance for a normal distribution of time constants results into a questionably high value of $45.4 \mu\text{F cm}^{-2}$. Since the capacitance formed by the oxynitridic surface layer

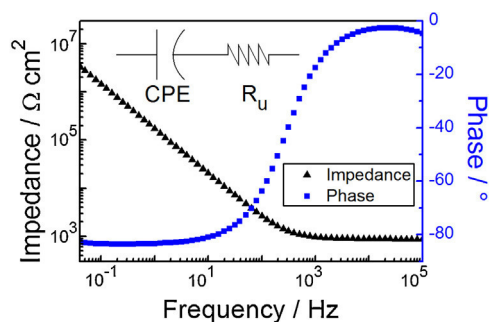


Fig. 3. Phase and impedance spectra of TiAlN oxidised due to exposure to air in borate buffer at 0.2 V OCP. The single time constant equivalent circuit derived from a constant phase element is illustrated in the inset.

is in series with the Helmholtz capacitance with approximately $16\text{--}18 \mu\text{F cm}^{-2}$ [37], the effective capacitance is determined by the Helmholtz layer. In this regard, the high effective capacitance indicates *metallic conductivity* of the TiAlN coating including the 3.5 nm thick oxynitridic region within the surface oxide film in the as deposited state. This assessment is consistent with quantum mechanical predictions: As N in TiAl(O,N) is substituted by O, the metallic bonding character was predicted to increase at the expense of the covalent character [38].

These findings emphasizes the importance of a closer understanding of the governing microscopic oxidation processes: in this regard, earlier experimental findings prove the presence of metal vacancies within the TiAl(O,N) phase [39], which are thus supposed to contribute to metal outward migration resulting ultimately into the observed Al enriched near-surface region. Simultaneously, significant inward migration of O defects must have taken place, which resulted into the formation of the observed thick TiAl(O,N) phase. In this regard, the relevance of interstitial O is indicated by recent simulations revealing O interstitials to be formed spontaneously in TiAl(O,N) [38]. Therefore, oxidation of TiAlN is supposed to proceed by inward migration of O interstitials, which exchange with N located at lattice sites within the TiAl(O,N) growth region. After subsequent irreversible formation of N₂ from interstitial N the replacement of one trivalent N by one divalent O at a lattice site requires another Ti electron to be ejected into the Ti 3d band. This proposed reaction pathway rationalises the metallic character of the oxynitridic region formed after deposition: due to the formation of an Al enriched top surface layer the inward migration of O is inhibited and the TiAl(O,N) phase turns metallic as a result of the irreversible oxidation reaction.

3.2. Electrochemical surface oxidation and analysis

Different electrochemical means of analysis were employed for the characterization of the electrochemical oxidation process of TiAlN. Cyclic voltammetry of TiAlN measured in borate buffer was performed over a wide potential range and is reported in Fig. 4.

During the anodic sweep, an irreversible anodic wave termed as wave P was found at 1.3 V indicating that oxidation of the surface has taken place. After the first sweep, a redox pair (RO and RR) was established at -1 V and related to Ti⁴⁺/Ti³⁺ according to the thermodynamic potential of TiO₂/Ti₂O₃ of -1.05 V [40].

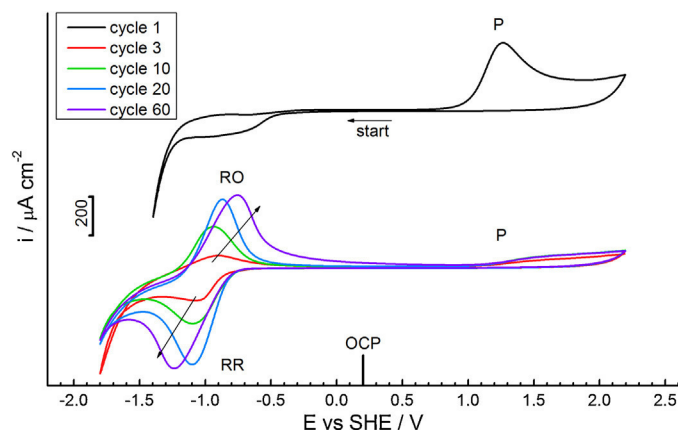


Fig. 4. Cyclic voltammogram of TiAlN at scan rate of 50 mV s^{-1} . Polarization was initiated at 0.2 V OCP in cathodic direction and continued for several cycles.

When comparing the charge converted during wave P within the first anodic sweep with the charge of wave RR during the followed cathodic sweep a charge ratio of RR:P=1:4 could be determined. Since the wave RR is a measure of the amount of Ti^{4+} in the sample that was formed during wave P, this charge mismatch indicates that during wave P electrons were drawn from both Ti^{3+} and N^{3-} resulting into the formation of Ti^{4+} along with N_2 as already observed in the case of other nitridic hard coatings such as TiN [15] or CrN [41].

Further, it is observed that the oxidation wave P set in constantly at a potential of 1.3 V though obviously a surface oxide layer must be formed. Contrary, the oxide film was expected to induce shifting of wave P to more positive potentials with increasing oxide film thickness when acting as a dielectric barrier. This finding could be rationalised by considering that due to the intermediary $\text{Ti}^{4+}/\text{Ti}^{3+}$ conversion at -1 V some Ti^{3+} defects were generated and left even after the wave RO within the surface oxide film, which were then subsequently oxidised again during wave P. This resulted into the potential to drop dominantly within the Helmholtz layer at the solid/electrolyte interface at the beginning of wave P and explains the observed constant oxidation potential. This interpretation is corroborated by Fig. S1 (Supplementary) which depicts a Mott-Schottky plot of the surface oxide film and reveals a positive slope indicative for n-type doping.

Additionally, it was observed that a steady behaviour of the oxidation wave P set in simultaneously with a steady current density observed at the cathodic turn, which was ascribed to H_2 formation and was possibly superposed by reduction of residual O_2 (the measurements were performed in oxygen containing electrolyte). Since the cathodic reduction of oxygen and hydrogen as electron transfer reactions depend strongly on the electronic structure of the electrode surface, this finding indicates an intimate correlation between the bulk surface oxide properties reflected by the behaviour of wave P and the surface reactivity. It is thus supposed that the bulk Ti^{3+} defects result into Ti^{3+} surface states at the electrolyte interface and thus govern the electrochemical reactivity towards oxidation and H_2 reduction. Hence, the rate-limiting step during the first part of the oxidation wave P is represented by the oxidation of surface Ti^{3+} defects during the later stages of cyclic voltammetry. In this regard, Fig. S2 exhibits cyclic voltammetry of the $\text{Ti}^{4+}/\text{Ti}^{3+}$ region performed subsequently after the formation of a surface oxide film. It could be observed that when omitting the oxidation wave P during voltammetry the surface reactivity of

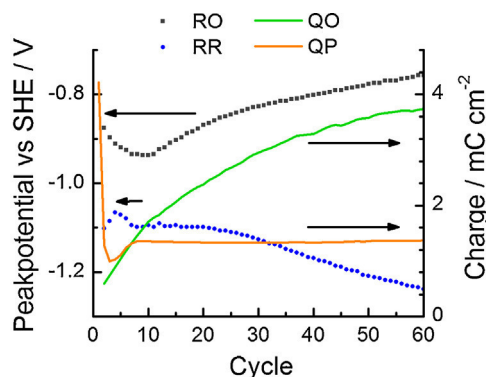


Fig. 5. Temporal development of charges and peak potentials of specific waves during CV. RO and RR refer herein to the peak potentials of the $\text{Ti}^{4+}/\text{Ti}^{3+}$ conversion in the oxide layer. The charges QO and QP resemble the charge converted during the anodic wave of the $\text{Ti}^{4+}/\text{Ti}^{3+}$ redox couple and the oxidation wave P respectively.

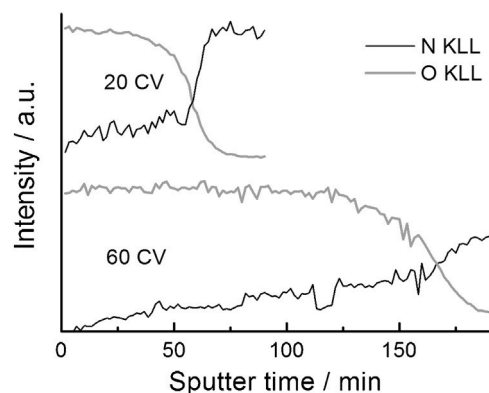


Fig. 6. X-Ray excited Auger depth profiles measured after 20 and 60 CVs. Profiling was performed using 3 kV Ar^+ ($5 \mu\text{A cm}^{-2}$, 2 Hz Zalar rotation). The O KLL and N KLL signals show a distinct drop and increase in intensity after 52 and 168 min of sputtering time for surface oxide films obtained after 20 and 60 cycles. The oxide films thus grow with a linear rate law.

the oxide film towards H_2 formation increased continuously. Regarding the aforementioned, this strongly indicates that the surface defect density increases due to formation of bulk Ti^{3+} defects during the oxide conversion and thus supports the proposed interpretation.

Pivotal characteristics of the cyclic voltammogram were extracted and are reported in Fig. 5: The peak potentials RR and RO of the $\text{Ti}^{4+}/\text{Ti}^{3+}$ conversion, the corresponding charge QO as taken from the redox couples anodic wave and the charge of the oxidation wave QP.

Following a transient period during the first seven cycles, the charge QP was found to become constant (1.7 mC cm^{-2}) thus reflecting a linear rate law of oxide film growth. Taking further into account the bulk stoichiometry of $\text{Ti}_{0.5}\text{Al}_{0.5}\text{N}$ as determined from the XPS characterisation of an Ar^+ etched sample (see table Table 1), a lattice constant of 0.4175 nm [38] and the fact that 3.5 electrons are gained by oxidation of one unit cell of TiAlN, the growth rate could be estimated to $0.52 \text{ nm cycle}^{-1}$ corresponding to about one unit cell thickness per cycle excluding the first passivation-like sweep.

Contrary to the observed linear rate law, the charge of the anodic wave of the $\text{Ti}^{4+}/\text{Ti}^{3+}$ couple QO, which similarly reflects the thickness of the surface oxide film, increased with decreasing rate. In order to clarify this situation, x-ray excited Auger depth profiles of the surface oxide films after 20 and 60 cycles were measured and are presented in Fig. 6. The respective sputter times required to reach the TiAlN interface were 52 and 168 min, which clearly validates the linear rate law. Further, the sub-linear increase of the charge QO reflects thus the formation of a buried electrochemically inactive oxide phase during the later stages of electrochemical oxidation, which does not hinder the oxidation of TiAlN. It should be further noted, that similarly after around 20 cycles the blackish colour of the oxide film turned to bluish, which is typical for Ti^{3+} defects in rutile [42] and might possibly indicate the formation of the electrochemically inactive layer by segregation.

During the later stages of cyclic voltammetry the peak potentials of the $\text{Ti}^{4+}/\text{Ti}^{3+}$ couple were found to continuously separate indicating an increasing degree of irreversibility. Similarly, after 20 cycles of voltammetry the surface oxide film can be regarded to be fully oxidised and to possess a stable stoichiometry as assessed from the XPS data presented in Table 1. Thus, the gain in irreversibility is explained by restructuring of the film.

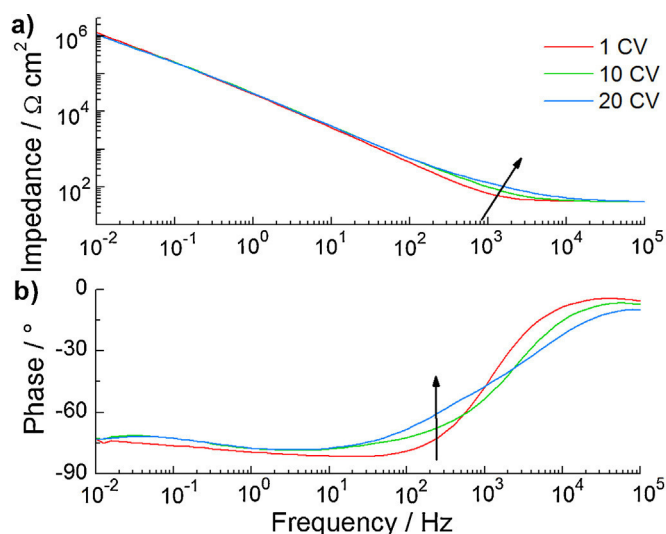


Fig. 7. Electrochemical impedance spectroscopy of cyclically polarized TiAlN measured at 0.2 V OCP. In (a) the impedance and in (b) the phase are illustrated.

Electrochemical impedance analysis of cyclically polarized samples was performed at different stages of oxidation and is illustrated in Fig. 7.

Continued cyclic voltammetry was observed to induce the inset of a second time constant at around 1 kHz. This frequency range is typical for time constants emerging from surface states, which is physically based on their slow capture and emission rate of electrons resulting into a sluggish response to potential alterations at high frequencies [43]. Since Ti^{3+} surface states and restructuring of the surface oxide, but no dielectric over layer formation, were observed as discussed above, the presence of the surface states is equally proposed to affect the impedance behaviour and to induce the inset of the mid-frequency time constant. In this regard, the surface states were initially screened, which can be rationalised based on the very large structural disorder provoked by the first oxidation sweep due to volume expansion and denitrification: it was shown that large structural disorder provides a homogeneous gap distribution of states within the limit of an amorphous semiconductor [44]. Physically, this resembles a missing structural and energetic discrimination of surface states from bulk electronic states and explains the initially missing surface state time constant.

3.3. X-Ray Photoelectron Spectroscopy (XPS)

The chemical properties of the oxide film formed during the different stages of cyclic voltammetry were investigated using XPS and are reported in the following.

The elemental stoichiometry of the TiAlN samples after electrochemical oxidation is shown in Table 1. Comparing the electrochemically oxidised samples with as deposited TiAlN, a very strong increase in the oxygen and a related decrease in the nitrogen concentration could be observed indicating the electrochemical formation of a rather thick oxide film. Moreover, the aluminium concentration was crucially affected by electrochemical oxidation. A significant decrease from 26 at% for the as deposited sample to 17–18 at% in all electrochemically treated samples was found, whereas the Ti concentrations remained unaffected. The reduction of the aluminium fraction in the near-surface region is most probably related to preferential dissolution of aluminium due to

the higher solubility of Al_2O_3 when compared to TiO_2 under the given conditions [40].

The nature of the formed oxide films was further investigated using XPS core level spectra of Ti 2p, N 1s, Al 2p and O 1s as depicted in Fig. 2. The O 1s spectra were decomposed into TiO_2 (530.6 eV) and $\text{Al}(\text{OH})_3$ (532.1 eV) based on their respective binding energies [45,46]. In this regard, the Al 2p signals of the different oxide films were located around 74.5 eV, which is similarly typical for hydrous Al^{3+} species [46]. The oxide films can be thus regarded as being slightly hydrated. This interpretation is further supported by the $(\text{O} + \text{N})/(\text{Ti} + \text{Al})$ ratios depicted in Table 1. When taking into account the progressive disappearance of N from the oxide, the $(\text{O} + \text{N})/(\text{Ti} + \text{Al})$ ratios shown in the table describe basically the $\text{O}/(\text{Ti} + \text{Al})$ ratios. Accordingly, if the near-surface region would consist of a stoichiometric mixture of TiO_2 and Al_2O_3 , the $\text{O}/(\text{Ti} + \text{Al})$ ratio would amount to a value of 1.7. Therefore the observed ratio of about 2 shows that there is a surplus of oxygen after electrochemical oxidation in accordance to the assignment of the core level signals.

The observation of two distinct O 1s components has another important implication: since the metastable TiAlO mixed oxide is known to exhibit one single O 1s signal at 530.4 eV [47], the oxide film cannot thus be mixed at nanoscopic scale but is supposed to be segregated into Al and Ti rich domains.

The N 1s core level signal showed three clearly differentiated components. The component at 396.1 eV was assigned to residual nitridic N located at lattice sites within the oxidic phase and is thus termed as TiAl(O,N) [48,49]. This component and especially the other two components located at 400.2 eV and 403.7 eV decreased after intense oxidation induced by 20 voltammetric sweeps. The latter signals are commonly assigned to molecular N_2 incorporated within the defective oxide film. In this regard, the corresponding chemical shifts vary largely between different matrices and authors (TiAlN and TiN: 402–403 eV [13,26–28], CrN: 404 eV [28]) and appear to be insufficiently discussed. Further, the binding energies of oxidised N species are expected similarly to be located at these energies [13,31,49]. Thus, the assignment of the observed both high binding energy signals is not feasible without supporting simulation methods and thus not attempted.

Regarding the Ti 2p spectra, the main signal was located at 458.8 eV and associated with TiO_2 [24]. Further, residual defect states were present as lower binding energy shoulders in the less oxidised sample after three CVs. These are referred to TiAl(O,N) in accordance to the assignment of the nitridic N signal, because Ti^{3+} defect states are known to be electronically stabilised by residual N acting as deep traps [50]. Thus, the oxynitridic TiAl(O,N) phase (or more precisely $\text{a}-(\text{TiO}_2)_x(\text{Al}(\text{OH})_3)_y\text{:N}$) represents an intermediary phase formed during the electrochemical oxidation process before the formation of the fully denitrified mixed oxide $\text{a}-(\text{TiO}_2)_x(\text{Al}(\text{OH})_3)_y$. This two-step oxidation mechanism is schematically shown in Fig. 8 and represents an analogy to thermal oxidation, which is essentially based on the fact that both oxidation processes are high-field activated [51,52]. Further, the depth profiles depicted in Fig. 6 reveal an increasing N content with increasing depth and indicate thus the extended TiAl(O,N) region to act as growth region. In accordance to the discussion on the surface oxide film of as deposited TiAlN, this similarly indicates that O inward migration dominates migrational transport.

The presence of the intermediary oxynitridic phase explains one yet undiscussed feature of the cyclic voltammetry data as presented in Fig. 5: during the first cycles of voltammetry, the charge of oxidation QP showed a minimum, although more nitridic N was available for oxidation. Obviously the trapping of Ti^{3+} defects by N hinders the inward migration of O. It is consequently

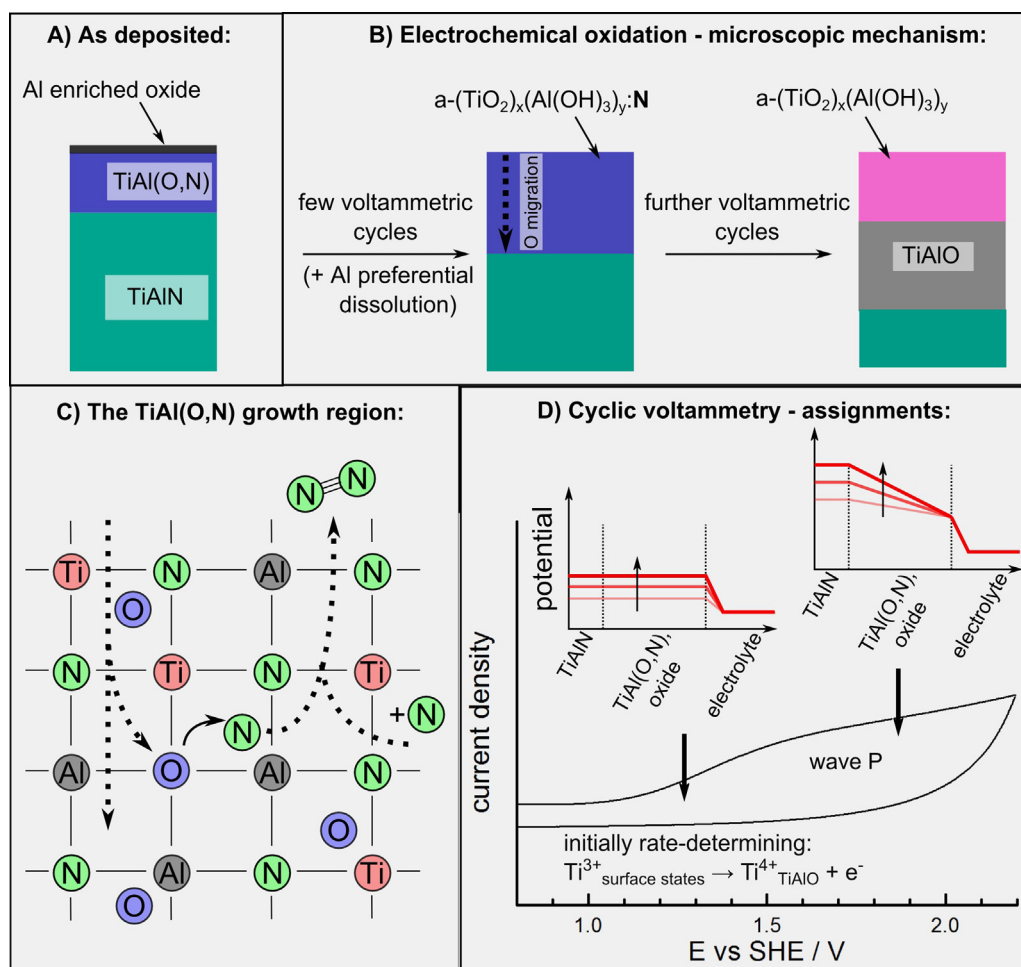


Fig. 8. Illustration of the different investigated stages of electrochemical oxidation of TiAlN. (A) Microscopic structure of as deposited TiAlN before electrochemical oxidation. (B) Stepwise formation of the multi-layered oxide film including the intermediary formed nitrogen doped TiAl(O,N) phase. Note that unlike in the cartoon, no sharp interfaces actually exist between the phases and the illustrations are not at scale. (C) The reactive migration of O interstitials within the TiAl(O,N) of as deposited TiAlN is shown, which is made responsible for the metallic conductivity of this layer. (D) The stationary oxidation wave P is assigned, which is at low voltages kinetically limited by surface defect oxidation.

proposed that the concentration of O defects within the film is reduced due to the presence of N traps, which compete for the Ti^{3+} defect electrons as discussed above.

4. Conclusions

The electrochemical surface oxidation of TiAlN HPPMS hard coatings was investigated by means of cyclic voltammetry and XPS. In the as deposited state, the surface of TiAlN consists essentially of oxynitridic TiAl(O,N) capped with a shallow Al enriched surface oxide layer. The electrochemical oxidation proceeds dominantly due to inward migration of O interstitials, which subsequently exchange with lattice N within the TiAl(O,N) growth region followed by irreversible formation of N_2 . This process could also explain the observed metallic conductivity of the TiAl(O,N) surface phase of as deposited TiAlN. During the first few cycles of voltammetry, residual nitrogen dissolved in the oxide film acts as a deep trap for the Ti^{3+} defects resulting into the formation of TiAl(O,N) (or more precisely $a-(TiO_2)_x(Al(OH)_3)_y:N$) as an intermediate phase. Ti^{3+} defects within the surface oxide film were formed repeatedly during each potential sweep, which resulted into an n-type semiconducting behaviour of the oxide film and a surface reactivity, which was solely determined by Ti^{3+}

surface states. Continued oxidation resulted ultimately into the formation of a complex multi-layered film comprising $a-(TiO_2)_x(Al(OH)_3)_y$ located on top of a more ordered electrochemically inactive oxide film. In conclusion, a detailed microscopic model of the electrochemical oxidation of TiAlN during cyclic voltammetry could be established using a combined electroanalytical and electron spectroscopic approach. The results are of high importance for understanding the oxidation and corrosion resistance of these hard coatings.

Acknowledgements

The authors gratefully acknowledge the financial support of the German Research Foundation (DFG) within the Transregional Collaborative Research Center TRR 87/2 "Pulsed high power plasmas for the synthesis of nanostructured functional layers" (SFB TRR 87, projects A02 and A03).

Appendix A. Supplementary data

Supplementary data associated with this article can be found, in the online version, at <http://dx.doi.org/10.1016/j.electacta.2016.05.011>.

References

- [1] H. Çalişkan, P. Panjan, S. Paskvale, Monitoring of Wear Characteristics of TiN and TiAlN Coatings at Long Sliding Distances, *Tribol. Trans.* 57 (2014) 496–502, doi:http://dx.doi.org/10.1080/10402004.2014.884254.
- [2] Y.X. Lin, H. Lin, Z.W. Han, Effect of Cutting Speed on Wear Property of TiAlN PVD Coated Tools in High-Speed Milling of AISI P20 Mold Steel, *Key Eng. Mater.* 621 (2014) 75–81, doi:http://dx.doi.org/10.4028/www.scientific.net/KEM.621.75.
- [3] W.-D. Münz, Titanium aluminum nitride films: A new alternative to TiN coatings, *J. Vac. Sci. Technol. A* 4 (1986) 2717–2725, doi:http://dx.doi.org/10.1116/1.573713.
- [4] T. Wongpinij, P. Wongpanya, C. Euaruksakul, P. Photongkam, N. Witit-anun, Corrosion behavior of TiAlN film on AISI 4140 steel, *J. Met. Mater. Miner.* 23 (2014) http://www.ojs.materialsconnex.com/index.php/jmmm/article/view/91 (accessed July 11, 2014).
- [5] Y. Kayali, The corrosion and wear behavior of TiN and TiAlN coated AISI 316 L stainless steel, *Prot. Met. Phys. Chem. Surf.* 50 (2014) 412–419, doi:http://dx.doi.org/10.1134/S207020511403006X.
- [6] M.M. Larijani, M. Manouchehrian, H. Seyedi, M. Yari, Corrosion behavior of solid solution (Ti, Al)N as a function of Al concentration, *Cryst. Res. Technol.* 47 (2012) 834–840, doi:http://dx.doi.org/10.1002/crat.201200039.
- [7] X. Ding, A.L.K. Tan, X.T. Zeng, C. Wang, T. Yue, C.Q. Sun, Corrosion resistance of CrAlN and TiAlN coatings deposited by lateral rotating cathode arc, *Thin Solid Films* 516 (2008) 5716–5720, doi:http://dx.doi.org/10.1016/j.tsf.2007.07.069.
- [8] V.K.W. Grips, V. Ezhil Selvi, H.C. Barshilia, K.S. Rajam, Effect of electroless nickel interlayer on the electrochemical behavior of single layer CrN, TiN, TiAlN coatings and nanolayered TiAlN/CrN multilayer coatings prepared by reactive dc magnetron sputtering, *Electrochimica Acta* 51 (2006) 3461–3468, doi:http://dx.doi.org/10.1016/j.electacta.2005.09.042.
- [9] L. Wang, D.O. Northwood, X. Nie, J. Housden, E. Spain, A. Leyland, et al., Corrosion properties and contact resistance of TiN, TiAlN and CrN coatings in simulated proton exchange membrane fuel cell environments, *J. Power Sources* 195 (2010) 3814–3821, doi:http://dx.doi.org/10.1016/j.jpowsour.2009.12.127.
- [10] Y. Li, L. Qu, F. Wang, The electrochemical corrosion behavior of TiN and (Ti,Al)N coatings in acid and salt solution, *Corros. Sci.* 45 (2003) 1367–1381, doi:http://dx.doi.org/10.1016/S0010-938X(02)00223-8.
- [11] D.K. Merl, P. Panjan, M. Panjan, M. Čekada, The Role of Surface Defects Density on Corrosion Resistance of PVD Hard Coatings, *Plasma Process. Polym.* 4 (2007) S613–S617, doi:http://dx.doi.org/10.1002/ppap.200731416.
- [12] R.M. Souto, H. Alanyali, Electrochemical characteristics of steel coated with TiN and TiAlN coatings, *Corros. Sci.* 42 (2000) 2201–2211, doi:http://dx.doi.org/10.1016/S0010-938X(00)00057-3.
- [13] I. Milošev, H.-H. Strehblow, B. Navinšek, Comparison of TiN, ZrN and CrN hard nitride coatings: Electrochemical and thermal oxidation, *Thin Solid Films* 303 (1997) 246–254, doi:http://dx.doi.org/10.1016/S0040-6090(97)00069-2.
- [14] S. Rudenja, J. Pan, I.O. Wallinder, C. Leygraf, P. Kulu, Passivation and Anodic Oxidation of Duplex TiN Coating on Stainless Steel, *J. Electrochem. Soc.* 146 (1999) 4082–4086, doi:http://dx.doi.org/10.1149/1.1392595.
- [15] N. Glandut, S. Valette, M. Brossard, Electrooxidation of substoichiometric titanium nitrides TiN_{1-x}, 0 < x < 0.5, *Electrochem. Commun.* 23 (2012) 63–67, doi:http://dx.doi.org/10.1016/j.elecom.2012.06.032.
- [16] C. Gnath, C. Kunze, M. Hans, M. to Baben, J. Emmerlich, J.M. Schneider, et al., Surface chemistry of TiAlN and TiAlNO coatings deposited by means of high power pulsed magnetron sputtering, *J. Phys. Appl. Phys.* 46 (2013) 084003, doi:http://dx.doi.org/10.1088/0022-3727/46/8/084003.
- [17] J.M. Schneider, B. Hjørvarsson, X. Wang, L. Hultman, On the effect of hydrogen incorporation in strontium titanate layers grown by high vacuum magnetron sputtering, *Appl. Phys. Lett.* 75 (1999) 3476–3478, doi:http://dx.doi.org/10.1063/1.125301.
- [18] C. Kunze, D. Music, M. to Baben, J.M. Schneider, G. Grundmeier, Temporal evolution of oxygen chemisorption on TiAlN, *Appl. Surf. Sci.* 290 (2014) 504–508, doi:http://dx.doi.org/10.1016/j.apsusc.2013.11.091.
- [19] D. Music, J.M. Schneider, Ab initio study of Ti_{0.5}Al_{0.5}N(001)—residual and environmental gas interactions, *New J. Phys.* 15 (2013) 073004, doi:http://dx.doi.org/10.1088/1367-2630/15/7/073004.
- [20] C. Maszl, W. Breilmann, J. Benedikt, A. von Keudell, Origin of the energetic ions at the substrate generated during high power pulsed magnetron sputtering of titanium, *J. Phys. Appl. Phys.* 47 (2014) 224002, doi:http://dx.doi.org/10.1088/0022-3727/47/22/224002.
- [21] C.J. Powell, A. Jablonski, NIST Electron Effective-Absorption-Length Database, National Institute of Standards and Technology, Gaithersburg, MD, 2011.
- [22] S. Hofmann, Auger- and X-Ray Photoelectron Spectroscopy in Materials Science, Springer, 2013.
- [23] S. Hofmann, H.A. Jehn, Selective oxidation and chemical state of Al and Ti in (Ti, Al)_n coatings, *Surf. Interface Anal.* 12 (1988) 329–333, doi:http://dx.doi.org/10.1002/sia.740120602.
- [24] NIST X-ray Photoelectron Spectroscopy Database, National Institute of Standards and Technology, Gaithersburg, 2012. http://srdata.nist.gov/xps/.
- [25] S. Hofmann, Formation and diffusion properties of oxide films on metals and on nitride coatings studied with Auger electron spectroscopy and X-ray photoelectron spectroscopy, *Thin Solid Films* 193–194 (Part 2) (1990) 648–664, doi:http://dx.doi.org/10.1016/0040-6090(90)90216-Z.
- [26] F. Esaka, K. Furuya, H. Shimada, M. Imamura, N. Matsubayashi, T. Kikuchi, et al., Composition dependence of the initial oxidation behaviour of Ti_{1-x}Al_xN (x=0.20, 0.45, 0.65) films studied by XAS and XPS, *Surf. Interface Anal.* 27 (1999) 1098–1106, doi:http://dx.doi.org/10.1002/(SICI)1096-9918(199912)27:12<1098::AID-SIA684>3.0.CO;2-1.
- [27] F. Esaka, K. Furuya, H. Shimada, M. Imamura, N. Matsubayashi, T. Sato, et al., Depth profiling of surface oxidized TiAlN film by synchrotron radiation excited X-ray photoelectron spectroscopy, *Surf. Sci.* 377–379 (1997) 197–200, doi:http://dx.doi.org/10.1016/S0039-6028(96)01350-7.
- [28] F. Esaka, K. Furuya, H. Shimada, M. Imamura, N. Matsubayashi, H. Sato, et al., Comparison of surface oxidation of titanium nitride and chromium nitride films studied by x-ray absorption and photoelectron spectroscopy, *J. Vac. Sci. Technol. A* 15 (1997) 2521–2528, doi:http://dx.doi.org/10.1116/1.580764.
- [29] G. Ketteler, S. Yamamoto, H. Bluhm, K. Andersson, D.E. Starr, D.F. Ogletree, et al., The Nature of Water Nucleation Sites on TiO₂(110) Surfaces Revealed by Ambient Pressure X-ray Photoelectron Spectroscopy, *J. Phys. Chem. C* 111 (2007) 8278–8282, doi:http://dx.doi.org/10.1021/jp068606i.
- [30] A. Arranz, C. Palacio, Screening effects in the Ti 2p core level spectra of Ti-based ternary nitrides, *Surf. Sci.* 600 (2006) 2510–2517, doi:http://dx.doi.org/10.1016/j.susc.2006.04.011.
- [31] J. Baltusaitis, P.M. Jayaweera, V.H. Grassian, XPS study of nitrogen dioxide adsorption on metal oxide particle surfaces under different environmental conditions, *Phys. Chem. Chem. Phys.* 11 (2009) 8295–8305, doi:http://dx.doi.org/10.1039/B907584D.
- [32] B. Hirschorn, M.E. Orazem, B. Tribollet, V. Vivier, I. Frateur, M. Musiani, Determination of effective capacitance and film thickness from constant-phase-element parameters, *Electrochimica Acta* 55 (2010) 6218–6227, doi:http://dx.doi.org/10.1016/j.electacta.2009.10.065.
- [33] B. Hirschorn, M.E. Orazem, B. Tribollet, V. Vivier, I. Frateur, M. Musiani, Constant-Phase-Element Behavior Caused by Resistivity Distributions in Films II. Applications, *J. Electrochem. Soc.* 157 (2010) C458–C463, doi:http://dx.doi.org/10.1149/1.3499565.
- [34] B. Hirschorn, M.E. Orazem, B. Tribollet, V. Vivier, I. Frateur, M. Musiani, Constant-Phase-Element Behavior Caused by Resistivity Distributions in Films I. Theory, *J. Electrochem. Soc.* 157 (2010) C452–C457, doi:http://dx.doi.org/10.1149/1.3499564.
- [35] T. Pajkossy, T. Wandlowski, D.M. Kolb, Impedance aspects of anion adsorption on gold single crystal electrodes, *J. Electroanal. Chem.* 414 (1996) 209–220, doi:http://dx.doi.org/10.1016/0022-0728(96)04700-6.
- [36] S. Ricciardi, J.C. Ruiz-Morales, P. Nuñez, Origin and quantitative analysis of the constant phase element of a platinum SOFC cathode using the state-space model, *Solid State Ion.* 180 (2009) 1083–1090, doi:http://dx.doi.org/10.1016/j.ssi.2009.05.017.
- [37] N. Sato, Chapter 5 – Electric double layer at electrode interfaces, in: N. Sato (Ed.), *Electrochem. Met. Semicond. Electrodes*, Elsevier Science, Amsterdam, 1998, pp. 119–199 http://www.sciencedirect.com/science/article/pii/B9780444828064500052 (accessed May 12, 2014).
- [38] M. to Baben, L. Raumann, J.M. Schneider, Phase stability and elastic properties of titanium aluminum oxynitride studied by ab initio calculations, *J. Phys. Appl. Phys.* 46 (2013) 084002, doi:http://dx.doi.org/10.1088/0022-3727/46/8/084002.
- [39] M. Hans, M. to Baben, D. Music, J. Ebenhöch, D. Primetzhofer, D. Kurapov, et al., Effect of oxygen incorporation on the structure and elasticity of Ti–Al–O–N coatings synthesized by cathodic arc and high power pulsed magnetron sputtering, *J. Appl. Phys.* 116 (2014) 093515, doi:http://dx.doi.org/10.1063/1.4894776.
- [40] M. Pourbaix, Atlas of Electrochemical Equilibria in aqueous solutions, Pergamon Press Ltd., 1974.
- [41] S. Gao, C. Dong, H. Luo, K. Xiao, X. Pan, X. Li, Scanning electrochemical microscopy study on the electrochemical behavior of CrN film formed on 304 stainless steel by magnetron sputtering, *Electrochimica Acta* 114 (2013) 233–241, doi:http://dx.doi.org/10.1016/j.electacta.2013.10.009.
- [42] V.M. Khomenko, K. Langer, H. Rager, A. Fett, Electronic absorption by Ti³⁺ ions and electron delocalization in synthetic blue rutile, *Phys. Chem. Miner.* 25 (1998) 338–346, doi:http://dx.doi.org/10.1007/s002690050124.
- [43] F. Di Quarto, S. Piazza, C. Sunseri, Amorphous semiconductor–electrolyte junction. Impedance study on the a-Nb₂O₅–electrolyte junction, *Electrochimica Acta* 35 (1990) 99–107, doi:http://dx.doi.org/10.1016/0013-4686(90)85045-O.
- [44] M.H. Dean, U. Stimming, Capacity of semiconductor electrodes with multiple bulk electronic states. 2. Applications to amorphous semiconductor electrodes, *J. Phys. Chem.* 93 (1989) 8053–8059, doi:http://dx.doi.org/10.1021/j100361a018.
- [45] M.C. Biesinger, L.W.M. Lau, A.R. Gerson, R.S.C. Smart, Resolving surface chemical states in XPS analysis of first row transition metals, oxides and hydroxides: Sc, Ti, V, Cu and Zn, *Appl. Surf. Sci.* 257 (2010) 887–898, doi:http://dx.doi.org/10.1016/j.apsusc.2010.07.086.
- [46] J.T. Klopogge, L.V. Duong, B.J. Wood, R.L. Frost, XPS study of the major minerals in bauxite: Gibbsite, bayerite and (pseudo-)boehmite, *J. Colloid Interface Sci.* 296 (2006) 572–576, doi:http://dx.doi.org/10.1016/j.jcis.2005.09.054.
- [47] R. Cremer, M. Witthaut, D. Neuschütz, Electron spectroscopy applied to metastable ceramic solution phases, *Fresenius J. Anal. Chem.* 365 (1999) 28–37, doi:http://dx.doi.org/10.1007/s002160051440.

- [48] C. Di Valentin, G. Pacchioni, A. Selloni, S. Livraghi, E. Giamello, Characterization of Paramagnetic Species in N-Doped TiO₂ Powders by EPR Spectroscopy and DFT Calculations, *J. Phys. Chem. B* 109 (2005) 11414–11419, doi:<http://dx.doi.org/10.1021/jp051756t>.
- [49] T. Morikawa, R. Asahi, T. Ohwaki, K. Aoki, Y. Taga, Band-Gap Narrowing of Titanium Dioxide by Nitrogen Doping, *Jpn. J. Appl. Phys.* 40 (2001) L561, doi:<http://dx.doi.org/10.1143/JJAP.40.L561>.
- [50] C. Di Valentin, G. Pacchioni, A. Selloni, Reduced and n-Type Doped TiO₂: Nature of Ti³⁺ Species, *J. Phys. Chem. C* 113 (2009) 20543–20552, doi:<http://dx.doi.org/10.1021/jp9061797>.
- [51] A.J. Bard, M. Stratmann, G.S. Frankel, *Encyclopedia of Electrochemistry, Volume 4, Corrosion and Oxide Films*, Wiley-VCH, 2003.
- [52] F.P. Fehlner, N.F. Mott, Low-temperature oxidation, *Oxid. Met.* 2 (1970) 59–99, doi:<http://dx.doi.org/10.1007/BF00603582>.

Supporting Information

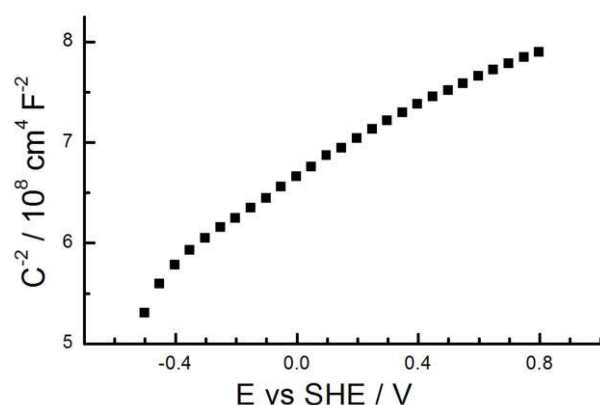


Figure S.1: Mott-Schottky analysis of oxidised TiAlN by means of 20 CVs. The measurement was performed at open circuit potential (0.2 V) and showed a distinct frequency dependence induced by structural distortions. However, the positive slope indicates n-type doping.

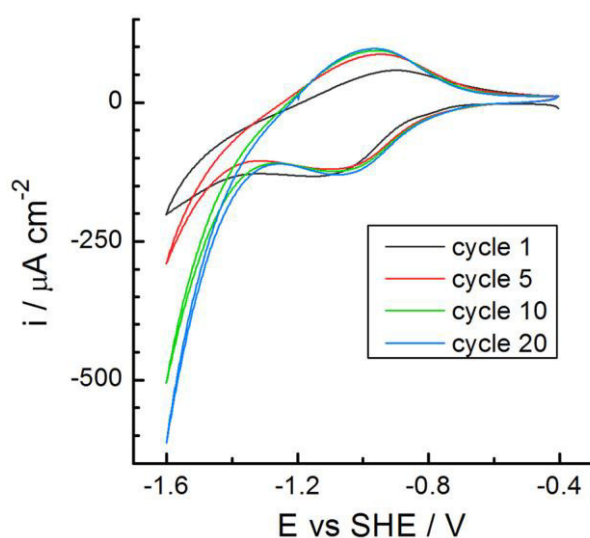


Figure S.2: Repeated CV along the $\text{Ti}^{4+}/\text{Ti}^{3+}$ reversible potential after 10 CV for oxide film formation. The increasing rate of H_2 reduction was related to the formation of Ti^{3+} defects within the surface oxide film.

4.3 Analysis of the inhibition of thermal degradation of molten polycarbonate at tool steel interfaces by thin TiAlN coatings

The manuscript was reproduced from the following publication:

Analysis of the inhibition of thermal degradation of molten polycarbonate at tool steel interfaces by thin TiAlN coatings

Wiesing, M., de los Arcos, T., to Baben, M., Rueß, H., Schneider, J. M., Grundmeier, G.

Polymer Degradation and Stability, 143, 196–206, 2017, doi:10.1016/j.polymdegradstab.2017.07.013

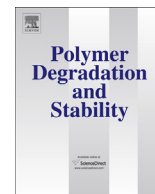
Copyright © 2017, Elsevier Ltd.

Author contributions:

- Planning/experimental work/interpretation/manuscript preparation **MW**
- Hard coating deposition/Proof reading **MB** and **HR**
- Proof reading/content check **GG**
- Proof reading **TA** and **JMS**

Placement:

Practical experiences show that a severe interfacial degradation and deposit formation of polycarbonate occurs at tool steel surfaces, which can largely be prevented by hard coatings. In order to reveal the origin of the reactive interactions, this empirical finding was herein investigated on a fundamental level by an optical, electron and force spectroscopic analysis of the interface formed between iron and $Ti_{0.5}Al_{0.5}N$ surfaces and polycarbonate melt. It could be shown, that polycarbonate degrades catalytically at iron surfaces due to the formation of an interphase with reactive Fe(II) species. This degradation was completely inhibited by the $Ti_{0.5}Al_{0.5}N$ hard coating, but a restructuring of the polycarbonate was observed as a result of the interaction forces. These results advances the fundamental understanding of the functional properties of hard coatings used for polymer melt processing applications and therefore paves the way for their rational design.



Analysis of the inhibition of thermal degradation of molten polycarbonate at tool steel interfaces by thin TiAlN coatings



M. Wiesing^a, T. de los Arcos^a, M. to Baben^b, H. Rueß^b, J.M. Schneider^b,
G. Grundmeier^{a,*}

^a Technical and Macromolecular Chemistry, University of Paderborn, Warburger Straße 100, 33098 Paderborn, Germany

^b Materials Chemistry, RWTH Aachen University, Aachen, Germany

ARTICLE INFO

Article history:

Received 1 February 2017

Received in revised form

4 June 2017

Accepted 10 July 2017

Available online 12 July 2017

Keywords:

Surface

Interface

Polycarbonate

Thermal degradation

TiAlN

Hard coating

HPPMS

ABSTRACT

The inhibition of the thermal degradation of molten polycarbonate at tool steel interfaces by magnetron sputtered TiAlN coatings was studied on fundamental level by means of in-situ and ex-situ spectroscopic and microscopic techniques. As reference systems, which enable the application of in-situ analytical techniques, oxide covered iron films were compared with atmosphere exposed Ti_{0.52}Al_{0.48}N_{1.14} hard coatings. Moreover, SiO₂ terminated silicon and glass substrates as prototypical insulating and inert materials were studied. Interface and interphase analysis of the inorganic substrates and the polymer were performed using confocal fluorescence spectroscopy as well as FTIR, UV/VIS and X-ray photoelectron spectroscopy (XPS). The degradation of polycarbonate at the Fe-oxide interface as revealed by FTIR and UV/VIS spectroscopy indicated the formation of aromatic esters, cyclic anhydrides and discoloring products including char. Simultaneous cross-linking could be verified by strong broadening of the polycarbonates Young's modulus at the Fe-oxide interface as measured by AFM. XPS results indicate that the Fe(III)-states in the Fe-oxide were reduced to Fe(II) states which are likely to act as catalytic sites for PC degradation. In contrast, the surface oxidized Ti_{0.52}Al_{0.48}N_{1.14} coatings effectively inhibited the thermal degradation but however induced slight restructuring of polycarbonate in comparison to the completely inert SiO₂ surface.

© 2017 Elsevier Ltd. All rights reserved.

1. Introduction

During processing of polymer melts, interfacial phenomena such as adsorption, degradation and corrosion affect the stability of the process itself and can lead to a loss of the surface quality of the produced polymer [1,2]. Especially, polymethylmethacrylate (PMMA) and polycarbonate (PC) show effects such as interfacial film formation, and discoloration of the extruded polymer surface occurs when degraded polymeric residues on the tools are torn off during processing [2].

The performance of tool steels used for polymer processing can be significantly enhanced by hard coatings deposited by physical vapor deposition (PVD) [2,3] such as TiAlN sputter-coatings. However, so far the improved performance of such coated tool steels has been studied on an empirical basis, so that a detailed understanding of the influence of the hard coating on the degradation of

the polymer and its interfacial behavior in general is missing though being of major relevance for e.g. the molding process [4,5].

The surface oxide formation of TiAlN at different temperatures and oxygen pressures was recently investigated by ex-situ and in-situ UHV spectroscopic studies [6–8]. A microscopic model of the surface oxidation process was developed in the regime of early oxidation and at elevated temperatures and pressures [8,9]. It was found that oxygen first chemisorbs self-limited at Ti surface sites and some oxygen also dissolves in subsurface layers. Then at higher pressures inward migration of oxygen results into the formation of an oxidic Al₂O₃ and TiO₂ containing top layer at room temperature and a mixed TiAlO top layer at 800 K both covering an oxynitridic TiAl(O,N) growth region [8].

The interfacial behavior of a polymer is supposedly determined by the surface oxide of the hard coating. This aspect is exemplified by recent Density Functional Theory (DFT) simulations of the interaction between CH₄ and an amorphous AlYB hard coating surface in the non-oxidized and oxidized state [10]. The adsorption energy of the CH₄ molecule, which was assumed to be prototypical

* Corresponding author.

E-mail address: g.grundmeier@tc.uni-paderborn.de (G. Grundmeier).

Table 1
Substrates and film thicknesses used for surface and interphase analysis.

Coating	Confocal fluorescence profiling	FTIR	XPS/AFM
TiAlN	glass cover slides/50 nm	Si wafer/1.2 μm	Al cuboids/1.2 μm
Fe	glass cover slides/15 nm	Si wafer/100 nm	Al cuboids/100 nm
SiO ₂	Quartz crystal/-	Si wafer/2 nm	–

for aliphatic polymers, was observed to increase upon oxidation from -0.07 eV to -0.30 eV as a result of increased van der Waals forces. Additionally, no chemical bond formation was observed in either case.

Several authors have investigated the bulk thermal degradation of polycarbonate at low temperatures and found different degradation pathways such as hydrolysis, shift reactions of the carbonate group, autoxidation and disproportionation of the isopropylidene group and oxidative coupling of phenyl rings explaining a wide range of degradation products and the yellow discoloration and gel formation of polycarbonate [11–13]. These mechanistic pathways were verified and more thoroughly elucidated at higher temperatures recently by means of advanced mass spectrometry methods [14–16]. The authors showed that the presence of oxidic interfaces affects the bulk thermal degradation mechanisms of polycarbonate.

In contrast to the accurate understanding of bulk degradation pathways, the influence of different metal oxides on the thermal degradation of polycarbonate interphase is scarcely investigated. An empiric study considered of the degradation of polycarbonate in contact with a variety of metal oxides including V, Cr, Cu, Mo, Zn, Al, Ti, Ce, Mn and Sn oxides by thermogravimetric analysis [17]. ZrO₂ and Cr₂O₃ were found not to catalyze the degradation process, while the other oxides including Al₂O₃ and TiO₂ promoted the bulk degradation. In this regard, Mizuguchi et al. claim specific adsorption of polycarbonate on the TiO₂ surface, which is supported by the observation of Sivalingam that the rate of chain scission reactions is influenced by the acidity of TiO₂ catalysts [18,19]. Furthermore, the role of iron oxide as a catalyst for the degradation of polycarbonate was also noted earlier [20]. An indication of the effect of iron ions in general was given within an investigation of the Fe chlorides catalyzed degradation of different polymers. Interferences of the Fe(II) or Fe(III) ion with radical reaction pathways and cracking of methoxy groups was observed and attributed to the electrophilicity of the metal ion [21].

However, the knowledge on interfacial degradation of polycarbonate in contact with uncoated and coated tool steels is very limited. Therefore, the objective of the here presented work is to improve the understanding of the interfacial degradation processes of a polycarbonate melt on a molecular level. Sputtered TiAlN films and an oxide covered iron film simulating the properties of a low alloy tool steel as well as SiO₂ as a reference material were studied with regard to their influence on the interphase formation and degradation. It is shown that polycarbonate restructures at the TiAlN interface but does not catalytically degrade. In contrast, organic Fe complexes form on the oxide covered iron surface and induce discoloration and catalytic degradation of polycarbonate by the formation of aromatic esters and cyclic anhydrides.

2. Experimental

2.1. Materials

Ti_{0.52}Al_{0.48}N_{1.14} hard coatings were deposited by High Power Pulsed Magnetron Sputtering (HPPMS) using a CemeCon CC-800/9 [22]. The respective substrates and thicknesses of each material were optimized for every measurement and are detailed out in

Table 1. A rectangular magnetron with a Ti_{0.5}Al_{0.5} compound target was used. The substrates were at a target-to-substrate distance of 80 mm, at floating potential and heated to 550 K. The base pressure was below 1 mPa and the gas flows during deposition were 200 sccm Ar and 50 sccm N₂ resulting in partial pressures of 368 mPa and 94 mPa, respectively. A Melec HPPMS generator with a frequency of 800 Hz, a duty cycle of 4% and a time-average power of 3000 W resulting in a peak power density of 400 W/cm² was used. The stoichiometry of the TiAlN hard coating was in the case of the 1.2 μm thick sample determined to Ti_{0.52}Al_{0.48}N_{1.14} as measured by Rutherford backscattering (RBS) and Time-of-Flight Elastic Recoil Detection Analysis (ToF-ERDA) [23,24]. The RBS measurement was performed at a backscattering angle of 170° and by using 2 MeV He⁺ ions. ToF-ERDA was measured using a 36 MeV I⁸⁺ primary ion beam at an angle of incidence of 67.5° relative to the surface normal and the recoil particles were detected within an angle of 45° relative to the incoming beam. The data were analyzed using the SIMNRA code and CONTES [23]. In comparison, the stoichiometries of both the 50 nm and the 1.2 μm TiAlN hard coatings were determined by XPS after removal of the surface oxide film using Ar⁺ ion beam irradiation at 3 kV until the stoichiometry was constant. The XPS stoichiometries normalized to the N concentration of 1.14 were Ti_{0.54}Al_{0.85}O_{0.05}N_{1.14} (1.2 μm film) and Ti_{0.60}Al_{0.88}O_{0.20}N_{1.14} (50 nm film). The slight deviations from the ion spectroscopy derived stoichiometries are presumably explained by preferential sputtering of especially the light elements [25,26]. The presence of oxygen within the TiAlN film is rationalized by oxygen contaminations present in the chamber during deposition [27]. Such contaminations are gettered during an extended deposition and are thus more relevant for short deposition times as in the case of the 50 nm thin film. However, the Ti/Al metal ratio was for both film thickness values basically unaffected indicating a high stability of the sputter process. It is further noted, that the hard coating surfaces were studied in the oxidized state and thus slight oxygen contaminations present in the bulk are assumed not to affect the chemical properties of the corresponding polymer melt interface significantly.

Iron films were prepared on optical substrates by thermal evaporation of Fe (99.99+%, Goodfellow) using a Sputter-Coater (Tetra, Germany) at a deposition rate of around 1 nm min⁻¹ and at a base pressure of 10⁻⁴ Pa.

Silicon substrates were cleaned prior use in H₂O₂/NH₃ solution (10 w%/10 w%) for at least 12 h leading to the formation of a SiO₂-film of about 2 nm thickness [28]. Additive-free polycarbonate (Makrolon 3108, Goodfellow) dried at 480 K and analytical grade chemicals were used throughout this study.

2.2. Thermal degradation

Thermal degradation of polycarbonate samples was always performed in N₂ at 595 K. The samples were exposed for up to 20 h in the case of optical spectroscopy but limited to 100 min for the samples investigated by XPS and AFM as a result of strong adhesion and cohesive cleavage encountered at longer durations.

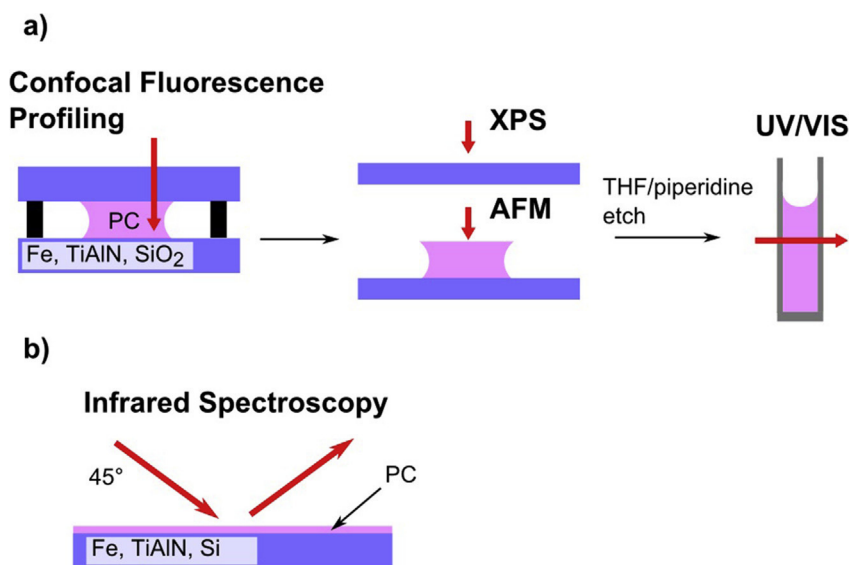


Fig. 1. Illustration of the sample geometries used for **a)** confocal fluorescence analysis, XPS and AFM measurements, UV/VIS and **b)** for FTIR reflection spectroscopy. Black bars in the left figure of **a)** indicate glass spacers.

2.3. Confocal fluorescence analysis

Stacked samples consisting of two coated cover slides spaced by 1 mm thick glass rods were prepared for measurement in backside geometry as shown in Fig. 1. Care was taken that the polycarbonate did not contact the glass spacers. Confocal fluorescence analysis was performed using a confocal Raman microscope (InVia, Renishaw) equipped with a 50x objective and a 532 nm Nd:YAG laser (17.5 mW). The depth resolution was 8 μm . The intensity at one position was determined by the integrated intensity measured in the range of 1750–2250 cm^{-1} using 391 channels and after normalizing to the measured bulk intensity of each profile.

2.4. XPS

Surface chemical analysis was performed using XPS on the coating side of cleaved stacked samples (see Fig. 1). Since degraded PC strongly adheres to surfaces, aluminum cuboids with a mirror-like surface finish coated with Fe (100 nm) or TiAlN (1.2 μm) were used as substrates for the stacked samples. The samples were mechanically cleaved after degradation at 595 K for 100 min. This corresponds to an exposure of the molding tool to PC of several hundreds of molding cycles [5]. XPS measurements were performed using monochromatized Al $K\alpha$ irradiation (1486.7 eV) in an ESCA + UHV system (ScientaOmicron, Taunusstein, Germany) at a base pressure $<1 \times 10^{-8}$ Pa. The depth of information was 5.5 nm at the emission angle of 15° relative to the surface normal and the spectral resolution was 0.77 eV as determined from measurements of the Ag3d_{5/2} core level [29]. If not otherwise stated, no charge neutralization was required and the binding energies are referenced against the Ag3d_{5/2} core level at 368.4 eV.

2.5. AFM

For mechanical analysis of the PC interface force volume spectroscopy was performed using an AFM (Nanowizard III, JPK Instruments). The force constant of the cantilevers used was around 20 nN nm^{-1} (NSC15, MikroMasch) and calibrated before use by means of the thermal noise method. In order to decrease the

pressure under the tip, the cantilevers were annealed at 1500 K for 1 h in air resulting in tip radii around 175 nm as determined by using a test grid (TGT1, NT-MDT, Russia) [30]. Force curves were measured with a scan speed of 200 nm s^{-1} and a maximum force of 100 nN relative to the baseline. The reduced Young's modulus was extracted from the data by fitting the force versus distance data of the approach according to the JKR model using Matlab (R2014a, Mathworks Ltd.) [31]. The measurements were performed on the XPS samples after annealing at 460 K, which is 35 K above the glass temperature, for 1 h in air in order to remove interfacial stresses induced by the mechanical cleavage.

2.6. FTIR reflection spectroscopy

PC thin films with 1 μm thickness were spin-coated from a 2.5 w % PC/chloroform solution (2000 rpm, 1 min) onto Fe, TiAlN and SiO₂. The optically opaque Fe (100 nm) and TiAlN (1.2 μm) thin films were deposited on Si wafers and measured in reflection geometry at an angle of incidence of 45° . In the case of SiO₂, a Si wafer with its native SiO₂ oxide film was used and a mirror was placed below. Note that the phase shift due to the measurement angle of 45° in combination with the wafer thickness of 650 μm allowed to mitigate interferences disturbing the measurement. The measurements were performed in vacuum (Vertex 80v, Bruker).

2.7. UV/VIS

The stacked samples from the Confocal Fluorescence Profile measurements were dissolved in tetrahydrofuran/piperidine at room temperature for 30 min. The samples were dried with N₂ after aminolysis and stored in vacuo for 24 h. UV/VIS was measured after dissolving the samples in methanol (Evolution 600, ThermoScientific).

3. Results and discussion

3.1. XPS of surface oxidized Fe and TiAlN

The Fe and TiAlN thin films after exposure to ambient atmosphere were characterized by means of XPS. The Fe2p_{3/2} line shape

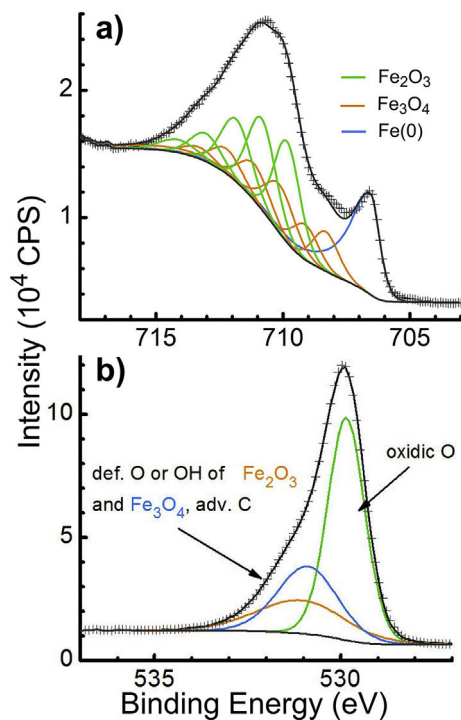


Fig. 2. XPS spectra of a) the $\text{Fe}2p_{3/2}$ and b) the $\text{O}1s$ signals of Fe thin films after deposition and exposure to ambient atmosphere.

as shown in Fig. 2 was analyzed following the procedure of Biesinger et al. [32].

Accordingly, the complex $\text{Fe}2p_{3/2}$ line shape was synthesized by selecting appropriate reference components via optimization of the RMS error. The resulting fits and their accuracy as shown in Fig. 2 are representative for the fits reported elsewhere in this study. This procedure allowed to describe the surface chemistry by a mixture of Fe^0 , Fe_3O_4 and $\gamma\text{-Fe}_2\text{O}_3$. Further, the $\text{O}1s$ spectrum was described by three components, which correspond to oxidic oxygen (529.9 eV) and a mixture of organic and defective oxygen including possibly also surface hydroxyl groups (530.9 and 531.5 eV) [32]. The $\text{C}1s$ spectrum showed the presence of adventitious carbon only (see Fig. S1).

The spectra of TiAlN after deposition and exposure to atmosphere are shown in Fig. 3. The $\text{Ti}2p$ spectrum could be described by three components located at 455.2, 456.8 and 458.5 eV, which are ascribed to the TiAlN substrate, an oxynitridic $\text{TiAl}(\text{O},\text{N})$ growth region and a $\text{Ti}(\text{IV})$ layer according to their binding energies [22,33]. The total thickness of the oxygen containing layers was around 3.5 nm [29]. The line shape of the TiAlN component is affected by intra-band transitions and screening effects by the metallic $\text{Ti}3d$ conduction band electrons and is thus of complex nature [34,35]. A more in-depth discussion of the different screening mechanisms can be found elsewhere [36].

The composition of the $\text{Ti}(\text{IV})$ containing outermost surface layer can principally be composed of mixed TiAlO or segregated Al_2O_3 and TiO_2 . In this regards, the discussion of the $\text{O}1s$ spectra after heating in contact with polycarbonate as reported below disclosed the presence of a mixed TiAlO .

The $\text{O}1s$ spectrum could be described using two components at 530.4 and 531.7 eV. The latter component is due its binding energy related to adventitious carbon or surface hydroxylation [22]. The component at 530.4 eV corresponds the mixed TiAlO according to its binding energy [37,38]. Further, it is supposed that this component is also affected by oxynitride of which the binding energy is observed within this range for $\text{Ti}(\text{O},\text{N})$ [39,40].

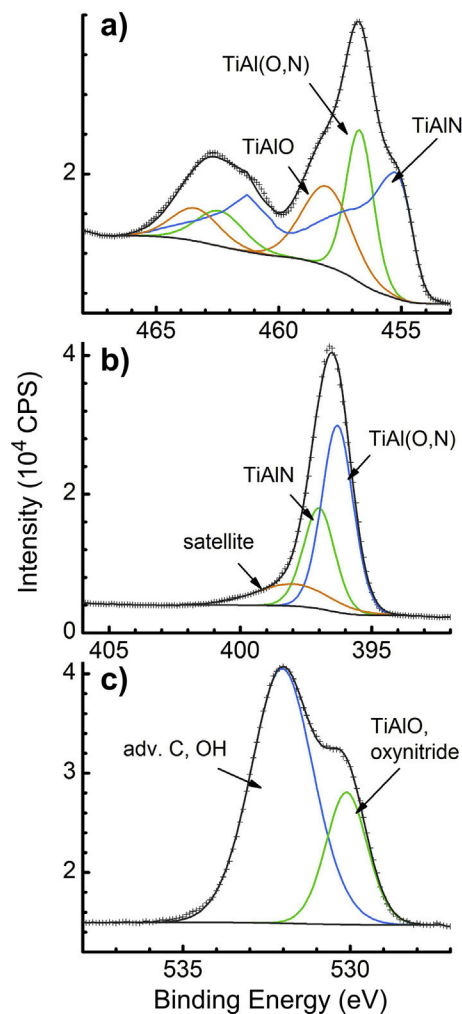


Fig. 3. XPS spectra of a) the $\text{Ti}2p$, b) the $\text{N}1s$ and c) the $\text{O}1s$ signals of TiAlN after deposition and exposure to atmosphere.

The $\text{N}1s$ spectrum was described using three components located at 397.7, 396.7 and 396.0 eV. The component at 396.7 eV was ascribed to TiAlN and that at 396.0 eV to oxynitridic $\text{TiAl}(\text{O},\text{N})$ [36,39]. Another component was observed at 397.7 eV and is termed as satellite. Similar asymmetry was also observed but scarcely investigated in literature [41]. A possible assignment could be surface N-O species [42,43]. In contrast, essentially oxygen-free single-crystalline Ti_2AlN (4 at.% O) shows also this distinct tailing and also structural defects or electronic shake-ups could account for this feature [34,39,44]. Based on the data reported a precise assignment of the satellite component was thereby not attempted. The $\text{C}1s$ spectrum showed only adventitious carbon contaminations and can be found in Fig. S2.

Based on the XPS results, the surfaces of the Fe and TiAlN thin films previous to contact with the PC, are generally covered by a complex surface oxide layer and are denoted as $\text{Fe}|\text{Fe}_x\text{O}_y$ and $\text{TiAlN}|\text{TiAl}(\text{O},\text{N})|\text{TiAlO}$ in the following.

3.2. FTIR and UV/VIS spectroscopy

The thermal degradation of polycarbonate at the $\text{Si}|\text{SiO}_2$, $\text{Fe}|\text{Fe}_x\text{O}_y$ and $\text{TiAlN}|\text{TiAl}(\text{O},\text{N})|\text{TiAlO}$ interfaces was investigated at 595 K, which is within the temperature range for polycarbonate molding. The corresponding IR spectra as obtained after 20 h are

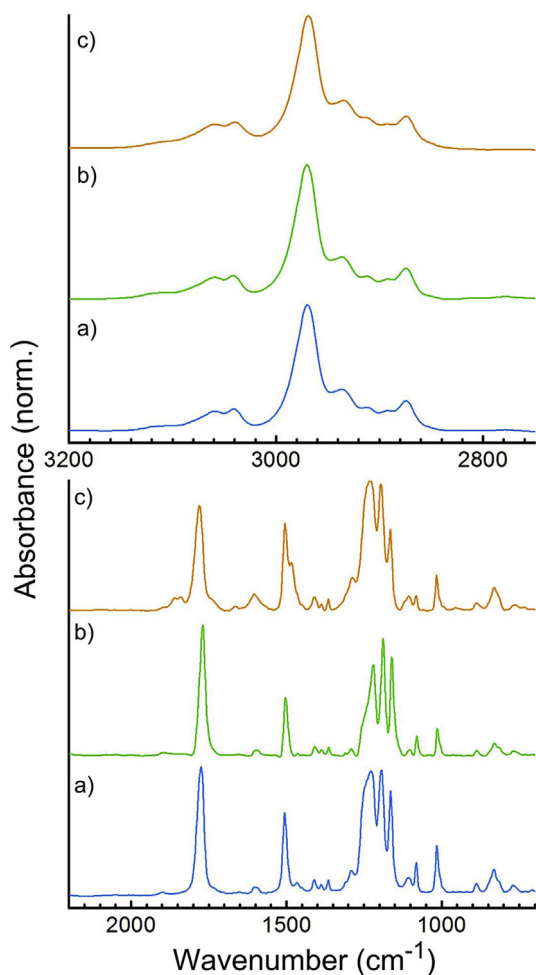


Fig. 4. FTIR spectra of spin cast PC films on a) Si/SiO₂, b) TiAlN/TiAl(O,N) and c) Fe/Fe_xO_y after heating in N₂ at 595 K for 20 h. The spectra were normalized and shifted vertically.

shown in Fig. 4 and a list of the vibrational assignments can be found in Table 2. It is noted that the signals located at 1193 and 1164 cm⁻¹ are related to vibrations of the isopropylidene and carbonate units, but a consistent assignment was not found in literature [45–48]. Similarly, some authors claim that the signal at 1016 cm⁻¹ corresponds to aromatic CH bending vibrations, whereas other relate this signal to C–O–C vibrations [45,46,49,50]. In this regard, the description of the polycarbonate spectrum by Kulczycki et al. was based on simulations and clearly no carbonate related vibrational transitions were present in the region from 900 to 1200 cm⁻¹ [51]. Thus, the assignment of the signal at 1016 cm⁻¹ to aromatic CH bending vibrations is followed here.

After heating polycarbonate in contact with Si/SiO₂ for 20 h at 595 K (case a), no spectral changes were observed. Instead, the sample showed the typical bands and line shape for amorphous polycarbonate (see Fig. 6A of Dybal et al. [47]). This indicates that no significant interactions between polycarbonate and SiO₂ took place.

After heating polycarbonate at the TiAlN/TiAl(O,N)/TiAlO interface (case b), no additional peaks were found but the relative intensities of the two signals of the C–O–C stretching region around 1235 cm⁻¹ changed crucially and sharpened. Since these signals reflect the cis-trans and trans-trans conformations of the carbonate moiety [47,48], this indicates restructuring of the polycarbonate and also explains the observed changes of the relative intensities of the other main signals in the spectrum [52].

Conversely, several signals established after heating polycarbonate in contact with Fe/Fe_xO_y: the most prominent signal developed at 1484 cm⁻¹ and might refer to CH deformation vibrations including possibly some aromatic contributions [46,51]. Two signals emerged at 1840 and 1860 cm⁻¹ and were assigned to cyclic anhydrides [13]. Another signal was observed at 1740 cm⁻¹ and could be ascribed to aromatic esters [46]. The presence of these carboxylic acid derivatives clearly shows that the polycarbonate was degraded. This further hints that shift reactions might be of relevance for the degradation, which are typically present in the early stages of the thermal degradation [11,53]. Since however the degradation is clearly catalyzed at the Fe/Fe_xO_y interface, no attempt is hereby made to specify reaction mechanisms.

Table 2

Band assignments of the FTIR spectra of spin cast polycarbonate films deposited on Si wafer, Fe and TiAlN after heating at 595 K for 20 h.

Peak position (cm ⁻¹)	Vibration	Sample	References
3000–3200	Aromatic CH stretch	Si, TiAlN, Fe	[45,46]
2970	CH ₃ asymmetric stretch	Si, TiAlN, Fe	[45,46]
2874	CH ₃ symmetric stretch	Si, TiAlN, Fe	[45,46]
1850–2500	Overtone and combination bands	Si, TiAlN, Fe	[54]
1899	Aromatic C–H out-of-plane wagging overtone and combination	Si, TiAlN, Fe	[45,46,50]
1840, 1860	Cyclic anhydride	Fe	[13,54]
1775 ^{a,b}	Carbonate C=O stretch	Si, TiAlN, Fe	[45,46,50,51]
1740	Aromatic esters	Fe	[46]
1602 ^a	Para aromatic ring quadrant stretch	Si, TiAlN, Fe	[45,46,48,50]
1506	Para aromatic ring semicircle stretch	Si, TiAlN, Fe	[45,46,50]
1484	Aliphatic and possibly some aromatic CH bend	Fe	[46,51]
1465	CH ₃ asymmetric deformation	Si, TiAlN, Fe	[46,50]
1409	Para aromatic ring semicircle stretch	Si, TiAlN, Fe	[45,46]
1387	(CH ₃) ₂ C vibration	Si, TiAlN, Fe	[51]
1365	CH ₃ symmetric (umbrella) deformation	Si, TiAlN, Fe	[45,46,50]
1292	aromatic C–H in-plane bend	Si, TiAlN, Fe	[46]
1230 ^a , 1245 ^a	C–O–C stretches of cis-/trans-configurations	Si, TiAlN, Fe	[45–48]
1193, 1164	(CH ₃) ₂ C vibration and carbonate stretch	Si, TiAlN, Fe	[45,46,51,53,55]
1107	Aromatic C–H in plane bend	Si, TiAlN, Fe	[46]
1082	aromatic ring C–C stretch	Si, TiAlN, Fe	[45,46,49–51]
1016	Para in-plane aromatic CH bend	Si, TiAlN, Fe	[45,46]
889	Symmetric carbonate stretch	Si, TiAlN, Fe	[46,50,51]
831	Para out-of-plane aromatic CH wag, two adjacent Hs	Si, TiAlN, Fe	[45,46,50]
770	out-of-plane skeletal vibration of carbonate and C–H deformation	Si, TiAlN, Fe	[46,50,51]

^a Conformation sensitive bands.

^b Band possibly affected by Fermi resonance [48].

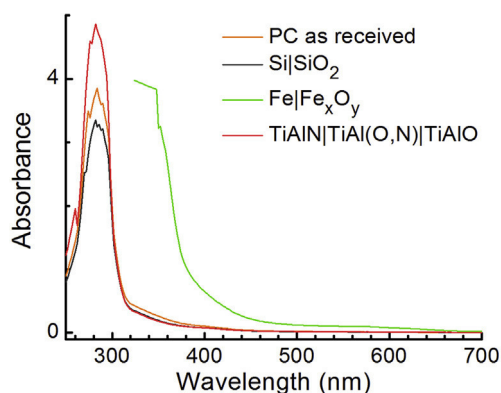


Fig. 5. UV/VIS spectra of polycarbonate after heating at 595 K for 20 h in contact with Si|SiO₂, TiAlN|TiAl(O,N)|TiAlO and Fe|Fe_xO_y and after etching in tetrahydrofuran/piperidine.

Notably, related signals such as carboxylic acids or hydroxyl containing functional groups could not be observed. This indicates that under the given conditions condensation reactions such as esterification and the formation of anhydrides are clearly favored.

Complementary chemical analysis was performed by means of UV/VIS spectroscopy of which the spectra are shown in Fig. 5. It was observed that the spectra of the polycarbonate at the Si|SiO₂ and TiAlN|TiAl(O,N)|TiAlO interface after heating at 595 K for 20 h essentially match the non-heated polycarbonate reference sample. The most intense absorption bands therein were located at 290 nm and ascribed to the π - π^* transition related to the phenyl ring as well as to the overlapping carbonate chromophoric unit, which extends up to 330 nm [13,56]. Further, a tailing was found up to 400 nm, which is in the region of the absorption of phenylsalicylates (320 nm) [57,58]. These compounds form due to shift reactions and could possibly originate from the thermal processing of the PC during manufacturing and sample preparation [11]. It is noted that no related signals were observed in the infrared spectra, which is explained by the lower sensitivity of FTIR spectroscopy for these compounds when compared to UV/VIS [57,58].

The heat treatment of polycarbonate in contact with Fe|Fe_xO_y showed after 20 h an opaque region up to 360 nm followed by an extended unstructured tailing up to 630 nm. Such tailing and yellow discoloration is also observed during photo degradation of polycarbonate or low temperature degradation and is typically

explained by the formation of a variety of degradation products, which commonly show extended aromatic π -systems and obscure a precise chemical assignment [12,13,57]. This interpretation also accounts for the observed inset of char formation and is in agreement with the results from IR spectroscopy, which similarly reflect catalytic degradation of polycarbonate at the Fe|Fe_xO_y interface.

To summarize, the optical spectroscopy revealed catalytic degradation and yellow discoloration of polycarbonate at the Fe|Fe_xO_y interface and the formation of a variety of degradation products including cyclic anhydrides and aromatic esters. At the TiAlN|TiAl(O,N)|TiAlO and Si|SiO₂ interfaces, polycarbonate is not catalytically degraded but restructures at the TiAlN|TiAl(O,N)|TiAlO interface.

3.3. XPS and confocal fluorescence analysis of the polycarbonate/thin film interfacial region

A more thorough analysis of the polycarbonate/thin film interfaces and interphases was performed by means of confocal fluorescence analysis and XPS. The corresponding fluorescence depth profiles are shown in Fig. 6.

The fluorescent signal measured of the heated Si|SiO₂|polycarbonate interface was observed to decay into the polymer bulk independent of the duration of the heating treatment. Assuming that the fluorescence is primarily induced by yellowing compounds, this indicates the presence of degradation products at the interface, which most probably originate from the thermal processing history of the sample as discussed above. Further, the absence of changes with time is in agreement with the UV/VIS spectra.

In the case of the TiAlN|TiAl(O,N)|TiAlO|polycarbonate interface a slight increase of the fluorescent signal was observed after heating. Considering that the magnitudes of the intensities were close to the bulk value, essentially no degradation products accumulated at the interface. This is tentatively explained by strong adsorption of polycarbonate to TiAlN, which is in accordance with the IR spectroscopy results.

The depth profile of the fluorescent signal of the Fe|Fe_xO_y|polycarbonate sample showed the highest intensities after heating and increasingly protruded into the polymer bulk with time. This clearly evidences that Fe|Fe_xO_y acts as a source of degradation products and that polymer degradation is therefore enhanced at the interface resulting into the formation of a diffusion layer of degradation products. This further highlights the potential

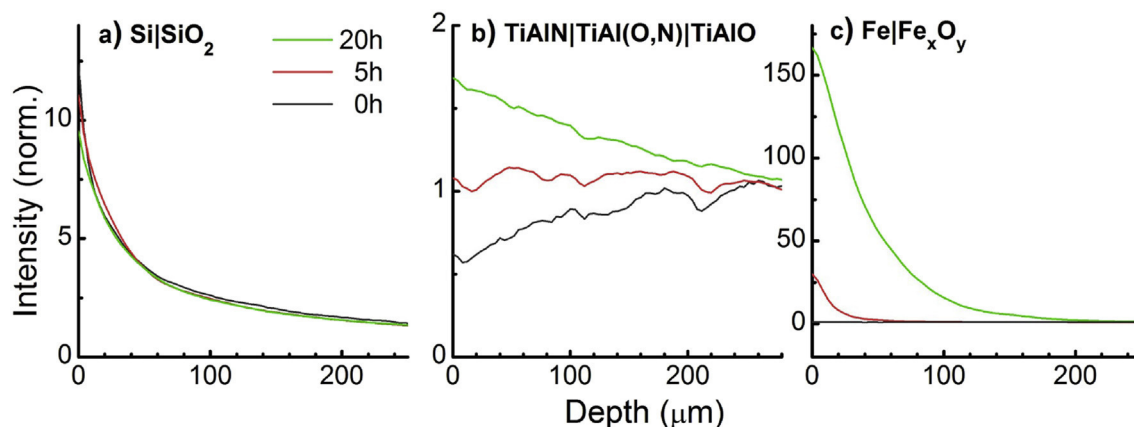


Fig. 6. Confocal fluorescence depth profiles of polycarbonate in contact with a) Si|SiO₂, b) TiAlN|TiAl(O,N)|TiAlO and c) Fe|Fe_xO_y after heating at 595 K for 20 h and measured using 532 nm excitation in the range of 1750–2250 cm⁻¹. The depth was referenced to zero at the respective interface and the intensity was normalized to the bulk value.

Table 3
XPS stoichiometry of the TiAlN|TiAl(O,N)|TiAlO|polycarbonate and Fe|Fe_xO_y|polycarbonate interface after heating to 595 K for 100 min and cleavage as calculated from survey spectra. A non-heated polycarbonate sample cleaved from SiO₂ covered Si wafer is also included.

Sample	C1s (at.%)	O1s (at.%)	N1s (at.%)	Fe2p (at.%)	Ti2p (at.%)	Al2p (at.%)	C/O
PC (non-heated)	84.5	15.5	–	–	–	–	5.5
PC-Fe	77.5	20.5	–	2.0	–	–	3.8
PC-TiAlN	77.5	15.9	2.2	–	1.0	3.5	4.9

of this technique for spatially resolved characterization of degradation structures for failure analysis.

In the following, the chemical changes of polycarbonate at the Fe|Fe_xO_y and TiAlN|TiAl(O,N)|TiAlO interfaces are discussed based on XPS measured after heating and cleaving the samples and measuring on the thin film sites. It is noted that the heating time was limited to 100 min, because the samples otherwise cleaved in the polycarbonate bulk due to the strong adhesion encountered. The stoichiometry of these samples including a non-heated spin cast polycarbonate reference is shown in Table 3. The corresponding high-resolution spectra of the reference spin cast polycarbonate sample can be found in Fig. S3. It was observed that among all samples the carbon concentration was very high, indicating that rests of a polycarbonate film were left on the surface after cleavage. Assuming an effective attenuation length of 2.8 nm and a density of 1.2 g cm⁻³ for polycarbonate, the thickness of this layer could be estimated to be around 10 nm [29,59].

In the case of the cleaved TiAlN|TiAl(O,N)|TiAlO|polycarbonate sample, only a slight overstoichiometry of 1.8 at.% for oxygen was observed as compared to non-heated polycarbonate, which can be easily explained by the presence of the surface oxide film on the TiAlN coating. However, a more precise calculation of the oxygen contribution of these surface oxides was prevented due to the presence of the thick organic layer, which distorts a reliable quantification due to the very different kinetic energies of the Ti2p and Al2p photoelectrons (overlayer effect) [59].

Further analysis of the chemical changes at the interfaces due to heating with and without being in contact with polycarbonate was attempted by high-resolution XPS of which the spectra are discussed in the following. The spectra of the Fe|Fe_xO_y sample after heating to 595 K for 100 min are depicted in Fig. 7a. The Fe2p_{3/2} signal showed a shift to higher binding energies and the absence of

Fe(0) when compared to the atmosphere exposed state shown in Fig. 2. The analysis of the line shape showed that the surface was dominated by the presence of Fe₂O₃. This was supported by the corresponding O1s spectrum that showed oxidic oxygen at 530.0 eV and a mixture of hydroxyl groups, defective and organic oxygen at 531.6 eV.

In comparison, the Fe2p_{3/2} line shape shown in Fig. 7b was crucially affected due to heating in contact with polycarbonate and did not correspond to mixtures of typical Fe-oxides or Fe-carbonates [32,60]. However, contributions from Fe₃O₄ or FeO are likely to contribute to the measured spectrum. The measured line shape was best mathematically described by including several components (708.5 eV, 1.78 eV FWHM; 710 eV, 1.91 eV FWHM; 711.4 eV, 2.64 eV FWHM; 713.4 eV, 2.28 eV FWHM; not shown). Most importantly, the analysis revealed a shoulder around 708.2 eV, which is indicative for the presence of Fe(II) according to Biesinger et al. [32] This interpretation is supported by the absence of Fe₂O₃, which is reflected by the disappearance of the spin-orbit shake-up component at 719.2 eV [60,61]. In this regard, it is noted that some contributions of Fe(III) states might still be present, because Fe₃O₄ does not show this shake-up [60]. Considering that the polycarbonate degrades catalytically at the iron oxide interface as evidenced by optical spectroscopy, this indicates that interfacial Fe(II)-enriched complexes form and act as catalytic centers for the degradation process. In conclusion, several components such as organic O-Fe complexes but also FeO and Fe₃O₄ might contribute to the complex Fe2p_{3/2} line shape.

The corresponding O1s signal of this sample was described by four components located at 534.0, 532.7, 531.1 and 530.0 eV. The two main components at 534.0 and 532.7 eV could be assigned to the C-O and C=O bonds of polycarbonate [62]. When comparing O1s spectra of different iron oxides and also of different polymers, it

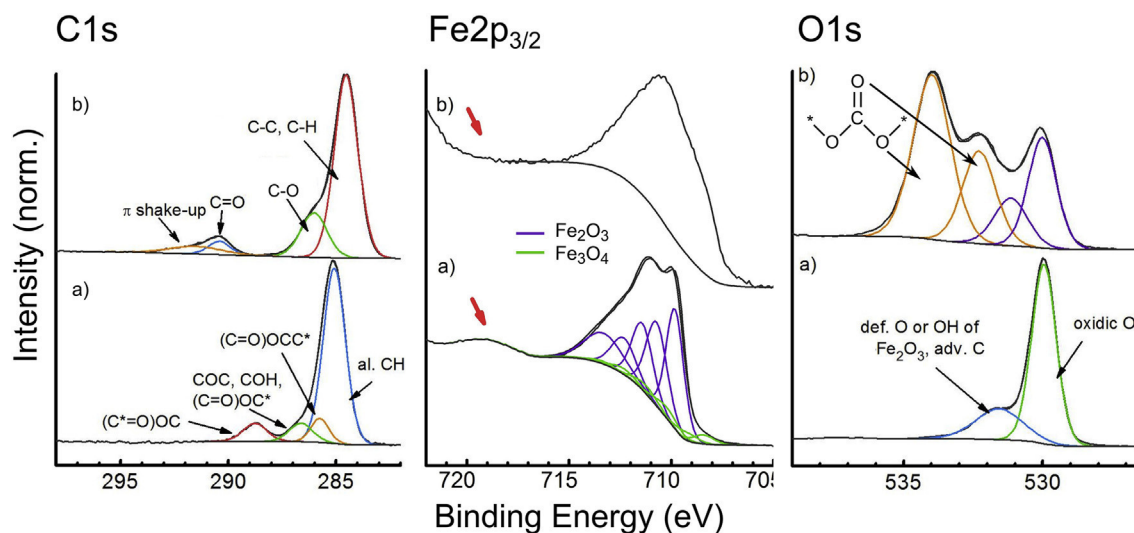


Fig. 7. High resolution XPS spectra of the Fe|Fe_xO_y thin film after heating to 595 K for 100 min **a)** without contact to polycarbonate and **b)** in contact with polycarbonate. The spectra were normalized and shifted vertically for better visualization. The characteristic multiplet shake-up of Fe(III) in Fe₂O₃ is highlighted with a red arrow in the Fe2p_{3/2} spectrum. (For interpretation of the references to colour in this figure legend, the reader is referred to the web version of this article.)

Table 4

Composition of the C1s spectrum (in at-%) measured on the cleaved Fe/Fe_xO_y/polycarbonate and TiAlN/TiAl(O,N)/TiAlO/polycarbonate samples after heating at 595 K for 100 min and of a non-heated spin cast polycarbonate sample.

Sample	C (284.5 eV)	C-O (286.0 eV)	C=O (290.4 eV)	π shake-up (291.5 eV)
PC (non-heated)	73.3	15.3	5.2	6.2
PC-Fe	70.0	18.9	4.7	6.4
PC-TiAlN	73.2	15.8	5.0	6.0

becomes clear that the component around 530.0 eV most probably relates to oxidic oxygen bound to Fe(II) [32,63]. Conversely, the component at 531.1 eV could relate to either the polymer top layer or the Fe substrate. In the latter case, this component could relate to surface hydroxylation of the oxide, defective oxygen or a hydrated oxide [32]. If this component is ascribed to the polymer top layer, the binding energy has to be referenced properly to the C1s (285.0 eV) for comparison with literature. This procedure results into a binding energy of 531.6 eV, which is indicative for aromatic esters [63,64]. In this regard, the presence of esters is not supported by the analysis of the C1s spectrum as discussed below, because the related carbonyl group expected at 288.4 eV (with reference to C1s at 284.5 eV) was not observed [64]. The O1s component at 531.1 eV is therefore also related to oxygen bound to iron.

The atomic concentration of oxygen corresponding to interphasial Fe species could be calculated based on the data of Table 3. It follows that around 7.0 at.% oxygen relate to 2.0 at.% Fe. This indicates that this oxygen does not completely bind to Fe, because the formal oxidation number of +II or even + III would be exceeded. Assuming consequently that some of this oxygen binds to carbon, organic Fe complexes are again supposed to be formed. Similar observations were made within recent investigations on the reaction of iron oxides with ethanol, where reduction of Fe(III) to Fe(II) was also observed around 575 K [65].

The C1s lines essentially reflected the typical spectrum of polycarbonate [62,66,67]. In this regard, the line shape was described by contributions from aliphatic and aromatic carbon at 284.5 eV, the carbonates C-O at 286.0 eV, the carbonates C=O at 290.4 eV and π -shake ups at 291.5 eV. The FWHM ratios were fixed according to the spectrum of a spin cast polycarbonate sample measured with the same experimental parameters. It is emphasized that no carbide or carbonate was found at 283.7 eV or around 289.4 eV [68,69]. Further, the presence of anhydrides and esters as indicated by IR

could not be seen in the C1s spectrum presumably due to their low concentrations.

As a result of the peak synthesis, the relative fraction of the C-O component, which is also typical for the C-O of ethers and alcohols, increased relatively to the non-heated polycarbonate by around 3.6% as shown in Table 4 [70]. Conversely, the carbonate unit was only decreased by 0.5%. This is consistent with an enrichment of oligomers, which is an entropy driven process typically encountered at polymer interfaces, cannot account for the increase of the C-O component, because the corresponding changes of the C-O component relative to the carbonate are then restricted to 2:1 [71,72]. Thus, the increase of the C-O component rather accounts for the observed total increase of the oxygen concentration and corresponds with regards to the O1s spectrum to the organic Fe species.

In the following the effect of the atmosphere exposed TiAlN hard coating on the interfacial chemistry is investigated based on the XPS spectra shown in Fig. 8 (N1s and Al2p spectra can be found in Fig. S2).

All Ti2p spectra were analyzed similar to the spectrum of atmosphere exposed TiAlN in Fig. 3 and were described by three components related to TiAlN at 455.2 eV, TiAl(O,N) at 456.8 eV and TiAlO at 458.5 eV [22,33]. When comparing the Ti2p spectra it becomes clear that the heating process increased the relative fraction of the oxynitridic growth region from 30 to 40% at the expense of the TiAlN substrate. Recent electrochemical investigations on the oxidation mechanism of TiAlN revealed that the surface oxide growth is dominated by inwards migration of interstitial oxygen, which undergoes reactive exchange with lattice nitrogen within the TiAl(O,N) growth region [22]. In view of this microscopic model the increased TiAl(O,N) growth region can be explained by enhanced defect migration and reaction due to the elevated temperatures.

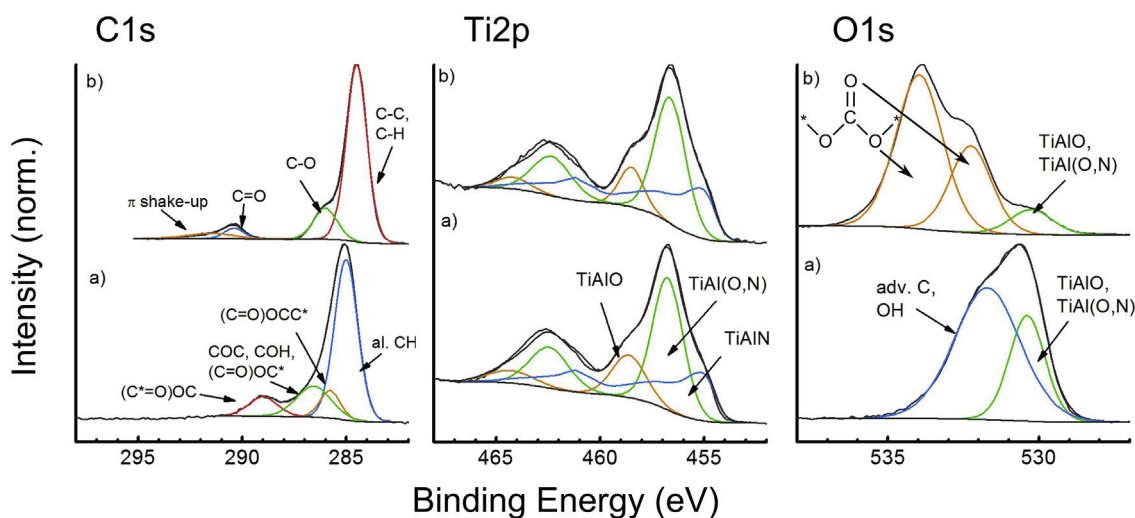


Fig. 8. High resolution XPS detail spectra of TiAlN/TiAl(O,N)/TiAlO after heating at 595 K for 100 min **a)** without and **b)** with being in contact with polycarbonate. The spectra were normalized and shifted vertically for better clarity.

The O1s spectrum of the heated TiAlN sample shown in Fig. 8a could be described similarly as the atmosphere exposed sample by means of two components at 530.4 related to TiAlO with possible contributions of TiAl(O,N) and at 531.7 eV related to adventitious carbon or surface hydroxylation [22]. The assignment of the Ti(IV) top layer related oxygen component is clarified when investigating the O1s spectrum after heating and cleavage from polycarbonate (Fig. 8b): This spectrum shows two components at 534.0 and 531.7 eV related to polycarbonate and a single oxidic component at 530.3 eV but no separated Al₂O₃ component, which would be expected in the range of 530.6–531.8 eV [73]. This corresponds exactly to the situation observed for mixed TiAlO [38]. Hence, the component around 530.3 eV is ascribed to mixed TiAlO with possible contributions from oxynitride.

The C1s spectrum of TiAlN after heating showed the presence of adventitious carbon. After heating in contact with polycarbonate, the C1s line shape indicated again the presence of a residual polycarbonate film. The results of the peak synthesis (see Table 4) revealed that the chemical composition of the polycarbonate was not affected by heating, which is in agreement with the IR and UV/VIS spectroscopy results. This highlights that in contrast to the Fe|Fe_xO_y interface neither the chemical structure of

the TiAlN hard coating nor of the polycarbonate were affected by heating.

To summarize, XPS revealed the reduction of Fe(III) species to Fe(II) in presence of polycarbonate. Furthermore, the Fe(III) states of the surface oxide are reduced to Fe(II) and most probably organic Fe complexes form at the PC|oxide interface being responsible for the catalytic degradation of polycarbonate. In the case of the TiAlN|TiAl(O,N)|TiAlO interface, no chemical changes were found in either the hard coating or the polycarbonate, demonstrating the protective properties of TiAlN hard coatings.

3.4. Mechanical properties at the polycarbonate-thin film interface

The influence of the chemical degradation at the Fe|Fe_xO_y|polycarbonate interface on the mechanical properties was investigated by AFM. The force curves were measured across a grid on the polymer side of the cleaved samples using a blunt SiO₂ tip, which reduces the stress within the contact and maintains the measurement within the elastic regime. The curves were analyzed within the contact region using the JKR model in order to extract the reduced Young's modulus. The combined height and modulus maps and histograms are shown in Fig. 9.

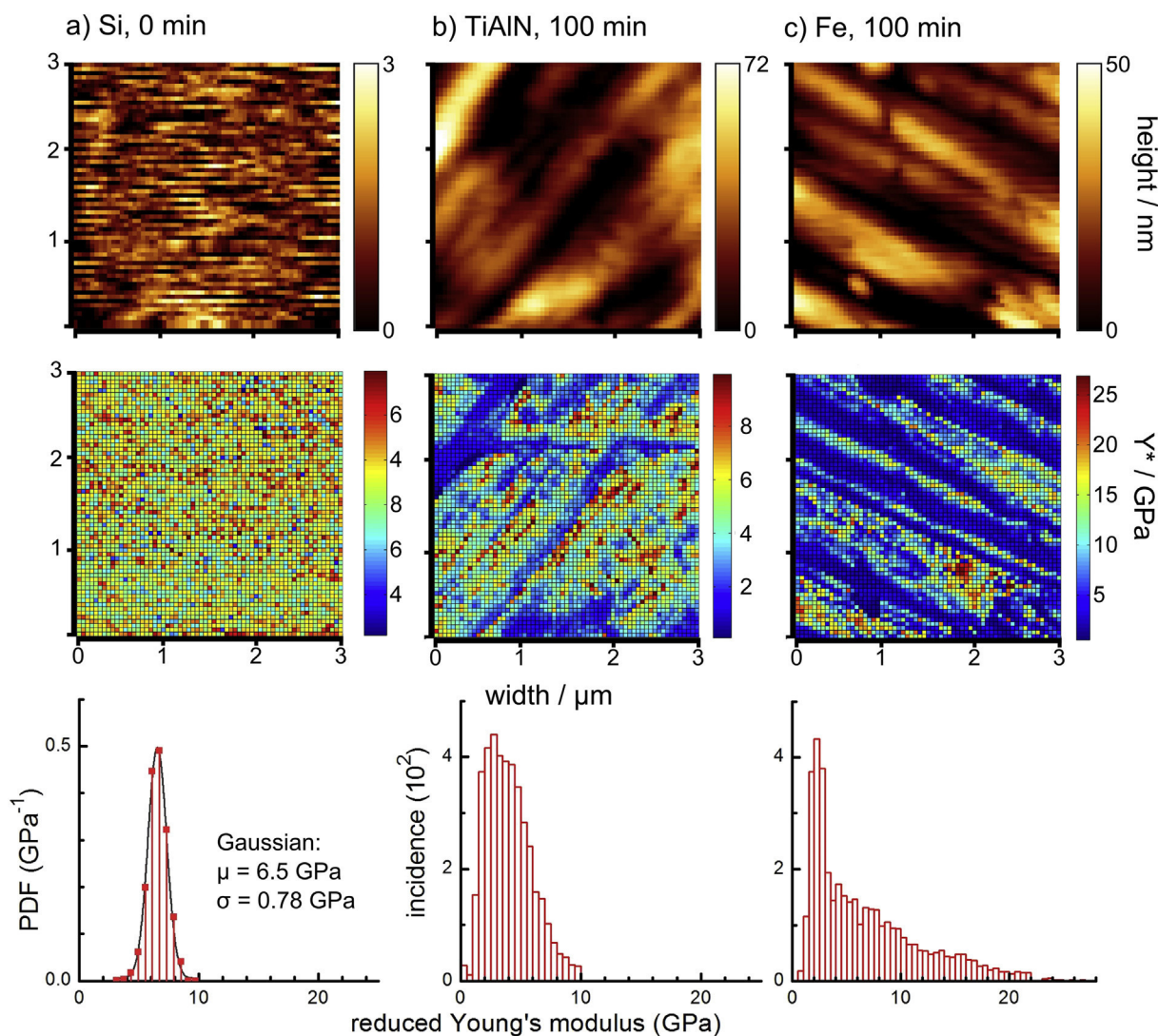


Fig. 9. Height and reduced Young's modulus maps and histograms measured with a SiO₂ tip on polycarbonate a) cleaved from Si wafer without prolonged heating treatment, b) cleaved from TiAlN|TiAl(O,N)|TiAlO and c) from Fe|Fe_xO_y after heating to 595 K for 100min. The fit of a Gauss distribution was included in the histogram of a).

In the case of polycarbonate stripped from a flat SiO₂ film covered Si wafer without prolonged heating treatment, the surface was flat, showed no patterning of the modulus and thereby a symmetric histogram, which could be fitted with a Gaussian typical for homogeneous surfaces. The residual uncertainty of the modulus most probably originates from slight deviations of the contact area and angle [74]. After heating in contact with TiAlN|TiAl(O,N)|TiAlO, the surface of the polycarbonate showed grooves due to adaption to the topography of the coating surface. Further, the histogram was no more symmetric but shifted to lower values. This decrease of the modulus is tentatively explained as a result of oligomer or head group enrichment at the interface, which is well known to affect AFM measurements [72]. It is noted that this finding is of relevance when considering that the adhesion encountered during the demolding process is expected to largely depend on the elastic properties of the polymer [75]. In contrast, the modulus after degradation at the Fe|Fe_xO_y interface showed both a decrease and an increase of elasticity as reflected by a long tailing to higher values. This interfacial toughening was especially observed within that regions of the polycarbonate surface, which were located in grooves on the iron substrate. In view of the fact that the polycarbonate is catalytically degraded at the Fe interface, this shows that the degradation reaction also involves cross-linking and that the degradation is kinetically enhanced in grooves due to confinement of the polycarbonate.

This finding is of high relevance for processing of polycarbonate melts, because at defect sites, where the melt is exposed to Fe, the formation of strongly adhering and toughened polycarbonate residuals is expected, which potentially deteriorate the molding process. Further, the confocal fluorescent background analysis might represent a valuable method for investigating such degradation structures with high lateral resolution.

4. Conclusions

The thermal degradation of polycarbonate was investigated at the TiAlN|TiAl(O,N)|TiAlO and Fe|Fe_xO_y interface in comparison to a Si|SiO₂ interface at 595 K. While no evidence of any specific structural change at the polycarbonate/SiO₂ interface covered substrates could be observed, infrared spectroscopy showed that the chemical structure of polycarbonate was not affected at the TiAlN|TiAl(O,N)|TiAlO interface, but the polycarbonate thin film restructured as indicated by a change of the carbonate group vibrations. In contrast, a degradation process including the formation of aromatic esters and anhydrides was observed after heating polycarbonate in contact with Fe|Fe_xO_y. Moreover, the onset of charring and yellow discoloration could be observed.

The analysis of the degradation process at the Fe|Fe_xO_y interface by means of in-situ confocal fluorescent background analysis revealed the formation of degradation products which diffuse into the bulk of molten polycarbonate. Due the high sensitivity and the high lateral and in-depth resolution, this method could represent a valuable tool to probe the chemical interaction between hard coatings and polymers prior to polymer processing.

The XPS analysis of the Fe|Fe_xO_y|polycarbonate interface showed that interaction of the molten polycarbonate with the Fe-oxide covered iron leads to the formation of Fe(II)-rich oxides. This can be explained by the reduced oxygen partial pressure at the interface. Consequently, organic Fe(II)-O complexes are likely to act as catalytic centers for the polymer degradation reaction. In contrast, the analysis of the TiAlN|TiAl(O,N)|TiAlO|polycarbonate interface disclosed essentially no chemical changes and demonstrated that unlike Fe_xO_y|Fe neither the hard coating nor the polycarbonate were significantly affected and only an additional incorporation of oxygen in the outer surface of the hard coating was

observed. In agreement with the findings concerning the interface and interphase chemistry, AFM revealed a small decrease of the surface elasticity of the polycarbonate at the TiAlN|TiAl(O,N)|TiAlO interface presumably due to enrichment of oligomers. Such a process was also observed in the case of Fe|Fe_xO_y, but the PC interphase was simultaneously locally toughened due to cross-linking, which was observed to be enhanced in grooves on the oxide covered iron surface due to local confinement of the polycarbonate. The results demonstrate that atmosphere exposed TiAlN hard coatings effectively hinder catalytic degradation of polycarbonate.

Acknowledgements

The authors acknowledge the financial support of the German Research Foundation within the project SFB-TR 87 sub projects A2 and A3.

Appendix A. Supplementary data

Supplementary data related to this article can be found at <http://dx.doi.org/10.1016/j.polymdegradstab.2017.07.013>.

References

- [1] E.J. Bienk, N.J. Mikkelsen, Application of advanced surface treatment technologies in the modern plastics moulding industry, *Wear* 207 (1–2) (1997) 6–9.
- [2] K. Bobzin, R. Nickel, N. Bagcivan, F.D. Manz, PVD—coatings in injection molding machines for processing optical polymers, *Plasma Process. Polym.* 4 (S1) (2007) S144–S149.
- [3] K. Bobzin, T. Brögelmann, G. Grundmeier, T. de los Arcos, M. Wiesing, N.C. Kruppe, (Cr,Al)N/(Cr,Al)ON Oxy-Nitride coatings deposited by hybrid dcMS/HPPMS for plastics processing applications, *Surf. Coat. Technol.* 308 (2016) 394–403.
- [4] F. Burmeister, C. Kohn, R. Kuebler, G. Kleer, B. Bläsi, A. Gombert, Applications for TiAlN- and TiO₂-coatings with nanoscale surface topographies, *Surf. Coat. Technol.* 200 (5–6) (2005) 1555–1559.
- [5] S. Kuhn, A. Burr, M. Kübler, M. Deckert, C. Bleesen, The reflectivity, wettability and scratch durability of microsurface features molded in the injection molding process using a dynamic tool tempering system, *J. Micromechanics Microengineering* 21 (2) (2011) 025024.
- [6] C. Kunze, D. Music, M. to Baben, J.M. Schneider, G. Grundmeier, Temporal evolution of oxygen chemisorption on TiAlN, *Appl. Surf. Sci.* 290 (2014) 504–508.
- [7] C. Gnoth, C. Kunze, M. Hans, M. to Baben, J. Emmerlich, J.M. Schneider, G. Grundmeier, Surface chemistry of TiAlN and TiAlNO coatings deposited by means of high power pulsed magnetron sputtering, *J. Phys. Appl. Phys.* 46 (8) (2013) 084003.
- [8] M. Wiesing, T. de los Arcos, G. Grundmeier, The thermal oxidation of TiAlN high power pulsed magnetron sputtering hard coatings as revealed by combined ion and electron spectroscopy, *Adv. Mater. Interfaces* (2017) 1600861.
- [9] D. Music, J.M. Schneider, Ab initio study of Ti_{0.5}Al_{0.5}N(001)—residual and environmental gas interactions, *New J. Phys.* 15 (7) (2013) 073004.
- [10] O. Hunold, M. Wiesing, T. de los Arcos, D. Music, G. Grundmeier, J.M. Schneider, Influence of O₂ exposure on the interaction between CH₄ and amorphous AlYB14, *Appl. Surf. Sci.* 392 (2017) 1165–1172.
- [11] I.B. Rufus, H. Shah, C.E. Hoyle, Identification of fluorescent products produced by the thermal treatment of bisphenol-A-based polycarbonate, *J. Appl. Polym. Sci.* 51 (9) (1994) 1549–1558.
- [12] A. Factor, Mechanisms of thermal and photodegradations of bisphenol A polycarbonate, in: *Polymer Durability: Advances in Chemistry*, vol. 249, American Chemical Society, 1996, pp. 59–76.
- [13] A. Rivaton, B. Mailhot, J. Soulestin, H. Varghese, J.L. Gardette, Comparison of the photochemical and thermal degradation of bisphenol-A polycarbonate and trimethylcyclohexane—polycarbonate, *Polym. Degrad. Stab.* 75 (1) (2002) 17–33.
- [14] S. Carroccio, P. Rizzarelli, D. Zampino, A snapshot of thermo-oxidative degradation products in poly(bisphenol A carbonate) by electrospray ionization mass spectrometry and matrix-assisted laser desorption ionization time of flight mass spectrometry, *Macromol. Chem. Phys.* 212 (24) (2011) 2648–2666.
- [15] S. Carroccio, C. Puglisi, G. Montaudo, Mechanisms of thermal oxidation of poly(bisphenol A carbonate), *Macromolecules* 35 (11) (2002) 4297–4305.
- [16] G. Montaudo, S. Carroccio, C. Puglisi, Thermal oxidation of poly(bisphenol A carbonate) investigated by SEC/MALDI, *Polym. Degrad. Stab.* 77 (1) (2002) 137–146.
- [17] M.C. Gupta, S.G. Viswanath, Role of metal oxides in the thermal degradation of

- bisphenol A polycarbonate, *J. Therm. Anal.* 46 (6) (1996) 1671–1679.
- [18] J. Mizuguchi, T. Shinbara, Disposal of used optical disks utilizing thermally-excited holes in titanium dioxide at high temperatures: a complete decomposition of polycarbonate, *J. Appl. Phys.* 96 (6) (2004) 3514–3519.
- [19] G. Sivalingam, K. Nagaveni, G. Madras, M.S. Hegde, Kinetics of catalytic degradation of polycarbonate in benzene, *Ind. Eng. Chem. Res.* 42 (4) (2003) 687–691.
- [20] A. Lagashetty, H. Vijayanand, S. Basavaraja, M.D. Bedre, A. Venkataraman, Preparation, characterization, and thermal studies of γ -Fe₂O₃ and CuO dispersed polycarbonate nanocomposites, *J. Therm. Anal. Calorim.* 99 (2) (2009) 577–581.
- [21] M. Blazsó, Thermal decomposition of polymers modified by catalytic effects of copper and iron chlorides, *J. Anal. Appl. Pyrolysis* 51 (1–2) (1999) 73–88.
- [22] M. Wiesing, M. to Baben, J.M. Schneider, T. de los Arcos, G. Grundmeier, Combined electrochemical and electron spectroscopic investigations of the surface oxidation of TiAlN HPPMS hard coatings, *Electrochim. Acta* 208 (2016) 120–128.
- [23] M. to Baben, M. Hans, D. Primetzhofer, S. Evertz, H. Ruess, J.M. Schneider, Unprecedented thermal stability of inherently metastable titanium aluminum nitride by point defect engineering, *Mater. Res. Lett.* 0 (0) (2016) 1–12.
- [24] Y. Zhang, H.J. Whitlow, T. Winzell, I.F. Bubb, T. Sajaara, K. Arstila, J. Keinonen, Detection efficiency of time-of-flight energy elastic recoil detection analysis systems, *Nucl. Instrum. Methods Phys. Res. Sect. B Beam Interact. Mater. At.* 149 (4) (1999) 477–489.
- [25] S. Hofmann, H.A. Jehn, Selective oxidation and chemical state of Al and Ti in (Ti, Al)_n coatings, *Surf. Interface Anal.* 12 (6) (1988) 329–333.
- [26] R.T. Haasch, T.-Y. Lee, D. Gall, J.E. Greene, I. Petrov, Epitaxial TiN(001) grown and analyzed in situ by XPS and UPS. II. Analysis of Ar⁺ sputter etched layers, *Surf. Sci. Spectra* 7 (3) (2000) 204–212.
- [27] J.M. Schneider, B. Hjörvarsson, X. Wang, L. Hultman, On the effect of hydrogen incorporation in strontium titanate layers grown by high vacuum magnetron sputtering, *Appl. Phys. Lett.* 75 (22) (1999) 3476–3478.
- [28] M. Morita, T. Ohmi, E. Hasegawa, M. Kawakami, M. Ohwada, Growth of native oxide on a silicon surface, *J. Appl. Phys.* 68 (3) (1990) 1272–1281.
- [29] C.J. Powell, A. Jablonski, NIST Electron Effective-attenuation-length Database, Version 1.3, National Institute of Standards and Technology, Gaithersburg, MD, 2011.
- [30] G. Hüttel, V. Klemm, R. Popp, F. Simon, E. Müller, Tailored colloidal AFM probes and their TEM investigation, *Surf. Interface Anal.* 33 (2) (2002) 50–53.
- [31] K.L. Johnson, K. Kendall, A.D. Roberts, Surface energy and the contact of elastic solids, *Proc. R. Soc. Lond. Math. Phys. Sci.* 324 (1958) (1971) 301–313.
- [32] M.C. Biesinger, B.P. Payne, A.P. Grosvenor, L.W.M. Lau, A.R. Gerson, R.S.C. Smart, Resolving surface chemical states in XPS analysis of first row transition metals, oxides and hydroxides: Cr, Mn, Fe, Co and Ni, *Appl. Surf. Sci.* 257 (7) (2011) 2717–2730.
- [33] S. Hofmann, Formation and diffusion properties of oxide films on metals and on nitride coatings studied with Auger electron spectroscopy and X-ray photoelectron spectroscopy, *Thin Solid Films* 193–194 (Part 2) (1990) 648–664.
- [34] I.leR. Strydom, S. Hofmann, XPS and EELS study of the valence band electronic structure of TiN and (Ti, Al)N coatings as influenced by the deposition parameters, *Vacuum* 41 (7–9) (1990) 1619–1623.
- [35] L. Porte, L. Roux, J. Hanus, Vacancy effects in the X-ray photoelectron spectra of $S_{\text{Ti}}(\text{Ti})_{\text{N}}$, *Phys. Rev. B* 28 (6) (1983) 3214–3224.
- [36] A. Arranz, C. Palacio, Screening effects in the Ti 2p core level spectra of Ti-Based ternary nitrides, *Surf. Sci.* 600 (12) (2006) 2510–2517.
- [37] G. Ketteler, S. Yamamoto, H. Bluhm, K. Andersson, D.E. Starr, D.F. Ogletree, H. Ogasawara, A. Nilsson, M. Salmeron, The nature of water nucleation sites on TiO₂(110) surfaces revealed by ambient pressure X-ray photoelectron spectroscopy, *J. Phys. Chem. C* 111 (23) (2007) 8278–8282.
- [38] R. Cremer, M. Witthaut, D. Neuschütz, Electron spectroscopy applied to metastable ceramic solution phases, *Fresenius J. Anal. Chem.* 365 (1–3) (1999) 28–37.
- [39] P. Prieto, R.E. Kirby, X-ray photoelectron spectroscopy study of the difference between reactively evaporated and direct sputter-deposited TiN films and their oxidation properties, *J. Vac. Sci. Technol. A* 13 (6) (1995) 2819–2826.
- [40] G. Greczynski, L. Hultman, Self-consistent modelling of X-ray photoelectron spectra from air-exposed polycrystalline TiN thin films, *Appl. Surf. Sci.* 387 (2016) 294–300.
- [41] A.J. Perry, On the existence of point defects in physical vapor deposited films of TiN, ZrN, and HfN, *J. Vac. Sci. Technol. A* 6 (3) (1988) 2140–2148.
- [42] D. Jaeger, J. Patscheider, A complete and self-consistent evaluation of XPS spectra of TiN, *J. Electron Spectrosc. Relat. Phenom.* 185 (11) (2012) 523–534.
- [43] I. Milošev, H.-H. Strehlow, B. Navinšek, M. Metikoš-Huković, Electrochemical and thermal oxidation of TiN coatings studied by XPS, *Surf. Interface Anal.* 23 (7–8) (1995) 529–539.
- [44] Z. Zhang, Y. Nie, L. Shen, J. Chai, J. Pan, L.M. Wong, M.B. Sullivan, H. Jin, S.J. Wang, Charge distribution in the single crystalline Ti₂AlN thin films grown on MgO(111) substrates, *J. Phys. Chem. C* 117 (22) (2013) 11656–11662.
- [45] T.M. Madkur, Polycarbonate, in: *Polymer Data Handbook*, Oxford University Press, 1999, p. 393.
- [46] A.S. Politou, C. Morterra, M.J.D. Low, Infrared studies of carbons. XII the formation of chars from a polycarbonate, *Carbon* 28 (4) (1990) 529–538.
- [47] J. Dybal, P. Schmidt, J. Baldrian, J. Kratochvíl, Ordered structures in polycarbonate studied by infrared and Raman spectroscopy, wide-angle X-ray scattering, and differential scanning calorimetry, *Macromolecules* 31 (19) (1998) 6611–6619.
- [48] P. Schmidt, J. Dybal, E. Turska, A. Kulczycki, Conformational structure of bisphenol A polycarbonate studied by infra-red spectroscopy, *Polymer* 32 (10) (1991) 1862–1866.
- [49] R.G. Kraus, E.D. Emmons, J.S. Thompson, A.M. Covington, Infrared absorption spectroscopy of polycarbonate at high pressure, *J. Polym. Sci. Part B Polym. Phys.* 46 (7) (2008) 734–742.
- [50] G. Apai, W.P. McKenna, Surface analysis of polycarbonate thin films by high-resolution electron energy loss spectroscopy. Negative ion resonances and surface vibrations, *Langmuir* 7 (10) (1991) 2266–2272.
- [51] A. Kulczycki, Calculation of the vibrational frequencies of crystalline bisphenol A polycarbonate, *Spectrochim. Acta Part Mol. Spectrosc.* 41 (12) (1985) 1427–1431.
- [52] F. L. B. O. de Oliveira, M.C.A.M. Leite, L.O. Couto, T.R. Correia, Study on bisphenol-A polycarbonates samples crystallized by acetone vapor induction, *Polym. Bull.* 67 (6) (2011) 1045–1057.
- [53] B.N. Jang, C.A.A. Wilkie, TGA/FTIR and mass spectral study on the thermal degradation of bisphenol A polycarbonate, *Polym. Degrad. Stab.* 86 (3) (2004) 419–430.
- [54] G. Socrates, *Infrared Characteristic Group Frequencies - Tables and Charts*, second ed., Wiley, 1980.
- [55] B. Montanari, P. Ballone, R.O. Jones, Density functional study of crystalline analogs of polycarbonates, *Macromolecules* 31 (22) (1998) 7784–7790.
- [56] S. Bahniwal, A. Sharma, S. Aggarwal, S.K. Deshpande, S.K. Sharma, K.G.M. Nair, Changes in structural and optical properties of polycarbonate induced by Ag⁺ ion implantation, *J. Macromol. Sci. Part B* 49 (2) (2010) 259–268.
- [57] A. Rivaton, Recent advances in bisphenol-A polycarbonate photodegradation, *Polym. Degrad. Stab.* 49 (1) (1995) 163–179.
- [58] M. Diepens, P. Gijmsman, Photodegradation of bisphenol A polycarbonate, *Polym. Degrad. Stab.* 92 (3) (2007) 397–406.
- [59] S. Hofmann, Auger- and X-Ray Photoelectron Spectroscopy in Materials Science, Springer, 2013.
- [60] T. Yamashita, P. Hayes, Analysis of XPS spectra of Fe²⁺ and Fe³⁺ ions in oxide materials, *Appl. Surf. Sci.* 254 (8) (2008) 2441–2449.
- [61] R.P. Gupta, S.K. Sen, Calculation of multiplet structure of core P -vacancy levels, *II. Phys. Rev. B* 12 (1) (1975) 15–19.
- [62] M.C. Burrell, J.J. Chera, Polycarbonate spin cast films by XPS, *Surf. Sci. Spectra* 6 (1) (1999) 1–4.
- [63] D. Briggs, G. Beamsom, XPS studies of the oxygen 1s and 2s levels in a wide range of functional polymers, *Anal. Chem.* 65 (11) (1993) 1517–1523.
- [64] G. Beamsom, D.T. Clark, N.W. Hayes, D.S.-L. Law, Effect of crystallinity on the XPS spectrum of poly(ethylene terephthalate), *Surf. Sci. Spectra* 3 (4) (1994) 357–365.
- [65] M.G. Rosmaninho, F.C.C. Moura, L.R. Souza, R.K. Nogueira, G.M. Gomes, J.S. Nascimento, M.C. Pereira, J.D. Fabris, J.D. Ardisson, M.S. Nazzarro, et al., Investigation of iron oxide reduction by ethanol as a potential route to produce hydrogen, *Appl. Catal. B Environ.* 115–116 (2012) 45–52.
- [66] R. Gustus, L. Wegewitz, S. Sedelmeier, O. Höfft, J. Wieser, M. Rehahn, F. Endres, W. Maus-Friedrichs, Monolayer deposition of bisphenol A polycarbonate oligomers on Au(111), *J. Phys. Chem. C* 119 (1) (2015) 228–233.
- [67] C. Seidel, H. Kopf, B. Gotsmann, T. Vieth, H. Fuchs, K. Reihls, Ar plasma treated and Al metallised polycarbonate: a XPS, Mass Spectrosc. SFM Study, *Appl. Surf. Sci.* 150 (1–4) (1999) 19–33.
- [68] F. Bonnet, F. Ropital, P. Lecour, D. Espinat, Y. Huiban, L. Gengembre, Y. Berthier, P. Marcus, Study of the oxide/carbide transition on iron surfaces during catalytic coke formation, *Surf. Interface Anal.* 34 (1) (2002) 418–422.
- [69] J.K. Heuer, J.F. Stubbins, An XPS characterization of FeCO₃ films from CO₂ corrosion, *Corros. Sci.* 41 (7) (1999) 1231–1243.
- [70] D. Briggs, J.T. Grant, *Surface Analysis by Auger and X-Ray Photoelectron Spectroscopy*, IMPublications and SurfaceSpectra, Chichester and Manchester, 2003.
- [71] R.A.L. Jones, R.W. Richards, *Polymers at Surfaces and Interfaces*, Cambridge University Press, 1999.
- [72] K. Tanaka, A. Takahara, T. Kajiyama, Effect of polydispersity on surface molecular motion of polystyrene films, *Macromolecules* 30 (21) (1997) 6626–6632.
- [73] T. Tsuchida, H. Takahashi, X-ray photoelectron spectroscopic study of hydrated aluminas and aluminas, *J. Mater. Res.* 9 (11) (1994) 2919–2924.
- [74] H. Wagner, D. Bedorf, S. Kuchemann, M. Schwabe, B. Zhang, W. Arnold, K. Samwer, Local elastic properties of a metallic glass, *Nat. Mater.* 10 (6) (2011) 439–442.
- [75] O.K.C. Tsui, X.P. Wang, J.Y.L. Ho, T.K. Ng, X. Xiao, Studying surface glass-to-rubber transition using atomic force microscopic adhesion measurements, *Macromolecules* 33 (11) (2000) 4198–4204.

Thermal degradation of molten polycarbonate at iron oxide and TiAlN hard coating interfaces

Supplementary Information

M. Wiesing, T. de los Arcos, M. to Baben, H. Rueß, J. M. Schneider, G. Grundmeier

Technical and Macromolecular Chemistry, University of Paderborn, Warburger Straße 100, 33098 Paderborn, Germany

Materials Chemistry, RWTH Aachen University, Aachen, Germany

Correspondence to: Guido Grundmeier (E-mail: guido.grundmeier@tc.uni-paderborn.de)

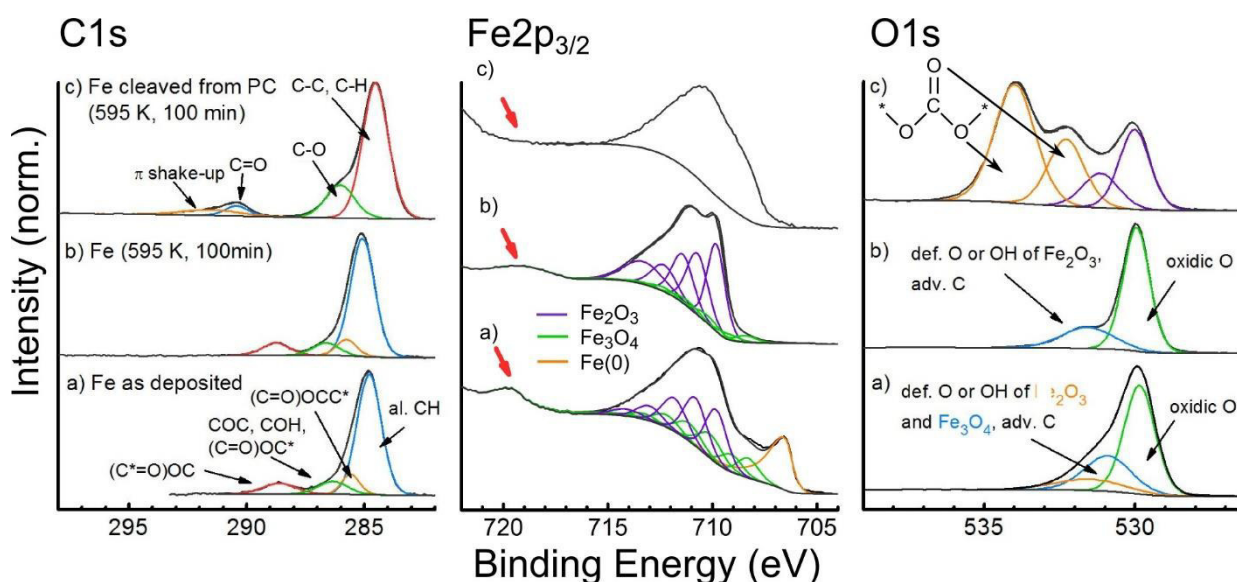


FIGURE S1: High resolution XPS element spectra of **a)** Fe after deposition, **b)** Fe heated at 595 K for 100 min and **c)** Fe cleaved from polycarbonate after heating at 595 K for 100 min. The spectra were normalized and shifted vertically for better visualization. The characteristic multiplet shake-up of Fe(III) is highlighted with a red arrow in the Fe2p_{3/2} spectrum.

As shown in FIGURE S1a, the C1s spectrum of the iron sample after deposition and exposure to atmosphere showed the typical line shape for adventitious carbon contaminations and was decomposed using four components with their chemical shifts taken from average values for polymers.¹ The component located at 284.7 eV could be thus assigned to aliphatic C-H, the component at 285.5 eV to the alpha carbon of esters C*COOC, the component at 286.3 eV to C-O of esters, ethers and alcohols and the component at 288.6 eV to the C=O of esters.

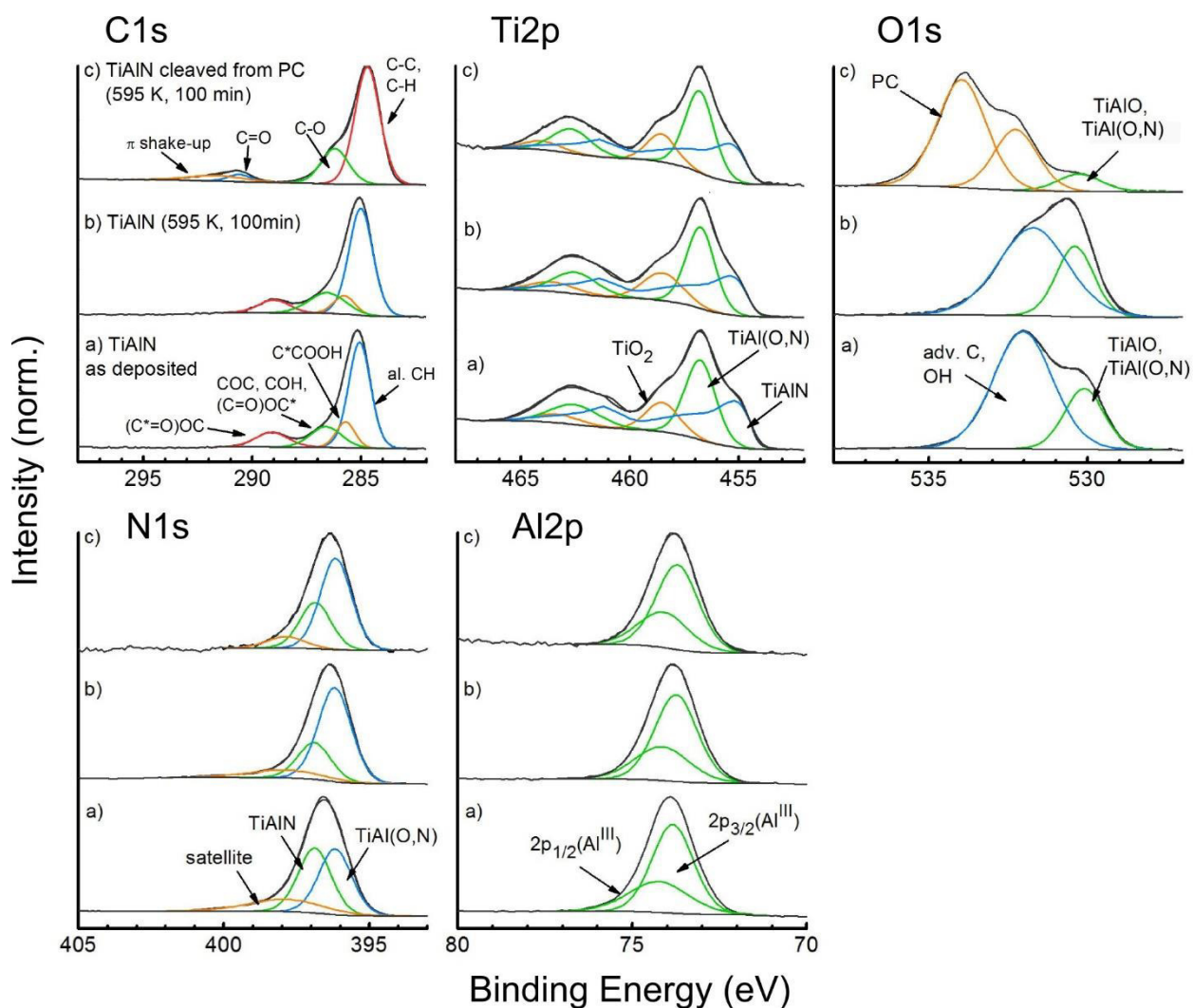


FIGURE S2: High-resolution XPS of TiAlN **a)** as deposited and atmosphere exposed, **b)** after heating to 595 K for 100 min and **c)** after heating to 595 K for 100 min in contact with polycarbonate and cleavage. The spectra were normalized and shifted vertically for better clarity.

FIGURE S2 shows the core level spectra of TiAlN as deposited, after heating and after heating and cleavage from polycarbonate. The C1s, Ti2p and O1s spectra were already discussed in the main text. The N1s spectrum was described using three components located at 397.7, 396.7 and 396.0 eV. The component at 396.7 eV was ascribed to TiAlN and that at 396.0 eV is assigned to oxynitride and was increased due to heating.^{2,3} This is consistent increase of the oxynitride signal in the Ti2p spectrum and indicates similarly that the TiAlN substrate is slightly oxidized to form oxynitride during the heating treatment.

The Al2p spectrum was described by two components located at 73.7 and 74.1 eV and ascribed to the 2p_{3/2} and 2p_{1/2} transition of Al(III). A more precise assignment is not attempted due to the very similar binding energies of Al within a nitridic or oxidic environment.⁴

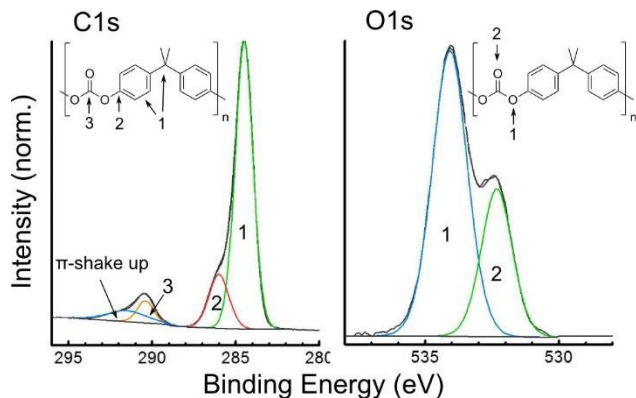


FIGURE S3: High-resolution XPS of the C1s and O1s spectra of a 40 nm polycarbonate reference sample spin cast on Si wafer. No neutralization was required during spectral acquisition.

REFERENCES AND NOTES

- (1) Briggs, D.; Grant, J. T. *Surface Analysis by Auger and X-Ray Photoelectron Spectroscopy*; IMPublications and SurfaceSpectra: Chichester and Manchester, 2003.
- (2) Arranz, A.; Palacio, C. Screening Effects in the Ti 2p Core Level Spectra of Ti-Based Ternary Nitrides. *Surf. Sci.* **2006**, *600* (12), 2510–2517.
- (3) Prieto, P.; Kirby, R. E. X-ray Photoelectron Spectroscopy Study of the Difference between Reactively Evaporated and Direct Sputter-deposited TiN Films and Their Oxidation Properties. *J. Vac. Sci. Technol. A* **1995**, *13* (6), 2819–2826.
- (4) Gnoth, C.; Kunze, C.; Hans, M.; Baben, M. to; Emmerlich, J.; Schneider, J. M.; Grundmeier, G. Surface Chemistry of TiAlN and TiAlNO Coatings Deposited by Means of High Power Pulsed Magnetron Sputtering. *J. Phys. Appl. Phys.* **2013**, *46* (8), 084003.

4.4 Lifshitz analysis of dispersion forces based on quantitative Reflection Electron Energy Loss Spectroscopy

The manuscript was reproduced from the following publication:

Lifshitz analysis of dispersion forces based on quantitative Reflection Electron Energy Loss Spectroscopy

Wiesing, M., Grundmeier, G.

Journal of Colloid and Interface Science, 514, 625-633, 2018, doi:10.1016/j.jcis.2017.12.069

Copyright © 2018, Elsevier Inc.

Author contributions:

- Planning/experimental work/interpretation/manuscript preparation **MW**
- Proof reading **GG**

Placement:

Polymer surfaces have typically low energies and predominantly interact by van der Waals forces. Moreover, nitridic hard coatings are highly polarizable metallic systems and this should even more increase the relevance of this type of force interactions. Therefore, a new spectroscopic approach is developed in the here presented study to predict van der Waals forces based on optical data with a surface sensitivity of a few nanometres and with an unprecedented accuracy. This method is key for understanding the origin of adhesion at the hard coating/polymer interface, because it allows to decompose experimental adhesion forces into individual force contributions and thereby to quantitatively assess the role of the van der Waals forces. Moreover, the effect of thin surface oxide layers on the adhesion can be directly studied and van der Waals force interactions can be predicted for arbitrary polymer-coating interactions. It is highlighted that especially the latter aspect enables a rational design of hard coatings. For these reasons, the here presented method is used in publications 5 and 6 to analyse experimental interaction forces.



Regular Article

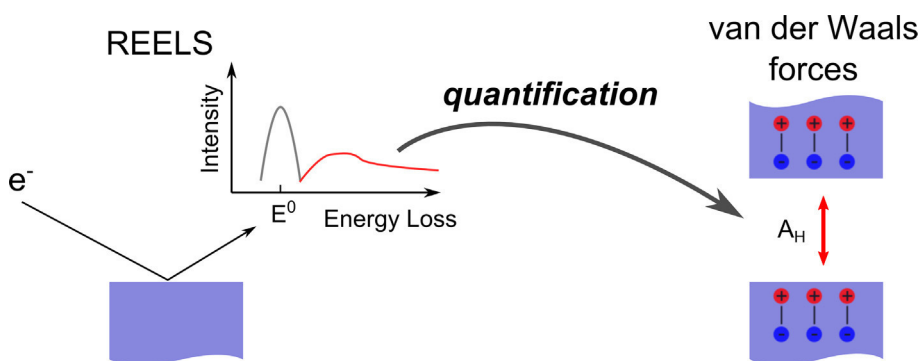
Lifshitz analysis of dispersion forces based on quantitative reflection electron energy loss spectroscopy

M. Wiesing*, G. Grundmeier

Technical and Macromolecular Chemistry, University of Paderborn, Warburger Straße 100, 33098 Paderborn, Germany



GRAPHICAL ABSTRACT



ARTICLE INFO

Article history:

Received 19 September 2017

Revised 22 December 2017

Accepted 26 December 2017

Available online 27 December 2017

Keywords:

Lifshitz

Hamaker constant

REELS

QUEELS

Energy loss

Retardation

ABSTRACT

Hypothesis: The energy loss experienced by an electron while moving through a solid is determined by the optical properties of the surrounding. Hence, quantitative Reflection Electron Energy Loss Spectroscopy (REELS) should allow the determination of optical data required for the calculation of Hamaker coefficients using Lifshitz theory. This approach might improve the accuracy of calculated Hamaker coefficients and should also enable to harness the unique capabilities of REELS to analyse nanostructured surfaces and thin-films with great spatial resolution and surface sensitivity.

Experiments: REELS spectra of a survey of insulating polymers and of metal-like $\text{Ti}_{0.23}\text{Al}_{0.32}\text{N}_{0.44}$ (TiAlN) were measured, the complex dielectric functions determined and the corresponding Hamaker coefficients across vacuum and water calculated. The sensitivity of the quantification procedure towards typical systematic errors was investigated. For polystyrene the results were comparatively analysed using vacuum ultraviolet spectroscopy (VUV).

Findings: The accuracy especially of the non-retarded vacuum Hamaker constants of the polymers was increased when compared to VUV reflectance spectroscopy due to the higher spectral range of REELS. Furthermore, a new correction procedure for the intricate case of unresolved inelastic losses in the REELS spectrum, such as encountered in the case of TiAlN, could be developed using spectroscopic ellipsometry as a complementary mean.

© 2018 Elsevier Inc. All rights reserved.

* Corresponding author.

E-mail address: wiesing@mail.upb.de (M. Wiesing).

1. Introduction

Dispersive interactions are of pivotal importance for understanding a wide range of complex systems and physical phenomena such as biological systems and colloids, polymer surfaces and interfaces, premelting processes and interphase formation, molecular electronic devices, wetting, contact deformation and adhesive phenomena [1–10]. An elaborate theoretical framework has thus been developed for the determination of the dispersion forces acting between two bodies based on the optical properties of the materials involved [11–13]. In this view, dispersion forces are governed by electromagnetic fluctuation forces spanning a wide range of energies ranging from around 0 eV to several tens eV. Thus, only few experimental methods can provide the optical data required for quantification within an adequate energy range. Among these, electron energy loss spectroscopy (EELS) represents a promising method due to its extended energy range and high spatial resolution. However, due to the complex physics of the reflection geometry a practical application of EELS for dispersion force analysis has been mostly limited to the transmission geometry as realized in transmission electron microscopes (TEM) [14,15].

Recently, the quantitative analysis of reflection electron energy loss spectra (REELS) has become a routine method with the development of the QUEELS- $\epsilon(\omega, k)$ -REELS software package by Tougaard and Yubero [16–19]. The formalism is based on the description of a moving electron within a material and across its surface within a dielectric response model. As a result, the quantitative analysis of the REELS spectra yields the complex dielectric function required for determining Hamaker constants by Lifshitz theory [15–18]. It is noted that due to the reflection geometry used in REELS further unique advantages emerge: standard Auger setups can be used for the measurement of REELS spectra and thereby a high spatial resolution could be easily realized. Further, the surface sensitivity is in the range of around 1 to 10 nm due to the low energies used and can be adjusted by the primary beam energy. In contrast to EELS performed in a TEM, the use of low energies also enables the non-destructive analysis of sensitive materials such as polymers [20]. Another distinct advantage is that the dielectric function $\epsilon(\omega, k)$ is obtained as a function of both the frequency ω and the wave vector k . This comprehensive description is a prerequisite for the consideration of additional non-local effects in dispersive interactions emerging at low distances [21–23].

In this view, the present work investigates the applicability of REELS for dispersion force analysis using TiAlN and different polymers (polycarbonate, polystyrene, syndiotactic polypropylene and a polysiloxane like plasma polymer). This includes the calculation of non-retarded Hamaker constants and the comparison with constants derived by vacuum ultraviolet spectroscopy. Apart from that, the relevance of inaccuracies within the highly non-linear evaluation scheme of the REELS spectra for the quality of the calculated Hamaker constants is assessed. In this regard, a correction procedure is developed for the intricate case of REELS spectra where inelastic and elastic parts largely overlap.

2. Experimental

2.1. Thin film deposition

TiAlN thin films with a thickness of around 1.2 μm were deposited by reactive High Power Pulsed Magnetron Sputtering (HPPMS) using a CC-800/9 (Cemecon) at a base pressure better than 0.2 mPa. The system was equipped with a rectangular magnetron and a $\text{Ti}_{0.5}\text{Al}_{0.5}$ compound target. The p-Si(0 0 1) substrates (1–5 Ωcm) were mounted at a distance of 80 mm in front of the target and were at floating potential. Reactive sputtering was performed in an Ar/N₂ atmosphere (200/50 sccm) using a HPPMS generator

(Melec) with a frequency of 800 Hz, a duty cycle of 4% and a time-averaged power of 3 kW corresponding to a peak power density of 450 W cm^{-2} . As determined by X-ray Photoelectron Spectroscopy (XPS) on an Ar⁺ sputter etched sample (15 $\mu\text{A cm}^{-2}$, 7 min), the stoichiometry of was $\text{Ti}_{0.22}\text{Al}_{0.32}\text{N}_{0.43}\text{O}_{0.02}$.

Polystyrene (192 kDa, SigmaAldrich) and polycarbonate (Macrolon 3108, 31 kDa, Goodfellow) thin films (PS, PC) were deposited on Si(1 0 0) wafers by spin-coating from 2 w% PS/toluene and PC/1,4-dioxane solutions using a rotational speed of 2000 rpm for 60 s and an acceleration of 1000 rpm s^{-1} . The solvents were of analytical grade and the polymers free of additives. Syndiotactic polypropylene (sPP) was deposited by spin-coating from a 0.47 w% sPP/xylene solution at 50 °C after stirring at 95 °C for 5 h. The substrate was spun at 3000 rpm for 60 s using an acceleration of 1000 rpm s^{-1} [24]. The surfaces were characterized by XPS and showed the typical properties of the polymers (see supporting information). Additionally, a plasma polymer thin film based on hexamethyldisiloxane (PP-HMDSO) was deposited on a Si(1 0 0) wafer using a custom audio frequency reactor. The deposition was performed at a total pressure of 30 Pa with an Ar/HMDSO ratio of 6 and at a voltage of 440 V corresponding to an energy density of 0.03 W cm^{-2} . The PP-HMDSO film was characterized by infrared spectroscopy and XPS and was composed of a mixture of Si-H, Si-CH_x and Si-O-Si groups (see supporting information).[25] As determined by spectroscopic ellipsometry using tabulated optical constants, all thin films were around 60 nm thick (optical properties of PP-HMDSO were approximated by those of polydimethylsiloxane) except for the sPP film of which the thickness was 30 nm.

2.2. Ellipsometry

Spectroscopic ellipsometry was measured using a nulling ellipsometer (Nanofilm Ep3, Accurion, Germany) within a spectral range of 363–996 nm and at a resolution of around 10 nm. The angle of incidence was 50° relative to the surface normal. The optical data in form of the energy loss function was fitted with Drude Lindhard oscillators in the optical limit (see supporting information) using Matlab (Mathworks Inc.).

2.3. REELS

REELS was measured using a Nanofocus 50 electron gun (StaiB Instruments, Germany) at primary energies of 1500 eV (TiAlN) and 450 eV (polymer thin films). The energy resolution was 1.0 eV and the beam was scanned during the measurement across an area of 0.07 mm^2 resulting into a current density of 0.44 $\mu\text{A cm}^{-2}$. The depths of information corresponding to 3λ , where λ is the Inelastic Mean Free Path (IMFP), were 2.7 nm (TiAlN) and 0.9–1.3 nm (polymers). The energy loss was measured up to 70 eV (polymer samples) or 150 eV (TiAlN). The angle of incidence α and the angle of detection θ were 30 degree relative to the surface

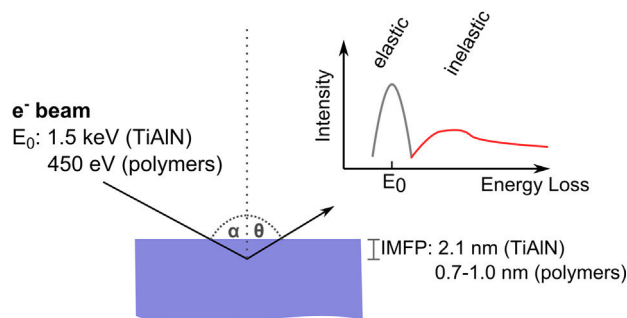


Fig. 1. Illustration of the REELS measurements performed on the surfaces of TiAlN and the different polymers (PS, PC, sPP, PP-HMDSO).

normal. The experimental setup is schematically shown in Fig. 1. The TiAlN surface was sputter cleaned before spectroscopy using a 3 kV Ar⁺ ion beam (15 $\mu\text{A cm}^{-2}$, 7 min). For the measurement on the polymer samples, the sample was continuously moved during the measurement in order to limit the dose to 7.1 $\mu\text{C cm}^{-2}$ and thereby to avoid beam damage [20]. The REELS data were evaluated using the QUEELS- $\epsilon(\omega, k)$ -REELS software package from Tougaard and Yubero [16–19]. For the correction of the cross section λK of TiAlN the loss spectrum was deconvoluted using the option “One spectrum without the elastic peak”. The elastic peak area was then adjusted by adjusting the parameter LK_Area.

3. Results and discussion

3.1. REELS based Lifshitz analysis of dispersion forces

In the following, the procedure of the REELS based analysis of dispersion forces using Lifshitz theory is outlined. In the first step, the REELS spectrum of a material is measured and quantitatively analysed using the QUEELS- $\epsilon(\omega, k)$ -REELS software package to give the optical data of the sample in form of the complex dielectric function ϵ . This data is then used for the calculation of non-retarded Hamaker constants and retarded Hamaker coefficients using Lifshitz theory.

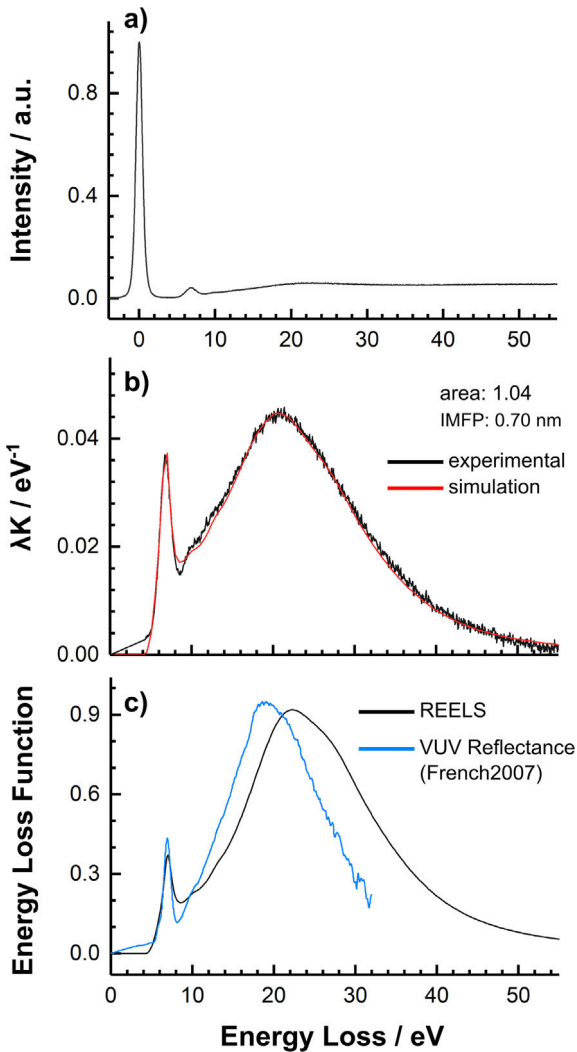


Fig. 2. (a) REELS spectrum, (b) experimental and simulated single electron scattering cross section λK of PS and (c) Energy Loss Function in comparison with values taken from French et al. [28].

Fig. 2 illustrates this quantification procedure at the example of PS. The experimental REELS spectrum (see Fig. 2a) was characterized by the presence of an elastic peak at an energy loss of 0 eV and by an inelastic loss region at higher energy losses. The inelastic loss region is a consequence of the scattering of electrons by optical transitions of the PS. The quantification therefore involves first the separation of the elastic peak from the inelastic region using the ELPSEP algorithm, which assumes a nearly symmetrical shape of the elastic peak [26]. The so obtained inelastic spectrum is then numerically deconvoluted in order to correct for multiple scattering events of the electrons and to determine the experimental single electron scattering cross section λK according to [26,27]

$$\lambda K(i) = \frac{j_i(i_p - i) - \sum_{m=1}^{i-1} \lambda \cdot K(i - m) \cdot j_i(i_p - m) \cdot E_{\text{step}}}{A_p} \quad (1)$$

where λ is the Inelastic Mean Free Path (IMFP) at the primary beam energy, A_p is the area of the elastic peak, E_{step} the energy separation of the single channels, j_i the intensity of channel i of the loss spectrum and $K(i)$ is the probability of an electron at the primary beam energy to lose iE_{step} energy per unit energy loss and travelled path length. The index i is zero for the lowest kinetic energy (highest energy loss) and i_p for the elastic peak channel. The experimentally determined single electron scattering cross section λK of PS is shown in Fig. 2b. It was observed that the cross section approaches zero at high energy losses of around 50 eV. Consequently, it follows that the spectral range covered by the REELS spectrum was sufficiently high and not limited at high energy losses, which is a prerequisite for an accurate quantification as discussed below. In accordance with that, the total area of the cross section was close to the theoretically expected value of one.

The experimental cross section λK was then used to determine the corresponding optical data in form of a parameterised empirical dielectric function ϵ . It is highlighted that no spectral components are fit to the λK spectrum within this quantification step in order to describe the overall lineshape but rather a theoretical cross section λK is simulated based on an empirically chosen dielectric function ϵ . The empirical parameters of the dielectric function are then varied until an optimal agreement between the simulated and experimental cross sections is found (see Fig. 2b). For the following discussion it is also important to note that the dielectric function is rescaled according to the Kramers-Kronig (KK) sum rule

$$\frac{2}{\pi} \int_0^{\infty} \text{Im} \left\{ -\frac{1}{\epsilon(\omega, k)} \right\} \frac{d\omega}{\omega} = 1 - \frac{1}{n^2} \quad (2)$$

where ω is the radial frequency, k the wave vector, $\text{Im}(-1/\epsilon(\omega, k))$ the energy loss function (ELF) and n the refractive index in the optical limit, which was 1.6 for PS.

Non-retarded Hamaker constants and retarded Hamaker coefficients were calculated according to the theory of Dzyaloshinskii, Lifshitz and Pitaevskii from the dielectric functions $\epsilon(\omega, 0)$ as determined by REELS [13]. The complex part of the dielectric function ϵ'' was obtained after performing a Kramers-Kronig transformation of the ELF using the build-in facilities of the QUEELS- $\epsilon(\omega, k)$ -REELS software package. The function ϵ'' was then converted to imaginary frequencies $i\xi_n$ according to the Kramers-Kronig transform [13]

$$\epsilon(i\xi_n) = 1 + \frac{2}{\pi} \int_0^{\infty} \frac{\omega \epsilon''(\omega, 0)}{\omega^2 + \xi_n^2} d\omega \quad (3)$$

with ω being the radial frequency and ξ_n being the discrete Matsubara frequencies as defined by

$$\xi_n = \frac{2\pi kT}{\hbar} n \quad (4)$$

The non-retarded Hamaker constants were calculated within the limit of distances approaching contact using [13]

$$A_h = \frac{3}{2} kT \sum_{l=0}^{\infty} \sum_{q=1}^{\infty} \frac{(\Delta_{Am} \Delta_{Bm})^q}{q^3} \quad (5a)$$

$$\Delta_{jm} = \frac{\varepsilon_j - \varepsilon_m}{\varepsilon_j + \varepsilon_m} \quad (5b)$$

where the stroke indicates that the first term of the sum is multiplied by 0.5. Hamaker coefficients including retardation effects were calculated for the geometry of two separated half-spaces according to [13]

$$A_h(d) = -\frac{3}{2} kT \sum_{n=0}^{\infty} \int_{r_n}^{\infty} x \ln[(1 - \bar{\Delta}_{Am} \bar{\Delta}_{Bm} e^{-x})(1 - e^{-x})] dx \quad (6a)$$

$$\bar{\Delta}_{im} = \frac{x_m \varepsilon_i - x_i \varepsilon_m}{x_m \varepsilon_i + x_i \varepsilon_m} \quad (6b)$$

$$x_i^2 = x_m^2 + \left(\frac{2l \xi_n}{c} \right)^2 (\varepsilon_i - \varepsilon_m), x_m = x \quad (6c)$$

$$r_n = \frac{2l \sqrt{\varepsilon_m} \xi_n}{c} \quad (6d)$$

where r_n is the pertinent ratio, which accounts for retardation, and l represents the distance. It is noted that for metallic materials (TiAlN) the limit of Eq. (6) for $n = 0$ implies $\bar{\Delta}_{im} \rightarrow 1$. For a proper numerical evaluation of this boundary, $\bar{\Delta}_{im}$ was therefore defined to 1 within the used algorithm. The intervening medium m was vacuum or water. In the latter case the spectral data was taken from literature [29].

The effect of retardation on the dispersive interactions can be represented by the correction factor f according to

$$A_h^{\text{retarded}} = f A_h^{\text{non-retarded}} \quad (7)$$

where A_h^{retarded} and $A_h^{\text{non-retarded}}$ represent Hamaker constants calculated with and without including the effect of retardation according to Eqs. (5) and (6).

3.2. Optical and dispersive properties of PS

The experimental and simulated cross sections λK of PS are shown in Fig. 2b and an excellent agreement was found indicating that the empirical optical data well represent the optical properties of the PS. Thus, the ELF could be calculated from the oscillator parameters and is shown in Fig. 2c in comparison with ELF data derived from VUV reflectance spectra reported elsewhere [28]. According to the peak energies of the oscillators (see the supporting information for the optical data of all materials investigated), the REELS-based ELF was characterized by a peak at 7.0 eV and the broad bulk plasmon centred at 22.3 eV with shoulders located around 10, 13 and 27 eV. The peak at 7.0 eV was associated with the π - π^* transition, the hump at 10 eV with the n - π^* and n - σ^* transitions and the residual higher energy peaks with σ - σ^* transitions [28]. The comparison of both ELFs shows a good agreement of the magnitudes and a high resemblance at lower energies below 10 eV. However, significant differences were found at higher energies and the energy scale of the VUV based ELF appears to be compressed. Though the precise origin of these discrepancies remains unclear, it is noted that the accuracy of optical data based on VUV reflectance measurements is affected at higher energies by the use of artificial wings extending the spectral range [9]. In contrast, REELS can be measured with great accuracy to cover the

whole energy range of interest and no wings are required. In consequence, especially the higher energy oscillators are thus expected to show an increased accuracy.

The relevance of a higher accuracy of the REELS-derived dielectric function in the higher energy range for the calculation of Hamaker coefficients is discussed in the following. Table 1 shows non-retarded Hamaker constants calculated within the limit of short distances for the symmetric contact PS|medium|PS with the intervening medium being vacuum (A_h^{vac}) or water ($A_h^{\text{H}_2\text{O}}$). It was found that the Hamaker constant of PS across vacuum was increased by around 40% from 63 to 90 zJ ($\text{zJ} = 10^{-21} \text{ J}$) when using the REELS based spectral data instead of the optical data derived from VUV reflectance [28]. This highlights that higher energy oscillators can significantly contribute to the overall dispersive interactions and also that REELS represents an alternative approach for dispersion force analysis.

3.3. Dispersive properties of PC, sPP and PP-HMDSO

In order to further validate the REELS-based approach for the analysis of dispersion forces based on Lifshitz theory, different polymers including polycarbonate (PC), syndiotactic polypropylene (sPP) and a hexamethyldisiloxane based plasma polymer (PP-HMDSO) as a non-polar reference material with properties similar to polydimethylsiloxane were investigated. The corresponding experimental and simulated cross sections λK as well as the ELFs are shown in Fig. 3 (see the supporting information for the REELS spectra) and again an excellent agreement of the cross sections was observed indicating that the empirical optical data well reflects the optical properties of the investigated polymers. The ELF of polycarbonate was characterized by the joined $\sigma + \pi$ plasmon around 22 eV and by a loss peak around 7 eV, which is ascribed to π - π^* transitions in agreement with the ELF of PS. In comparison, only a broad plasmon loss structure around 21 eV was observed in the case of sPP and PP-HMDSO, which is in accordance with the decreased polarizabilities of these polymers.

The non-retarded Hamaker constants of the polymers were calculated and are presented in Table 1. When comparing the Hamaker constants of PS and PC across vacuum, it was found that they were basically identical and amounted around 90 zJ. This finding is in agreement with the similar optical properties of the polymers, which are both characterized by transitions of unsaturated and saturated C bonds, and is also supported by literature where the values for the constants of PS (50.8 zJ) and PC (55.6 zJ) also differ only slightly [9].

In comparison to PS and PC, the Hamaker constant of sPP across vacuum was 77 zJ and that of PP-HMDSO around 51 zJ. This interestingly shows that the absence of π -electrons in the sPP decreases the polarizability of the polymer and consequently the also the vacuum Hamaker constant. However, this decrease is limited to

Table 1

Non-retarded Hamaker constants calculated for the symmetric material|medium|material case with the intervening medium being vacuum (A_h^{vac}) or water ($A_h^{\text{H}_2\text{O}}$).

Material	$A_h^{\text{vac}}/10^{-21} \text{ J}$	$A_h^{\text{H}_2\text{O}}/10^{-21} \text{ J}$
PS	90	11.2
PC	92	12.0
sPP	77	7.6
PP-HMDSO	51	3.4
TiAlN	220	100
Optical data from VUV reflectance		
PS [28]	63	5.5
Effect of inaccurate spectral data		
PS (limited spectral range)	86	10.1
PS (refractive index of 2)	160	44
TiAlN (uncorrected λK)	244	117

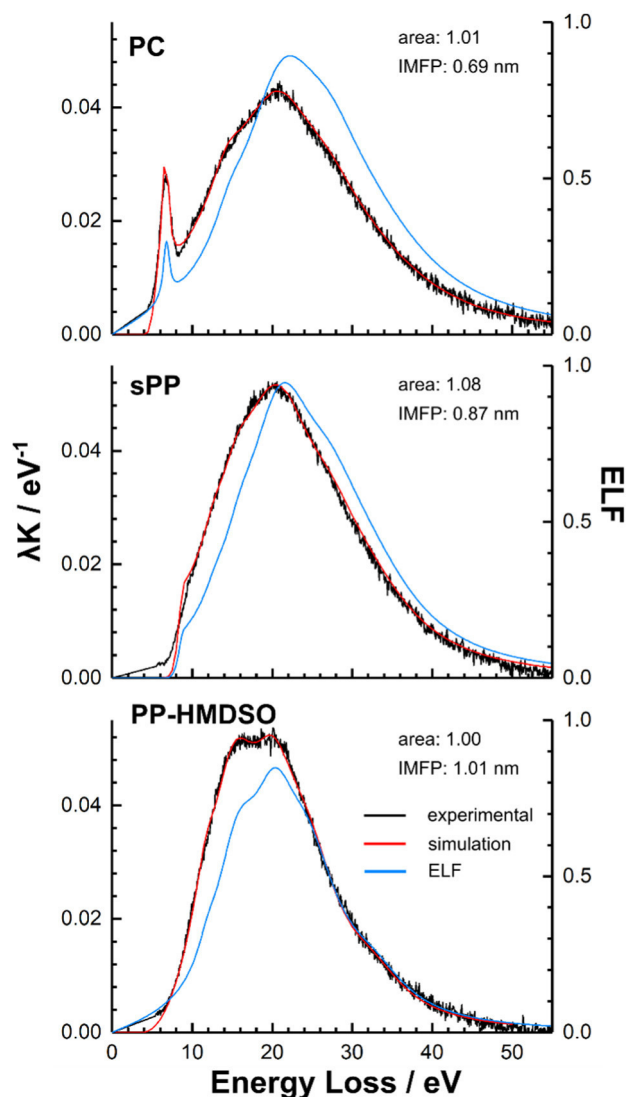


Fig. 3. Experimental and simulated scattering cross sections λK and ELFs of PC, sPP and PP-HMDSO as determined by REELS.

around 15% and it thus follows that the dispersive properties of PS and PC in vacuum are governed by high energy transitions related to the σ -electrons. In this regards, the low vacuum Hamaker constant found for PP-HMDSO indicates an even more decreased polarizability of the polymer, which is in accordance with the low surface energy of the chemically related polydimethylsiloxane [5].

This situation was slightly different in the case of water being the intervening medium and Hamaker constants of 12.0 (PC), 11.2 (PS), 7.6 (sPP) and 3.4 zJ (PP-HMDSO) were found. In this case an overall decrease was observed and the differences among the polymer Hamaker constants were more pronounced than across vacuum. Since water has a high band gap of around 7 eV, this can be rationalized to be the result of the screening of the interactions by water especially at higher energies. As a consequence, the individual optical properties of the polymers in the low energy range are reflected more directly in the related Hamaker constants.

Retarded Hamaker coefficients were also calculated for the geometry of two separated half-spaces and the corresponding correction factors f are presented in Fig. 4. It was found that the correction factor across vacuum dropped to around 10–15% at a distance of 200 nm for all materials investigated and only slight

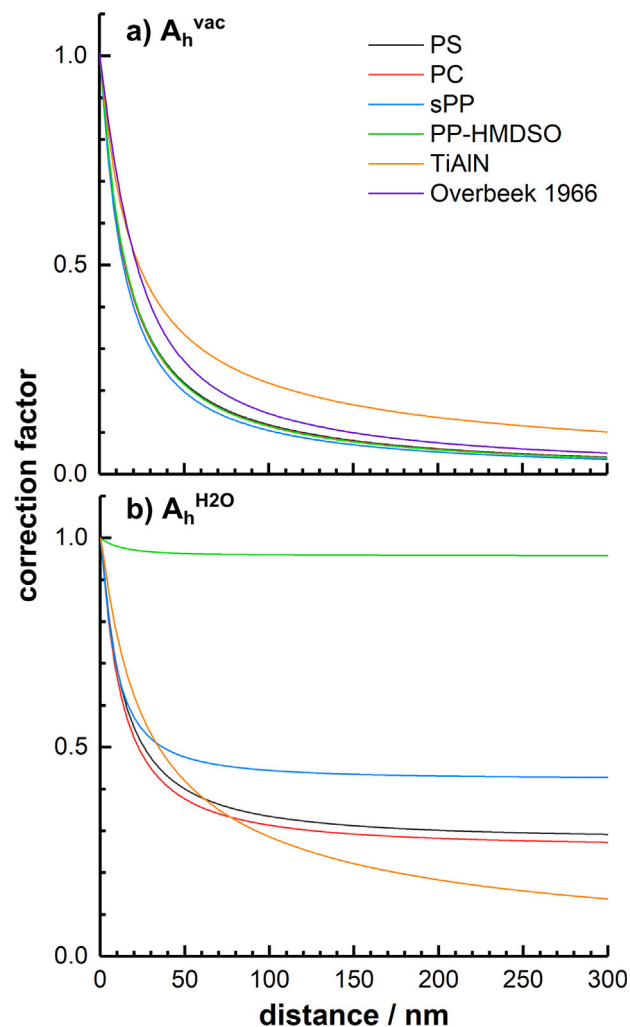


Fig. 4. Correction factors of the Hamaker constants of PS, PC, sPP, PP-HMDSO and TiAlN for the symmetric material combinations as reported in Table 1 across (a) vacuum and (b) water.

differences were present. This can be rationalized when considering that the retardation behaviour is primarily determined by the fact that the oscillators become out of step and specific material optical properties are as a consequence of less relevance. To corroborate this interpretation, the Overbeek's expression for the correction factor is shown in Fig. 4a. This expression approximates the retardation behaviour of the Casimir interactions between two model half-spaces showing only a single excitation wavelength, which is usually assumed to be 100 nm (corresponding to 12.4 eV) [30,31]. When comparing the Overbeek's correction factor of the model material with the factors calculated for the real materials, a good agreement is found. This validates that specific optical properties are of lower relevance for the retardation of dispersive interactions in vacuum.

The situation was found to be contrary in the case of water being the intervening medium as shown in Fig. 4b. The retardation behaviour depended strongly on the individual optical properties of the materials and the correction factor of especially those materials with higher non-retarded Hamaker constants decreased more strongly and within a higher range of distances. This can be again rationalized when considering that water efficiently screens predominantly oscillators at higher energies: in the case of PP-HMDSO basically only the static polarizability contributes to the interaction forces and therefore almost no retardation occurred

in the here discussed case of two separated half spaces as indicated by the only slight decrease of the correction factor. In contrast, the correction factor decreased with increasing distance in the case of PS, PC, sPP and TiAlN due to significant contributions of low energy oscillators. In this regards, the correction factor of sPP, PS and PC reached constant values after around 100 nm, whereas a decrease for TiAlN was still noticed at distances up to 300 nm. Since higher energy oscillators are retarded first with increasing distance followed by the retardation of oscillators in the visible and the infrared range, this indicates that the dispersive interactions of TiAlN across water mainly originate from such low energy contributions [32]. This interpretation is in agreement with the high polarizability of the metal-like TiAlN.

3.4. Sensitivity of Hamaker constants towards uncertainties in the evaluation of REELS spectra

So far the discussion has shown that the quality of the optical data is of pivotal importance for a reliable calculation of Hamaker coefficients. Thus, the sensitivity of Hamaker constants towards possible inaccuracies related to the quantitative analysis of the REELS spectra is discussed in the following.

The first aspect investigated is the use of REELS spectra with a limited spectral range. In such spectra the lower energy range of relevance for the calculation of Hamaker coefficients is completely measured but the tailing at higher energies is not resolved. This situation can easily emerge during the measurement due to the rather unstructured shape of the REELS spectra at higher energies. Fig. 5 shows the cross section λK of PS as obtained from a REELS spectrum measured only up to an energy loss of 40 eV instead of 70 eV. The comparison with the cross section derived from the completely measured spectrum disclosed that the shape of the imprecise cross section was only slightly affected and was characterized by a subtle increase of its magnitude around 20 eV accompanied by a related decrease at energies above 30 eV. The relevance of this error for the precise value of the Hamaker constant was therefore also low and a value of 86 zJ was found instead of 90 zJ (see Table 1). Interestingly, the shape of the cross section remained completely unchanged when limiting the energy range of the REELS spectrum even further to 31 eV. It follows that lower energy oscillators are rather unaffected by errors induced by a limited spectral range, but higher energy oscillators located outside the range of the spectrum can obviously not be determined any more. Another consequence is that the integrated area of the cross section, which is theoretically around one and decreases with a

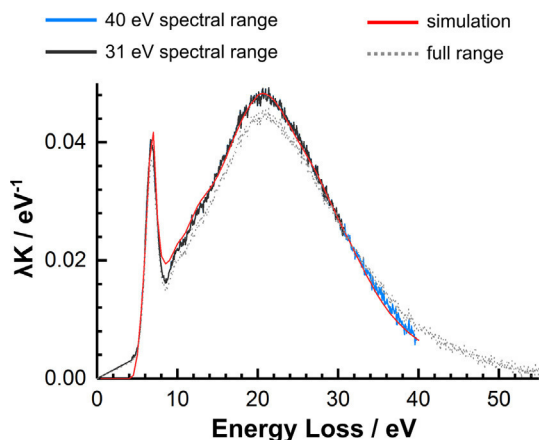


Fig. 5. Effect of a limited spectral range of the REELS spectrum on the cross section λK of PS.

decreasing spectral range accordingly, does not directly reflect the quality of the derived optical data or of the Hamaker constant. Instead, the area of the cross section should be at its maximum value around one in order to obtain the most reliable dielectric function and Hamaker coefficients.

Another inaccuracy within the quantitative analysis of the REELS spectrum can be caused by the use of an imprecise refractive index for the KK sum rule. According to the definition of the KK sum rule in Eq. (2), such an error does not affect the resonant frequencies or damping of the oscillators but directly translates into the oscillator strengths. Since the dispersive interactions mainly originate from the resonant interactions of electromagnetic fluctuations, an incorrect refractive index causes crucial inaccuracies in the calculated Hamaker coefficients. To exemplify this aspect, the non-retarded Hamaker constant of PS was calculated after rescaling the dielectric function in form of the ELF to a refractive index of 2 instead of 1.6 (at 0.4 eV) [33]. As shown in Table 1, the resulting value of the Hamaker constant is then around 160 zJ in contrast to 90 zJ and therefore highly overestimated.

In the case of low band gap semiconductors or metals another more complex error can be induced by the low energy resolution of the primary electron beam used for REELS (in this case 1.0 eV). As an example, TiAlN was investigated and in this case transitions within the Ti3d band significantly contribute to the optical response at energy losses around 1–3 eV [34]. Since these contributions partly overlap with the elastic peak of the primary electron beam, a precise decomposition of the complete REELS spectrum into the elastic peak and the inelastic loss region cannot be performed. Consequently, an experimental cross section derived from such an erroneous loss spectrum is affected by not only the absence of low energy oscillators but also by an overestimated area of the elastic peak.

In this view, it is instructive to investigate the structure of the deconvolution scheme in Eq. (1) in order to rationalize and eventually to mitigate resulting inaccuracies. When inspecting Eq. (1) it becomes clear that the cross section λK is determined iteratively starting at the highest energy losses and ending at the elastic peak energy at channel i_p . The cross section at a certain channel i is obtained after taking the intensity of channel i_p-i at the other end of the spectrum, correcting it by a sum of weighed cross sections calculated in before and after dividing the resulting value by the elastic peak area A_p . The poorly resolved intraband transitions in the loss spectrum therefore result into an underestimation of the cross section at higher energies, because the cross section is at these energies directly calculated from the low energy loss region. In turn, the cross section becomes at low energies overestimated and this results ultimately into an overestimation of oscillator strengths in that energy range. When considering further the additional effect of the overestimated elastic peak area A_p , it becomes clear that the biasing of the cross section by the poorly resolved intraband transitions is enhanced with the same tendencies. It follows that an appropriate adjustment of the elastic peak area A_p before performing the deconvolution should not only remove the error solely related to the overestimation of A_p but should also mitigate the inaccuracies related to the poorly resolved low loss spectrum.

This correction procedure was validated in the case of TiAlN. Fig. 6 shows the experimental cross section as obtained directly after the elastic peak separation and deconvolution but without performing further corrections. In agreement with the arguments given above, it was observed that the best matching simulation found for this situation did not precisely follow the experimental cross section at energies above 35 eV. However, it is noted that for the correction procedure presented in the following this simulation of the uncorrected cross section serves as a starting point in order to increase the robustness of the procedure.

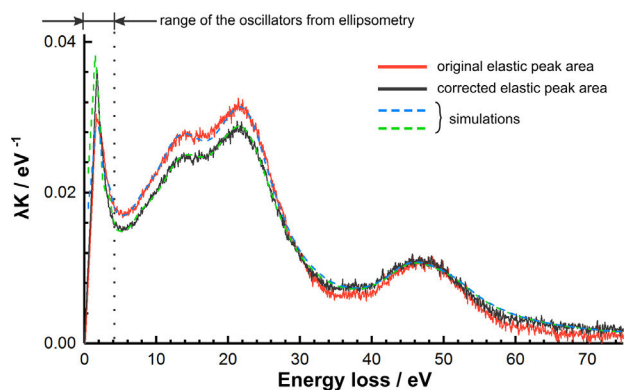


Fig. 6. Experimental and simulated cross sections λK of TiAlN before and after the correction including the adjustment of the elastic peak area used for the deconvolution of the loss spectrum under the assistance of ellipsometry data.

In order to correct for the inaccuracies related to the poorly resolved loss spectrum, the intraband oscillators were firstly determined using spectroscopic ellipsometry as an absolute method. Fig. 8 shows the ELF as measured by ellipsometry and fitted using two Drude-Lindhard type oscillators. The resonance frequencies of the oscillators were located at 1.95 ± 0.02 and 3.55 ± 0.23 eV and can be ascribed to transitions within the d-band and between the N2p and the d-band (see the supporting information for the other parameters) [41,42].

The ellipsometry derived optical data were then included into the simulation of the λK spectrum but with the oscillator parameters being fixed. In the next step, the experimental loss spectrum was deconvoluted but after adjusting the elastic peak area such that an optimal agreement between the simulation and the corrected cross section was found at low energy losses (1.7–4 eV). This procedure is justified when considering that the simulated cross section in this range is governed by the ellipsometry derived oscillators and as a consequence can be therefore assumed to approach the unknown true cross section. In this regard, it is noted that an overlap of around 1–2 eV of the ellipsometry based optical data and the experimental inelastic cross section was found to be required in order to perform a reliable and robust correction of the experimental cross section. In the next step, the simulation

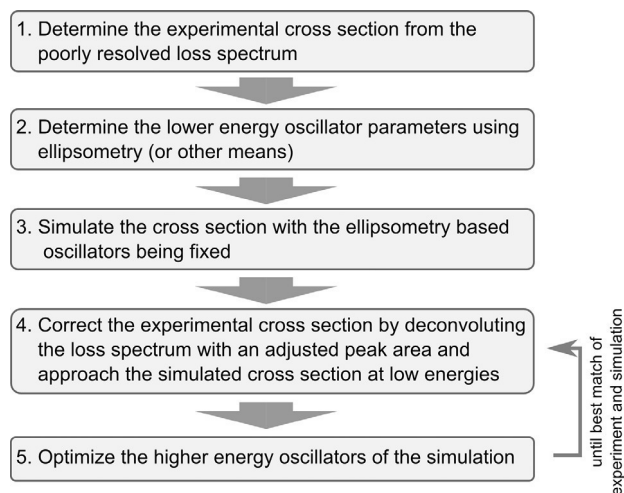


Fig. 7. Quantitative evaluation scheme of REELS spectra for mitigating inaccuracies related to poorly resolved low energy losses as a result of strongly overlapping elastic and inelastic loss spectra.

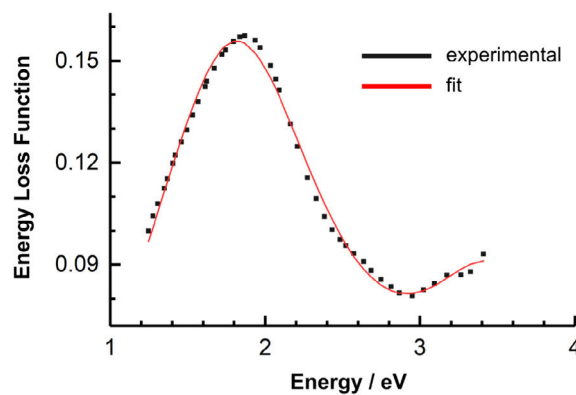


Fig. 8. ELF of TiAlN as measured by spectroscopic ellipsometry and fitted using two Drude-Lindhard type oscillators (see supporting information).

was optimized at higher energies by adjusting the parameters of the empirically chosen oscillators to match the experimental cross section. This adjustment also resulted into slight changes in the low energy range of the simulated cross section and consequently the latter two steps were iterated a few times in order to improve the overall consistency between the simulated and experimental cross section. For the sake of clarity, the correction procedure is also outlined in Fig. 7. As a result of this procedure, the consistency of the experimental and simulated cross sections was improved in the higher energy range above 30 eV and also the experimental cross section around 4–30 eV was decreased in agreement with the discussion above. This indicates that the accuracy of the optical data was increased by the correction procedure. However, most strikingly the oscillators at low energy losses as determined by ellipsometry showed increased oscillator strengths than those otherwise derived directly from the uncorrected cross section.

In order to assess the relevance of an imprecise separation of REELS spectra into the elastic and inelastic parts, the non-retarded Hamaker constants of TiAlN across vacuum and water were calculated using both the corrected and the uncorrected spectral data as shown in Table 1. It was found that the Hamaker constants using the uncorrected optical data across vacuum and water were 244 and 117 zJ, whereas after the correction values of 220 and 100 zJ were obtained. The discrepancies are thus in this specific case around 10% for the Hamaker constant across vacuum and around 20% for the constant across water. Again it is noted that the deviations are increased in the case of water due to the higher relevance of low energy contributions. In conclusion, the proposed correction procedure based on additional complementary optical data represents a useful method for increasing the accuracy of both the optical data and of Hamaker constants derived from REELS spectra with indistinguishable elastic and inelastic regions.

For completeness, also Hamaker constants were calculated using REELS based optical data taken from literature and are reported in Table 2. It is highlighted that the data found in literature was in some cases not scaled to fulfil the KK sum rule. According to the aforementioned, the accuracy of the calculated Hamaker constants was thus increased by rescaling the literature optical data according to the corresponding refractive indices reported by the authors. It turned out that the Hamaker constants for polyethylene across vacuum and water were identical with those of the SPP investigated in this publication, which is also consistent with their chemical and electronic structure. This indicates that Hamaker constants as determined by REELS can show a high reproducibility among different authors when considering possible inaccuracies in the quality of the optical data. In comparison, the reproducibility of VUV reflectivity based Hamaker constants is known to be limited between different authors due to inaccuracies

Table 2

Non-retarded Hamaker constants of symmetric material interfaces across vacuum (material|vacuum|material) and water (material|H₂O|material) as calculated from REELS derived optical data as reported in literature. *The original spectral data did not fulfil the Kramers-Kronig sum rule and were rescaled according to the refractive indices reported in the corresponding publication.

Material	Reference	$A_h^{vac}/10^{-21}$	$A_h^{H_2O}/10^{-21}$
Polyethylene	[20]	77.0*	7.5*
Poly(methyl methacrylate)		73.5*	6.7*
Polyvinyl chloride		80.6*	8.5*
Polyethylene terephthalate		85.7*	10.0*
Polypyrrole		70.1*	5.9*
Polyamide (PA6)		75.8*	7.2*
Ti	[35]	344	210
TiC		324	182
TiN		310*	171*
TiO ₂		155*	41*
NiO	[36]	158	54
SiO ₂	[37]	46.4	3.5
ZrO ₂		124	25
α -Al ₂ O ₃	[38]	148	36
Amorphous Al ₂ O ₃		136	30
Cu ₂ O	[39]	178*	58*
CuO		188*	63*
Fe	[40]	254*	135*
Cu		236	118
Ag		241*	123*
Au		276	145

in the boundary conditions used for the Kramers-Kronig dispersion relationship, which allows for the calculation of the complex dielectric function from the reflectivity.[9]

4. Conclusions

Dispersion forces could be investigated for the first time by Lifshitz theory based on the quantitative evaluation of REELS spectra. The use of REELS allows to analyse dispersion forces of nanoscale structures and thin-films and to determine optical data, which covers the whole range of relevance for the dispersive interactions. In comparison, existing methods such as VUV reflectivity measurements or spectroscopic ellipsometry suffer from a limited spectral range or can only be applied to a few systems as in the case of transmission electron energy loss spectroscopy [9,14]. This work therefore continues to establish electron spectroscopy for the analysis of dispersion forces and contributes thereby to improve the accuracy of the calculation of Hamaker coefficients, which has been so far a major obstacle for the theoretical analysis of dispersion forces in colloid and interface science [14,15].

Among the results, the investigation of different saturated and unsaturated polymers showed that the high accuracy of REELS especially in the high energy loss range significantly improves the quality of calculated non-retarded Hamaker constants. In the case of polystyrene the corresponding Hamaker constant across vacuum PS|vac|PS was around $90 \cdot 10^{-21}$ J and therefore increased when compared to the value derived from VUV reflectance spectroscopy, which was reported to be around $63 \cdot 10^{-21}$ J [28].

The sensitivity analysis of the quantification scheme towards typical systematic errors revealed that a limited REELS spectral range, where the high energy tailing of the loss spectrum is unresolved, causes a slight decrease of calculated Hamaker constants by below 10%. In contrast, the use of imprecise refractive indices or the presence of indistinguishable elastic and inelastic sections in the REELS spectrum can deteriorate the accuracy of calculated Hamaker constants strongly. A correction procedure for mitigating the negative effect of overlapping elastic and inelastic regions in the REELS spectrum such as observed in the case of TiAlN was

therefore developed based on optical data derived from spectroscopic ellipsometry. Consequently, the accuracy of the low energy oscillators and of the calculated Hamaker constant could be increased.

Future studies are under way using the REELS based analysis of dispersion forces for understanding adhesion force measurements [43,44].

Acknowledgment

We gratefully acknowledge the financial support by the German Research Foundation (DFG) within the projects SFB-TR 87 A2 and A3. The authors thank Holger Ruess and Jochen M. Schneider (Chair for Materials Chemistry at the RWTH Aachen) for the preparation of the hard coatings.

Appendix A. Supplementary material

Supplementary data associated with this article can be found, in the online version, at <https://doi.org/10.1016/j.jcis.2017.12.069>.

References

- [1] M. Boström, D.R.M. Williams, B.W. Ninham, Specific Ion Effects: why DLVO theory fails for biology and colloid systems, *Phys. Rev. Lett.* 87 (2001) 168103, <https://doi.org/10.1103/PhysRevLett.87.168103>.
- [2] M. Boström, D.R.M. Williams, B.W. Ninham, Surface tension of electrolytes: specific ion effects explained by dispersion forces, *Langmuir* 17 (2001) 4475–4478, <https://doi.org/10.1021/la0102298>.
- [3] J. Carrasco, J. Klimeš, A. Michaelides, The role of van der Waals forces in water adsorption on metals, *J. Chem. Phys.* 138 (2013) 024708, <https://doi.org/10.1063/1.4773901>.
- [4] J. Carrasco, B. Santra, J. Klimeš, A. Michaelides, To wet or not to wet? dispersion forces tip the balance for water ice on metals, *Phys. Rev. Lett.* 106 (2011) 026101, <https://doi.org/10.1103/PhysRevLett.106.026101>.
- [5] M.K. Chaudhury, Interfacial interaction between low-energy surfaces, *Mater. Sci. Eng. R Rep.* 16 (1996) 97–159, [https://doi.org/10.1016/0927-796X\(95\)00185-9](https://doi.org/10.1016/0927-796X(95)00185-9).
- [6] M. Elbaum, M. Schick, Application of the theory of dispersion forces to the surface melting of ice, *Phys. Rev. Lett.* 66 (1991) 1713–1716, <https://doi.org/10.1103/PhysRevLett.66.1713>.
- [7] N. Nerngchamng, L. Yuan, D.-C. Qi, J. Li, D. Thompson, C.A. Nijhuis, The role of van der Waals forces in the performance of molecular diodes, *Nat. Nanotechnol.* 8 (2013) 113–118, <https://doi.org/10.1038/nnano.2012.238>.
- [8] F.W. DeRío, M.P. de Boer, J.A. Knapp, E. David Reedy, P.J. Clews, M.L. Dunn, The role of van der Waals forces in adhesion of micromachined surfaces, *Nat. Mater.* 4 (2005) 629–634, <https://doi.org/10.1038/nmat1431>.
- [9] R.H. French, Origins and applications of London dispersion forces and Hamaker constants in ceramics, *J. Am. Ceram. Soc.* 83 (2000) 2117–2146, <https://doi.org/10.1111/j.1151-2916.2000.tb01527.x>.
- [10] V.M. Muller, V.S. Yushchenko, B.V. Derjaguin, General theoretical consideration of the influence of surface forces on contact deformations and the reciprocal adhesion of elastic spherical particles, *J. Colloid Interface Sci.* 92 (1983) 92–101, [https://doi.org/10.1016/0021-9797\(83\)90119-4](https://doi.org/10.1016/0021-9797(83)90119-4).
- [11] H. Casimir, On the attraction between two perfectly conducting plates, *Proc. KNAW.* 51 (1948) 793–795.
- [12] I.E. Dzyaloshinskii, E.M. Lifshitz, L.P. Pitaevskii, General theory of van der waals' forces, *Sov. Phys. Uspekhi.* 4 (1961) 153, <https://doi.org/10.1070/PU1961v004n02ABEH003330>.
- [13] V.A. Parsegian, *Van der Waals Forces: A Handbook for Biologists, Chemists, Engineers, and Physicists*, Cambridge University Press, Cambridge, 2005.
- [14] R.H. French, H. Müllejans, D.J. Jones, G. Duscher, R.M. Cannon, M. Rühle, Dispersion forces and Hamaker constants for intergranular films in silicon nitride from spatially resolved-valence electron energy loss spectrum imaging, *Acta Mater.* 46 (1998) 2271–2287, [https://doi.org/10.1016/S1359-6454\(98\)80008-6](https://doi.org/10.1016/S1359-6454(98)80008-6).
- [15] G.L. Tan, R.H. French, Optical properties, electronic structure and London dispersion interactions for nanostructured interfacial and surficial films, *Mater. Sci. Eng. A.* 422 (2006) 136–146, <https://doi.org/10.1016/j.msea.2006.01.010>.
- [16] S. Tougaard, I. Chorkendorff, Differential inelastic electron scattering cross sections from experimental reflection electron-energy-loss spectra: application to background removal in electron spectroscopy, *Phys. Rev. B.* 35 (1987) 6570–6577, <https://doi.org/10.1103/PhysRevB.35.6570>.
- [17] F. Yubero, S. Tougaard, Quantitative analysis of reflection electron energy-loss spectra, *Surf. Interface Anal.* 19 (1992) 269–273, <https://doi.org/10.1002/sia.740190152>.

- [18] S. Tougaard, F. Yubero, QUEELS software package for calculation of surface effects in electron spectra, *Surf. Interface Anal.* 36 (2004) 824–827, <https://doi.org/10.1002/sia.1774>.
- [19] F. Yubero, D. Fujita, B. Ramskov, S. Tougaard, Experimental test of model for angular and energy dependence of reflection–electron–energy–loss spectra, *Phys. Rev. B* 53 (1996) 9728–9732, <https://doi.org/10.1103/PhysRevB.53.9728>.
- [20] D. Tahir, S. Tougaard, Electronic and optical properties of selected polymers studied by reflection electron energy loss spectroscopy, *J. Appl. Phys.* 111 (2012) 054101, <https://doi.org/10.1063/1.3688327>.
- [21] J. Heinrichs, Non-local effects in the macroscopic theory of Van der Waals and adhesive forces, *Solid State Commun.* 13 (1973) 1595–1598, [https://doi.org/10.1016/0038-1098\(73\)90245-7](https://doi.org/10.1016/0038-1098(73)90245-7).
- [22] J.-L. Li, H.C. Schniepp, I.A. Aksay, R. Car, Phonon-induced anisotropic dispersion forces on a metallic substrate, *Nano LIFE.* 02 (2012) 1240001, <https://doi.org/10.1142/S1793984411000505>.
- [23] R. Esquivel-Sirvent, G.C. Schatz, Spatial nonlocality in the calculation of hamaker coefficients, *J. Phys. Chem. C* 116 (2012) 420–424, <https://doi.org/10.1021/jp209577v>.
- [24] B. Ozkaya, S. Grosse-Kreul, C. Corbella, A. von Keudell, G. Grundmeier, Combined in situ XPS and UHV-chemical force microscopy (CFM) studies of the plasma induced surface oxidation of polypropylene, *Plasma Process. Polym.* 11 (2014) 256–262, <https://doi.org/10.1002/ppap.201300105>.
- [25] I. Tajima, M. Yamamoto, Spectroscopic study on chemical structure of plasma-polymerized hexamethyldisiloxane, *J. Polym. Sci. [A1]* 23 (1985) 615–622, <https://doi.org/10.1002/pol.1985.170230303>.
- [26] S. Tougaard, Algorithm for analysis of low-energy-resolution REELS; determination of inelastic electron scattering cross-sections and applications in quantitative XPS, *Surf. Sci.* 464 (2000) 233–239, [https://doi.org/10.1016/S0039-6028\(00\)00684-1](https://doi.org/10.1016/S0039-6028(00)00684-1).
- [27] S. Tougaard, J. Kraaer, Inelastic–electron–scattering cross sections for Si, Cu, Ag, Au, Ti, Fe, and Pd, *Phys. Rev. B* 43 (1991) 1651–1661, <https://doi.org/10.1103/PhysRevB.43.1651>.
- [28] R.H. French, K.I. Winey, M.K. Yang, W. Qiu, Optical properties and van der waals–london dispersion interactions of polystyrene determined by vacuum ultraviolet spectroscopy and spectroscopic ellipsometry, *Aust. J. Chem.* 60 (2007) 251–263, <https://doi.org/10.1071/CH06222>.
- [29] T. Ederth, Computation of Lifshitz–van der waals forces between alkythiol monolayers on gold films, *Langmuir* 17 (2001) 3329–3340, <https://doi.org/10.1021/la001607w>.
- [30] J.Th.Gregory, quoted by A. van Silhout, *Proc Konigs Akad Wetensch B* 69, 1966, 501.
- [31] A. Anandarajah, J. Chen, Single correction function for computing retarded van der waals attraction, *J. Colloid Interface Sci.* 176 (1995) 293–300, <https://doi.org/10.1006/jcis.1995.9964>.
- [32] D.C. Prieve, W.B. Russel, Simplified predictions of Hamaker constants from Lifshitz theory, *J. Colloid Interface Sci.* 125 (1988) 1–13, [https://doi.org/10.1016/0021-9797\(88\)90048-3](https://doi.org/10.1016/0021-9797(88)90048-3).
- [33] N. Sultanova, S. Kasarova, I. Nikolov, Dispersion properties of optical polymers, *Acta Phys. Pol. A* 116 (2009) 585–587, <https://doi.org/10.12693/APhysPolA.116.585>.
- [34] I. LeR, Strydom, S. Hofmann, XPS and EELS study of the valence band electronic structure of TiN and (Ti, Al)N coatings as influenced by the deposition parameters, *Vacuum* 41 (1990) 1619–1623, [https://doi.org/10.1016/0042-207X\(90\)94035-O](https://doi.org/10.1016/0042-207X(90)94035-O).
- [35] G.G. Fuentes, E. Elizalde, F. Yubero, J.M. Sanz, Electron inelastic mean free path for Ti, TiC, TiN and TiO₂ as determined by quantitative reflection electron energy-loss spectroscopy, *Surf. Interface Anal.* 33 (2002) 230–237, <https://doi.org/10.1002/sia.1205>.
- [36] N. Pauly, F. Yubero, F.J. García-García, S. Tougaard, Quantitative analysis of Ni 2p photoemission in NiO and Ni diluted in a SiO₂ matrix, *Surf. Sci.* 644 (2016) 46–52, <https://doi.org/10.1016/j.susc.2015.09.012>.
- [37] N. Pauly, S. Tougaard, Determination of the surface excitation parameter for oxides: TiO₂, SiO₂, ZrO₂ and Al₂O₃, *Surf. Sci.* 602 (2008) 1974–1978, <https://doi.org/10.1016/j.susc.2008.03.039>.
- [38] D. Tahir, H.L. Kwon, H.C. Shin, S.K. Oh, H.J. Kang, S. Heo, J.G. Chung, J.C. Lee, S. Tougaard, Electronic and optical properties of Al₂O₃/SiO₂ thin films grown on Si substrate, *J. Phys. Appl. Phys.* 43 (2010) 255301, <https://doi.org/10.1088/0022-3727/43/25/255301>.
- [39] D. Tahir, S. Tougaard, Electronic and optical properties of Cu, CuO and Cu₂O studied by electron spectroscopy, *J. Phys. Condens. Matter.* 24 (2012) 175002, <https://doi.org/10.1088/0953-8984/24/17/175002>.
- [40] S. Hajati, O. Romanyuk, J. Zemek, S. Tougaard, Validity of Yubero-Tougaard theory to quantitatively determine the dielectric properties of surface nanofilms, *Phys. Rev. B* 77 (2008) 155403, <https://doi.org/10.1103/PhysRevB.77.155403>.
- [41] L. An, S.T. Ali, T. Søndergaard, J. Nørgaard, Y.-C. Tsao, K. Pedersen, Optimization of TiAlN/TiAlON/Si₃N₄ solar absorber coatings, *Sol. Energy* 118 (2015) 410–418, <https://doi.org/10.1016/j.solener.2015.05.042>.
- [42] P. Patsalas, N. Kalfagiannis, S. Kassavetis, Optical properties and plasmonic performance of titanium nitride, *Materials* 8 (2015) 3128–3154, <https://doi.org/10.3390/ma8063128>.
- [43] M. Wiesing, T. de los Arcos, M. Gebhard, A. Devi, G. Grundmeier, Analysis of dispersive interactions at polymer/TiAlN interfaces by means of dynamic force spectroscopy, *Phys. Chem. Chem. Phys.* (2017), <https://doi.org/10.1039/C7CP05373H>.
- [44] M. Wiesing, T. de los Arcos, G. Grundmeier, UHV AFM based colloidal probe studies of adhesive properties of VAIN hard coatings, *Appl. Surf. Sci.* 428 (2018) 767–774, <https://doi.org/10.1016/j.apsusc.2017.09.208>.

Lifshitz analysis of dispersion forces based on quantitative Reflection Electron Energy Loss Spectroscopy

- Supporting Information -

M. Wiesing, G. Grundmeier

Technical and Macromolecular Chemistry, University of Paderborn, Warburger Straße 100, 33098 Paderborn, Germany,

Correspondence to: Martin Wiesing (e-mail: wiesing@mail.upb.de)

X-ray Photoelectron Spectroscopy of the PC and PS spin coated thin films

Experimental. XPS was measured using an ESCA+ system at pressures below $2 \cdot 10^{-8}$ Pa with a monochromatized Al K α source (1486.7 eV). The energy resolution was 0.77 eV as determined from the FWHM of the Ag3d_{5/2} line. The angle of emission was 60° relative to the surface normal and the depth of information was around 5 nm. For neutralization an electron flood gun was used and the binding energy was referenced to the C1s signal at 285.0 eV.

Results. The PC and PS polymer thin films were investigated by X-ray Photoelectron Spectroscopy (XPS) before performing the REELS measurement. The surface atomic stoichiometries are shown in Table S 1 and are resemble the typical properties of the polymers.[1,2]

Table S 1: XPS stoichiometries of the PC, PS, PP-HMDSO and sPP thin films before the REELS measurements.

	C1s / at%	O1s / at%	Si2p / at%
PC	84.8	15.2	-
PS	100	-	-
PP-HMDSO	40.5	28.0	31.5
sPP	100	-	-

A more detailed characterization of the surface chemistry was performed by measuring high-resolution C1s spectra as shown in Figure S 1. The lineshape of the C1s spectrum of PC was typical for PC and could be decomposed into four components related to CC and CH bonds (284.8 eV), to C-O (286.3 eV), to the carbonate (290.7 eV) and to the π shake-up (291.5 eV).[1] The C1s spectrum of PS was characterized by the absence of oxygen bearing functional groups and was described by the CC and CH component at 284.8 eV and the π shake-up at 291.5 eV.[2] Similarly, the spectrum of the sPP thin film showed the presence of aliphatic CH and CC groups in agreement with its chemical structure.

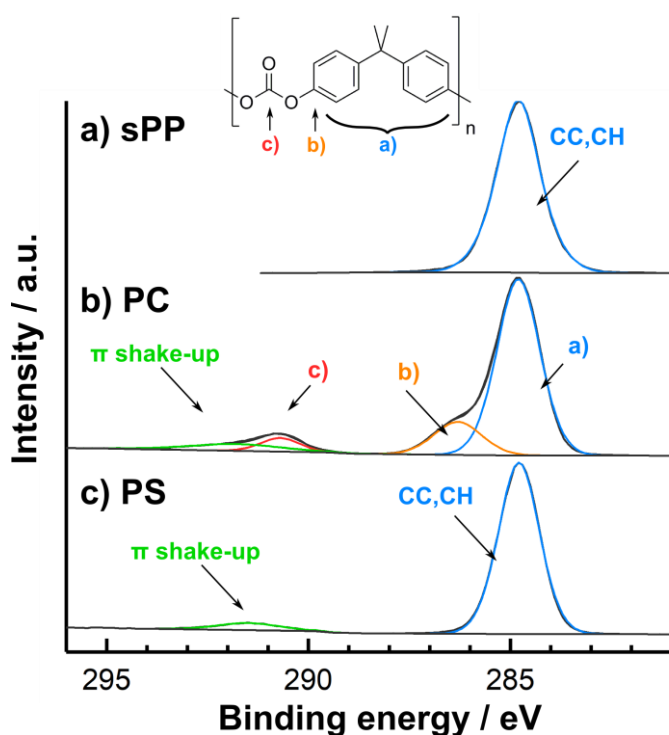


Figure S 1: High-resolution C1s spectra of the a) sPP, b) PC and c) PS thin films.

Surface chemical properties of the PP-HMDSO

The PP-HMDSO was characterized using XPS and Infrared Spectroscopy. As shown in Table S 1, the surface was composed by 40.5 at% C, 28.0 at% O and 31.5 at% Si and thus differed from the monomer composition of 60 at% C, 10 at% O and 20 at% Si by an increased oxygen and decreased carbon content.

This might presumably be the result of a slight oxygen incorporation of the polymer due to residual oxygen contaminations present in the deposition chamber during deposition.

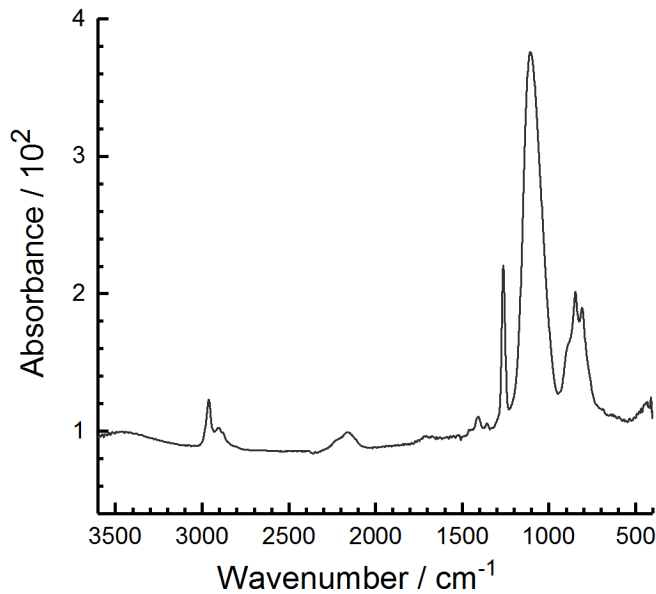


Figure S 2: Infrared absorbance spectrum of PP-HMDSO after deposition on an Al mirror.

The bulk properties were further investigated by Infrared Spectroscopy measured on an Al mirror after the deposition of the PP-HMDSO thin film. The absorbance spectrum is shown in Figure S 2 and shows the typical bands of the HMDSO Ar⁺ plasma polymer at 2960 (CH₃ stretch), 2908 (CH₂ stretch), 2154 (Si-H), 1264 (Si-CH₃ sym. deformation), 1107 (Si-O-Si, Si-O-C stretch), 847 (Si-CH₂ sym. rocking) and 809 cm⁻¹ (Si-CH₂ asym. rocking).[3] The polymer is thus composed by a mixture of Si-H, Si-CH_{2/3} and Si-O groups.

REELS spectra

The REELS spectra of the materials investigated in this work are shown in figure s 3.

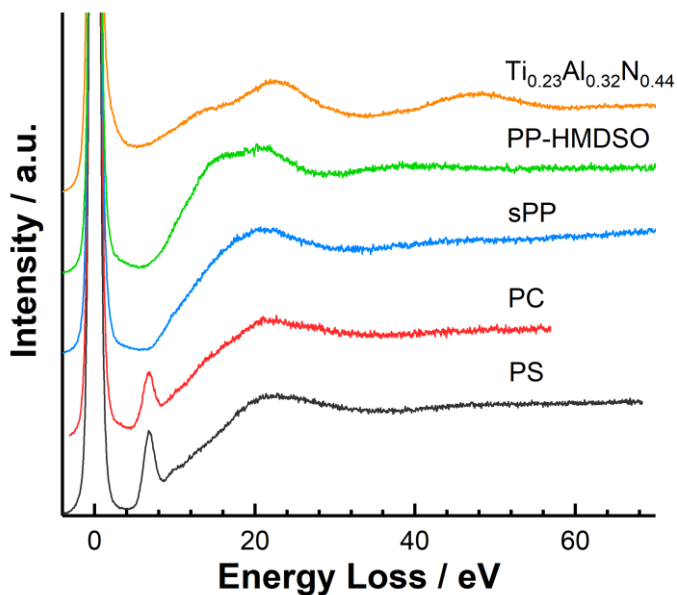


Figure S 3: REELS spectra of $Ti_{0.23}Al_{0.32}N_{0.44}$, PS, PC, sPP and PP-HMDSO. The spectra were normalized to the elastic peak and shifted vertically for better visualization.

Spectroscopic ellipsometry of TiAlN

The dielectric function of TiAlN was determined by spectroscopic ellipsometry within the range of 1.25 to 3.4 eV. The spectral data in form of the Energy Loss Function (ELF) was described by two Drude Lindhard oscillators in the optical limit where k approaches zero. The Drude Lindhard oscillators are defined as [4–6]

$$\text{Im}\left(-\frac{1}{\varepsilon(\omega, k)}\right) = \theta(\hbar\omega - E_g) \cdot f(\hbar\omega) \cdot \sum_i \frac{A_i \gamma_i \hbar\omega}{(\hbar^2 \omega_{0,i}^2(k) - \hbar^2 \omega^2)^2 + \gamma_i^2 \hbar^2 \omega^2} \quad (\text{S1a})$$

$$\hbar\omega_{0,i}(k) = \hbar\omega_{0,i} + \alpha_i \frac{\hbar^2 k^2}{2m_e} \quad (\text{S1b})$$

$$f(\hbar\omega) = \left[\frac{a2(\hbar\omega - E_g)^p}{\hbar^2 \omega^2} \right]^{tmp1}, \text{ if } E_g < \hbar\omega < E_g + a1 \quad (\text{S1c})$$

$$tmp1 = \cos^2\left(\frac{\pi \hbar\omega - E_g}{2 a1}\right) \quad (\text{S1d})$$

$$f(\hbar\omega) = 1, \text{ if } \hbar\omega > E_g + a1 \quad (\text{S1e})$$

where $\varepsilon(\omega, k)$ is the dielectric function, $\hbar\omega$ the energy, E_g the band gap energy, A_i the oscillator strength of oscillator i , γ_i and $\hbar\omega_{0,i}$ the damping and resonance frequency, α_i the momentum dispersion coefficient, k the wave vector and m_e the electron mass. The function $\theta(\hbar\omega - E_g)$ is one at $\hbar\omega > E_g$ and zero at $\hbar\omega < E_g$. The function $f(\hbar\omega)$ serves to smoothen the near band gap region based on the empirical parameters $a1$ and $a2$. The parameter p is 0.5 or 2 for a direct and an indirect band gap.

The oscillator parameters derived from ellipsometry are included in Table S 2.

Drude Lindhard oscillator parameters of the polymers and TiAlN

Table S 2 lists the oscillator parameters of PC, PS, sPP, PP-HMDSO and that of TiAlN as obtained after performing the correction procedure under the assistance of the optical data as derived from ellipsometry.

Table S 2: Drude Lindhard oscillator parameters of PC, PS, sPP, PP-HMDSO and TiAlN (after correction) as determined by REELS and ellipsometry. *parameters were obtained by spectroscopic ellipsometry.

		$\hbar\omega_0 / \text{eV}$	A_0 / eV^2	$\hbar\gamma / \text{eV}$	α
PC		6.8	1.2	0.95	0
E_g	4.2	14.9	6.4	4.9	0
$a1$	3.2	22.2	189.5	13	0
$a2$	9	32.5	184.1	20	0
p	2	27.6	38.7	9	0
n	1.6				
PS		7	2.1	1.23	0
E_g	4.2	10	0.5	2	0
$a1$	3.2	13	0.5	2	0
$a2$	9	22.2	206.1	13	0
p	2	27.6	48.2	9	0
n	1.6	32.5	140.0	18	0
sPP		13	2.06	3.5	0
E_g	5.2	16.1	9.29	5	0

<i>a</i> 1	3.8	21.7	172.4	11	0
<i>a</i> 2	0.01	27.6	66.0	10	0
<i>p</i>	2	32.5	125.9	16	0
<i>n</i>	1.5				
PP-HMDSO					
<i>E_g</i>	3.8	12	2.17	3	0
<i>a</i> 1	8	16	47.2	7	0
<i>a</i> 2	1.3	20.5	61.6	7	0
<i>p</i>	2	25	106.2	10	0
<i>n</i>	1.4	33	35.7	10	0
TiAlN		1.95 ± 0.02*	0.42 ± 0.03*	1.52 ± 0.07*	0.6
<i>metallic</i>		3.55 ± 0.23*	0.31 ± 0.15*	1.28 ± 0.4*	0.6
		5.0	0.41	3	0.6
		8.7	4.23	6	0.6
		14.8	47.5	8.3	0.6
		22.5	230.8	9.8	0.6
		37.0	1.00	7	0.6
		45.1	178.7	10	0.6
		50.4	75.5	8.5	0.6

Bibliography

- [1] M.C. Burrell, J.J. Chera, Polycarbonate Spin Cast Films by XPS, Surf. Sci. Spectra. 6 (1999) 1–4. doi:10.1116/1.1247900.
- [2] M.C. Burrell, J.J. Chera, Polystyrene Spin Cast Films by XPS, Surf. Sci. Spectra. 6 (1999) 27–30. doi:10.1116/1.1247899.
- [3] I. Tajima, M. Yamamoto, Spectroscopic study on chemical structure of plasma-polymerized hexamethyldisiloxane, J. Polym. Sci. [A1]. 23 (1985) 615–622. doi:10.1002/pol.1985.170230303.
- [4] S. Tougaard, F. Yubero, QUEELS software package for calculation of surface effects in electron spectra, Surf. Interface Anal. 36 (2004) 824–827. doi:10.1002/sia.1774.
- [5] F. Yubero, D. Fujita, B. Ramskov, S. Tougaard, Experimental test of model for angular and energy dependence of reflection-electron-energy-loss spectra, Phys. Rev. B. 53 (1996) 9728–9732. doi:10.1103/PhysRevB.53.9728.
- [6] F. Yubero, J.M. Sanz, B. Ramskov, S. Tougaard, Model for quantitative analysis of reflection-electron-energy-loss spectra: Angular dependence, Phys. Rev. B. 53 (1996) 9719–9727. doi:10.1103/PhysRevB.53.9719.

4.5 Analysis of dispersive interactions at polymer/TiAlN interfaces by means of dynamic force spectroscopy

Reproduced from

Analysis of dispersive interactions at polymer/TiAlN interfaces by means of dynamic force spectroscopy

Wiesing, M., Arcos, T. de los, Gebhard, M., Devi, A., Grundmeier, G.

Physical Chemistry and Chemical Physics, 20, 180–190, 2018, doi:10.1039/C7CP05373H

with permission from the PCCP Owner Societies.

Author contributions:

- Planning/experimental work/interpretation/manuscript preparation **MW**
- Deposition of PEALD TiO₂ and Al₂O₃ thin films/proof reading **MG**
- Proof reading **GG, TA and AD**

Placement:

The adhesive interactions between hard coatings and polymers determine their wetting behaviour, the accumulation of polymer on the surface of the coated tool and the release forces required to remove the product from coated mould insert. This study therefore investigates the interaction forces between polycarbonate and Ti_{0.5}Al_{0.5}N hard coatings with focus on the role of the hard coatings surface chemical, electronic and structural properties for the van der Waals forces. The results show that the hard coatings surface is highly polarizable after deposition though being oxidized by exposure to the ambient air. It could be thereby shown that an enhanced oxidation by an oxidative treatment after deposition to form a shallow, fully oxidized mixed Ti_{0.21}Al_{0.45}O surface oxide decreases the van der Waals interactions. Moreover, the quantitative investigation of the chemical origin of the van der Waals forces showed that an increased aluminium concentration within the surface oxide decreases the surfaces polarizability and thereby the adhesion forces even further. Concluding, these results disclose the precise role of the surface chemistry for the van der Waals forces and provide a rational guidance for minimizing these interactions.



Cite this: *Phys. Chem. Chem. Phys.*,
2018, 20, 180

Analysis of dispersive interactions at polymer/ TiAlN interfaces by means of dynamic force spectroscopy†

M. Wiesing, ^a T. de los Arcos,^a M. Gebhard, ^b A. Devi ^b and G. Grundmeier*^a

The structural and electronic origins of the interactions between polycarbonate and sputter deposited TiAlN were analysed using a combined electron and force spectroscopic approach. Interaction forces were measured by means of dynamic force spectroscopy and the surface polarizability was analysed by X-ray photoelectron valence band spectroscopy. It could be shown that the adhesive interactions between polycarbonate and TiAlN are governed by van der Waals forces. Different surface cleansing and oxidizing treatments were investigated and the effect of the surface chemistry on the force interactions was analysed. Intense surface oxidation resulted in a decreased adhesion force by a factor of two due to the formation of a 2 nm thick $\text{Ti}_{0.21}\text{Al}_{0.45}\text{O}$ surface oxide layer. The origin of the residual adhesion forces caused by the mixed $\text{Ti}_{0.21}\text{Al}_{0.45}\text{O}$ surface oxide was clarified by considering the non-retarded Hamaker coefficients as calculated by Lifshitz theory, based on optical data from Reflection Electron Energy Loss Spectroscopy. This disclosed increased dispersion forces of $\text{Ti}_{0.21}\text{Al}_{0.45}\text{O}$ due to the presence of Ti(IV) ions and related Ti 3d band optical transitions.

Received 8th August 2017,
Accepted 20th November 2017

DOI: 10.1039/c7cp05373h

rsc.li/pccp

Introduction

The thermal processing of polymer melts is affected by different interfacial phenomena such as interfacial polymer degradation, corrosion and polymer adhesion to tool surfaces.¹ Especially in the case of polymers used for optical applications such as polycarbonate (PC), these phenomena deteriorate the stability of the process and the quality of the resulting product due to strong adhesion of the polymer to the steel surfaces.² In this regard, the adhesion of polycarbonate is decreased by the application of nitridic hard coatings such as TiAlN, resulting in a reduction of the demoulding forces.² However, PC can still adhere strongly to TiAlN, leading in the case of coated screws to the formation of strongly adhering degradation layers, which form discoloured speckles in extruded films by shear induced release.^{1,2} These phenomena illustrate that the adhesive properties of TiAlN hard coatings for plastic processing applications are of high relevance for the performance of coated tools and a more detailed understanding of the origin of the adhesive interactions is required. This aspect is therefore approached in this

work by investigating the adhesive force interactions of TiAlN hard coatings in contact with polycarbonate.

An important factor for understanding adhesion is the surface chemistry of the interface. For the case of the TiAlN surface earlier studies based on X-ray Photoelectron Spectroscopy (XPS) showed that the residual oxygen in the reactor and the ambient atmosphere results in surface oxidation and the formation of a Ti(IV) containing cover layer.³ Furthermore, sputter depth profiling of TiAlN hard coatings after deposition and exposure to atmosphere disclosed that the surface oxidation of TiAlN includes surface enrichment of aluminium and is accompanied by reactive inward migration of oxygen and the formation of an buried oxynitride growth region.^{4,5} This principal oxidation mechanism was further validated by investigating the early oxidation of TiAlN at reduced pressures of 10^{-6} Pa and at room temperature.^{6,7} Notably, the chemisorption of oxygen on the Ar^+ sputter cleaned TiAlN surface was shown to proceed selectively at superficial Ti atoms due to the interaction with the Ti 3d spill-over electrons. An oxynitride growth region and ultimately a Ti(IV)-containing top layer then develops at increasing pressures. It could be shown that the Ti(IV)-containing top layer was nitrogen doped and segregated when formed at room temperature but was mixed at an atomic scale when oxidizing at elevated temperatures.

In the work presented here, Dynamic Force Spectroscopy (DFS) is used to probe the complex force interactions between TiAlN coated tips and thin polycarbonate films. DFS was

^a Technical and Macromolecular Chemistry, University of Paderborn,
Warburger Straße 100, 33098 Paderborn, Germany.

E-mail: g.grundmeier@tc.uni-paderborn.de

^b Inorganic Chemistry II, Ruhr-Universität Bochum, Universitätsstraße 150,
44801 Bochum, Germany

† Electronic supplementary information (ESI) available: Complementary spectroscopic data, parameters and calculations. See DOI: 10.1039/c7cp05373h

developed recently as a routine method in Ultra High Vacuum Atomic Force Microscopy (UHV-AFM) studies for the investigation interaction forces.^{8–11} This method is based on the measurement of the frequency shift of a vibrating cantilever induced by the tip–sample forces. The frequency shift can then be deconvoluted to obtain the tip–sample force.^{12,13} The key benefit of this method is the stability of the vibrating cantilever, which gives access to the near-contact regime, where soft cantilevers become unstable and snap onto the surface due to the tip–sample forces.¹² Based on the continuity of the determined force curve, this approach allows to distinguish between individual force contributions according to their different decay lengths.¹⁴ Furthermore, three dimensional potential volumes can be probed with pico-newton sensitivity, which is of high relevance for understanding not only atomic scale adhesion but also friction.^{11,15} So far, DFS has not widely been used for studying adhesion to polymeric surfaces and only its general applicability has been demonstrated.¹⁶

The influence of the surface oxidation of a hard coating on adhesion was investigated earlier for the case of amorphous AlYB₁₄ in contact with polyethylene using *ab initio* simulation and UHV atomic force spectroscopy.¹⁷ It was found that the loss of metallic conductivity of AlYB₁₄ upon oxidation increased the adhesion of the polyethylene due to dominating force contributions by dipolar interactions. In addition, the relevance of chemical binding contributions for adhesion has been highlighted for the case of polypropylene and TiAlN.¹⁸ *Ab initio* calculations indicated that the work of separation of polypropylene was largely affected by abstraction of hydrogen atoms or by chain scission, which increase the work of separation by two orders of magnitude. These examples illustrate the complexity of the interactions between hard coatings and polymers. Thus, the forces between PC and TiAlN hard coatings are herein investigated regarding the effect of different surface chemical compositions and structures: TiAlN covered by a complex multi-layered oxide as a result of exposure to ambient atmosphere after deposition and TiAlN after intentional strong surface oxidation.

The results section first presents the chemical properties of the investigated surfaces as they critically affect the adhesion forces. The interaction forces between TiAlN and polycarbonate as determined by DFS are then discussed on the basis of the varying substrate surface chemistries. Finally, the detailed discussion of the electronic origin of the adhesion is supported by comparison with reference materials, valence band spectroscopy and the calculation of Hamaker constants.

Experimental

Thin film deposition

TiAlN and TiAl(O,N) hard coatings were deposited by High Power Pulsed Magnetron Sputtering (HPPMS) using a CemeCon CC-800/9 at the Materials Chemistry division of the RWTH Aachen.³ A rectangular magnetron with a Ti_{0.5}Al_{0.5} compound target was used. The p-Si(100) wafer (1–5 Ω cm) and cantilever (NSC15, Mikromasch) substrates were mounted at a target-to-substrate

Table 1 Bulk stoichiometries of the TiAlN and TiAl(O,N) thin films as determined by XPS after Ar⁺ ion sputtering

Coating	O 1s/at%	N 1s/at%	Ti 2p/at%	Al 2p/at%	Ti/Al
TiAlN	7.6	40.0	21.2	31.2	0.67
TiAl(O,N)	30.2	23.5	18.8	26.8	0.70

distance of 80 mm and were neither heated nor cooled. The base pressure was below 0.2 mPa and the gas flows during deposition were 200 sccm Ar and 50 sccm N₂ for TiAlN and 200 sccm Ar, 50 sccm N₂ and 7 sccm O₂ for TiAl(O,N) resulting in partial pressures of 358 mPa, 91 mPa and 9 mPa, respectively. A Melec HPPMS generator with a frequency of 800 Hz, a duty cycle of 4% and a time-averaged power of 3000 W resulting in peak power densities of around 450 W cm⁻² was used. Thin film deposition was carried out at floating potential. The films deposited on Si wafer were then used for surface chemical analysis by XPS.

The bulk compositions of the coatings were determined by XPS after removal of the surface oxidation layers by Ar⁺ ion sputtering (3 kV, 30 μA cm⁻², 5 min). Due to preferential sputtering of especially the light elements, these values only represent estimates for the stoichiometries of the original films.^{4,19} The bulk stoichiometries shown in Table 1 revealed the presence of around 7 at% oxygen in the TiAlN film presumably as a result of oxygen contaminations present in the chamber during deposition.

As reference materials, TiO₂ and Al₂O₃ thin films of 45 nm thickness were deposited at the Chair II of Inorganic Chemistry at the Ruhr University Bochum on Si-wafer substrates and cantilevers by means of Plasma Enhanced Atomic Layer Deposition (PEALD) employing tetrakis(dimethylamido)-titanium(IV) (TDMAT) and trimethyl-aluminum (TMA) as precursors. TDMAT was synthesized according to literature and was found to be spectroscopically pure (¹H-NMR), while TMA was purchased by Strem Chemicals.²⁰ All depositions were carried out in the reactor chamber described elsewhere; in the case of TiO₂ an earlier optimized process with a growth rate of 0.92 Å per cycle was adopted.²¹ The deposition process for Al₂O₃ was as follows: TMA (STREM, min. 98%) was kept in a stainless steel container at constantly 273 K. The precursor was pulsed for 13 ms followed by Ar-purging (25 sccm, 99.999%, Alfa gas) for 950 ms to remove excess of precursor. After a total of 1000 ms, O₂ was introduced over a time of 500 ms (25 sccm, 99.995%, Alfa gas) while the plasma ignition took place 100 ms after starting the O₂ flow. The plasma step took 200 ms and was again followed by an Ar-purge step to remove reaction by-products and excess of O₂. For all depositions, the substrate holder and reactor chamber were heated to 373 and 333 K, respectively. The growth rate for this Al₂O₃-PEALD process was found to be 1.4 Å per cycle. The TiO₂ and Al₂O₃ PEALD thin films were X-ray amorphous.

A thin plasma polymer film based on hexamethyldisiloxane (PP-HMDSO) was used as reference material with a low surface energy and was deposited on flat Si wafer using a home-built radio frequency reactor. The total pressure during deposition was 30 Pa and the Ar/HMDSO ratio was 6.

The voltage during deposition was 440 V and the power density 0.03 W cm^{-2} . The film was analysed by FTIR and XPS and the results can be found in the ESI.† In essence, the PP-HMDSO is composed of Si–H, Si–CH_x and Si–O–Si groups.

Polymer thin films of polystyrene and polycarbonate were deposited by spin-coating onto Si wafer substrates using 2 wt% polycarbonate/1,4-dioxane and 2 wt% polystyrene/toluol solutions (room temperature, 2000 rpm). All chemicals were of analytical grade and the bisphenol-A polycarbonate (Makrolon 3108, Goodfellow) as well as the polystyrene (193 000 *M_w*, Aldrich) were free of additives. The thickness of the thin films was around 60 nm as determined by spectroscopic ellipsometry and the use of tabulated optical constants (PP-HMDSO was approximated by polydimethylsiloxane (PDMS)).

Electron spectroscopy

X-ray photoelectron spectroscopy was performed on the flat samples using an ESCA+ system (ScientaOmicron) at a base pressure of $<1 \times 10^{-8}$ Pa. Monochromatized Al K α irradiation (1486.7 eV) was used for excitation resulting in an energy resolution of 0.77 eV for high resolution and 2.2 eV for wide-range survey spectra as determined from the FWHM of the Ag 3d_{5/2} line. The angle of emission was 60° relative to the surface normal resulting into a depth of information of 2.8 nm.²² The binding energy scale was referenced to the binding energy of Ag 3d_{5/2} at 368.0 eV. Data evaluation was performed using CasaXPS (v2.3.16). Reflection Electron Energy Loss Spectroscopy (REELS) was measured using an electron beam (Nanofocus 50, Staib Instruments) at an energy of 450 eV for polycarbonate and the O beam oxidized TiAlN and at an energy of 1050 eV for the Al₂O₃ and TiO₂ PEALD thin films. (In the case of the PEALD films the surfaces were cleaned from organic contaminations using the surface cleansing procedure described below.) The energy resolution was 1.0 eV and the angles of incidence and emission were both 30°. The beam was rastered across an area of 0.07 mm² resulting into a current density of 0.44 $\mu\text{A cm}^{-2}$. In order to prevent beam damage, the polycarbonate sample was continuously moved during the measurement limiting the dose to 7.1 $\mu\text{C cm}^{-2}$, where no beam damage was observed.²³

Ion beam treatments

Cantilevers were cleansed before use (“surface cleansing”) by means of an oxygen beam at 0 eV acceleration voltage for 7 min

(GenII, Tectra, Germany). The source was operated in the downstream mode so that the ions were largely thermalized and no net current was observed when biasing the sample to 3.3 V. A more detailed characterization of the source can be found in literature.^{24,25} The UHV system allowed the transfer of the surface-cleansed cantilevers into the AFM while maintaining a pressure of below 1×10^{-7} Pa. Intense oxidation of the TiAlN surface (“O beam oxidation”) was achieved by irradiating the sample with an O beam accelerated by 1.5 kV for 2 min at normal incidence with a flux of around 40 $\mu\text{A cm}^{-2}$. During operation the background pressure of the chamber was around 5×10^{-2} Pa. For XPS valence band spectroscopy and bulk stoichiometric analysis the surface oxides present on the TiAlN and TiAl(O,N) thin films were removed by Ar⁺ sputtering at 3 keV and a flux of 30 $\mu\text{A cm}^{-2}$ for 5 min (Fig05 Ion Gun, Physical Electronics, USA) until the oxygen concentration as determined by XPS was constant.

UHV-AFM

Dynamic Force Spectroscopy (DFS) was measured using a variable temperature AFM (ScientaOmicron) directly attached to the ESCA+ system at a base pressure of $<2 \times 10^{-8}$ Pa. Force spectroscopy was performed in constant amplitude mode using the coated cantilevers with *q* factors of around 3500–4000 mounted on adhesive carbon pads. The frequency shift curves were measured with 25 pm height resolution and a dwell time of 40–60 ms. Around 20 curves were acquired at the same position and averaged for data evaluation. The individual spring constants of the cantilevers were calibrated using the Sader method.^{26,27} The amplitude was calibrated using the constant frequency shift method with increasing amplitudes until the sensitivity was constant (typically 45–50 mV nm⁻¹).²⁸ The frequency shifts were transformed to interaction potentials based on the theoretical approach of Sader and Jarvis.¹³

Results and discussion

Surface chemical characterization by XPS

For DFS measurements the cantilevers coated with the TiAlN hard coating were used after removal of adventitious organic contaminations by means of oxygen beam irradiation at 0 V acceleration voltage for 7 min (“surface cleansing”). The stoichiometry of the TiAlN surface before and after surface cleansing is shown in

Table 2 XPS stoichiometries of the surfaces employed in this study. Surface cleansing refers to the removal of surface organic contaminations present on the atmosphere exposed samples by irradiating the surfaces with an O beam at 0 V acceleration voltage for 7 min. O beam oxidation implies the oxidation of the surfaces by using an O beam accelerated with 1.5 kV for 2 min

Coating	Treatment	C 1s/at%	O 1s/at%	N 1s/at%	Ti 2p/at%	Al 2p/at%	Ti/Al
TiAlN	Atmosphere exposed	25.5	31.1	15.3	7.2	20.8	0.35
	Surface cleansed	1.2	38.7	20.2	11.4	28.5	0.40
	O beam oxidized	0.4	55.2	8.0	11.8	24.6	0.48
TiAl(O,N)	Surface cleansed	0.8	50.0	11.0	13.0	25.2	0.52
TiO ₂	Surface cleansed	0.5	71.3	—	28.2	—	—
Al ₂ O ₃	Surface cleansed	0.3	58.2	—	—	41.5	—

Table 2 and it was observed that the carbon concentration as derived from the C 1s signal was decreased from 25.5 at% to 1.2 at%. The surface cleansing therefore effectively removes the superficial organic contaminations. Concomitantly, the Ti/Al ratio increased from 0.35 to 0.40. This finding is most probably not explained by outward migration of Ti but rather by the loss of the organic contamination layer, which screens the slower Ti 2p photoelectrons more effectively than the faster Al 2p electrons.²⁹ Further, when considering that the bulk Ti/Al ratio is around 0.7 (Table 1), it follows that Al is enriched at the oxidized surface due to outward migration, which is typical for TiAlN hard coatings.⁴ The surface cleansing procedure was also applied to the TiAl(O,N), TiO₂ and Al₂O₃ coated cantilevers and similarly the amount of organic contaminations could be decreased to below 1.0 at% (see Table 2).

For investigating the effect of enhanced surface oxidation on the interaction forces the TiAlN coated cantilevers were oxidized by O beam irradiation at 1.5 kV acceleration voltage for 2 min ("O beam oxidation"). As shown in Table 2, the concentration of oxygen increased after O beam oxidation from 31.1 at% to 55.2 at% indicating intense surface oxidation. The Ti/Al ratio also slightly increased from 0.40 to 0.48 as a result most probably of sputtering damage.³⁰

A more detailed characterization of the surface cleansed and O beam oxidized samples was performed by high-resolution XPS. For the sake of clarity, the discussion is limited to the Ti 2p spectrum but a detailed discussion of the N 1s, O 1s and Al 2p core level spectra can be found in the ESI.†

As shown in Fig. 1a and b, the Ti 2p spectra of the atmosphere exposed and surface cleansed TiAlN surface could be mathematically described by three components located at

455.1, around 456.7 and at 458.3 eV. These peaks are ascribed to the well screened component of non-oxidized TiAlN (455.1 eV), to the oxynitridic TiAl(O,N) growth region and the poorly screened component of non-oxidized TiAlN (both at 456.7 eV) and to a surface oxide with Ti being in the +IV state (458.3 eV). The peak separation due to spin-orbit coupling was fixed to 5.7 eV. The overall line shape is complicated by many-body processes as well as shake-ups and is discussed in detail elsewhere.^{7,31–33} Among these effects, it is noted that in the TiAlN substrate the Ti 2p core hole is supposed to be only partially screened by free d-electrons during the photoemission process.^{31,34} In this regards, electrostatic interactions between the core hole and the valence band pull a d-state down to below the Fermi level. This state can then be filled by a d-electron resulting into a relaxed state and a Ti 2p signal at lower binding energies ("well screened" component) or can be left unoccupied leading to a higher binding energy "poorly screened" component. In accordance to previous reports, the poorly screened component is expected around 457 eV and should overlap with the TiAl(O,N) signal.^{31,32} This shows that different spectral components not necessarily reflect different chemical species.

The components present in the spectrum indicate a complex multi-layered surface oxide which can be described from the bulk to the surface as TiAlN|TiAl(O,N)|(Ti(IV),Al) oxide in agreement with literature.^{5,35} It is noted that the oxynitridic TiAl(O,N) layer resembles the growth region of the surface oxide and develops due to the reactive inward migration of oxygen.⁷ The reactive inward migration mechanism also implies most probably the existence of composition gradients and smooth transitions between the different surface phases.

After surface cleansing, the spectrum in Fig. 1b shows an increase of the Ti(IV) component from 36.8% to 42.3% of the total Ti 2p peak area indicating that the surface was slightly oxidized. As deduced from the fraction of the Ti(IV) and TiAl(O,N) components and by using an effective attenuation length of 1.9 nm, the thicknesses of the Ti(IV) and the TiAl(O,N) layers were 0.5 and 1.8 nm.^{22,29} It is noted that the thickness values herein reported were calculated based on a surface layer model with sharp interfaces, which is not necessarily the case as mentioned above. However, despite the possible presence of related systematic errors such thickness values are supposed to reflect the spatial expansion of layers even in the case of smooth boundaries according to literature.²⁹ Apart from the slight increase of the Ti(IV) component by around 5% and the effective removal of carbon the original surface chemistry was not affected by the surface cleansing procedure and this clearly shows that the cleansed TiAlN cantilevers adequately resemble the surface chemistry of the hard coating.

In contrast, the line shape of the TiAlN surface after O beam oxidation was governed by the presence of the Ti(IV) component at 458.7 eV, which was increased at the expense of the TiAl(O,N) component at 457.1 eV. Further, the component of the non-oxidized TiAlN substrate at 455.1 eV was completely absent. According to its binding energy, the Ti(IV) component might either relate to segregated TiO₂ or mixed TiAlO oxide. This situation was clarified by the O 1s modified Auger

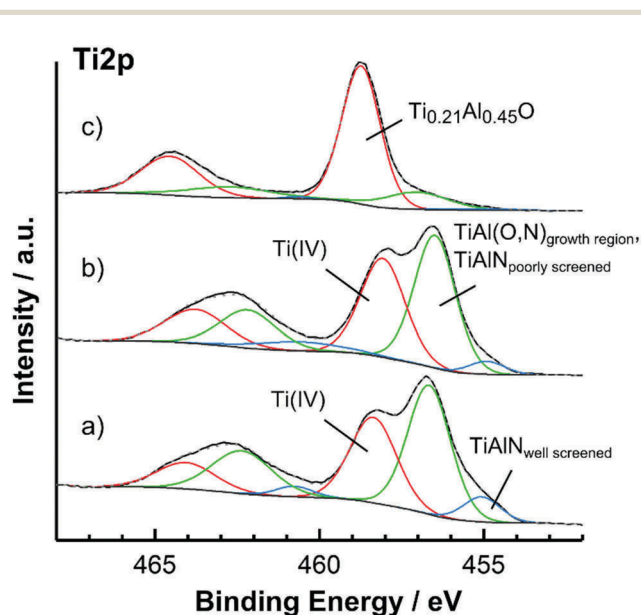


Fig. 1 High resolution Ti 2p spectra of (a) TiAlN after deposition and atmosphere exposure, (b) after surface cleansing by using an O beam at 0 eV for 7 min and (c) after O beam oxidation using an O beam at 1.5 kV for 2 min. The spectra were normalized and shifted vertically for better visualization.

parameter, which was determined to be 1040.6 ± 0.1 eV and indicated by comparison with literature the presence of mixed TiAlO.³⁶ In contrast, the precise composition of the TiAlO at the surface is less clear due to the surface enrichment of Al. However, the composition of this layer can be estimated from the Ti:Al:O ratios obtained by XPS (see Table 2) to be $\text{Ti}_{0.21}\text{Al}_{0.45}\text{O}$. The thickness of the $\text{Ti}_{0.21}\text{Al}_{0.45}\text{O}$ top layer was around 2.0 nm and was increased by O beam oxidation as compared with the thickness of the Ti(IV) top layer of the surface cleansed TiAlN coating. Again it is noted that most probably smooth layer boundaries are present due to atomic mixing during the oxygen bombardment.³⁰ However, the surface oxide layer structure after O beam oxidation is formally described as $\text{TiAlN}|\text{TiAl(O,N)}|\text{Ti}_{0.21}\text{Al}_{0.45}\text{O}$.

The spectra of the atmosphere exposed and surface cleansed TiAl(O,N) films were similar to the case of TiAlN as described above and the same surface oxide layering was observed with the only difference that after surface cleansing the Ti(IV) layer was increased to 0.6 nm and the TiAl(O,N) layer to 2.6 nm thickness. The corresponding spectra can be found in the ESI.†

Contact formation: processes and structures formed during DFS

The interaction forces between the surface cleansed TiAlN and the underlying PC as well as an HMDSO plasma polymer (PP-HMDSO) were analysed by means of DFS. The spectroscopic and topographic analysis of the thin polymer films is shown in the ESI.†

Fig. 2a shows a single frequency shift Δf curve in comparison with an average from subsequently measured curves. It was observed that the frequency shift during approach and retraction of the tip were basically identical but slightly shifted on the height axis, presumably as a result of piezo hysteresis. Furthermore, when measuring repeatedly at the same spot, no

changes of the frequency shift were observed and the contact could be considered as mechanically stable. This fundamental observation shows that the measurement between TiAlN and PC is reversible and reproducible. Consequently, multiple curves were measured and averaged for data evaluation.

It is worth mentioning that the frequency shift did not show discontinuities, which are uniquely related to hysteretic forces.³⁷ This result is counterintuitive, because the polymeric substrate is expected to relax by the formation of a neck accompanied by a hysteresis in the approach and retract curve.^{37,38} This finding is explained when considering that the measured frequency shift is time averaged and that binding and unbinding are statistical processes.³⁷ However, the shape of the Δf curve is further complicated by the formation of single-molecular polymer bridges between tip and sample as discussed below.

Fig. 2b shows minima of averaged frequency shift curves measured on different sample locations alternating on PC and the PP-HMDSO film. PP-HMDSO was studied as a highly cross-linked reference polymer with a low surface energy in analogy to the chemically related polydimethylsiloxane (PDMS). It was observed that the frequency shift minimum reversibly switches when changing the substrate from around -120 Hz in the case of the PP-HMDSO to around -200 Hz when measuring on PC. Consequently, it can be concluded that the unbinding of the TiAlN tip from the polymer substrate occurs reversibly and no material is transferred to the tip.

The measured frequency shift Δf curves were deconvoluted to the related tip-sample forces F_{ts} using the method of Sader and Jarvis and a typical force curve is shown in Fig. 3a.¹³ In order to investigate the effect of the softness of the polymeric substrate, a simulated approach curve based on the MYD model was included for comparison.³⁹ This model describes the contact mechanics based on elastic interactions due to van der Waals forces continuously not only in the contact, but also in the near-contact region. As discussed below, the required

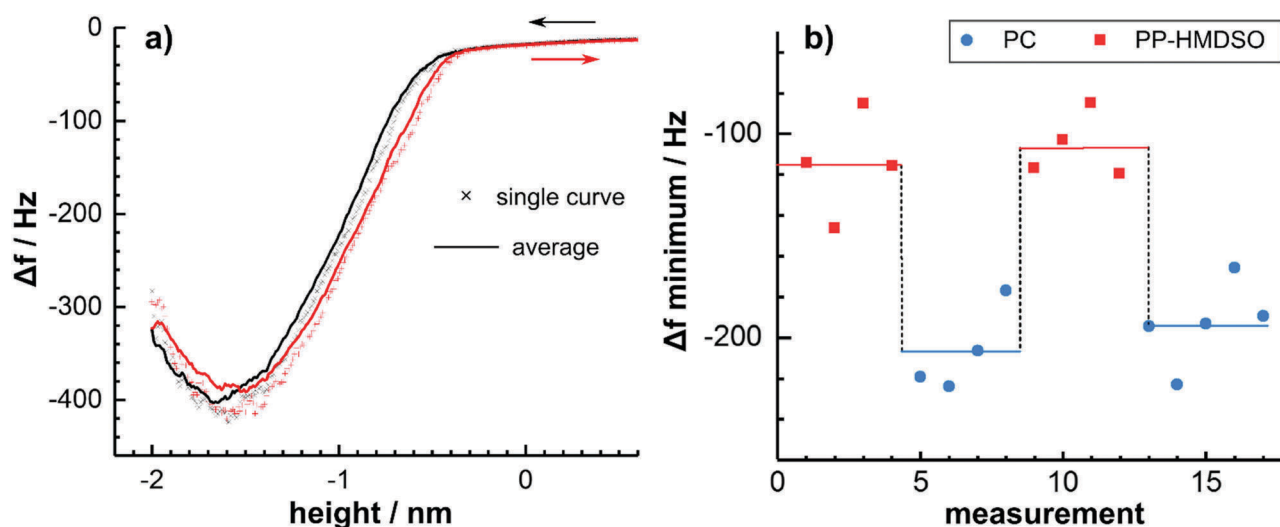


Fig. 2 (a) Single and averaged frequency shift Δf curves measured with the surface cleansed TiAlN tip on PC at the same location; (b) Δf minima of several (averaged) curves when switching the substrate from PP-HMDSO to PC. The lines are guides to the eye and represent the mean value of a measurement series.

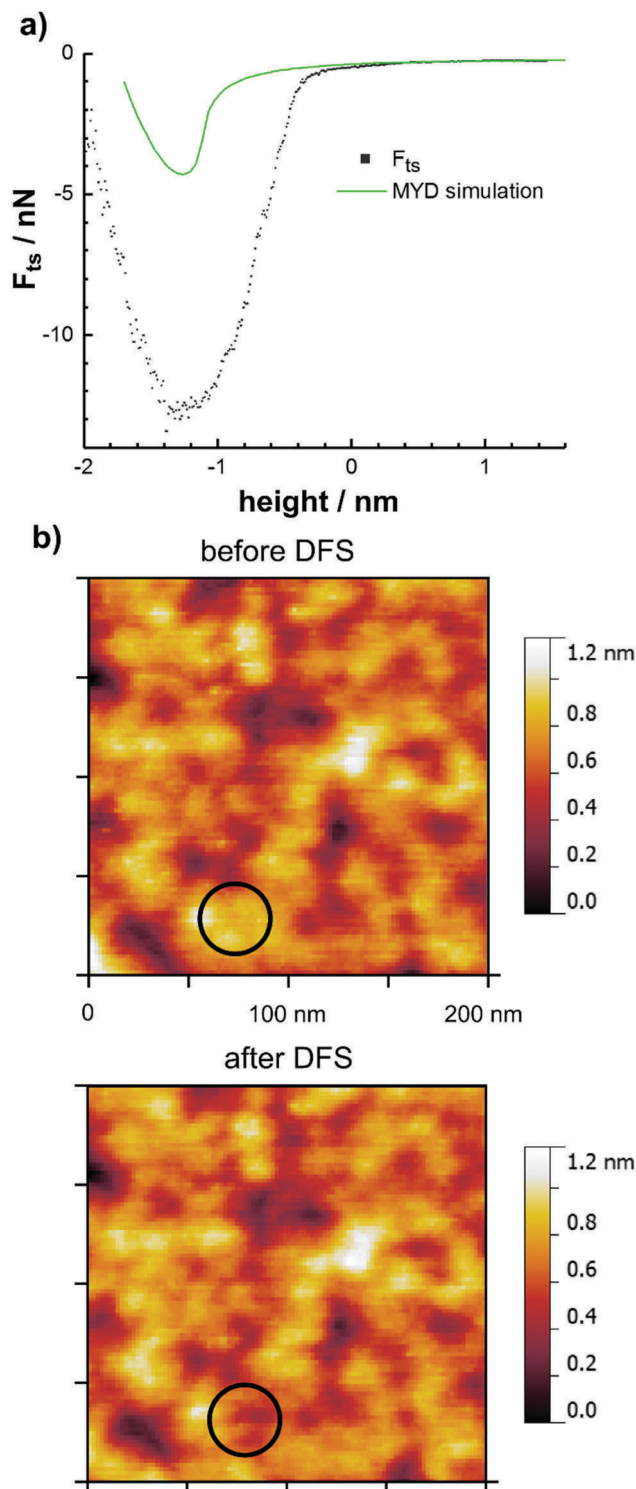


Fig. 3 (a) Typical tip–sample force F_{ts} of the surface cleansed TiAlN tip in contact with PC measured at an amplitude of 19.8 nm. A simulated approach force curve using the MYD model is shown for comparison. (b) Non-contact topographical images before and after acquisition of a frequency shift curve within the highlighted area.

non-retarded Hamaker constant for the interface between polycarbonate and the surface cleansed TiAlN was not available

but was approximated by the constant of the mixed $Ti_{0.21}Al_{0.45}O$ surface oxide in contact with polycarbonate.

The simulated curve shows at a height of around -1 nm a rapid contact formation during the approach due to the formation of an unstable neck as a result of the softness of the polycarbonate.³⁸ However, when comparing the simulated and experimental curves, it follows that these elastic interactions do not describe the situation with sufficient accuracy. As discussed in the following, the shape of the force curve is rather explained by inelastic deformation and the reversible formation of single polymer bridges.

The occurrence of inelastic deformation was revealed by measuring the surface topography before and after DFS as shown in Fig. 3b. The images clearly show that the surface within the contact area deformed during the measurement and this was observed for all investigated tips.

The reversible formation of molecular bridges was observed at a low oscillation amplitude of 3.3 nm in the case of the surface cleansed TiAlN and TiAl(O,N) tips due to strong interaction forces. Fig. 4 shows two typical consecutively measured frequency shift curves.

Upon approach, a positive frequency shift and an increased noise accompanied by an increased excitation amplitude was observed to set in within the non-contact region around -70 Hz (corresponding to 0.3 nN). This behaviour was preserved during retraction and the frequency shift was characterized by discontinuities until a height of around 4 nm. Above this height, the initial behaviour was rapidly recovered. When considering that this behaviour was not observed for large amplitudes, this points to the formation of molecular bridges between the tip and the substrate with a length of around 7 nm. The molecular bridges are thus only stable during an oscillation cycle at lower amplitudes. This interpretation is further corroborated by the fact that the frequency shift induced by the bridge is positive.

This was also observed recently when stretching a dextrane molecule linked to a vibrating cantilever tip and is a result of the increase of the restoring force with separation.⁹ Consequently, the question arises how many polymer chains contribute to bridge formation. As shown in Fig. 4, the stripping-off occurs repeatedly at a height of 4 nm and it is therefore reasonable to assume that basically only a single macromolecule forms the bridge. This is also consistent with the small interaction area involved. The energy dissipation caused by the presence of the molecular polymer bridge tethering the cantilever to the surface was calculated from the excitation amplitude and amounted around 320 eV per oscillation cycle. Since discontinuities were observed in the frequency shift, which require the presence of non-conservative hysteretic forces, the dissipation is explained by inelastic processes as a result of possibly viscoelastic effects or molecular processes induced by the polymer bridge entangled in the surface. In this regards, the related inelastic forces do not significantly contribute to the total interaction force and to adhesion. This follows from the fact that the frequency shift curve of the tethered cantilever is still highly similar to the unbound situation; the differences in the frequency shift are at maximum 20 Hz and would contribute to the complete frequency shift curve as shown

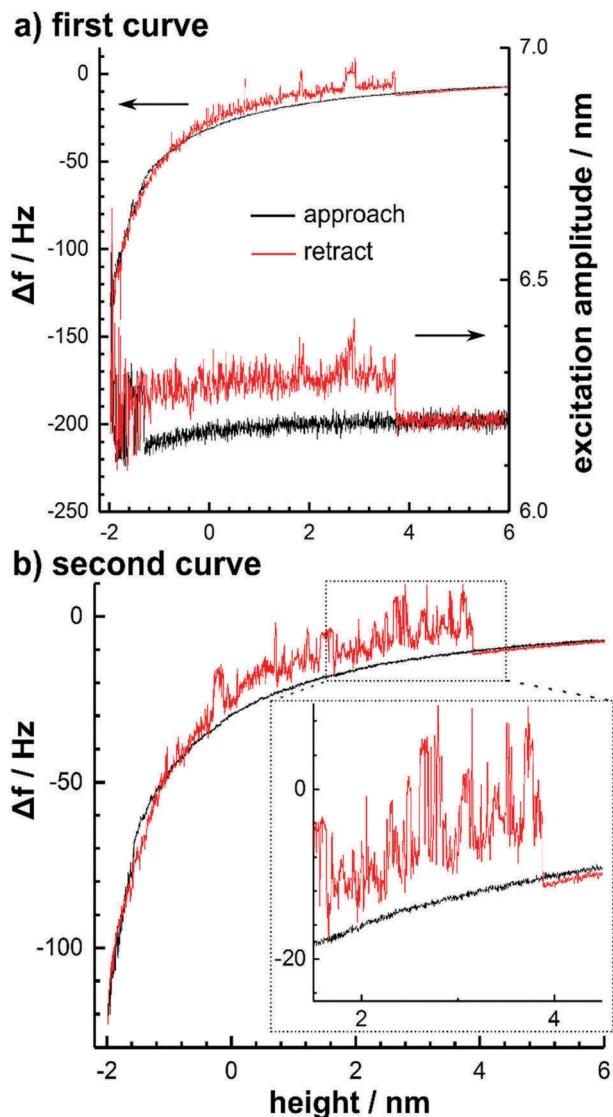


Fig. 4 Two consecutively measured Δf curves on polycarbonate using the surface cleansed TiAlN coated cantilever at an amplitude of 3.3 nm. In (a) the first curve including the excitation amplitude is shown. The subsequently measured Δf curve including a magnification of the snap-off of the polymer chain is shown in (b).

in Fig. 2a only with 1.4 Hz after rescaling to the corresponding amplitude.¹²

Adhesion forces: structural and electronic origins

The interactions between the TiAlN coated tips and the polymer films were investigated after surface cleansing and after O

beam oxidation of the sputter coating. From a chemical perspective no chemical bonds are expected to form between polystyrene and the surface cleansed TiAlN due to its termination with a surface oxide/oxy-nitride. Consequently, the interactions between the surface cleansed TiAlN and polystyrene are assumed to be purely governed by van der Waals interactions.

The results are shown in Table 3. It was observed that the adhesion forces of the surface cleansed TiAlN tip on polycarbonate and polystyrene were not significantly different. This indicates that the carbonate moiety does not significantly affect the adhesion forces and that the interactions between the polycarbonate and the surface cleansed TiAlN coating are governed by van der Waals forces, too.

In contrast, the adhesion force was decreased from 13.5 to 6.9 nN and no molecular bridges were observed after performing the O beam oxidation of the hard coating. This can be explained by a decrease of the van der Waals forces due to the formation of the 2.0 nm thick $\text{Ti}_{0.21}\text{Al}_{0.45}\text{O}$ oxide layer which is accompanied by a loss of polarizability, because the free d-electrons are captured by oxygen during oxidation.

More interestingly, this shows that in the case of the surface cleansed TiAlN the adhesion is substantially increased by the oxy-nitride layer and possibly also the pure nitride phase beneath. This interpretation is consistent with a recent electrochemical characterization of the TiAlN hard coating where the oxy-nitride layer was shown to be highly polarizable.³⁵

Since the van der Waals forces are ultimately related to the electronic properties of the materials, the samples were investigated by XPS valence band spectroscopy. Fig. 5 shows the spectra of TiAlN as obtained after surface cleansing and O beam oxidation. For comparison, the spectra of TiAlN and also that of the TiAl(O,N) coating are included as obtained after removal of the surface oxides by means of Ar^+ sputter cleansing.

The valence band spectra of all samples were characterized by two bands located between 11 to 3 eV and at 0.5 eV, which are ascribed to the mixed N 2p/O 2p/Al 3p band hybridized with Ti 3d states and to the Ti 3d band.⁴⁰ As shown earlier by REELS, these bands provide the optical response of the surfaces up to energies of around 15 eV.⁴⁰ In contrast, higher binding energy levels present in the valence band such as the N 2s and O 2s levels are not relevant for the optical properties. Thus, only the p- and d-band related transitions can be considered to determine the dispersive properties of the surfaces.

When comparing all valence band spectra it was found that the d-electron density and therefore the amount of metal-like electrons were highest in the Ar^+ sputter cleansed TiAlN and TiAl(O,N) coatings. In the case of the surface cleansed TiAlN the

Table 3 Adhesion forces between the surface cleansed and O beam oxidized TiAlN tip and polycarbonate or polystyrene thin film substrates. The measurements were performed using a single cantilever with a tip radius of 23 nm and the adhesion force was determined as an average of seven measurements

Tip	Surface chemical structure	Polymer	F_{ad} (nN)	Bridge formation
Surface cleansed TiAlN	TiAlN TiAl(O,N) (Ti(IV),Al) oxide	PC	13.5 ± 1.1	Yes
Surface cleansed TiAlN	TiAlN TiAl(O,N) (Ti(IV),Al) oxide	PS	14.3 ± 1.3	Yes
O beam oxidized TiAlN	TiAlN TiAl(O,N) $\text{Ti}_{0.21}\text{Al}_{0.45}\text{O}$	PC	6.9 ± 0.70	No

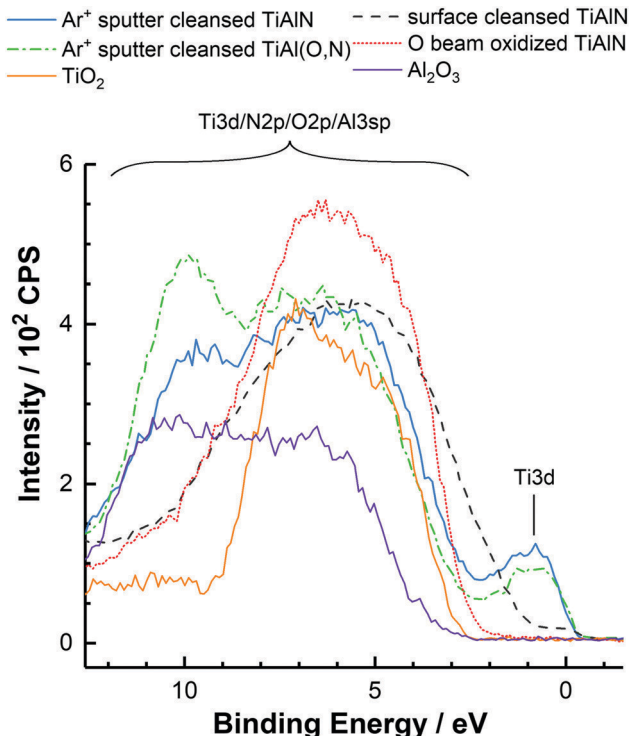


Fig. 5 XPS valence band spectra of the TiAlN coating after surface cleansing, O beam oxidation and Ar⁺ sputter cleaning. For comparison, the spectrum of a deposited TiAl(O,N) sample after Ar⁺ sputter cleansing is shown together with the spectra of TiO₂ and Al₂O₃ PEALD samples after surface cleansing.

d-electron density was decreased as a result of oxidation at ambient conditions after the deposition of the hard coating. In addition to that, also the band gap region between the p- and d-bands at around 1.5 eV was filled with states from the p-band probably as a result of nitrogen doping.⁷ Following O beam oxidation the occupied states near the Fermi level up to a binding energy of 2.5 eV were basically completely removed. These findings clearly show that significant amounts of states close to the Fermi level are occupied in the near-surface region of the surface cleansed TiAlN in contrast to the O beam oxidized case. This in turn indicates an increased polarizability of the surface cleansed TiAlN in agreement with the measured adhesion forces.

Moreover, the valence band spectra disclosed a high degree of resemblance of the valence band structures of Ar⁺ sputter cleansed TiAlN and TiAl(O,N). Only the d-electron density in the Ar⁺ sputter cleansed TiAl(O,N) was decreased by around 13% and the intensity around 10 eV was increased as a result of increased O 2p contributions.⁴¹ This shows that the exchange of lattice nitrogen atoms in TiAlN with oxygen to form TiAl(O,N) does not require the loss of the metallic properties in terms of the Ti 3d electron density. Thus, the characterization of the adhesive properties of the TiAlN hard coating so far should also principally apply to the case of TiAl(O,N) coatings. This supposition was validated by measuring the adhesion on polycarbonate with a TiAl(O,N) coated tip after oxidation due to

Table 4 Adhesion forces and non-retarded Hamaker constants across vacuum as calculated from Lifshitz theory by REELS based optical data. The relative uncertainty of the adhesion forces due to the calibration procedures was estimated to 20%

Interface	A_h (10^{-21} J)	F_{ad} (nN nm ⁻¹)	Polymer bridging
Surface cleansed TiAlN PC	—	0.60 ± 0.12	Yes
Surface cleansed TiAl(O,N) PC	—	0.53 ± 0.10	Yes
Ti _{0.21} Al _{0.45} O PC	134	0.29 ± 0.06^a	No
TiO ₂ PC	149	0.52 ± 0.10	No
Al ₂ O ₃ PC	111	0.31 ± 0.06	No

^a As measured with the O beam oxidized TiAlN tip covered with 2 nm Ti_{0.21}Al_{0.45}O.

exposure to atmosphere and surface cleansing. As shown in Table 4 the adhesion was 0.53 ± 0.10 nN nm⁻¹ and did thus not significantly differ from the adhesion measured with the surface cleansed TiAlN tip, which was around 0.60 ± 0.12 nN nm⁻¹.

So far, the influence of the only partially oxidized and highly polarizable sublayers of surface cleansed TiAlN on the adhesion forces has been investigated. In the following, the role of the Ti(IV) and Al(III) ions in the Ti_{0.21}Al_{0.45}O mixed oxide, which terminates the surface of TiAlN after the intense O beam oxidation, is clarified based on DFS measurements and a complementary Lifshitz calculation of non-retarded Hamaker constants.

The calculation was based on optical data derived from REELS spectra measured on smooth amorphous TiO₂ and Al₂O₃ PEALD films samples after removal of organic contaminations by surface cleansing. The advantage of the determination of the optical data by means of REELS is that the Ti_{0.21}Al_{0.45}O mixed oxide can be investigated directly in form of the 2 nm thin surface oxide layer on the O beam oxidized TiAlN sample. This is possible due to the low energy of the primary electron beam (450 eV) resulting into a depth-information of around 1 nm. The same beam energy was also used for the polycarbonate and polystyrene surfaces in order to avoid beam damage.²³ The beam energy used for the TiO₂ and Al₂O₃ samples was instead set to 1050 eV corresponding to a depth-information of around 2 nm in order to mitigate possible surface effects. The optical data of these materials were determined in form of the band gaps and the UV dielectric functions by quantitative evaluation of the REELS spectra using the QUEELS- $\epsilon(\omega, k)$ -REELS software package.^{23,42,43} It is noted that this procedure involves first the separation of the main elastic peak in a REELS spectrum from the loss region, which is then deconvoluted in order to correct for losses from multiple scattering events and to obtain then the experimental single electron scattering cross section λK . This cross section is on the other hand simulated based on an empirical dielectric function, which is optimized until optimal agreement between experiment and simulation is found. However, in the case of the TiAlN and TiAl(O,N) hard coatings intraband transitions remained unresolved and these materials could thus not be analysed due to an erroneous experimental cross section.

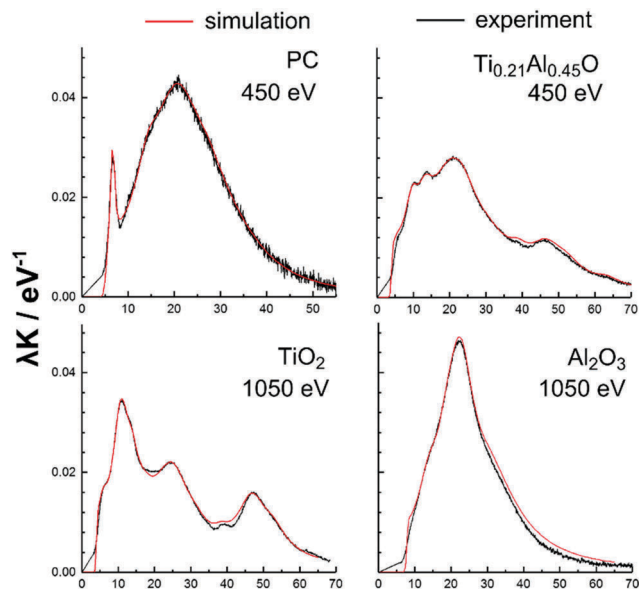


Fig. 6 Experimental (grey) and simulated (red) inelastic scattering cross sections λK of polycarbonate, TiO_2 , Al_2O_3 and the $\text{Ti}_{0.21}\text{Al}_{0.45}\text{O}$ surface oxide are shown in Fig. 6 for comparison. An excellent agreement was found between the experimental and theoretical curves illustrating the high quality of the dielectric function. In this regards, the band gaps used for the dielectric functions were 4.2 eV for polycarbonate and 3.2 eV for TiO_2 and thus in agreement with literature.⁴⁴ The band gap of Al_2O_3 was found to be 6.2 eV and was thus decreased when compared with the literature values of $\gamma\text{-Al}_2\text{O}_3$ (7.1 eV) and $\alpha\text{-Al}_2\text{O}_3$ (8.4 eV) as a result of its amorphous structure.⁴⁵ The band gap of the mixed $\text{Ti}_{0.21}\text{Al}_{0.45}\text{O}$ could be determined to 3.4 eV. This value is close to TiO_2 and reveals that the optical response of $\text{Ti}_{0.21}\text{Al}_{0.45}\text{O}$ near the band gap originates from Ti 3d-band related transitions due to the presence of the $\text{Ti}(\text{iv})$ ion.

The experimental and simulated inelastic scattering cross sections λK of polycarbonate, TiO_2 , Al_2O_3 and the $\text{Ti}_{0.21}\text{Al}_{0.45}\text{O}$ surface oxide are shown in Fig. 6 for comparison. An excellent agreement was found between the experimental and theoretical curves illustrating the high quality of the dielectric function. In this regards, the band gaps used for the dielectric functions were 4.2 eV for polycarbonate and 3.2 eV for TiO_2 and thus in agreement with literature.⁴⁴ The band gap of Al_2O_3 was found to be 6.2 eV and was thus decreased when compared with the literature values of $\gamma\text{-Al}_2\text{O}_3$ (7.1 eV) and $\alpha\text{-Al}_2\text{O}_3$ (8.4 eV) as a result of its amorphous structure.⁴⁵ The band gap of the mixed $\text{Ti}_{0.21}\text{Al}_{0.45}\text{O}$ could be determined to 3.4 eV. This value is close to TiO_2 and reveals that the optical response of $\text{Ti}_{0.21}\text{Al}_{0.45}\text{O}$ near the band gap originates from Ti 3d-band related transitions due to the presence of the $\text{Ti}(\text{iv})$ ion.

The influence of this electronic effect in $\text{Ti}_{0.21}\text{Al}_{0.45}\text{O}$ on adhesion is investigated in the following by calculating the non-retarded Hamaker constants across vacuum based on the UV dielectric functions. It is noted that generally the consideration of UV frequencies above the cut-off wavelength only as in the present case is supposed to be sufficient for typical insulators.⁴⁶ The calculation of the non-retarded constants was based on the exact Lifshitz formula for non-magnetic materials and is along with a parametric description of the dielectric functions documented in the ESI.† The non-retarded Hamaker constants of the different tip-sample contacts are shown in Table 4. The non-retarded Hamaker constants were 149×10^{-21} J for $\text{TiO}_2|\text{PC}$, 134×10^{-21} J for the mixed $\text{Ti}_{0.21}\text{Al}_{0.45}\text{O}|\text{PC}$ and 111×10^{-21} J for $\text{Al}_2\text{O}_3|\text{PC}$. Consequently, the dispersive interactions of $\text{Ti}_{0.21}\text{Al}_{0.45}\text{O}$ with polycarbonate increase with the Ti/Al ratio as a result of an enhanced polarizability due to contributions of d-band related optical transitions caused by the $\text{Ti}(\text{iv})$ ion.

Further, the Hamaker constant of $\text{Ti}_{0.21}\text{Al}_{0.45}\text{O}$ is located in between that of the pure Ti- and Al-oxides and therefore follows the bulk Ti/Al metal ratio of the TiAlN , which is around 1.

In comparison, the corresponding experimental adhesion forces of TiO_2 and Al_2O_3 were 0.52 and 0.31 nN nm^{-1} and that of the $\text{Ti}_{0.21}\text{Al}_{0.45}\text{O}$ covered tip 0.29 nN nm^{-1} . Considering that the accuracy is not better than 20% when comparing different cantilevers as a result of the spring and sensitivity calibrations and that also the slightly different tip shapes affect the comparability (see the ESI,† for electron microscopy images of the tips employed), these findings are generally in good agreement with the calculated Hamaker constants.

Moreover, the formation of polymer bridges between polycarbonate and TiO_2 and Al_2O_3 was not observed (as opposed to the case of TiAlN and $\text{TiAl}(\text{O},\text{N})$), which is in agreement with the observed lower adhesion forces. The valence band spectra of TiO_2 and Al_2O_3 shown in Fig. 5 show a structureless band gap without the presence of significant amounts of occupied states below the Fermi level, which reflect the insulating character of TiO_2 and Al_2O_3 and therefore their decreased polarizability compared with TiAlN or $\text{TiAl}(\text{O},\text{N})$.

Conclusions

The surface chemical analysis of the TiAlN hard coating by XPS showed that the surface was oxidized due to exposure to atmosphere after deposition and could be described by a complex multi-layered surface oxide consisting of an oxynitridic growth region covered by a fully oxidized top layer including $\text{Ti}(\text{iv})$ ions. It was further shown that organic contaminations present on this surface could be effectively removed by an *in vacuo* surface cleansing procedure involving an oxygen beam without significantly oxidizing the hard coatings surface itself (“surface cleansed”). This surface treatment enabled defined adhesion DFS measurements by means of the UHV-AFM.

The investigation of the interaction forces between spin-cast PC and a cantilever coated with surface cleansed TiAlN by means of DFS was shown to be reversible without the occurrence of material transfer. However, single-molecular polymer bridges formed reversibly between the tip and the polycarbonate as a result of the strong interactions between these materials. In this regards, the analysis of the adhesion force showed that the interactions were governed by van der Waals forces, which mainly originate from the interactions of the polycarbonate with the only partially oxidized and therefore highly polarizable subsurface region of the coating. In agreement with this result, intense surface oxidation of the TiAlN coated tip decreased the adhesion force by a factor of two due to the formation of a 2.0 nm thick mixed $\text{Ti}_{0.21}\text{Al}_{0.45}\text{O}$ oxide top layer and inhibited the formation of molecular bridges.

The electronic origin of the high polarizability of the subsurface region of surface cleansed TiAlN was revealed by XPS valence band spectroscopy and could be related to a joint effect of residual metal-like Ti 3d electrons at the Fermi level and the presence of p-band related occupied states at low binding

energies. Further, the comparison of the valence band spectra of TiAlN and TiAl(O,N) after removal of the surface oxides showed that the formation of TiAl(O,N) by exchange of lattice nitrogen atoms in TiAlN with oxygen does basically not affect the metallic properties of the coating. As supported by adhesion force measurements, the dispersive interaction forces of TiAl(O,N) hard coatings can thus also be understood based on the TiAlN model system employed in this study.

In the case of fully oxidized TiAlN, which is covered by $\text{Ti}_{0.21}\text{Al}_{0.45}\text{O}$, the combined analysis of REELS spectra, non-retarded Hamaker constants and adhesion forces revealed that the Ti(IV) ion present in the mixed oxide provides Ti 3d band related transitions close to the band gap of 3.4 eV and thereby enhances the polarizability of the oxide. In consequence, also the van der Waals and adhesion forces increase with the Ti/Al ratio of the mixed oxide.

Conflicts of interest

The authors declare no competing financial interest.

Acknowledgements

We gratefully acknowledge the financial supports of the German Research Foundation within the collaboration research centre SFB TR-87 subprojects A2, A3 and B4. We also kindly thank Holger Rieß and Prof. Dr Jochen M. Schneider from the Materials Chemistry division of the RWTH Aachen for providing the hard coatings.

References

- 1 E. J. Bienk and N. J. Mikkelsen, Application of advanced surface treatment technologies in the modern plastics moulding industry, *Wear*, 1997, **207**, 6–9.
- 2 K. Bobzin, R. Nickel, N. Bagcivan and F. D. Manz, PVD—Coatings in Injection Molding Machines for Processing Optical Polymers, *Plasma Processes Polym.*, 2007, **4**, S144–S149.
- 3 C. Gnoth, C. Kunze, M. Hans, M. Baben, J. Emmerlich, J. M. Schneider and G. Grundmeier, Surface chemistry of TiAlN and TiAlNO coatings deposited by means of high power pulsed magnetron sputtering, *J. Phys. D: Appl. Phys.*, 2013, **46**, 084003.
- 4 S. Hofmann and H. A. Jehn, Selective oxidation and chemical state of Al and Ti in $(\text{Ti,Al})_n$ coatings, *Surf. Interface Anal.*, 1988, **12**, 329–333.
- 5 S. Hofmann, Formation and diffusion properties of oxide films on metals and on nitride coatings studied with Auger electron spectroscopy and X-ray photoelectron spectroscopy, *Thin Solid Films*, 1990, **193–194**(Part 2), 648–664.
- 6 C. Kunze, D. Music, M. Baben, J. M. Schneider and G. Grundmeier, Temporal evolution of oxygen chemisorption on TiAlN, *Appl. Surf. Sci.*, 2014, **290**, 504–508.
- 7 M. Wiesing, T. de los Arcos and G. Grundmeier, The Thermal Oxidation of TiAlN High Power Pulsed Magnetron Sputtering Hard Coatings as Revealed by Combined Ion and Electron Spectroscopy, *Adv. Mater. Interfaces*, 2017, 1600861.
- 8 P. U. D. Schwarz and D. H. Hölscher, in *Scanning Probe Microscopy*, ed. S. Kalinin and A. Gruverman, Springer, New York, 2007, pp. 506–533.
- 9 H. Hölscher, D. Ebeling, J.-E. Schmutz, M. M. Schäfer and B. Anczykowski, in *Scanning Probe Microscopy in Nanoscience and Nanotechnology*, ed. B. Bhushan, Springer Berlin Heidelberg, 2010, pp. 3–21.
- 10 M. Z. Baykara and U. D. Schwarz, in *Noncontact Atomic Force Microscopy*, ed. S. Morita, F. J. Giessibl, E. Meyer and R. Wiesendanger, Springer International Publishing, 2015, pp. 9–28.
- 11 A. Schirmeisen, H. Hölscher and U. D. Schwarz, in *Noncontact Atomic Force Microscopy*, ed. S. Morita, F. J. Giessibl and R. Wiesendanger, Springer Berlin Heidelberg, 2009, pp. 95–119.
- 12 F. J. Giessibl, Forces and frequency shifts in atomic-resolution dynamic-force microscopy, *Phys. Rev. B: Condens. Matter Mater. Phys.*, 1997, **56**, 16010–16015.
- 13 J. E. Sader and S. P. Jarvis, Accurate formulas for interaction force and energy in frequency modulation force spectroscopy, *Appl. Phys. Lett.*, 2004, **84**, 1801–1803.
- 14 M. Guggisberg, M. Bammerlin, C. Loppacher, O. Pfeiffer, A. Abdurixit, V. Barwich, R. Bennewitz, A. Baratoff, E. Meyer and H.-J. Güntherodt, Separation of interactions by noncontact force microscopy, *Phys. Rev. B: Condens. Matter Mater. Phys.*, 2000, **61**, 11151–11155.
- 15 E. T. Herruzo, H. Asakawa, T. Fukuma and R. Garcia, Three-dimensional quantitative force maps in liquid with 10 piconewton, angstrom and sub-minute resolutions, *Nanoscale*, 2013, **5**, 2678–2685.
- 16 A. Schirmeisen, D. Weiner and H. Fuchs, Measurements of metal–polymer adhesion properties with dynamic force spectroscopy, *Surf. Sci.*, 2003, **545**, 155–162.
- 17 O. Hunold, M. Wiesing, T. de los Arcos, D. Music, G. Grundmeier and J. M. Schneider, Influence of O_2 exposure on the interaction between CH_4 and amorphous AlYB14, *Appl. Surf. Sci.*, 2017, **392**, 1165–1172.
- 18 D. Music, D. Lange, L. Raumann, M. Baben, F. von Fragstein and J. M. Schneider, Polypropylene–MAIN (M = Ti, Cr) interface interactions, *Surf. Sci.*, 2012, **606**, 986–989.
- 19 R. T. Haasch, T.-Y. Lee, D. Gall, J. E. Greene and I. Petrov, Epitaxial TiN(001) Grown and Analyzed In situ by XPS and UPS. II. Analysis of Ar^+ Sputter Etched Layers, *Surf. Sci. Spectra*, 2000, **7**, 204–212.
- 20 D. C. Bradley and I. M. Thomas, 765. Metallo-organic compounds containing metal–nitrogen bonds. Part I. Some dialkylamino-derivatives of titanium and zirconium, *J. Chem. Soc.*, 1960, 3857–3861.
- 21 M. Gebhard, F. Mitschker, M. Wiesing, I. Giner, B. Torun, T. de los Arcos, P. Awakowicz, G. Grundmeier and A. Devi, An efficient PE-ALD process for TiO_2 thin films employing a new Ti-precursor, *J. Mater. Chem. C*, 2016, **4**, 1057–1065.

- 22 C. J. Powell and A. Jablonski, *NIST Electron Effective-Absorption-Length Database*, National Institute of Standards and Technology, Gaithersburg, MD, 2011.
- 23 D. Tahir and S. Tougaard, Electronic and optical properties of selected polymers studied by reflection electron energy loss spectroscopy, *J. Appl. Phys.*, 2012, **111**, 054101.
- 24 C. Corbella, S. Grosse-Kreul, O. Kreiter, T. de los Arcos, J. Benedikt and A. von Keudell, Particle beam experiments for the analysis of reactive sputtering processes in metals and polymer surfaces, *Rev. Sci. Instrum.*, 2013, **84**, 103303.
- 25 R. Anton, T. Wiegner, W. Naumann, M. Liebmann, C. Klein and C. Bradley, Design and performance of a versatile, cost-effective microwave electron cyclotron resonance plasma source for surface and thin film processing, *Rev. Sci. Instrum.*, 2000, **71**, 1177–1180.
- 26 J. E. Sader, J. A. Sanelli, B. D. Adamson, J. P. Monty, X. Wei, S. A. Crawford, J. R. Friend, I. Marusic, P. Mulvaney and E. J. Bieske, Spring constant calibration of atomic force microscope cantilevers of arbitrary shape, *Rev. Sci. Instrum.*, 2012, **83**, 103705.
- 27 M. J. Higgins, R. Proksch, J. E. Sader, M. Polcik, S. M. Endoo, J. P. Cleveland and S. P. Jarvis, Noninvasive determination of optical lever sensitivity in atomic force microscopy, *Rev. Sci. Instrum.*, 2006, **77**, 013701.
- 28 G. H. Simon, M. Heyde and H.-P. Rust, Recipes for cantilever parameter determination in dynamic force spectroscopy: spring constant and amplitude, *Nanotechnology*, 2007, **18**, 255503.
- 29 S. Hofmann, *Auger- and X-Ray Photoelectron Spectroscopy in Materials Science*, Springer, 2013.
- 30 S. Hofmann, Sputter depth profile analysis of interfaces, *Rep. Prog. Phys.*, 1998, **61**, 827.
- 31 L. Porte, L. Roux and J. Hanus, Vacancy effects in the X-ray photoelectron spectra of TiN_x, *Phys. Rev. B: Condens. Matter Mater. Phys.*, 1983, **28**, 3214–3224.
- 32 A. Arranz and C. Palacio, Screening effects in the Ti 2p core level spectra of Ti-based ternary nitrides, *Surf. Sci.*, 2006, **600**, 2510–2517.
- 33 G. Greczynski and L. Hultman, Self-consistent modelling of X-ray photoelectron spectra from air-exposed polycrystalline TiN thin films, *Appl. Surf. Sci.*, 2016, **387**, 294–300.
- 34 P. Prieto and R. E. Kirby, X-ray photoelectron spectroscopy study of the difference between reactively evaporated and direct sputter-deposited TiN films and their oxidation properties, *J. Vac. Sci. Technol., A*, 1995, **13**, 2819–2826.
- 35 M. Wiesing, M. Baben, J. M. Schneider, T. de los Arcos and G. Grundmeier, Combined Electrochemical and Electron Spectroscopic Investigations of the Surface Oxidation of TiAlN HPPMS Hard Coatings, *Electrochim. Acta*, 2016, **208**, 120–128.
- 36 R. Cremer, M. Witthaut and D. Neuschütz, Electron spectroscopy applied to metastable ceramic solution phases, *Fresenius' J. Anal. Chem.*, 1999, **365**, 28–37.
- 37 B. Gotsmann and H. Fuchs, The measurement of hysteretic forces by dynamic AFM, *Appl. Phys. A: Mater. Sci. Process.*, 2014, **72**, S55–S58.
- 38 D. Krüger, B. Anczykowski and H. Fuchs, Physical properties of dynamic force microscopies in contact and noncontact operation, *Ann. Phys.*, 1997, **509**, 341–363.
- 39 V. M. Muller, V. S. Yushchenko and B. V. Derjaguin, General theoretical consideration of the influence of surface forces on contact deformations and the reciprocal adhesion of elastic spherical particles, *J. Colloid Interface Sci.*, 1983, **92**, 92–101.
- 40 I. leR. Strydom and S. Hofmann, XPS and EELS study of the valence band electronic structure of TiN and (Ti,Al)N coatings as influenced by the deposition parameters, *Vacuum*, 1990, **41**, 1619–1623.
- 41 M. Baben, L. Raumann and J. M. Schneider, Phase stability and elastic properties of titanium aluminum oxynitride studied by ab initio calculations, *J. Phys. D: Appl. Phys.*, 2013, **46**, 084002.
- 42 S. Tougaard and F. Yubero, QUEELS software package for calculation of surface effects in electron spectra, *Surf. Interface Anal.*, 2004, **36**, 824–827.
- 43 S. Tougaard and I. Chorkendorff, Differential inelastic electron scattering cross sections from experimental reflection electron-energy-loss spectra: Application to background removal in electron spectroscopy, *Phys. Rev. B: Condens. Matter Mater. Phys.*, 1987, **35**, 6570–6577.
- 44 M. D. Migahed and H. M. Zidan, Influence of UV-irradiation on the structure and optical properties of polycarbonate films, *Curr. Appl. Phys.*, 2006, **6**, 91–96.
- 45 D. Tahir, H. L. Kwon, H. C. Shin, S. K. Oh, H. J. Kang, S. Heo, J. G. Chung, J. C. Lee and S. Tougaard, Electronic and optical properties of Al₂O₃/SiO₂ thin films grown on Si substrate, *J. Phys. D: Appl. Phys.*, 2010, **43**, 255301.
- 46 V. A. Parsegian, *van der Waals Forces: A Handbook for Biologists, Chemists, Engineers, and Physicists*, Cambridge University Press, Cambridge, 2005.

Analysis of dispersive interactions at polymer/TiAlN interfaces by means of Dynamic Force Spectroscopy

M. Wiesing^{a)}, T. de los Arcos^{a)}, M. Gebhard^{b)}, A. Devi^{b)}, G. Grundmeier^{a)}

^{a)} Technical and Macromolecular Chemistry, University of Paderborn, Warburger Straße 100, 33098 Paderborn, Germany

^{b)} Inorganic Chemistry II, Ruhr-Universität Bochum, Universitätsstraße 150, 44801 Bochum, Germany

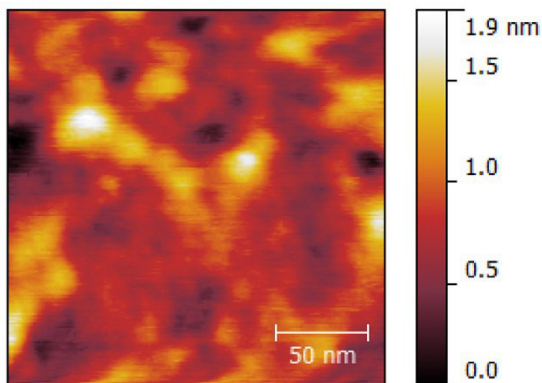
Correspondence to: Guido Grundmeier (E-mail: g.grundmeier@tc.uni-paderborn.de)

Supporting Information

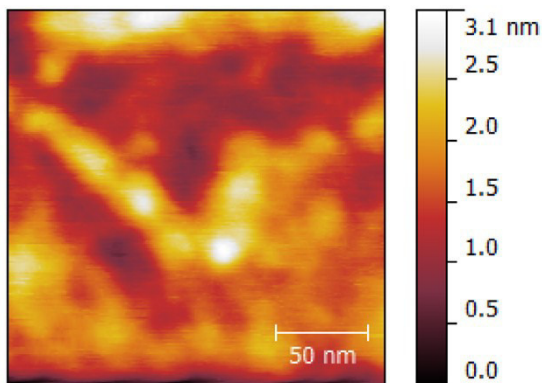
Surface topography of the polymer thin films

The surface topographies of the employed polymer thin films are shown in Figure S 1.

a) PC



b) PS



c) PP-HMDSO

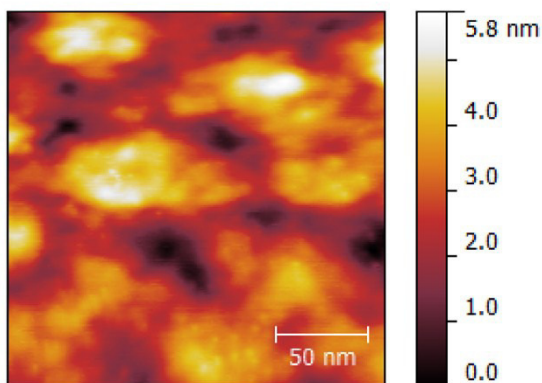


Figure S 1: Non-contact AFM surface topographies of the **a)** PC, **b)** PS and **c)** PP-HMDSO polymer thin films measured with an XSC11 cantilever (Mikromasch, $k = 45 \text{ N m}^{-1}$).

Surface chemical analysis of the polymer thin films by FTIR and XPS

Figure S 2 shows the FTIR spectrum of the PP-HMDSO deposited on an Al mirror and measured in reflection geometry. The bands observed were typical for the HMDSO plasma polymer and were located at 2960 (CH_3 stretch), 2908 (CH_2 stretch), 2154 (Si-H), 1264 (Si- CH_3 sym. deformation), 1107 (Si-O-Si, Si-O-C stretch), 847 (Si- CH_2 sym. rocking) and 809 cm^{-1} (Si- CH_2 asym. rocking).[1] The main building blocks of the PP-HMDSO were therefore Si-H, Si- $\text{CH}_{2/3}$ and Si-O groups.

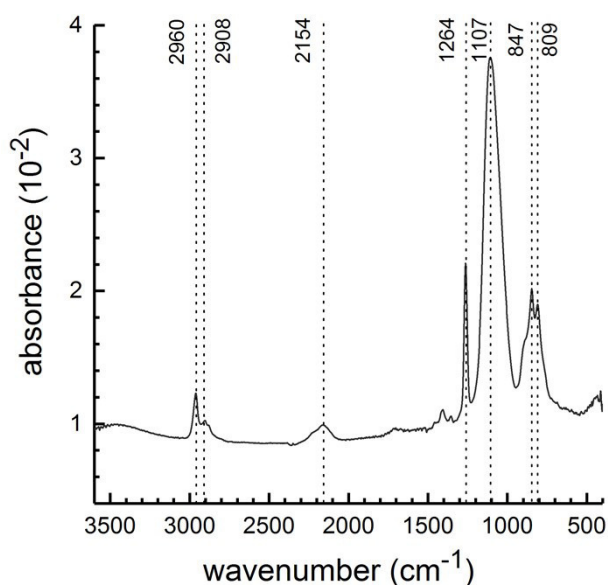


Figure S 2: FTIR of the PP-HMDSO deposited on an Al mirror and measured in reflection geometry.

The XPS stoichiometry of the PP-HMDSO film was as shown in 28 at% O, 40.5 at% C and 31.5 at% Si as shown in Table S 1. Compared with the monomer composition of 11 at% O, 66 at% C and 23 at% Si the O concentration was therefore increased at the expense of the C concentration. This might be a result from oxidation due to residual oxygen present in the plasma chamber.

Table S 1: Surface stoichiometries of the polymer thin films as measured by XPS at an angle of emission of 15° relative to the surface normal.

	C1s / at%	O1s / at%	Si2p / at%
PC	84.8	15.2	-
PS	100	-	-
PP-HMDSO	40.5	28.0	31.5

The high-resolution spectra of PC and PS are shown in Figure S 3. The PC spectrum was described by the CC and CH component at 284.8 eV, the CO component at 286.3 eV, the carbonate at 290.7 eV and the π shake-up at 291.8 eV. The overall atomic stoichiometry was as shown in Table S 1 characterized by 84.8 at% carbon and 15.2 at% oxygen. The lineshape as well as the stoichiometry are in agreement with literature.[2] This situation was also found in the case of the polystyrene sample.[3]

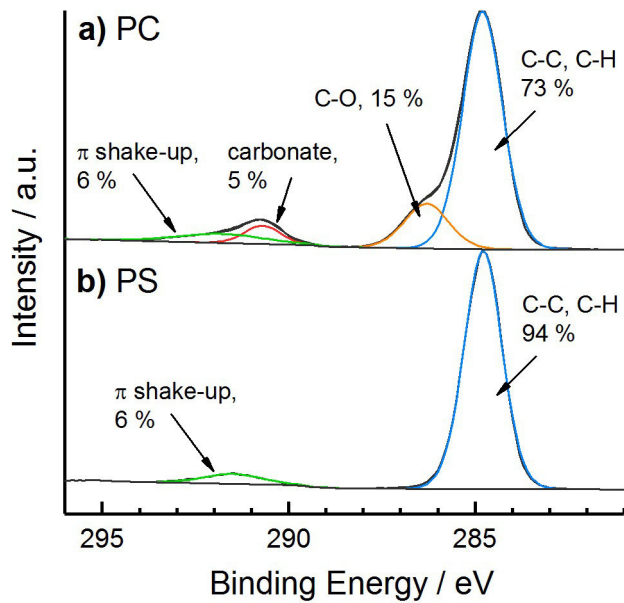


Figure S 3: High resolution XPS spectra of the **a)** PC and **b)** PS thin films measured at an angle of emission of 15° relative to the surface normal. The binding energy scale was corrected for charging by shifting the joint CC and CH component to 284.8 eV. The intensities are normalized and shifted on the ordinate for improved visualization.

XPS of TiAlN and TiAl(O,N)

Figure S 4 shows the high resolution spectra of TiAlN after atmosphere exposure and O beam treatments. The N1s spectrum was described by up to four components located at 395.9, 397.0, 398.4 and 402.0 eV. The components at 395.9 and 397.0 eV are related to TiAl(O,N) and non-oxidized TiAlN according to their binding energies.[4–7] The nature of the satellite component at 398.4 eV is under debate and the relevance of surface N-O compounds or defects is discussed.[8,9] The component at 402.0 eV is commonly assigned to N₂ incorporated into the defective surface oxide film and was observed to represent a main component of the N1s signal after intense oxidation using the O beam at 1.5 kV.[10,11] It is noted that the TiAl(O,N) components of all core level signals could not be correlated inter alia by stoichiometric considerations due to the uncertain composition of the TiAl(O,N) phase.

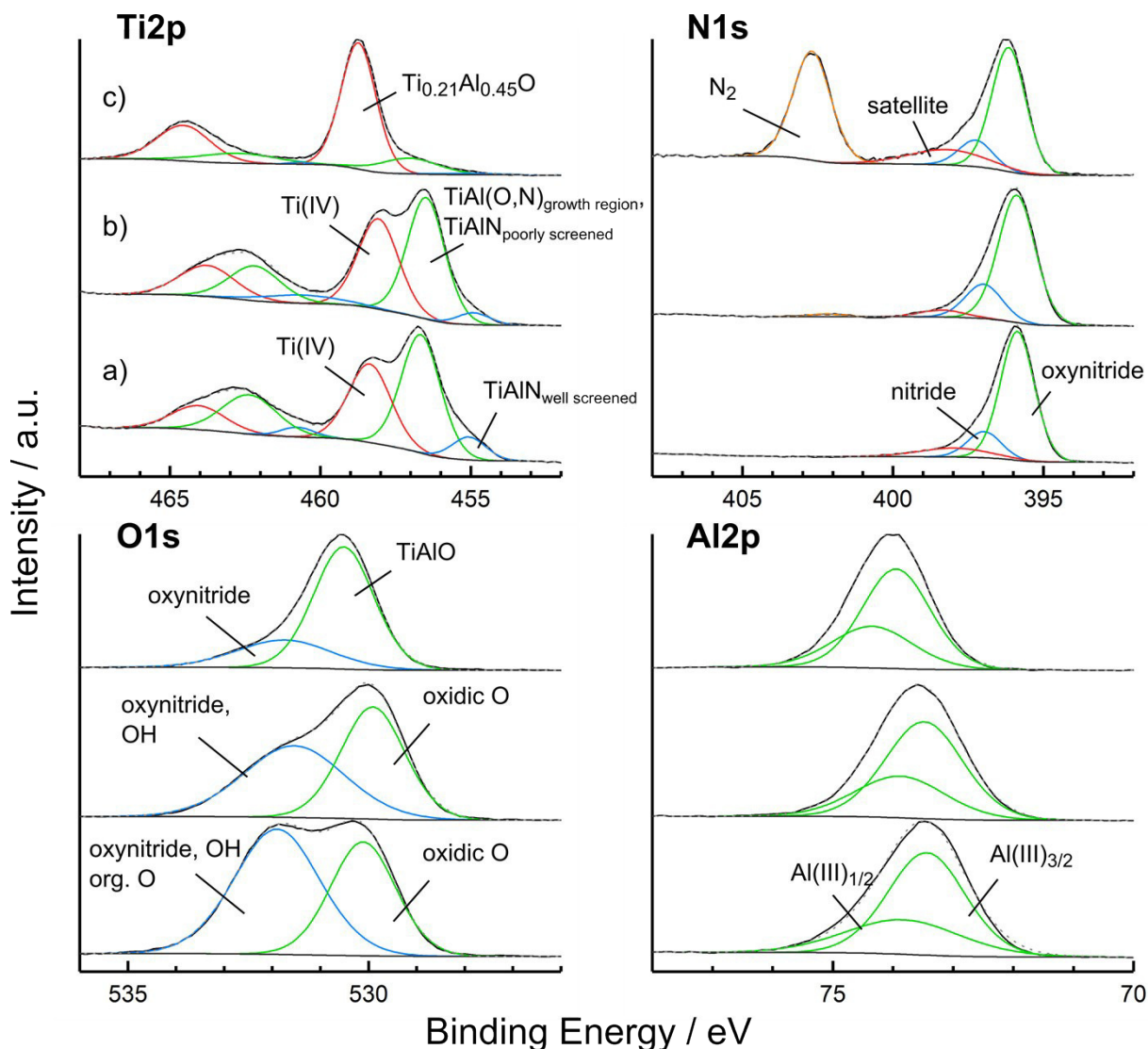


Figure S 4: High resolution core level spectra of **a)** TiAlN after deposition and atmosphere exposure, **b)** after removal of adventitious contaminations using an O beam at 0 eV for 1 min and **c)** after intense oxidation using an O beam at 1.5 kV for 45 s. The intensities are normalized and shifted on the ordinate for improved visualization.

The O1s spectrum of the atmosphere exposed surface was described by two components at 530.0 and 532.0 eV. The component at 530.0 eV was assigned to oxidic oxygen when considering that the O1s binding energy of TiO₂ is 530.0 eV and that of TiAlO is located around 530.6 eV.[12,13] At 532.0 eV several compounds overlap such as TiAl(O,N), surface hydroxyl groups Ti-OH, Al₂O₃ and adventitious contaminations.[8,9,12,14,15] The modified Auger parameter as determined from the barycentre of the O1s signal obtained after cleansing amounted 1040.8±0.1 eV and is typical for a ternary mixed TiAlO.[13] Thus, segregation of the surface oxide on atmosphere exposed TiAlN into Al₂O₃ and TiO₂ as indicated by the binding energies of the two O1s components was not supported by the investigation of the Auger parameter. Consequently, the precise chemical state of the surface oxide on atmosphere exposed TiAlN could not be entirely resolved based on the spectra investigated.

In this regard, the situation after intense surface oxidation using an O beam at 1.5 kV was unambiguous. The two components of the O1s signal were located at 530.5 eV and 531.8 eV and related to TiAlO and TiAl(O,N) based on their binding energies.[13] The modified Auger parameter was 1040.6±0.1 eV and therefore located within the region of mixed TiAlO.[13]

The Al2p signal was described by two components split due to spin-orbit coupling by 0.4 eV. In the case of atmosphere exposed TiAlN and after surface cleansing the Al2p signal was located at 73.6 eV. After

intense surface oxidation using the O beam at 1.5 kV the Al2p was shifted to 74.0 eV. In this regard, earlier investigations indicated no shift of the Al2p component due to oxidation and this finding might therefore rather be related to structural changes induced by the O beam.[7,9] A more precise deconvolution of the Al2p signal into components related to the oxidic, oxynitridic or nitridic layers could not be performed due to the very similar binding energies of the Al(III) ion in these phases.[7]

Table S 2: Surface composition of TiAl(O,N) in the as deposited and atmosphere exposed state and after surface cleansing using an O beam at 0 eV for 7 min.

treatment	C1s / at%	O1s / at%	N1s / at%	Ti2p / at%	Al2p / at%	Al/Ti
atmosphere exposed	26.0	38.2	8.8	8.4	18.6	2.2
surface cleansed	0.8	49.8	11.0	13.2	25.2	1.9

The stoichiometry of the TiAl(O,N) cantilevers was also investigated on flat samples and the XPS derived stoichiometries of the surfaces in the atmosphere exposed and cleaned state are shown in table s 2. Similar to TiAlN, surface enrichment of Al was observed and the effectiveness of the cleaning procedure using the O beam at 0 V is demonstrated by the reduction of the C1s concentration to below 0.8 at%.

Angle-resolved XPS measurements have been performed on the TiAlN sample after O beam oxidation in order to verify the presence of the $Ti_{0.21}Al_{0.45}O$ layer at the outermost surface. The corresponding Ti2p spectrum is shown in figure S 5 and an increase of the intensity of the $Ti_{0.21}Al_{0.45}O$ component was observed when increasing the angle of emission from 15° to 60° relative to the surface normal. This validates the superficial enrichment of $Ti_{0.21}Al_{0.45}O$.

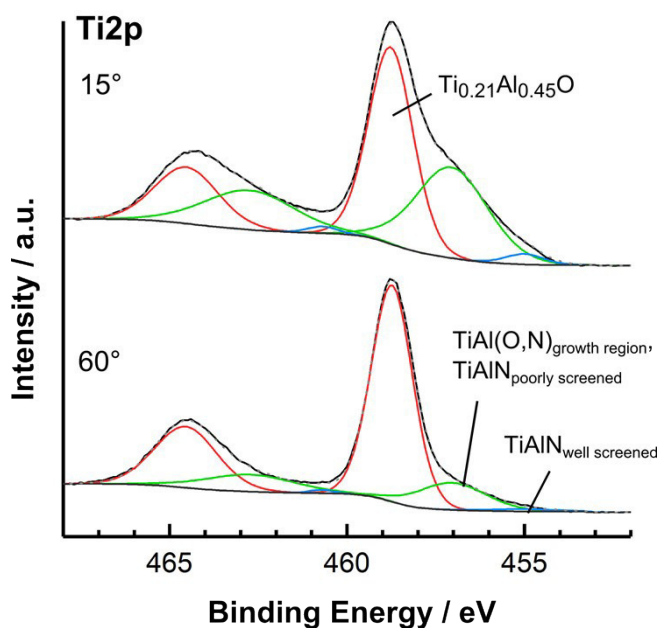


Figure S 5: Angle-resolved XPS of the Ti2p spectrum of TiAlN after O beam oxidation at emission angles of 15° and 60° relative to the surface normal.

The high resolution core level spectra of the TiAl(O,N) surface are shown in figure 5 and were analysed in analogy to the TiAlN surfaces.

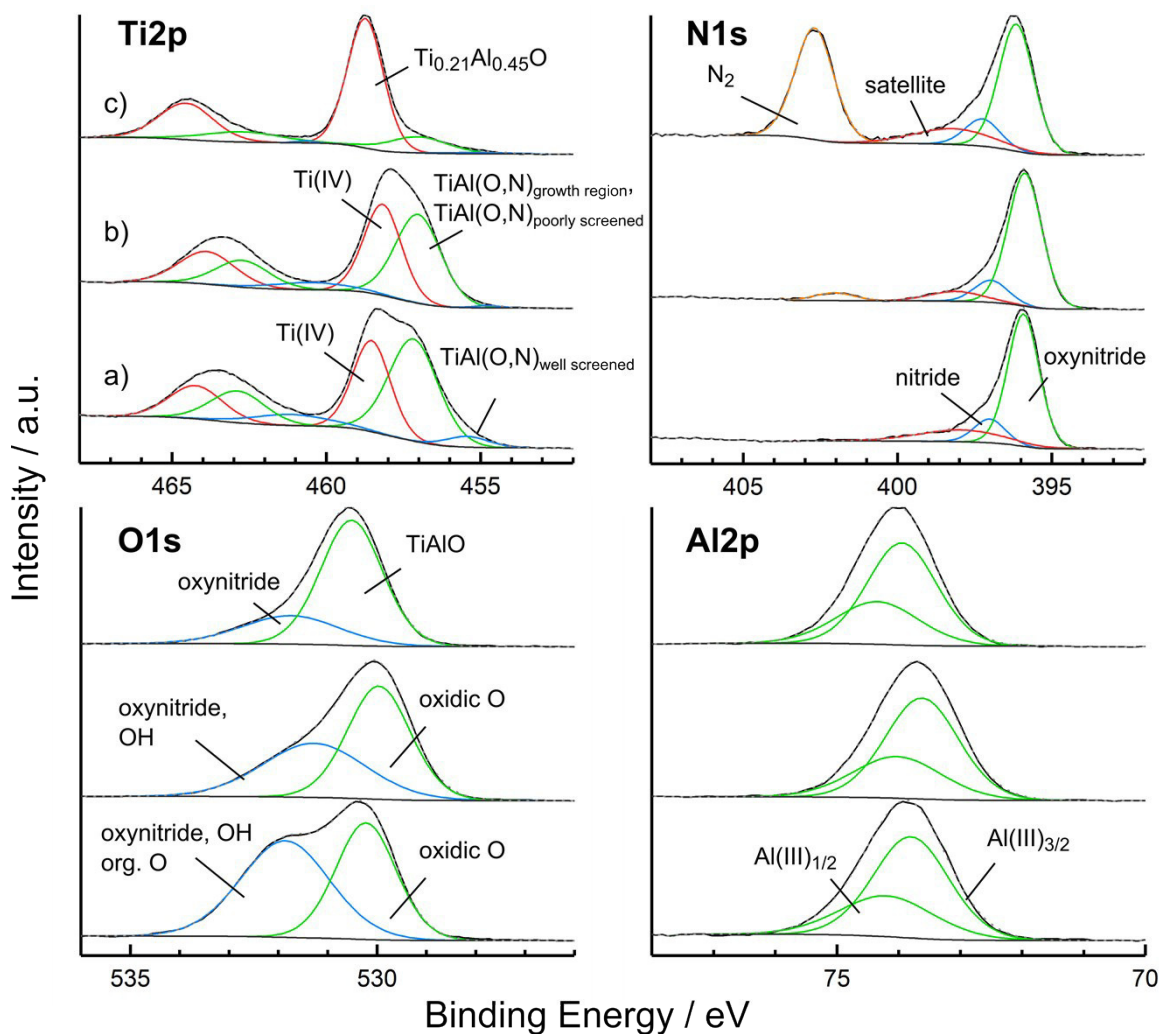


Figure 5 6: High resolution core level spectra of **a)** TiAl(O,N) after deposition and atmosphere exposure, **b)** after removal of organic contamination using an O beam at 0 eV for 1 min and **c)** after intense oxidation using an O beam at 1.5 kV for 45 s. The intensities are normalized and shifted on the ordinate for improved visualization.

Electron microscopy images of tips after DFS measurements

This section lists electron microscopy images of the used TiAlN, TiAl(O,N), TiO₂ and Al₂O₃ tips after DFS measurements for documentation of the quality of the tips. The measurements were performed using a FE-SEM (Zeiss Neon 40).

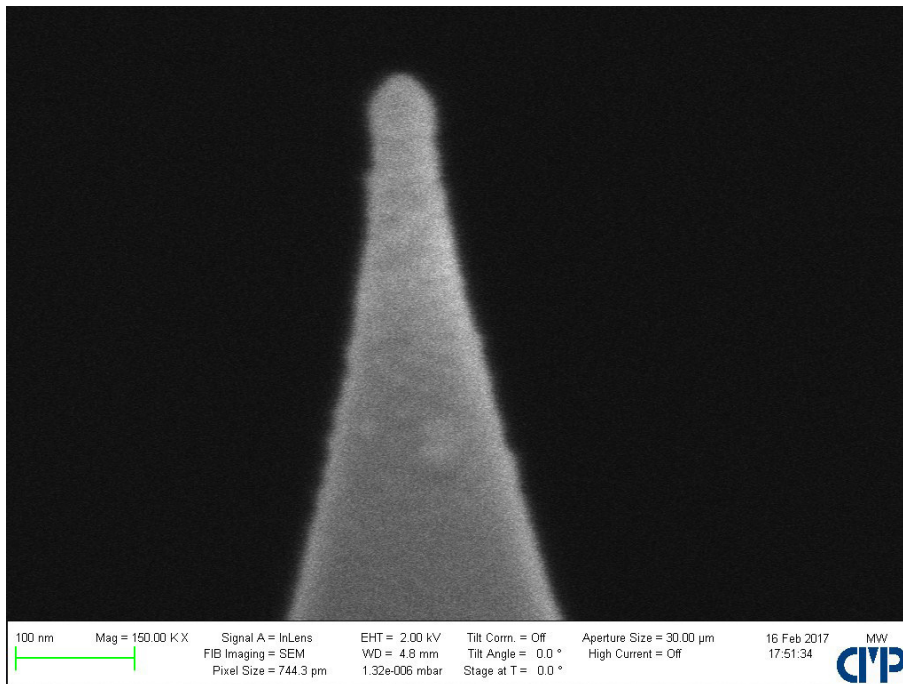


Figure S 7: TiAlN coated tip used within this study after DFS measurements and intense surface oxidation using the O beam at 1.5 kV for 45 s.

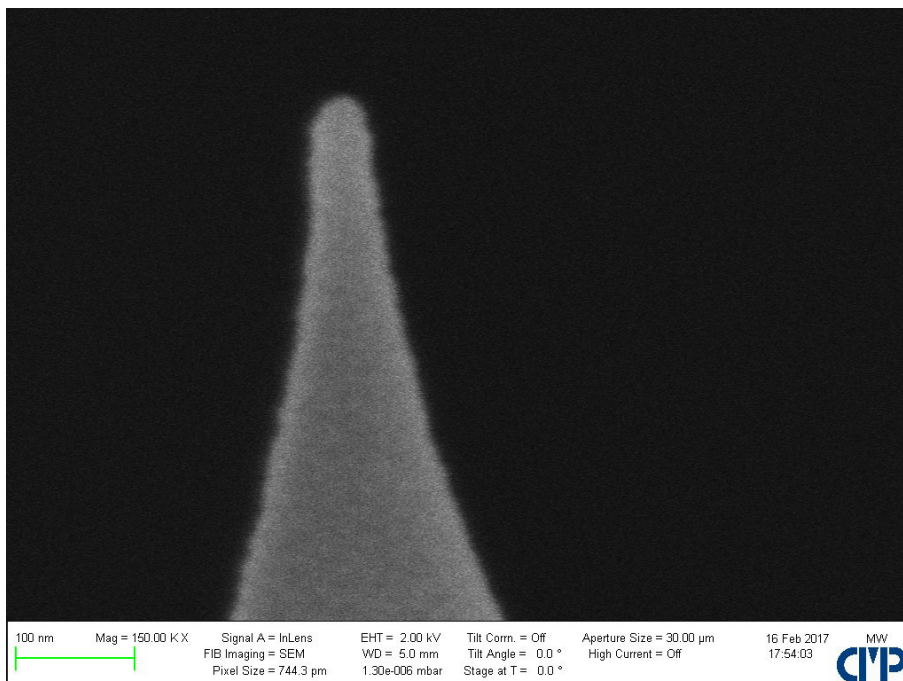


Figure S 8: TiAl(O,N) coated tip used within this study after DFS measurements.

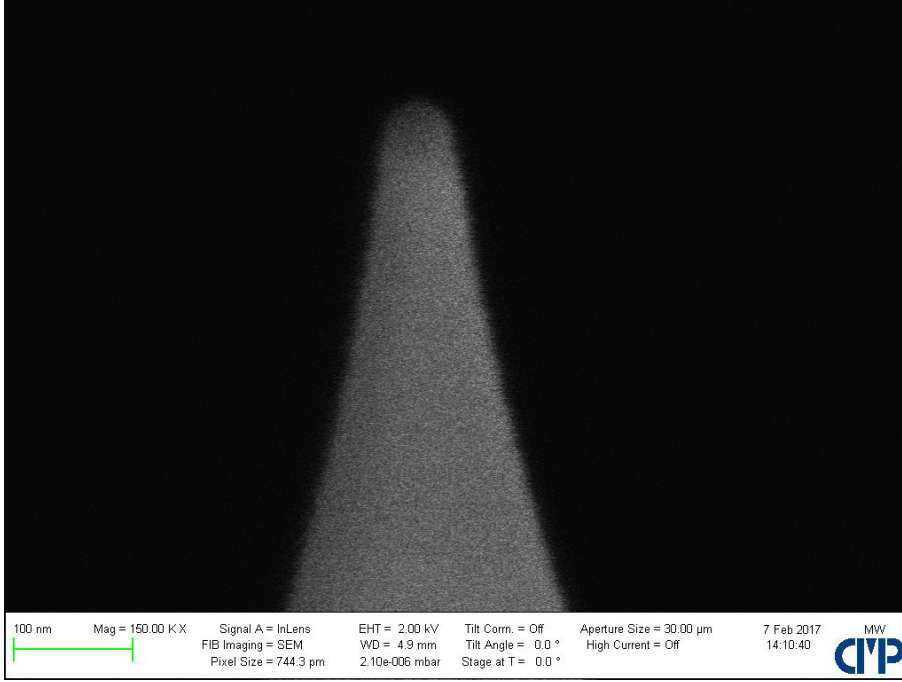


Figure S 9: Al_2O_3 coated tip used in this study after DFS measurements.

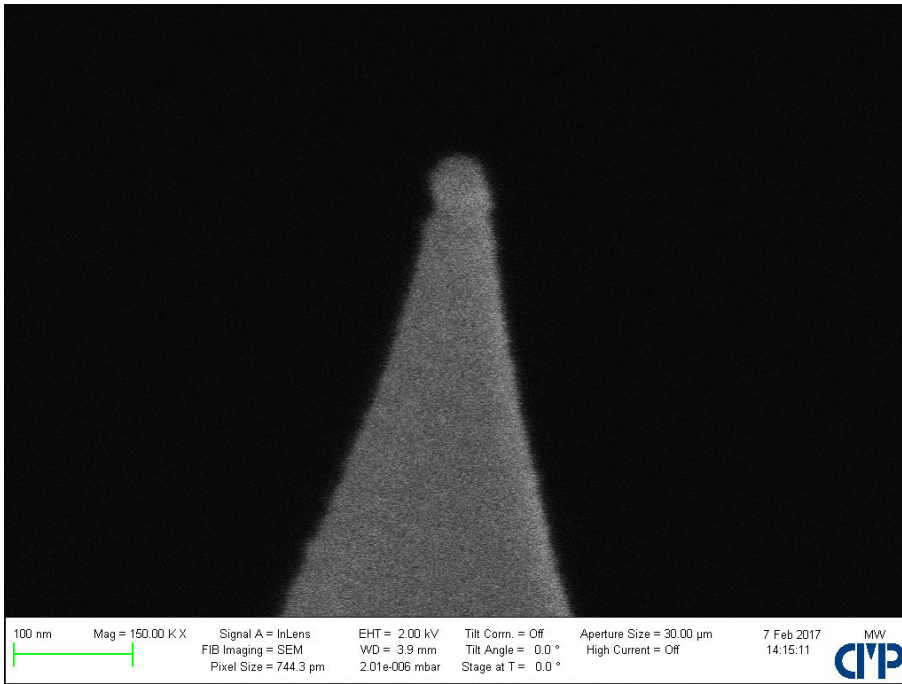


Figure S 10: TiO_2 coated tip used in this study after DFS measurements.

Lifshitz analysis and optical data

Within the QUEELS- $\epsilon(\omega,k)$ -REELS software package the dielectric function is defined by the energy loss function (ELF) as [16–18]

$$Im\left(-\frac{1}{\epsilon(\omega,k)}\right) = \theta(\hbar\omega - E_g) \cdot f(\hbar\omega) \cdot \sum_i \frac{A_i \gamma_i \hbar\omega}{(\hbar^2 \omega_{0,i}^2(k) - \hbar^2 \omega^2)^2 + \gamma_i^2 \hbar^2 \omega^2} \quad (S1a)$$

$$\hbar\omega_{0,i}(k) = \hbar\omega_{0,i} + \alpha_i \frac{\hbar^2 k^2}{2m_e} \quad (S1b)$$

$$f(\hbar\omega) = \left[\frac{a2(\hbar\omega - E_g)^p}{\hbar^2\omega^2} \right]^{tmp1}, \text{ if } E_g < \hbar\omega < E_g + a1 \quad (S1c)$$

$$tmp1 = \cos^2\left(\frac{\pi\hbar\omega - E_g}{2a1}\right) \quad (S1d)$$

$$f(\hbar\omega) = 1, \text{ if } \hbar\omega > E_g + a1 \quad (S1e)$$

With $\epsilon(\omega, k)$ being the dielectric function, $\hbar\omega$ the energy, E_g the band gap energy, A_i the strength of oscillator i , γ_i the damping and $\hbar\omega_{0,i}$ the resonance frequency, α_i the momentum dispersion coefficient k the wave vector and m_e the electron mass. $\theta(\hbar\omega - E_g)$ is a step function, which is unity at $\hbar\omega > E_g$ and zero at $\hbar\omega < E_g$. The function $f(\hbar\omega)$ is introduced to smoothen the region close to the band gap by using the parameters $a1$ and $a2$. The exponent p is 0.5 or 2 for a direct and an indirect band gap.

The oscillator parameters used throughout this study are shown in Table S 3.

Table S 3: Oscillator parameters of polycarbonate, polystyrene, TiO_2 , Al_2O_3 and $Ti_{0.21}Al_{0.45}O$ as determined by REELS.

		$\hbar\omega_0 / \text{eV}$	A_0 / eV^2	$\hbar\gamma / \text{eV}$	α
PC		6.8	1.2	0.95	0
E_g	4.2	14.9	6.4	4.9	0
$a1$	3.2	22.2	189.5	13	0
$a2$	9	32.5	184.1	20	0
p	2	27.6	38.7	9	0
PS		7	2.1	1.23	0
E_g	4.2	10	0.5	2	0
$a1$	3.2	13	0.5	2	0
$a2$	9	22.2	206.1	13	0
p	2	27.6	48.2	9	0
		32.5	140.0	18	0
TiO_2		6.2	1.0	3	0.05
E_g	3.2	12	27.5	4.7	0.05
$a1$	1	14.3	18.0	3.7	0.05
$a2$	0.1	17.7	25.8	7	0.05
p	2	25.5	211.5	11	0.05
		31.5	21.0	7	0.05
		38.4	19.8	5	0.05
		46.8	279.8	9	0.05
		52.7	69.6	7	0.05
Al_2O_3		14.4	9.6	6	0.02
E_g	6.3	22.7	210.0	7.8	0.02
$a1$	2	32	271.8	18	0.02
$a2$	0.1				
p	2				
$TiAlO$		5.85	0.4	3	0.05
E_g	3.2	10.2	4.9	3.9	0.05

a_1	1.5	14	12.5	5.2	0.05
a_2	8	23.2	288.9	14	0.05
p	2	32	51.6	11	0.05
		38.6	28.9	6	0.05
		46.6	167.8	11	0.05
		52.3	56.2	9	0.05
		63	32.7	7	0.05

The Hamaker coefficients were calculated according to [19]

$$A_h(d) = -\frac{3}{2}kT \sum_{n=0}^{\infty} \int_{r_n}^{\infty} x \ln[(1 - \Delta_{Am} \Delta_{Bm} e^{-x})(1 - e^{-x})] dx \quad (S2a)$$

$$\Delta_{im} = \frac{x_m \varepsilon_i - x_i \varepsilon_m}{x_m \varepsilon_i + x_i \varepsilon_m} \quad (S2b)$$

$$x_i^2 = x_m^2 + \left(\frac{2l\xi_n}{c}\right)^2 (\varepsilon_i - \varepsilon_m), x_m = x \quad (S2c)$$

$$r_n = \frac{2l\sqrt{\varepsilon_m}}{c} \xi_n \quad (S2d)$$

$$\hbar \xi_n = 2\pi kTn \quad (S2d)$$

where ξ_n is the n th Matsubara frequency, ε_m the relative permittivity of the medium (vacuum in this case) and r_n is the pertinent ratio, which accounts for retardation.[19] The first term with $n = 0$ in equation S2a is multiplied by 0.5. In equation S2 the dielectric function ε was supplied directly as $\varepsilon(\omega)$ from the QUEELS- $\varepsilon(\omega, k)$ -REELS software package after conversion to the imaginary axis according to the Kramers-Kronig transform

$$\varepsilon(i\xi_n) = 1 + \frac{2}{\pi} \int_0^{\infty} \frac{\omega_R \varepsilon''(\omega_R)}{\omega_R^2 + \xi_n^2} d\omega_R \quad (S3)$$

where ω_R is the radial frequency. The non-retarded constants were obtained as limiting values for low distances around 0.3 nm.

References

- [1] I. Tajima, M. Yamamoto, Spectroscopic study on chemical structure of plasma-polymerized hexamethyldisiloxane, *J. Polym. Sci. [A1]*. 23 (1985) 615–622. doi:10.1002/pol.1985.170230303.
- [2] M.C. Burrell, J.J. Chera, Polycarbonate Spin Cast Films by XPS, *Surf. Sci. Spectra*. 6 (1999) 1–4. doi:10.1116/1.1247900.
- [3] M.C. Burrell, J.J. Chera, Polystyrene Spin Cast Films by XPS, *Surf. Sci. Spectra*. 6 (1999) 27–30. doi:10.1116/1.1247899.
- [4] P. Prieto, R.E. Kirby, X-ray photoelectron spectroscopy study of the difference between reactively evaporated and direct sputter-deposited TiN films and their oxidation properties, *J. Vac. Sci. Technol. A*. 13 (1995) 2819–2826. doi:10.1116/1.579711.
- [5] A. Arranz, C. Palacio, Screening effects in the Ti 2p core level spectra of Ti-based ternary nitrides, *Surf. Sci.* 600 (2006) 2510–2517. doi:10.1016/j.susc.2006.04.011.
- [6] G. Greczynski, J. Jensen, J.E. Greene, I. Petrov, L. Hultman, X-ray Photoelectron Spectroscopy Analyses of the Electronic Structure of Polycrystalline Ti_{1-x}Al_xN Thin Films with $0 \leq x \leq 0.96$, *Surf. Sci. Spectra*. 21 (2014) 35–49. doi:10.1116/11.20140506.
- [7] C. Gnoth, C. Kunze, M. Hans, M. to Baben, J. Emmerlich, J.M. Schneider, G. Grundmeier, Surface chemistry of TiAlN and TiAlNO coatings deposited by means of high power pulsed magnetron sputtering, *J. Phys. Appl. Phys.* 46 (2013) 084003. doi:10.1088/0022-3727/46/8/084003.

- [8] G. Greczynski, L. Hultman, Self-consistent modelling of X-ray photoelectron spectra from air-exposed polycrystalline TiN thin films, *Appl. Surf. Sci.* 387 (2016) 294–300. doi:10.1016/j.apsusc.2016.06.012.
- [9] M. Wiesing, T. de los Arcos, G. Grundmeier, The Thermal Oxidation of TiAlN High Power Pulsed Magnetron Sputtering Hard Coatings as Revealed by Combined Ion and Electron Spectroscopy, *Adv. Mater. Interfaces.* (2017) 1600861. doi:10.1002/admi.201600861.
- [10] I. Milošev, H.-H. Strehblow, B. Navinšek, Comparison of TiN, ZrN and CrN hard nitride coatings: Electrochemical and thermal oxidation, *Thin Solid Films.* 303 (1997) 246–254. doi:10.1016/S0040-6090(97)00069-2.
- [11] F. Esaka, K. Furuya, H. Shimada, M. Imamura, N. Matsubayashi, T. Kikuchi, H. Ichimura, A. Kawana, Composition dependence of the initial oxidation behaviour of Ti_{1-x}Al_xN (x = 0.20, 0.45, 0.65) films studied by XAS and XPS, *Surf. Interface Anal.* 27 (1999) 1098–1106. doi:10.1002/(SICI)1096-9918(199912)27:12<1098::AID-SIA684>3.0.CO;2-I.
- [12] E. McCafferty, J.P. Wightman, Determination of the concentration of surface hydroxyl groups on metal oxide films by a quantitative XPS method, *Surf. Interface Anal.* 26 (1998) 549–564. doi:10.1002/(SICI)1096-9918(199807)26:8<549::AID-SIA396>3.0.CO;2-Q.
- [13] R. Cremer, M. Witthaut, D. Neuschütz, Electron spectroscopy applied to metastable ceramic solution phases, *Fresenius J. Anal. Chem.* 365 (1999) 28–37. doi:10.1007/s002160051440.
- [14] M.C. Biesinger, L.W.M. Lau, A.R. Gerson, R.S.C. Smart, Resolving surface chemical states in XPS analysis of first row transition metals, oxides and hydroxides: Sc, Ti, V, Cu and Zn, *Appl. Surf. Sci.* 257 (2010) 887–898. doi:10.1016/j.apsusc.2010.07.086.
- [15] P.C. Snijders, L.P.H. Jeurgens, W.G. Sloof, Structural ordering of ultra-thin, amorphous aluminium-oxide films, *Surf. Sci.* 589 (2005) 98–105. doi:10.1016/j.susc.2005.05.051.
- [16] S. Tougaard, F. Yubero, QUEELS software package for calculation of surface effects in electron spectra, *Surf. Interface Anal.* 36 (2004) 824–827. doi:10.1002/sia.1774.
- [17] F. Yubero, D. Fujita, B. Ramskov, S. Tougaard, Experimental test of model for angular and energy dependence of reflection-electron-energy-loss spectra, *Phys. Rev. B.* 53 (1996) 9728–9732. doi:10.1103/PhysRevB.53.9728.
- [18] F. Yubero, J.M. Sanz, B. Ramskov, S. Tougaard, Model for quantitative analysis of reflection-electron-energy-loss spectra: Angular dependence, *Phys. Rev. B.* 53 (1996) 9719–9727. doi:10.1103/PhysRevB.53.9719.
- [19] V.A. Parsegian, *Van der Waals Forces: A Handbook for Biologists, Chemists, Engineers, and Physicists*, Cambridge University Press, Cambridge, 2005.

4.6 UHV AFM based colloidal probe studies of adhesive properties of VAIN hard coatings

The manuscript was reproduced from the following publication:

UHV AFM based colloidal probe studies of adhesive properties of VAIN hard coatings

Wiesing, M., de los Arcos, T., Grundmeier, G.

Applied Surface Science, 428, 767–774, 2018, doi:10.1016/j.apsusc.2017.09.208

Copyright © 2017, Elsevier B.V.

Author contributions:

- Planning/experimental work/interpretation/manuscript preparation **MW**
- Proof reading/content check **GG**
- Proof reading **TA**

Placement:

Based on the analysis of the van der Waals interactions within publication 5, this study expands the investigation of the origin of the adhesive interactions between hard coatings and polymers at the molecular level by considering additional acid-base interactions. The focus was placed on the role of the oxidation states of the polymers and the hard coatings surfaces for adhesion, because oxidative ageing affects both surface chemistries during the process. Therefore, the effect of the incorporation of oxygen-bearing functional groups into the surface of polystyrene on the adhesion was analysed. Similarly, a gentle oxidation of the hard coating was performed resulting into a surface oxide with a structure similar to an oxide as obtained after deposition and exposure to atmosphere. It was found that the non-oxidized surfaces interact by van der Waals forces only, whereas upon oxidation additional acid-base interactions increase the adhesion force. Interestingly, the van der Waals forces of both surfaces were always unaffected by oxidation. In the case of the hard coating, this could be explained by a high polarizability of the surface oxide in agreement with the findings in publication 5. In conclusion, these results provide a molecular understanding of the effect of oxidation on the overall adhesion to approach the tailoring of hard coatings.



Full Length Article

UHV AFM based colloidal probe studies of adhesive properties of VAIN hard coatings



M. Wiesing, T. de los Arcos, G. Grundmeier*

Technical and Macromolecular Chemistry, University of Paderborn, Warburger Straße 100, 33098 Paderborn, Germany

ARTICLE INFO

Article history:

Received 27 July 2017

Received in revised form

13 September 2017

Accepted 25 September 2017

Keywords:

VAIN

Adhesion

Oxidation

HPPMS

Hard coating

Colloidal probe

ABSTRACT

The adhesion of polystyrene (PS) on $V_{0.27}Al_{0.29}N_{0.44}$ and the related influence of the oxidation states of both surfaces was investigated using X-Ray Photoelectron Spectroscopy (XPS) and Colloidal Force Spectroscopy (CFS) in Ultra-High Vacuum (UHV). Complementary, the intimate relation between the adhesion force, the chemical structure and surface polarizability was investigated by XPS valence band spectroscopy and the calculation of non-retarded Hamaker coefficients using Lifshitz theory based on optical data as derived from Reflection Electron Energy Loss Spectroscopy (REELS) spectra. The combined electron and force spectroscopic analysis of the interaction forces disclosed quantitatively the separation of the adhesion force in van der Waals and Lewis acid-base contributions. Further, the surface polarizability of VAIN was shown to be unaffected by oxygen incorporation due to the formation of an only gradually oxidized surface comprising a range of vanadium oxidation states. In contrast, the adhesion force analysis revealed additional Lewis acid-base interactions between the oxidized and non-oxidized VAIN surfaces and carboxyl groups present in the surface of PS after an oxidative oxygen beam treatment.

© 2017 Elsevier B.V. All rights reserved.

1. Introduction

The melt processing of optical polymers such as polycarbonate is affected by a variety of interfacial phenomena such as corrosive and adhesive wear of the tool steel and the accumulation of strongly adhering polymeric degradation products at the tool surfaces [1,2]. As a consequence the stability of the polymer moulding process is deteriorated due to the transfer of corrosion products to the products surface or the formation of discoloured speckles in the extruded polymer by shear-induced release of degraded polymeric debris from the tool surfaces. In this regard, it is further observed that the affinity of the tool to accumulate degradation products can be enhanced by corrosive processes [1]. In order to mitigate these problems, nitridic ternary hard coatings such as VAIN are widely used as tool coatings in polymer processing [1–3]. Despite this efficient empirical approach, an in-depth understanding of the origin of adhesion of polymers and their degradation products to the surfaces of nitridic hard coatings remains unresolved.

In the here presented work this problem is approached by investigating the adhesion of a polystyrene (PS) bead on $V_{0.27}Al_{0.29}N_{0.44}$ surfaces as measured by Colloidal Probe Spectroscopy (CFS) using

an UHV-Atomic Force Microscope. The surfaces investigated are the oxygen-free and oxidized surfaces of VAIN and the non-oxidized and oxidized surfaces of PS. This allows to directly assess the relevance of the superficial surface oxide layer present on the hard coating and the role of oxygen bearing functional groups in the polymer phase for adhesion. Recently, the effect of the presence of a surface oxide film on $AlYB_{14}$ on the adhesion of polyethylene has been also investigated using CFS and Density Functional Theory [4]. It was shown that upon oxidation the surface was transformed from a metal-like to a semiconducting state. Simultaneously, the electronic interactions of CH_4 , which was used as a test molecule in the DFT simulation, changed and the adsorption energy increased as confirmed by CFS using a polyethylene colloidal probe. However, this study did not consider the interactions of polar functional groups with the hard coatings surface and also the chemical structure of boride and nitride based hard coatings differ.

It is further highlighted that optical data as determined by Reflection Electron Energy Loss Spectroscopy (REELS) are used in this study for the calculation of Hamaker coefficients using Lifshitz theory. This spectral approach to the interaction forces was already used earlier but was based on loss spectra measured in transmission using a Transmission Electron Microscope (TEM) [5]. In contrast to the transmission mode, the derivation of the dielectric function from electron loss spectra measured in reflection is more complex due to the physics involved but has become a rou-

* Corresponding author.

E-mail address: g.grundmeier@tc.uni-paderborn.de (G. Grundmeier).

tine method with the development of the QUEELS software package by Tougaard and Yubero [6–9]. The advantage of the use of REELS lies in the low energy of the primary beam, which allows for a very high and adjustable surface sensitivity and also for the investigation of polymer surfaces without beam damage using common Auger setups [10]. This method is therefore especially well-suited for analysing the partitioning of adhesion forces, which originates from the chemical and electronic properties of the topmost surface layers.

2. Experimental

2.1. Thin film deposition

VAIN and VAl(O,N) thin films were deposited on Si (100) substrates by combinatorial High Power Pulsed Magnetron Sputtering (HPPMS) in an Ar/N₂/O₂ atmosphere using a CemeCon CC800/9 system with a base pressure of below 0.4 mPa [11]. The two triangular shaped split V and Al targets were mounted on a magnetron powered by a Melec HPPMS power supply. For deposition, the magnetrons were operated at –608 V and at a pulse frequency of 500 Hz corresponding to a duty cycle of 2.5%. The peak target power density was 316 W/cm² for VAIN and 345 W/cm² for VAl(O,N). The Ar and N₂ gas flows were kept constant at 200 and 75 sccm, while for VAl(O,N) an O₂ flow of 1.8 sccm was used. The substrates were mounted at a target-to-substrate distance of 80 mm and were degassed at 300 °C before deposition. The thin film deposition was carried out at floating potential. The RMS roughness of the VAIN hard coating was 2.4 nm as determined by Atomic Force Microscopy (AFM) in ambient atmosphere after deposition (see Fig. S1). Polystyrene thin film samples were deposited by spin coating using *p*-Si(100) wafer substrates and a 2 w% polystyrene/toluene solution. The toluene was of analytical grade and the polystyrene free of additives (192 kM_w, SigmaAldrich). The thickness of the thin film was around 60 nm as determined by ellipsometry using tabulated optical constants.

2.2. XPS

XPS was performed using an ESCA+ system (ScientaOmicron, Taurusstein) equipped with a monochromatized Al K α x-ray source (1486.7 eV) at a base pressure of below 10^{–8} Pa. The spectra were measured at an angle of emission of 60° relative to the surface normal resulting into a depth of information of around 4.5 nm if not stated otherwise [12]. The spectral resolution for the high-resolution core level and valence band spectra was 0.77 eV as determined from the width of the Ag3d_{5/2} line. The binding energy was also referenced to the Ag3d_{5/2} signal at 368.4 eV. For the XPS measurements on polystyrene thin films an electron flood gun was used for charge neutralization and the binding energy of the C1 s signal was set to 285.0 eV.

2.3. REELS

REELS was measured using the built-in electron gun for Auger spectroscopy of the ESCA system (Nanofocus 50, Staib Instruments, Germany) with an energy resolution of 1.0 eV. The beam was rastered across an area of 0.07 mm² during the measurement resulting into a current density of 0.44 μ A cm^{–2}. The primary beam energies used for the VAIN surfaces and polystyrene thin film were 1050 and 450 eV. For the sputter cleaned and oxidized VAIN surfaces the angle of incidence was 0° and the angle of emission was 60° relative to the surface normal. In the case of the PS thin film sample the angles of incidence and emission were set to 30°. The depth of information was therefore in both cases around 1 nm. The spectra were measured up to an energy loss of 90 eV including the

reflected elastic peak. The decreased beam energy used for PS prevented beam damage and for these reasons also the sample was moved during the acquisition resulting into a maximum dose of 7.1 μ C cm^{–2} [10].

2.4. LEIS

LEIS was measured on the sputtered and oxidized surfaces of VAIN using He⁺ projectiles at an energy of 1 keV while rastering across a surface of 1 mm² resulting into a current density of 4.6 μ A cm^{–2}. The angle of incidence and reflection were 30° and 60° and the backscattering angle was 135°. The measurement of a single spectrum took 70 s and the corresponding dose was 0.32 mC cm^{–2}. It is noted that the measurement under these conditions is destructive and slight sputtering took place during the measurement especially on the oxidized sample. However, this effect was relatively low as shown by consecutively measured spectra (see Fig. S2) and did thus not affect the qualitative interpretation of the spectra.

2.5. Colloidal Force Spectroscopy

The cantilevers used for Colloidal Force Spectroscopy (CFS) were prepared using tipless cantilevers (40 N m^{–1}, TL-NCL, NanoSensors) and polystyrene beads with an average diameter of 2.8 μ m (Polybead, Polysciences Inc.). It is noted that the beads were free of detergents and synthesized using a solvent-free method. The beads were attached to the cantilevers with conventional solvent-free two component epoxy glue by using a micromanipulator and an inverted microscope. Before use, the quality of the bond between bead and cantilever was checked using a scanning electron microscope (Zeiss Neon 40). The force constants of the cantilevers used were individually supplied by the manufacturer. The AFM measurements were performed in Ultra High Vacuum (UHV) using an UHV-AFM (VT-AFM, ScientaOmicron) directly attached to the ESCA system, which allowed the transfer of samples throughout the facility while maintaining a pressure of below 5 \times 10^{–7} Pa. The adhesion force measurements were performed on a 10 \times 10 grid overlaid on a quadratic surface with an edge length of 1 μ m using a custom MATE script. This script allowed the relocation of the probe to the grid points while being retracted from the surface. Force spectroscopy was then performed at the grid points with a height resolution of 35 pm and a dwell time of 0.5 μ s. Each surface was investigated by measuring 100 curves. In order to smooth the surface of the polystyrene beads, the colloidal probe was conditioned before the first use by measuring a force curve up to 10 μ N [13].

2.6. Ion beam treatments

Sputter cleaning of the VAIN surfaces was performed using 3 kV Ar⁺ ions (15 μ A cm^{–2}, 120 s) using a sputter gun (Fig 05, Physical Electronics). The surface oxidation of the sputter cleaned VAIN surface, the PS thin film and the colloidal probe was performed using an oxygen beam (GenII, Tectra Physikalische Instrumente, Germany). More details about the source can be found elsewhere [14,15]. The background pressure during operation of the source was 5 \times 10^{–2} Pa. The sputter cleaned VAIN surface was irradiated for 60 s while the polystyrene thin film and the colloidal probe were exposed for 90 s to the mixed atom/ion beam. The effect of the O beam oxidation of the polystyrene was the introduction of a mixture of COC/COH, C=O, and COOH groups into the surface and the corresponding XPS spectra can be found in the supporting information (see Fig. S3).

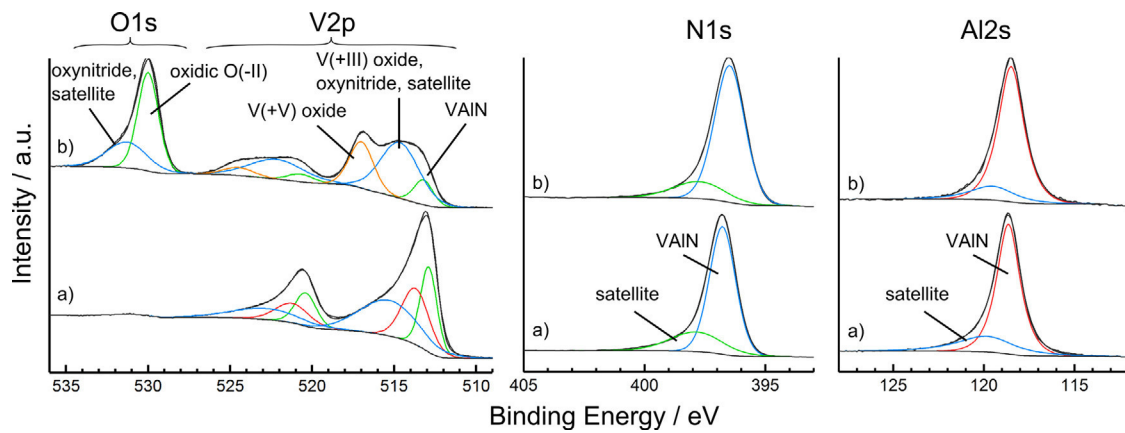


Fig. 1. High-resolution XPS spectra of VAIN after a) Ar⁺ sputter cleaning and b) subsequent oxidation by means of an O beam with 0 V acceleration voltage for 60 s.

Table 1

XPS stoichiometries of VAIN after deposition and atmosphere exposure, after Ar⁺ sputter cleaning and after oxidizing the sputter cleaned surface using an oxygen beam at 0 V acceleration voltage for 60 s.

sample	Al2s/at%	N1s/at%	O1s/at%	V3p/at%	C1s/at%	V/Al
atmosphere exposed	22.1	24.4	25.2	12.3	16.0	0.56
sputtered	29.2	43.8	0.2	27.0	–	0.93
oxidized	22.8	25.4	30.7	21.0	–	0.92

3. Results and discussion

3.1. Surface chemical analysis

The surface of $V_{0.27}Al_{0.29}N_{0.44}$ was investigated by XPS after exposure to atmosphere following the deposition, after Ar⁺ sputter cleaning and after oxidizing the sputter cleaned surface using the non-accelerated mixed oxygen atom/ion beam. The stoichiometries of these surfaces are shown in Table 1. It was found that after sputter cleaning no carbon signal could be detected and the residual oxygen concentrations dropped to below 0.2 at%. The sputter cleaning thus efficiently removes organic as well as oxidic surface contaminations. Following the exposure of this surface to the oxygen beam, the oxygen concentration increased to 30.7 at% as a result of oxidation. This oxygen concentration was higher than the amount of oxygen present in the atmosphere exposed surface indicating that the oxidation using the non-accelerated O beam results into a slightly higher oxidation state of the surface than otherwise encountered on surfaces after deposition. It was further observed that the V/Al ratios of both the sputtered and the O beam oxidized VAIN surfaces were around 0.92 and thus identical. In contrast, the V/Al ratio of the atmosphere exposed sample was 0.56 and therefore significantly decreased. Assuming that the surface after sputter cleaning resembles the bulk stoichiometry of VAIN, the decreased V/Al ratio of the atmosphere exposed surface clearly indicates a superficial Al enrichment as a consequence of preferential Al outward migration during atmospheric oxidation. However, the identical V/Al ratios observed for the sputter cleaned and O beam oxidized VAIN surfaces show that under the conditions of the O beam oxidation the surface oxidation proceeds by the reactive inward migration of oxide anions only.

In order to investigate the surface oxides composition in more detail, high-resolution XPS spectra of sputter cleaned and O beam oxidized VAIN are shown in Fig. 1. In the case of the sputter cleaned VAIN sample it was found that the principal line shape as well as the peak binding energy of the V2p spectrum at 513.0 eV are in agreement with literature and are typical for VAIN [16]. The spectrum could be described by means of three components located at 512.9

eV, 513.7 eV and 515.3 eV. The physical origins of these components are not settled yet and the role of screening, intraband transitions and structural effects for understanding the complex line-shape are under discussion [17–20]. The N1 s spectrum was characterized by two components located at 396.8 eV and 397.9 eV. In this regard, the former component at 396.8 eV is ascribed to VAIN, whereas the latter satellite component at 397.9 eV accounts for the asymmetric line-shape. The situation was similar in the case of the Al2 s spectrum where the main component was located at 118.6 eV and the satellite at 119.8 eV. Such asymmetric line-shapes are typically observed for nitridic hard coatings, but again their origin remains unclear and might be related to intraband excitations or structural effects [17,18,21].

After oxidation using the non-accelerated O beam, the three components of the V2p signal were located at 513.3 eV, 514.7 eV and 517.0 eV. Based on its binding energy, the latter component can be clearly assigned to oxidic vanadium in the +V state [22]. Similarly, when considering the spectrum of the sputter cleaned surface the component at 513.3 eV is assigned to non-oxidized VAIN due to its binding energy. The intermediate component at 514.7 eV covers a binding energy range where several signals may contribute to the line-shape. This component is therefore assigned to satellites from VAIN, oxides of vanadium in the +III, +IV or in intermediate states and also to oxynitride [22–24]. In this regards, the formation of oxynitride within the satellite region is also commonly observed for TiAlN as a result of the formation of a growth region during oxidation by reactive inward migration of oxygen, which is also the oxidation mechanism observed in this case [17,25]. The presence of oxynitride in the oxidized surface of VAIN is further supported by the analysis of the O1s lineshape below. The thickness of the overall oxygen containing top layer can be estimated from the fraction of the VAIN substrate component (12.8 %) and the Effective Attenuation Length (EAL) as approximated by the Inelastic Mean Free Path (IMFP) of 1.5 nm as determined by REELS (see below) [26]. The result is that the overall oxygen containing cover layer was around 1.5 nm thick. In comparison, the mean thickness of the topmost V(+V) related cover layer was 0.2 nm. Since this is significantly smaller than a unit cell (around 0.4 nm), the surface can be considered to be composed of a mixture of oxidic V(+V) states and vanadium sites with a decreased oxidation state being probably in an oxynitridic environment.

The O1s signal was characterized by two components at 530.0 eV and 531.4 eV. Whereas the former is related to the oxide ions in the vanadium oxides, the latter one is ascribed to oxynitride based on the XPS spectra of a VAl(O,N) reference sample (see Fig. S4) [22]. For completeness it is noted that the component at 531.4 eV is

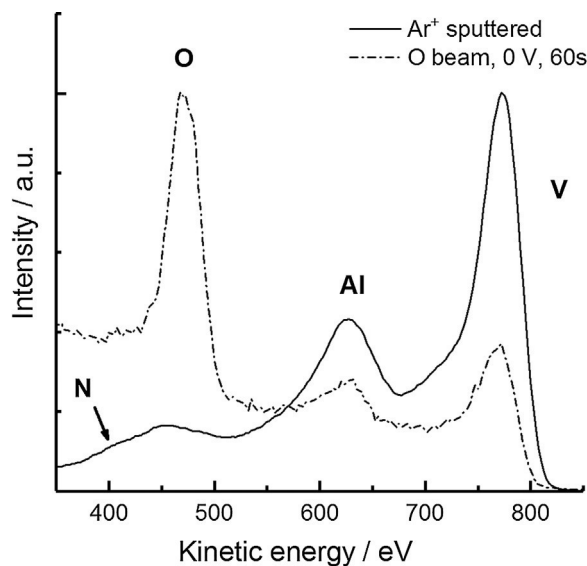


Fig. 2. LEIS spectra of Ar⁺ sputter cleaned and O beam oxidized VAIN measured with 1 kV He⁺ projectiles.

also slightly affected by satellites related to the V2p signals of the surface oxide [22].

The N1s signal shifted from 396.8 to 396.5 eV upon oxidation. This behaviour was also observed in the case of TiAlN and could be related to the formation of the oxynitridic growth region [17,18]. However, the spectra of the VAl(O,N) reference sample (see Fig. S3) showed the N1s signal at 396.9 eV and therefore no shift. These discrepancies might presumably result from the different structures of the sputter cleaned TiAl(O,N) sample and the oxynitridic growth region. However, based on the spectral data presented in this work the situation still remains unclear.

In order to clarify the surface termination of the sputter cleaned and O beam oxidized VAIN samples, LEIS spectra were measured as illustrated in Fig. 2.

The spectrum of sputter cleaned VAIN shows signals at 411, 454, 626 and 773 eV, which are ascribed to N, O, Al and V according to their kinetic energies [27]. Considering that LEIS probes predominantly the composition of the topmost atomic layer, it follows that the surface after sputter cleaning is covered by these atoms. In contrast, the spectrum as obtained after O beam oxidation was dominated by the O signal but the V and Al signals could be still detected. This shows that the metal ions were still accessible though the surface was covered by oxygen. Moreover, the V/Al ratio did not appear to be significantly affected by oxidation as estimated from the ratio of the V and Al signal areas, which is in agreement with the XPS analysis as discussed above.

3.2. Colloidal Force Spectroscopy

The interaction forces between pristine and O beam oxidized PS in contact with sputter cleaned and O beam oxidized VAIN were investigated by CFS and typical force curves are shown in Fig. 3. It was observed that during the measurement with the non-oxidized PS probe the retraction curves showed a sawtooth pattern within the non-contact region up to distances of above 100 nm. This behaviour is explained by polystyrene chains tethering to the PS bead and the surfaces of VAIN as similarly observed in single molecule force spectroscopy [28]. The absence of such extended polymeric tethers in the case of the O beam oxidized PS is presumably explained by the presence of low weight fragments at the surface as a consequence of the O beam etching, which might be stripped off more easily [29]. However, the individual rup-

ture forces observed in the case of the non-oxidized PS within the non-contact region were around 2–7 nN and therefore typical for covalent binding energies [30]. These findings show that strong interactions develop between PS and the sputtered and oxidized surfaces of VAIN.

Considering the interaction forces present during the approach, the curves measured with the non-oxidized PS probe showed a typical “jump-in” behaviour in the near-contact regime due to the attractive van der Waals forces. In contrast, the approach curves measured following the O beam oxidation of PS showed repulsive interactions within the near-contact regime presumably as a result of electrostatic forces. This might be the result of residual charges from the O beam oxidation procedure, which are fixed on the surface of the PS bead and cause repulsive interactions depending on the state of surface charge of the grounded VAIN samples. However, the here discussed data do not allow to unambiguously conclude on the precise origin of the electrostatic interactions. Moreover, the influence of the electrostatic interactions on the force required to pull off the PS-sphere could not be quantified. Instead, it is supposed that as the VAIN-coating is electrically conductive and grounded any transferred electrical charge in the contact region will be rather diminished. Consequently, the contribution of electrostatic interactions to the measured adhesion force is thus expected to be significantly smaller than the contributions by van der Waals and acid-base interactions.

As a consequence of the strong interaction forces present, material transfer from the bead to the surface might occur and this was tested by adhesion force measurements performed repeatedly on the same spot as shown in Fig. 4. The result was that among all probe-surface combinations investigated the adhesion value decreased after several contacts indicating material transfer from the probe to the sample.

In the case of the non-oxidized PS the reduction of the adhesion force was around 5 % and the material transfer is thus of lower relevance. In contrast, the decrease observed after oxidizing the PS was around 25–40 % therefore indicating that large amounts of material are transferred upon contact probably as a joint result of both the high interaction forces and the presence of low weight fragments at the surface.

For a more thorough investigation of the force interactions averaged adhesion forces were thus determined from force curves measured at 100 different positions on the sample and the results are shown in Table 2. It was observed that the adhesion was highest in the case of the contact between the oxidized PS and the oxidized VAIN followed by the contact between oxidized PS and sputter cleaned VAIN. This can obviously be related to the incorporation of a mixture of COC/COH, C=O, and COOH groups into the PS surface by the O beam oxidation (see Fig. S3).

The lowest adhesion force values were found in the case of the non-oxidized PS in contact with the oxidized and the non-oxidized surfaces of VAIN. In fact, in these cases the adhesion forces were equal though the surface chemistries of both VAIN surfaces were different as discussed above.

In order to understand these findings, the partitioning of the adhesion force in polar and van der Waals contributions is analysed based on different spectroscopic means and the results are presented in the following.

3.2.1. PS in contact with the non-oxidized and O beam oxidized surfaces of VAIN

The origin of the adhesion forces between non-oxidized PS and the non-oxidized and O beam oxidized surfaces of VAIN was investigated by analysing surface polarizabilities using XPS valence band and REELS spectra and by calculating the non-retarded Hamaker constants using Lifshitz theory. Fig. 5 shows the valence band spectra of the sputter cleaned and O beam oxidized VAIN. The spectra

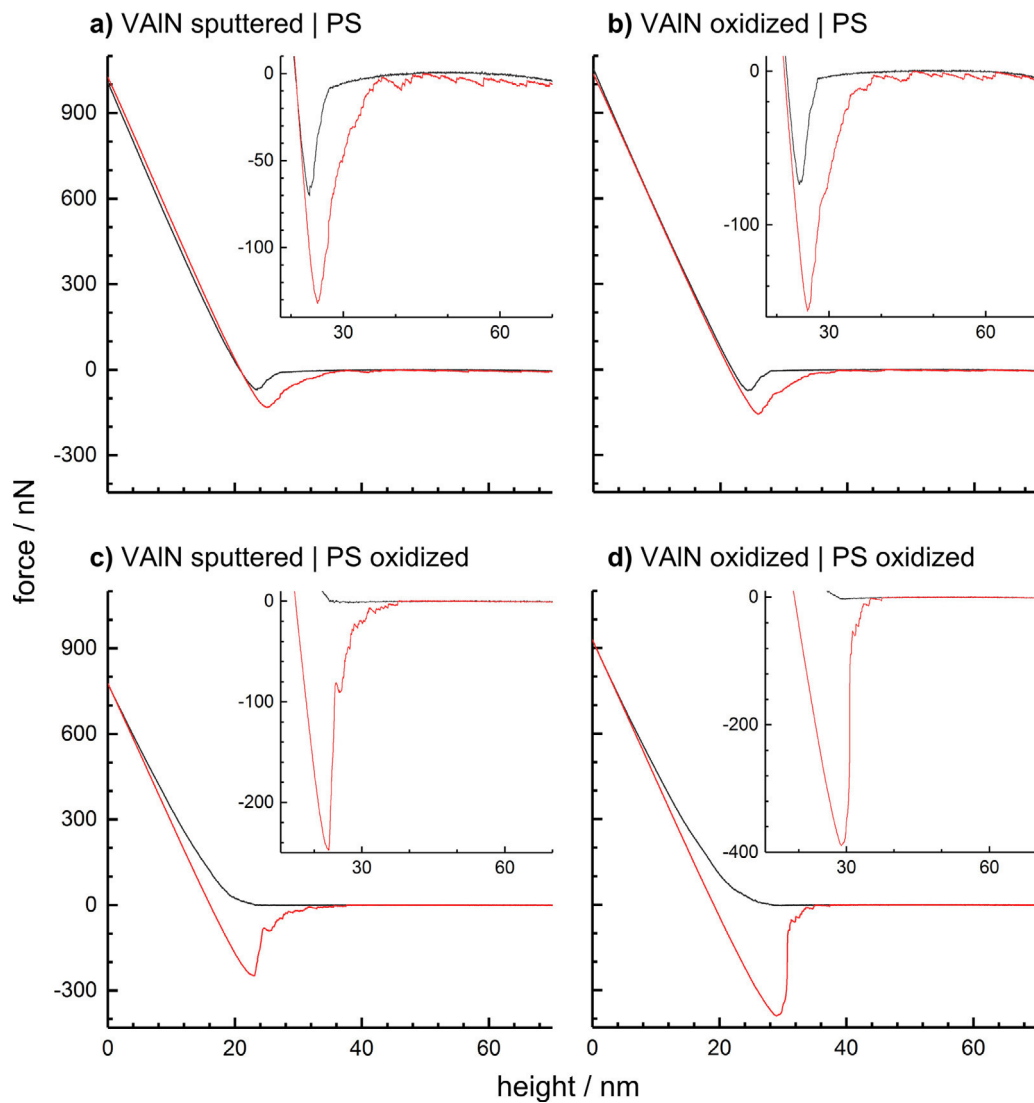


Fig. 3. typical force curves measured during grid spectroscopy between PS and VAIN in the a) sputtered and the b) oxidized states and between oxidized PS and c) sputtered and d) oxidized VAIN. The insets show a magnification of the pull-off region.

were characterized by four bands located at 17.8, 16.5, 9–2.5 and 0.4 eV and were ascribed according to the spectra of TiAlN to the O2s and N2s transitions, a mixed N2p/Al3p/O2p band (“p-band”) and to the V3d band [17,31,32]. Following sputter cleaning, a high intensity of the V3d band at the Fermi level was observed indicating that the surface showed the metal-like properties typical for nitridic hard coatings. In comparison, surface oxidation resulted into a decrease of the V3d intensity due to capture of the metal-like d-electrons during oxidation. However, the surface was not converted into a semiconductor but still showed within the depth of information of around 4.0 nm metal-like properties and therefore a high polarizability [12]. Since according to the XPS results the surface layers were gradually oxidized, this finding is generally in agreement with the electronic properties of vanadium suboxides: V₂O₃ is at room temperatures metal-like and VO₂ is a semiconductor but with a small band gap of 0.5 eV [33].

Another aspect revealed by the valence band spectra was an increased p-band intensity around 5 eV due to oxidation. This can be explained by the incorporation of oxygen and the related high photoelectric scattering cross section of the O2p state, which exceeds that of the N2p by a factor of three [34]. More importantly, the p-band was shifted by around 1 eV to lower binding energies. Since p-band related transitions significantly contribute to the optical

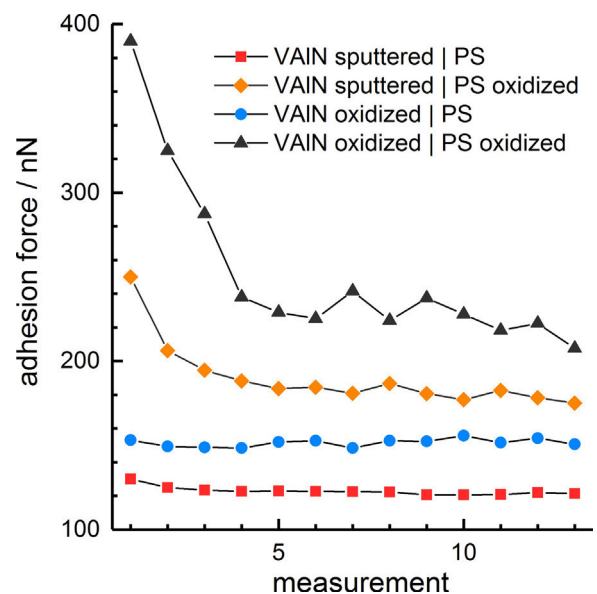


Fig. 4. Typical adhesion forces measured consecutively at the same spot.

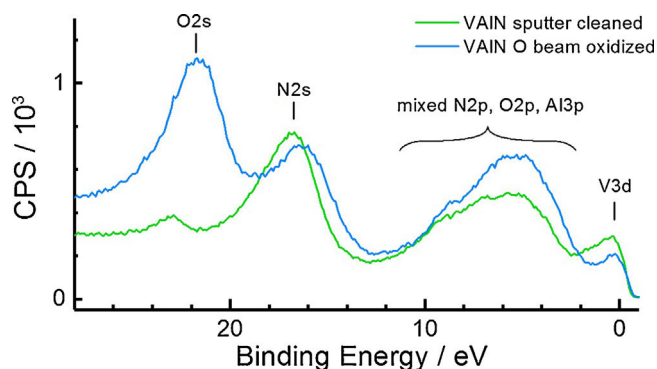


Fig. 5. XPS valence band spectra of VAIN after sputtering and after surface oxidation measured at an angle of emission of 60° relative to the surface normal.

response of VAIN as shown earlier for TiAlN, this shift possibly increases the polarizability [31].

The influence of these electronic effects on the polarizabilities of the surfaces (which are physically more precisely defined by the corresponding dielectric functions describing their optical response) and ultimately on the adhesion forces was investigated more directly by REELS.

The REELS spectra measured on the sputter cleaned and O beam oxidized VAIN surfaces and on the non-oxidized and oxidized PS surfaces were evaluated by using the QUEELS- $\varepsilon(\omega, k)$ -REELS software package from Tougaard and Yubero [6,7,9,35]. This involves first the determination of the experimental single electron inelastic scattering cross section λK_{exp} from the REELS spectra, which describes the energy loss of an electron due to optical and electronic transitions. This cross section is then simulated based on an empirically found dielectric function, which is specific for the material investigated and obtained after optimization until experimental and theoretical cross sections merge. The result of this procedure is shown in Fig. 6 and for the sake of clarity for the VAIN surfaces only (see Fig. S5 for the loss spectra of the PS surfaces). An excellent agreement between theoretical and experimental cross sections was found indicating a high quality of the dielectric functions (the parametric descriptions can be found in the supporting information).

Beside the dielectric functions, the QUEELS analysis also determines the Inelastic Mean Free Path (IMFP), which was 1.5 nm for both VAIN surfaces. The depth of information of the REELS spectra was therefore around 1.1 nm. In consequence, the dielectric function determined for the oxidized VAIN surface resembles an average across the upper part of the 1.5 nm thick oxygen containing layers but is unaffected by the non-oxidized substrate.

Considering now in more detail the properties of the VAIN cross sections, the assignment of the peaks in Fig. 6 was performed in analogy to TiAlN, which is motivated by the highly similar electronic structures of TiAlN and VAIN as evident from the valence band spectra [31]. Accordingly, the loss peak located at 2.6 eV was ascribed to V3d intraband transitions, the peaks at 9.0 and 13.8 eV to transitions from the p -band to unoccupied states in the V3d and V4s band and the peak at 21.8 eV to the volume plasmon. The losses around 50 eV are ascribed to V3p and V3s related transitions.

After surface oxidation, the losses due to V3d intraband transitions decreased and the p -band related loss within the range of 5–16 eV restructured in agreement with the analysis of the valence band spectra. In contrast, the decreased loss in the low energy range was in parts compensated by an increase of the volume plasmon related loss near 20 eV. This change was due to the nature of the plasmon not resembled in the valence band spectra and this shows that the combined analysis of the loss and valence band spectra is justified for distinguishing chemical and electronic effects when

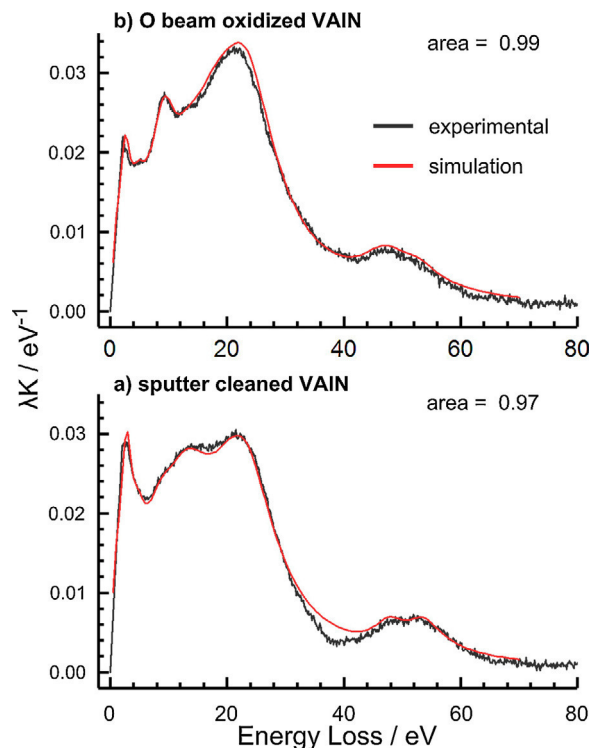


Fig. 6. Experimental and theoretical single electron inelastic scattering cross sections λK as obtained from REELS spectra measured on the a) sputter cleaned and b) O beam oxidized VAIN surfaces using the QUEELS- $\varepsilon(\omega, k)$ -REELS software package.

investigating polarizability changes. In conclusion, the surface oxidation affected the loss spectra and therefore the optical response of the surface especially at low energies but did not induce crucial changes of the overall behaviour. Hence, the van der Waals interactions between polystyrene and both the oxidized and non-oxidized surfaces of VAIN should be comparable, because the dispersive force interactions emerge from the integrated optical response of the surfaces within the whole energy range.

This interpretation was validated by the calculation of the non-retarded Hamaker constants between PS and the oxidized and non-oxidized VAIN surfaces across vacuum by Lifshitz theory using the REELS based dielectric functions (the calculation is detailed out in the supporting information). In both cases the non-retarded Hamaker constants were around $(1.6 \pm 0.1) \times 10^{-19}$ J in agreement with the observed adhesion forces. In conclusion, the adhesive interactions of polystyrene with the oxidized and sputter cleaned surfaces of VAIN are explained by van der Waals forces only. This is in accordance with the non-polar properties of PS and its chemical inertness. Furthermore, the inhibition of a decreased adhesion as a possible effect of the superficial oxidation was ultimately prevented by the mechanism of the reactive inward migration, which resulted into an only gradually oxidized nitrogen rich surface with a still high polarizability.

3.2.2. O beam oxidized PS in contact with the non-oxidized and O beam oxidized surfaces of VAIN

After oxidizing the polystyrene surface with the O beam, the adhesion force measured on the sputter cleaned VAIN was increased by a factor of two from 125 ± 31 nN to 263 ± 64 nN (see Table 2). When measuring with the oxidized polystyrene bead on the oxidized VAIN surface an even higher increase from around 127 ± 33 nN to 397 ± 70 nN was found.

The partitioning of these adhesion forces was again investigated by analysing the corresponding Hamaker constants. As calculated from the REELS derived optical data of the surfaces, the Hamaker

Table 2

Averaged adhesion forces measured by CFS using a PS probe before and after oxidation on the VAIN surface in the sputter cleaned and oxidized states. The average was calculated from 100 curves.

		F _{ad} (PS)/nN	
		non-oxidized	O beam oxidized
VAIN	sputter cleaned	125 ± 31	263 ± 64
	O beam oxidized	127 ± 33	397 ± 70

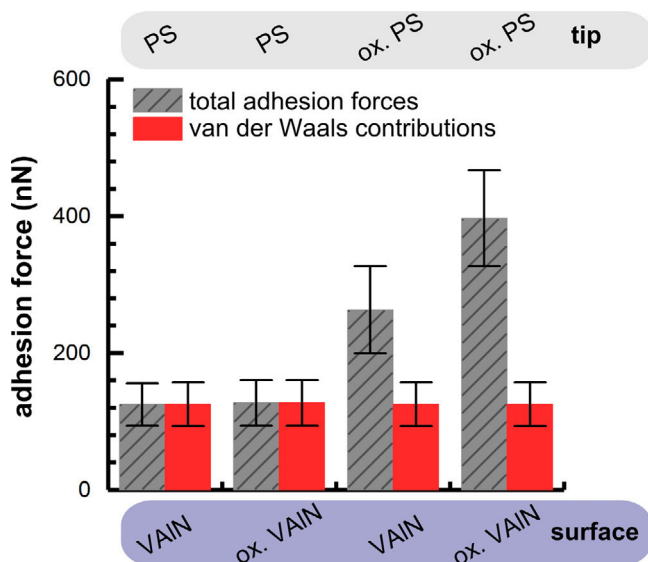


Fig. 7. Van der Waals contributions to the total adhesion force as measured between the oxidized and non-oxidized surfaces of PS and VAIN.

constants were around $(1.7 \pm 0.1) \times 10^{-19}$ J and essentially match the values found for the case of the non-oxidized PS. This finding discloses that the surface oxidation of PS only slightly affects the van der Waals interactions. Consequently, the adhesion force contributions specifically related to the van der Waals interactions can be directly estimated by the adhesion force values as measured with the non-oxidized polystyrene as shown in Fig. 7. The observed increase of the adhesion forces is therefore quantitatively attributed to the presence of strong acid-base interactions superimposed by slight electrostatic contributions. The joined acid-base and electrostatic interactions contribute with 50% (sputter cleaned VAIN) and 70% (oxidized VAIN) to the overall adhesion force. The Lewis acid-base interactions most probably originate from the coordination of carboxylic acid groups in the surface of the oxidized polystyrene with metal centres of the oxidized VAIN surface acting as Lewis acids.

In conclusion, the presence of carboxylic acid groups in polystyrene most probably increases the adhesion forces due to coordinative bonding with surface metal cations. However, a comprehensive understanding of adhesion still requires the consideration of the van der Waals interactions of the subsurface volume, which similarly contribute to the overall adhesion force.

4. Conclusions

The adhesive interactions between VAIN thin films and polystyrene were investigated by means Colloidal Force Spectroscopy (CFS) and XPS under UHV conditions as a function of their surface chemistry. The surface oxidation of VAIN was achieved by exposure of the oxygen-free VAIN to a non-accelerated oxygen beam. The oxidized surface was characterized by an extended oxynitridic growth region with a gradient composition including

vanadium ions with mixed oxidation states ranging from +III in the bulk to +V at the surface. Adhesion force measurements on the oxidized and oxygen-free surfaces of VAIN using a non-oxidized PS colloidal probe showed that the superficial oxidation of VAIN does not significantly affect the van der Waals interactions. This could be explained by a high polarizability of the VAIN surface even after partial oxidation as revealed by the combined analysis of REELS and XPS valence band spectra and the calculation of non-retarded Hamaker constants using Lifshitz theory.

In contrast, the adhesion forces measured with an oxygen beam treated PS colloidal probe containing surface carboxylic acid groups on both oxygen-free and oxidized VAIN were strongly increased due to Lewis acid-base interactions. It can be assumed that the surface carboxylic acid groups form coordination bonds with surface metal atoms both in the nitride and the oxynitride surface. The analysis of the partitioning of adhesion forces by Lifshitz analysis showed that even in the presence of acid-base interactions the van der Waals interactions were almost not affected and contributed in a similar range as the acid-base interactions to the overall measured adhesion forces.

Acknowledgments

We gratefully acknowledge the financial support by the German Research Foundation (DFG) within the projects SFB-TR 87 A2 and A3. The authors thank Holger Ruess and Prof. Dr. Jochen M. Schneider from the Materials Chemistry division of the RWTH Aachen for the preparation of the hard coatings.

Appendix A. Supplementary data

Supplementary data associated with this article can be found, in the online version, at <https://doi.org/10.1016/j.apsusc.2017.09.208>.

References

- [1] E.J. Bienk, N.J. Mikkelsen, Application of advanced surface treatment technologies in the modern plastics moulding industry, *Wear* 207 (1997) 6–9, [http://dx.doi.org/10.1016/S0043-1648\(96\)07503-5](http://dx.doi.org/10.1016/S0043-1648(96)07503-5).
- [2] K. Bobzin, R. Nickel, N. Bagcivan, F.D. Manz, PVD-Coatings in Injection Molding Machines for Processing Optical Polymers, *Plasma Process. Polym.* 4 (2007) S144–S149, <http://dx.doi.org/10.1002/ppap.200730507>.
- [3] M. Rebelo de Figueiredo, C. Bergmann, C. Ganser, C. Teichert, C. Kukla, C. Mitterer, Adhesion tendency of polymers to hard coatings, *Int. Polym. Process.* 28 (2013) 415–420, <http://dx.doi.org/10.3139/217.2767>.
- [4] O. Hunold, M. Wiesing, T. de los Arcos, D. Music, G. Grundmeier, J.M. Schneider, Influence of O₂ exposure on the interaction between CH₄ and amorphous AlYB14, *Appl. Surf. Sci.* 392 (2017) 1165–1172, <http://dx.doi.org/10.1016/j.apsusc.2016.09.092>.
- [5] R.H. French, H. Müllejans, D.J. Jones, G. Duscher, R.M. Cannon, M. Rühle, Dispersion forces and Hamaker constants for intergranular films in silicon nitride from spatially resolved-valence electron energy loss spectrum imaging, *Acta Mater.* 46 (1998) 2271–2287, [http://dx.doi.org/10.1016/S1359-6454\(98\)80008-6](http://dx.doi.org/10.1016/S1359-6454(98)80008-6).
- [6] S. Tougaard, F. Yubero, QUEELS software package for calculation of surface effects in electron spectra, *Surf. Interface Anal.* 36 (2004) 824–827, <http://dx.doi.org/10.1002/sia.1774>.
- [7] S. Tougaard, I. Chorkendorff, Differential inelastic electron scattering cross sections from experimental reflection electron-energy-loss spectra: application to background removal in electron spectroscopy, *Phys. Rev. B* 35 (1987) 6570–6577, <http://dx.doi.org/10.1103/PhysRevB.35.6570>.
- [8] F. Yubero, S. Tougaard, Model for quantitative analysis of reflection-electron-energy-loss spectra, *Phys. Rev. B* 46 (1992) 2486–2497, <http://dx.doi.org/10.1103/PhysRevB.46.2486>.
- [9] F. Yubero, D. Fujita, B. Ramskov, S. Tougaard, Experimental test of model for angular and energy dependence of reflection-electron-energy-loss spectra, *Phys. Rev. B* 53 (1996) 9728–9732, <http://dx.doi.org/10.1103/PhysRevB.53.9728>.
- [10] D. Tahir, S. Tougaard, Electronic and optical properties of selected polymers studied by reflection electron energy loss spectroscopy, *J. Appl. Phys.* 111 (2012) 054101, <http://dx.doi.org/10.1063/1.3688327>.
- [11] K.P. Shaha, H. Rueß, S. Rotert, M. Baben, D. Music, J.M. Schneider, Nonmetal sublattice population induced defect structure in transition metal aluminum

- oxynitrides, *Appl. Phys. Lett.* 103 (2013) 221905, <http://dx.doi.org/10.1063/1.4833835>.
- [12] C.J. Powell, A. Jablonski, NIST Electron Effective-Attenuation-Length Database, National Institute of Standards and Technology, Gaithersburg MD, 2011.
- [13] G.W. Tormoen, J. Drellich, Deformation of soft colloidal probes during AFM pull-off force measurements: elimination of nano-roughness effects, *J. Adhes. Sci. Technol.* 19 (2005) 181–198, <http://dx.doi.org/10.1163/1568561054352603>.
- [14] C. Corbella, S. Grosse-Kreul, O. Kreiter, T. de los Arcos, J. Benedikt, A. von Keudell, Particle beam experiments for the analysis of reactive sputtering processes in metals and polymer surfaces, *Rev. Sci. Instrum.* 84 (2013) 103303, <http://dx.doi.org/10.1063/1.4826066>.
- [15] R. Anton, T. Wiegner, W. Naumann, M. Liebmann, C. Klein, C. Bradley, Design and performance of a versatile, cost-effective microwave electron cyclotron resonance plasma source for surface and thin film processing, *Rev. Sci. Instrum.* 71 (2000) 1177–1180, <http://dx.doi.org/10.1063/1.1150420>.
- [16] A. Arranz, C. Palacio, The formation of V-Al-N thin films by reactive ion beam mixing of V/Al interfaces, *Appl. Phys. A* 97 (2009) 217–224, <http://dx.doi.org/10.1007/s00339-009-5181-7>.
- [17] M. Wiesing, T. de los Arcos, G. Grundmeier, The thermal oxidation of TiAlN high power pulsed magnetron sputtering hard coatings as revealed by combined ion and electron spectroscopy, *Adv. Mater. Interfaces* (2017) 1600861, <http://dx.doi.org/10.1002/admi.201600861>.
- [18] G. Greczynski, L. Hultman, Self-consistent modelling of X-ray photoelectron spectra from air-exposed polycrystalline TiN thin films, *Appl. Surf. Sci.* 387 (2016) 294–300, <http://dx.doi.org/10.1016/j.apsusc.2016.06.012>.
- [19] R. Sanjinés, C. Wiemer, F. Lévy, Chemical bonding and electronic structure in binary VNy and ternary T1-xVxNy nitrides, *J. Appl. Phys.* 83 (1998) 1396–1402, <http://dx.doi.org/10.1063/1.366843>.
- [20] G. Indlekofer, J.-M. Mariot, W. Lengauer, E. Beauprez, P. Oelhafen, C.F. Hague, Electronic structure of stoichiometric and substoichiometric vanadium nitride from photoelectron spectroscopy, *Solid State Commun.* 72 (1989) 419–423, [http://dx.doi.org/10.1016/0038-1098\(89\)90590-5](http://dx.doi.org/10.1016/0038-1098(89)90590-5).
- [21] P. Prieto, R.E. Kirby, X-ray photoelectron spectroscopy study of the difference between reactively evaporated and direct sputter-deposited TiN films and their oxidation properties, *J. Vac. Sci. Technol. A* 13 (1995) 2819–2826, <http://dx.doi.org/10.1116/1.579711>.
- [22] R. Zimmermann, R. Claessen, F. Reinert, P. Steiner, S. Hüfner, Strong hybridization in vanadium oxides: evidence from photoemission and absorption spectroscopy, *J. Phys. Condens. Matter* 10 (1998) 5697, <http://dx.doi.org/10.1088/0953-8984/10/25/018>.
- [23] H. Wiame, L. Bois, P. Lharidon, Y. Laurent, P. Grange, Synthesis and XPS characterization of a novel aluminovanadate oxynitride basic catalyst: influence of nitridation temperature, *Solid State Ion* 101 (1997) 755–759, [http://dx.doi.org/10.1016/S0167-2738\(97\)00291-9](http://dx.doi.org/10.1016/S0167-2738(97)00291-9).
- [24] M. Demeter, M. Neumann, W. Reichelt, Mixed-valence vanadium oxides studied by XPS, *Surf. Sci.* 454–456 (2000) 41–44, [http://dx.doi.org/10.1016/S0039-6028\(00\)00111-4](http://dx.doi.org/10.1016/S0039-6028(00)00111-4).
- [25] S. Hofmann, Formation and diffusion properties of oxide films on metals and on nitride coatings studied with Auger electron spectroscopy and X-ray photoelectron spectroscopy, *Thin Solid Films* 193–194 (1990) 648–664, [http://dx.doi.org/10.1016/0040-6090\(90\)90216-z](http://dx.doi.org/10.1016/0040-6090(90)90216-z) (Part 2).
- [26] S. Hofmann, Auger- and X-Ray Photoelectron Spectroscopy in Materials Science, Springer, 2013.
- [27] H.H. Brongersma, M. Draxler, M. de Ridder, P. Bauer, Surface composition analysis by low-energy ion scattering, *Surf. Sci. Rep.* 62 (2007) 63–109, <http://dx.doi.org/10.1016/j.surfrep.2006.12.002>.
- [28] A. Noy, R.W. Friddle, Practical single molecule force spectroscopy: how to determine fundamental thermodynamic parameters of intermolecular bonds with an atomic force microscope, *Methods* 60 (2013) 142–150, <http://dx.doi.org/10.1016/j.ymeth.2013.03.014>.
- [29] C.C. Dupont-Gillain, Y. Adriaensen, S. Derclaye, P.G. Rouxhet, Plasma-oxidized polystyrene: wetting properties and surface reconstruction, *Langmuir* 16 (2000) 8194–8200, <http://dx.doi.org/10.1021/la000326l>.
- [30] M. Grandbois, M. Beyer, M. Rief, H. Clausen-Schaumann, H.E. Gaub, How strong is a covalent bond? *Science* 283 (1999) 1727–1730, <http://dx.doi.org/10.1126/science.283.5408.1727>.
- [31] I. leR. Strydom, S. Hofmann, XPS and EELS study of the valence band electronic structure of TiN and (Ti, Al)N coatings as influenced by the deposition parameters, *Vacuum* 41 (1990) 1619–1623, [http://dx.doi.org/10.1016/0042-207X\(90\)94035-o](http://dx.doi.org/10.1016/0042-207X(90)94035-o).
- [32] M. to Baben, L. Raumann, J.M. Schneider, Phase stability and elastic properties of titanium aluminum oxynitride studied by ab initio calculations, *J. Phys. Appl. Phys.* 46 (2013) 084002, <http://dx.doi.org/10.1088/0022-3727/46/8/084002>.
- [33] M.M. Qazilbash, A.A. Schafgans, K.S. Burch, S.J. Yun, B.G. Chae, B.J. Kim, H.T. Kim, D.N. Basov, Electrodynamics of the vanadium oxides $\text{V}_{1-x}\text{O}_{2-x}$ and $\text{V}_{1-x}\text{O}_{3-x}$, *Phys. Rev. B* 77 (2008) 115121, <http://dx.doi.org/10.1103/PhysRevB.77.115121>.
- [34] J.H. Scofield, Hartree-Slater subshell photoionization cross-sections at 1254 and 1487 eV, *J. Electron Spectrosc. Relat. Phenom.* 8 (1976) 129–137, [http://dx.doi.org/10.1016/0368-2048\(76\)80015-1](http://dx.doi.org/10.1016/0368-2048(76)80015-1).
- [35] F. Yubero, S. Tougaard, Quantitative analysis of reflection electron energy-loss spectra, *Surf. Interface Anal.* 19 (1992) 269–273, <http://dx.doi.org/10.1002/sia.740190152>.

UHV AFM based colloidal probe studies of adhesive properties of VAIN hard coatings

-Supporting Information-

M. Wiesing, T. de los Arcos, G. Grundmeier

Technical and Macromolecular Chemistry, University of Paderborn, Warburger Straße 100, 33098
Paderborn, Germany

Correspondence to: Guido Grundmeier (E-mail: g.grundmeier@tc.uni-paderborn.de)

Surface topography of VAIN

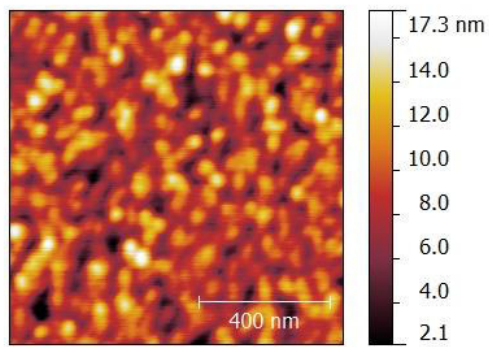


Figure S 1: Surface topography of the VAIN surface after deposition as determined by atmospheric AFM in alternating contact mode.

Sputtering during the LEIS measurement

Figure S 2 shows subsequently measured LEIS spectra and it was found that the spectra change only slightly over time. This indicates the first spectrum as used in the discussion sufficiently resembles the structure of the undamaged surface.

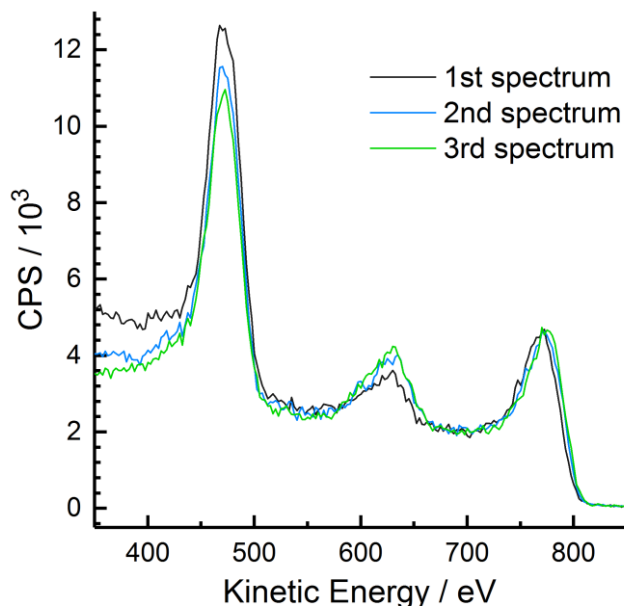


Figure S 2: Subsequently measured LEIS spectra on O beam oxidized VAIN using 1 keV He⁺. The acquisition speed per spectrum was 70 s.

O beam oxidation of polystyrene

The oxidation of polystyrene by the mixed atom/ion O beam was investigated by XPS. It was found that the pristine polystyrene surface was composed of 100 at% carbon. After oxidation the surface contained 83.2 at% carbon and 16.8 at% oxygen. A more detailed characterization of the surface chemistry was performed by means of high-resolution XPS core level spectra as shown in Figure S 3.

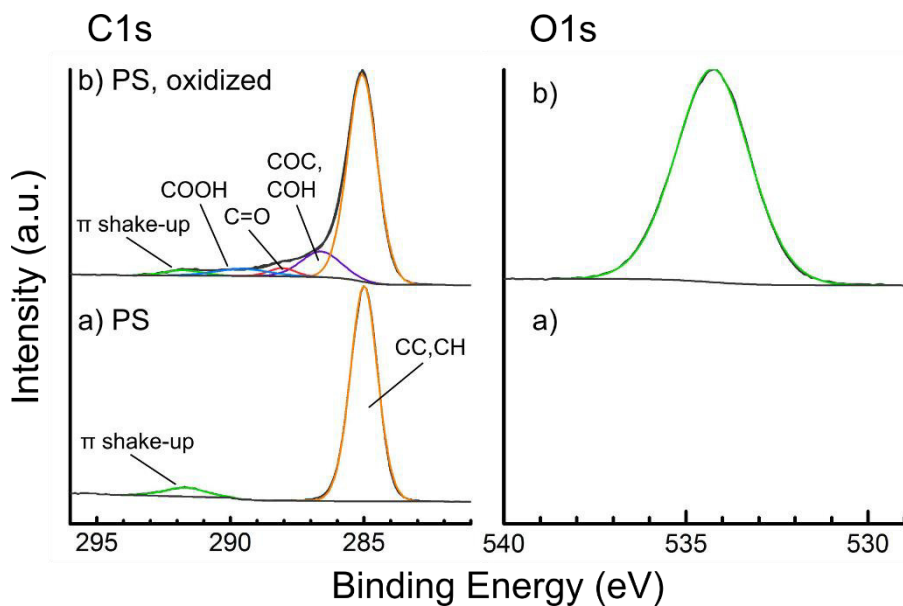


Figure S 3: High-resolution XPS spectra of the C1s and O1s core levels **a)** before and **b)** after surface oxidation by means of the O beam at 0 V acceleration voltage for 90 s.

After O beam oxidation, the C1s spectrum could be described by 5 components ascribed to CC and CH at 285.0 eV, COC and COH at 286.5 eV, C=O at 287.9 eV, COOH at 289.5 eV and the π shake-up at 291.7 eV using typical C1s shifts of polymers.[1] The relative fractions of the components to the overall C1s signal can be found in Table S 1. It was thus found that the surface was covered by a mixture of oxygen functional groups including carboxylic acids, which is typical for oxygen plasma oxidized polystyrene.[2] Further, the fraction of the π shake-up was decreased from 6 to 2 % due to oxidation indicating that the phenyl groups of the PS were etched.

Table S 1: Fractions of the components used for the description of the C1s signal.

components	PS	oxidized PS
CC, CH	0.94	0.77
COC, COH	-	0.12
C=O	-	0.04
COOH	-	0.05
π shake-up	0.06	0.02

XPS of Ar⁺ sputter cleaned VAl(O,N)

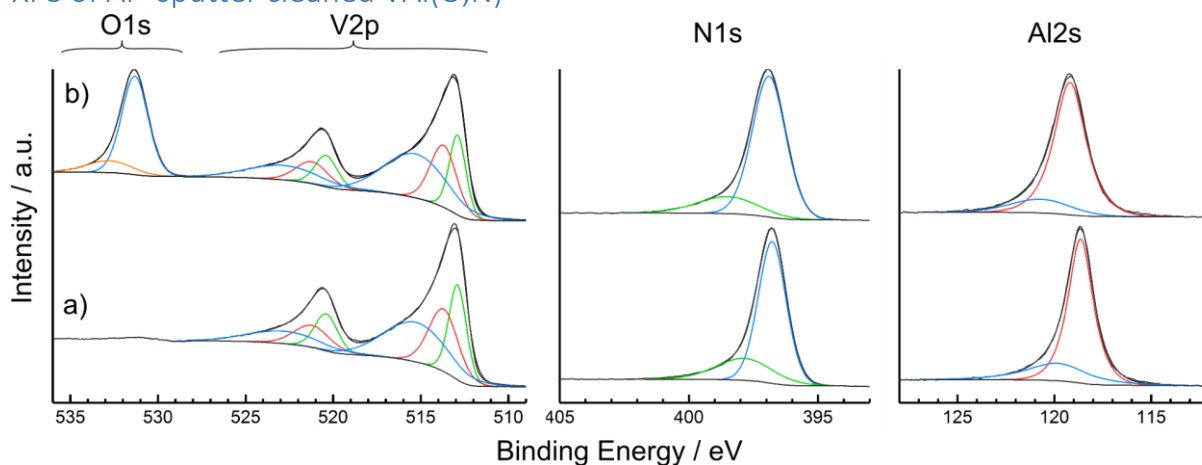


Figure S 4: High-resolution XPS spectra of sputter cleaned **a)** VAlN and **b)** VAl(O,N).

Figure S 4 shows the high resolution XPS spectra of sputter cleaned VAlN and VAl(O,N). In comparison, the lineshapes and related fit components of VAl(O,N) and VAlN are very similar among the V2p and N1s core level signals and their common binding energies and assignments are given in the main text. In contrast, the binding energy of the Al2s signal in VAl(O,N) was 119.2 eV and was therefore shifted by 0.6 eV to higher binding energies when compared to VAlN. However, the origin of this binding energy shift is unclear when considering that the changes in the bonding environment of Al as observed after O beam oxidation of VAlN did not involve shifts of the Al2s signal. Another difference between the VAlN and the VAl(O,N) spectrum was the occurrence of an O1s signal in the VAl(O,N) spectrum. In this regard, the O1s signal related to the oxynitride was located at 531.35 eV and was again slightly asymmetric, which was accounted for by fitting a satellite component at 532.85 eV.

QUEELS analysis of REELS spectra

The experimental and simulated single electron energy loss spectra are shown in Figure S 5.

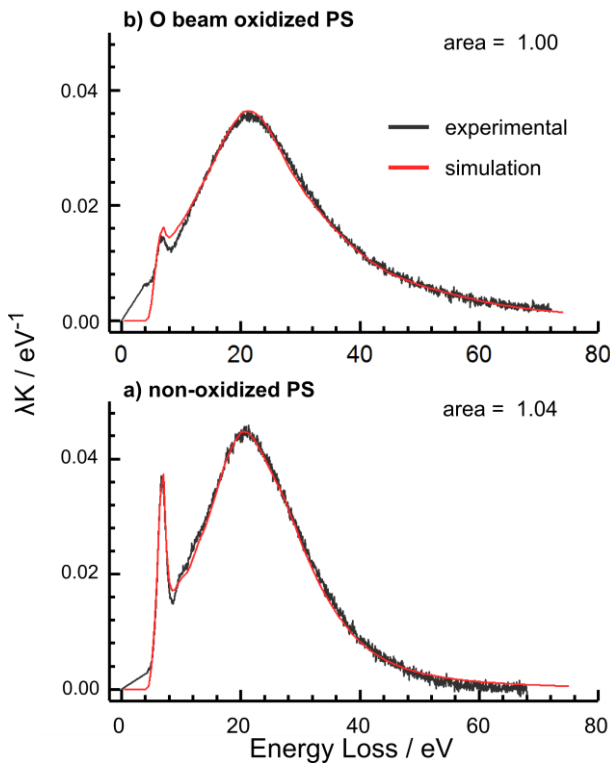


Figure S 5: Experimental and theoretical single electron inelastic scattering cross sections λK as obtained from REELS spectra measured on the **a)** non-oxidized PS and the **b)** O beam oxidized PS surfaces using the QUEELS- $\epsilon(\omega, k)$ -REELS software package.

The dielectric function within the QUEELS- $\epsilon(\omega, k)$ -REELS software package are defined in terms of the energy loss function as [3–5]

$$\text{Im}\left(-\frac{1}{\epsilon(\omega, k)}\right) = \theta(\hbar\omega - E_g) \cdot f(\hbar\omega) \cdot \sum_i \frac{A_i \gamma_i \hbar\omega}{(\hbar^2 \omega_{0,i}^2(k) - \hbar^2 \omega^2)^2 + \gamma_i^2 \hbar^2 \omega^2} \quad (\text{S1a})$$

$$\hbar\omega_{0,i}(k) = \hbar\omega_{0,i} + \alpha_i \frac{\hbar^2 \omega^2}{2m_e} \quad (\text{S1b})$$

$$f(\hbar\omega) = \left[\frac{a2(\hbar\omega - E_g)^p}{\hbar^2 \omega^2} \right]^{tmp1}, \text{ if } E_g < \hbar\omega < E_g + a1 \quad (\text{S1c})$$

$$tmp1 = \cos^2\left(\frac{\pi \hbar\omega - E_g}{2 a1}\right) \quad (\text{S1d})$$

$$f(\hbar\omega) = 1, \text{ if } \hbar\omega > E_g + a1 \quad (\text{S1e})$$

where $\epsilon(\omega, k)$ is the dielectric function, $\hbar\omega$ the energy, E_g the band gap, A_i and γ_i the strength and damping of an oscillator i , $\hbar\omega_{0,i}$ the resonance frequency and, α_i the momentum dispersion coefficient, k the wave vector and m_e the mass of an electron. $\theta(\hbar\omega - E_g)$ represents a step function, which is unity at $\hbar\omega > E_g$ and zero at $\hbar\omega < E_g$. $f(\hbar\omega)$ is introduced to adapt the lineshape near the band gap by using the empirical parameters a_1 and a_2 . Direct and indirect band gaps are considered by the exponent p , which is 0.5 (direct) or 2 (indirect).

The parameters of the oscillators as determined by the QUEELS analysis are shown in Table S 2. The IMFPs of the VAIN surfaces were 1.5 nm at a kinetic energy of 1050 eV and that of the polystyrene surfaces were 0.6 nm at 460 eV.

Table S 2: Parameters of the dielectric functions of PS, oxidized PS, sputter cleaned VAIN and oxidized VAIN..

		$\hbar\omega_0 / \text{eV}$	A_0 / eV^2	$\hbar\gamma / \text{eV}$	α
PS		7	2.1	1.23	0
E_g	4.2	10	0.5	2	0
a_1	3.2	13	0.5	2	0
a_2	9	22.2	206.1	13	0
p	2	27.6	48.2	9	0
		32.5	140.0	18	0
oxidized PS		7	0.306	1.23	0
E_g	4.2	10	0.08	2	0
a_1	3.2	13	0.2	2	0
a_2	9	24	250.4	16	0
p	2	35	235.8	25	0
		55	94.2	30	0
sputtered VAIN		3.2	0.627	2.2	0.5
<i>metal</i>		5.1	0.828	3	0.5
		9.4	4.05	6	0.5
		15.3	55.7	10	0.5
		23.4	308	11	0.5
		47	66.4	6	0.5
		52.8	86.7	6	0.5
oxidized VAIN		2.9	0.308	2	0.5
<i>metal</i>		5.1	0.591	3	0.5
		10	7.690	4.6	0.5
		14.2	10.14	7	0.5
		23.4	402	11	0.5
		46.5	133	9	0.5
		52	45.5	6	0.5

Calculation of non-retarded Hamaker constants by Lifshitz analysis

The Hamaker coefficients were determined by Lifshitz theory according to [6]

$$A_h(d) = -\frac{3}{2}kT \sum_{n=0}^{\infty} \int_{r_n}^{\infty} x \ln[(1 - \bar{\Delta}_{Am}\bar{\Delta}_{Bm}e^{-x})(1 - e^{-x})] dx \quad (S2a)$$

$$\bar{\Delta}_{im} = \frac{x_m \varepsilon_i - x_i \varepsilon_m}{x_m \varepsilon_i + x_i \varepsilon_m} \quad (S2b)$$

$$x_i^2 = x_m^2 + \left(\frac{2l\xi_n}{c}\right)^2 (\varepsilon_i - \varepsilon_m), x_m = x \quad (S2c)$$

$$r_n = \frac{2l\sqrt{\varepsilon_m}}{c} \xi_n \quad (S2d)$$

$$\hbar\xi_n = 2\pi kTn \quad (S2d)$$

where ξ_n is the nth Matsubara frequency, ε_m the relative permittivity and in this case set to unity and r_n is the pertinent ratio. The first term in equation S2a ($n = 0$) is multiplied by 0.5. Equation S2a was evaluated by means of the dielectric functions as obtained by the QUEELS analysis and following the conversion of the dielectric function to the imaginary axis by

$$\varepsilon(i\xi_n) = 1 + \frac{2}{\pi} \int_0^{\infty} \frac{\omega_R \varepsilon''(\omega_R)}{\omega_R^2 + \xi_n^2} d\omega_R \quad (S3)$$

where ω_R is the radial frequency. The non-retarded Hamaker constants were obtained in the limit of low distances ($d = 0.3$ nm).

References

- [1] D. Briggs, J.T. Grant, Surface analysis by Auger and x-ray photoelectron spectroscopy, IMPublications and SurfaceSpectra, Chichester and Manchester, 2003.
- [2] R.W. Paynter, Degradation during ARXPS measurements of polystyrene treated with an oxygen plasma, Surf. Interface Anal. 33 (2002) 862–868. doi:10.1002/sia.1464.
- [3] S. Tougaard, F. Yubero, QUEELS software package for calculation of surface effects in electron spectra, Surf. Interface Anal. 36 (2004) 824–827. doi:10.1002/sia.1774.
- [4] F. Yubero, D. Fujita, B. Ramskov, S. Tougaard, Experimental test of model for angular and energy dependence of reflection-electron-energy-loss spectra, Phys. Rev. B. 53 (1996) 9728–9732. doi:10.1103/PhysRevB.53.9728.
- [5] F. Yubero, J.M. Sanz, B. Ramskov, S. Tougaard, Model for quantitative analysis of reflection-electron-energy-loss spectra: Angular dependence, Phys. Rev. B. 53 (1996) 9719–9727. doi:10.1103/PhysRevB.53.9719.
- [6] V.A. Parsegian, Van der Waals Forces: A Handbook for Biologists, Chemists, Engineers, and Physicists, Cambridge University Press, Cambridge, 2005. <http://ebooks.cambridge.org/ref/id/CBO9780511614606> (accessed June 15, 2016).

5 Overall discussion

5.1 Surface chemical structure of hard coatings

The surface chemistry and oxidation behaviour of ternary nitridic hard coatings were investigated within the first section of this thesis at the example of $\text{Ti}_{0.5}\text{Al}_{0.5}\text{N}$ and mechanisms for the thermal and electrochemical oxidation could be developed. It is therefore the scope of the following discussion to clarify whether these model can also explain the surface oxidation behaviour of $\text{Ti}_{0.5}\text{Al}_{0.5}\text{N}$ as encountered in practice and whether they may be even transferrable to related hard coating systems such as e.g. $\text{Cr}_{0.5}\text{Al}_{0.5}\text{N}$ or $\text{V}_{0.5}\text{Al}_{0.5}\text{N}$.

In this regards, the surface chemical structure of $\text{Ti}_{0.5}\text{Al}_{0.5}\text{N}$ as obtained after oxidation at reduced oxygen pressures (see publication I, figure 3) shows the same layer structure as that observed after deposition and exposure to ambient atmosphere (see publication II, figure 2). Only a slightly increased thickness and more pronounced superficial aluminium enrichment is found in the latter case. However, these both findings may be explained according to the principles of the high-field oxidation by the increased oxygen partial pressures at ambient conditions, which cause higher electrical field strengths during oxidation. The mechanism of the thermal oxidation developed in this work therefore also applies to the situation encountered after deposition and atmospheric exposure. In fact, the surface oxidation layer of $\text{Cr}_{0.8}\text{Al}_{0.2}\text{N}$, which behaves similar as $\text{Ti}_{0.5}\text{Al}_{0.5}\text{N}$ as discussed below, found in other works is also in accordance with the herein developed mechanism and was further shown to increase only slightly upon oxidation in air at operating temperatures of 570 K.^{285,286} It follows that the oxidation mechanism is most probably also valid at even more elevated temperatures and for other nitridic hard coatings.

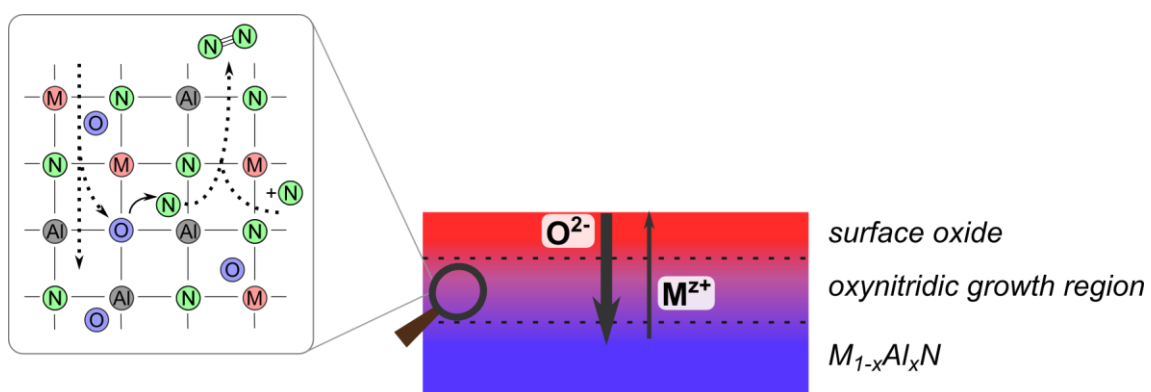


Figure 19: Predicted oxynitridic growth region during the oxidation of hard coatings.

This supposition can corroborated by comparing the thermal and electrochemical oxidation: it follows that the reactive inward migration of oxygen is a main mechanism responsible for oxidation and thereby a central aspect for both oxidation mechanisms. As a consequence, an extended interdiffusion region of oxygen and nitrogen and therefore an intermediary oxynitridic phase develops in both cases.

Based on the ab initio studies of Rotert et al., this finding is explained by the thermodynamically favoured formation of the oxynitride out from the nitride.⁵⁴ However, the formation of stable oxynitride phases is also expected for a wide range of transition metal nitrides according to these authors. Thus, the here developed mechanisms may be transferrable to other nitridic hard coatings and indeed the same oxidation behaviour was observed for $V_{0.5}Al_{0.5}N$ in publication VI and also for $Cr_{0.5}Al_{0.5}N$ elsewhere.^{285,286} In conclusion, hard coatings are expected to oxidize either thermally or anodically mainly by oxygen inwards migration, which results into the formation of an intermediary oxynitride acting as growth region within the multi-layered surface oxide as illustrated in figure 19. The oxidic top layers formed out from the oxynitride are therefore initially nitrogen doped and lose continuously nitrogen in the course of oxidation so that finally only molecular nitrogen incorporated into the defective surface oxide may be found. Therefore, no sharp but rather diffuse phase boundaries develop.

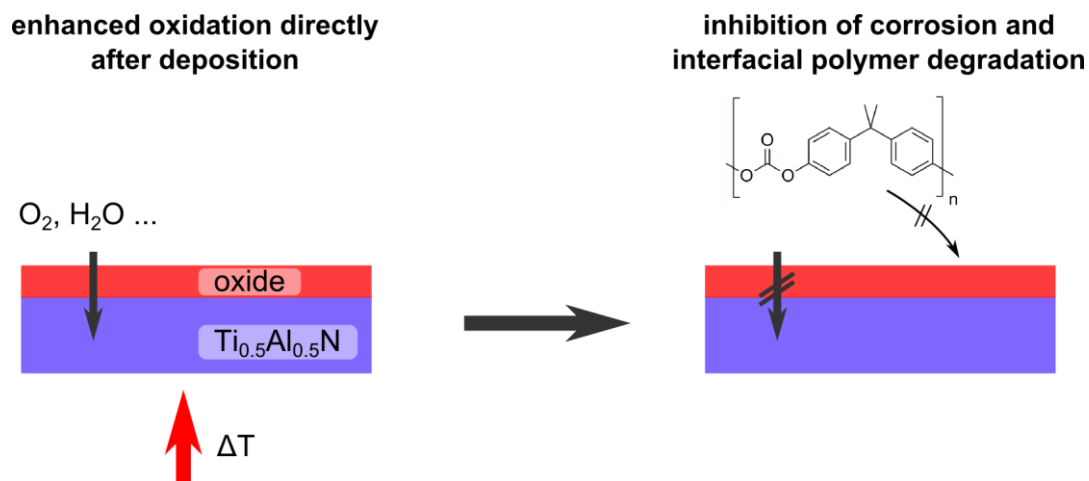


Figure 20: Possible inhibition of the accelerated polymer degradation and of the corrosion of hard coatings as encountered at operating conditions by an oxidative post-treatment of the coatings directly after deposition.

However, the comparison of the thermal and electrochemical oxidation mechanisms show that they do not result both into a passivation of the surface: the thermal oxidation induces a metal to semiconductor transition and results into surface passivation as reflected by the self-limited formation of a dense surface oxide film. In contrast, the electrochemical oxidation is characterized by the continuous build-up of a defective and hydrous surface oxide with a high reactivity due to the presence of Ti(III) surface states. This converse behaviour may presumably be explained by structural distortions caused by the expansion of the molecular nitrogen formed during the enhanced electrochemical oxidation, which may then result into defect formation and hydration. It is noted that these findings are highly relevant ... for plastics injection moulding: practical experiences show that an accelerated degradation of the polymeric phase is observed particularly in the presence of electrochemical corrosion.⁴ Based on the here reported studies, it is therefore hypothesized that the formation of surface defects during corrosion may affect the degradation and accumulation of the polymer. Thus,

an oxidative treatment of hard coatings directly after deposition to form a thick and inert well defined surface oxide layer may possibly suppress the corrosion and the related polymer degradation as illustrated in figure 20. In this regards, the results presented in publication I provide guidance to design such a post-deposition treatment, because it could be shown that a segregation of the surface oxide is expected at low oxidation temperatures.

5.2 Interfacial adhesive and reactive interactions

Based on the thorough characterization of the surface chemistry of $Ti_{0.5}Al_{0.5}N$, the interface formation to molten polycarbonate was investigated in publication III. The results highlight that the hard coating inhibits the deleterious catalytic degradation of polycarbonate by the presence of the protective passivating surface oxide film. In contrast, a catalytic degradation of polycarbonate occurs at uncoated iron surfaces, which results into the interfacial accumulation of strongly degraded and insoluble polymeric debris. This explains for the first time the practical experience that iron surfaces show a poor performance in technical polymer melt processing applications.

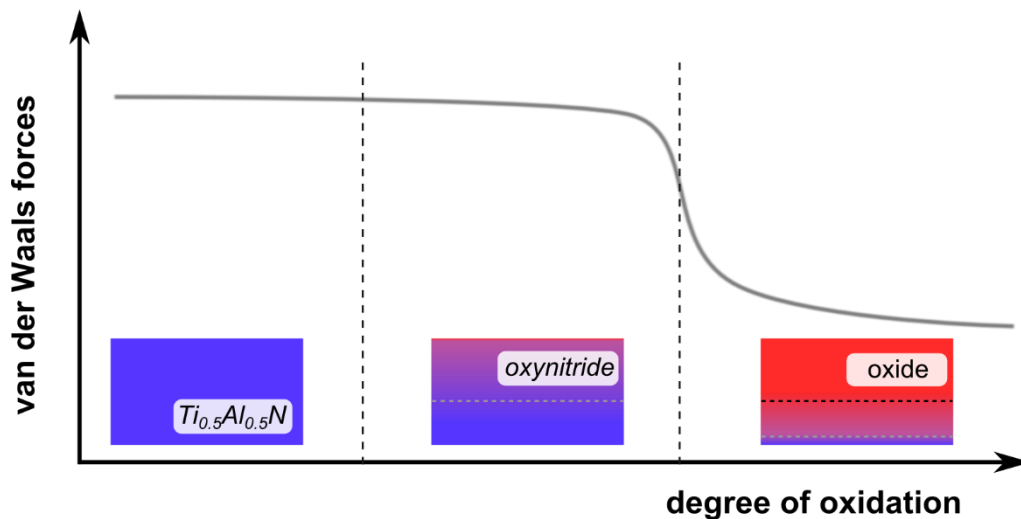


Figure 21: Non-linear decrease of the van der Waals forces of $Ti_{0.5}Al_{0.5}N$ in contact with polymers with increasing degree of surface oxidation.

However, the herein reported experiments obviously fail to explain the interfacial degradation of polycarbonate observed at hard coating surfaces such as $Ti_{0.5}Al_{0.5}N$ in practice. This might be the consequence of the simplified model experiments, which do not cover the influence of water and oxygen or the presence of the shear field and related degradation products. Nonetheless, it could be shown that even under these conditions a restructured, strongly adsorbed interphase develops in the polycarbonate melt as a result of the strong force interactions with the hard coating. It is highlighted that this interphase most probably interferes with interfacial reactions such as corrosion and degradation and may also affect the adhesive wear. In this regards, future studies should not only expand the field of parameters to more directly resemble the operating conditions, but should also clarify the role of the restructured polymeric interphase. Obviously, this requires the in-depth

understanding of the interaction forces and their surface chemical origin, which is revealed by the joint analysis of the publications IV to VI as discussed in the following.

When considering the role of surface oxidation of the hard coating for adhesion, it turned out in publication VI that the formation of a surface oxidation layer on $Ti_{0.5}Al_{0.5}N$ with the typical multi-layered structure nitride|oxynitride|oxide out from the nitride does not directly result into decreased van der Waals forces as would be typically expected. As shown in publication III and IV and as illustrated in figure 21, a significant decrease could be only accomplished upon enhanced surface oxidation and the formation of an extended oxidic top layer, which results into the relocation of the highly polarizable oxynitridic growth region into increasingly deeper sub layers. It follows that the van der Waals forces decrease non-linearly with the degree of surface oxidation. Consequently, an oxidative post-treatment after deposition such as that already proposed in figure 20 should reduce the van der Waals interactions in practice.

Complementary to the investigation of the effect of oxidation, the force and electron spectroscopic experiments in publication IV and V disclose the effect of the type of metal ion on the van der Waals forces. In this regards, it was shown that the van der Waals interactions can be minimized by increasing the aluminium concentration in the surface oxide. Based solely on these results, it is not clear whether the same applies for other hard coatings such as CrAlN, but the calculation of Hamaker coefficients introduced in publication IV allows to predict van der Waals forces and to rapidly screen materials and their combinations if their optical properties have once been determined by REELS. In this context, a table of Hamaker constants of ceramic materials and polymers has been compiled in publication III based on the yet available optical data.

In addition to the analysis of the van der Waals interaction forces, the significance of chemical acid-base interactions was highlighted in publication VI. The presented results demonstrate that the presence of polar oxygen-bearing functional groups in the surface of the polymer causes increased adhesion forces due to additional acid-base interactions with the oxidized surface. In the context of polymer injection moulding, this shows that oxidized degradation products of the polymer adhere more strongly to hard coating surfaces as does the pristine polymer.

6 Conclusions

The interfacial adhesive and reactive interactions of nitridic hard coatings in contact with polymers were investigated within this work and could be related to their surface chemical structure at the example of $\text{Ti}_{0.5}\text{Al}_{0.5}\text{N}$ and polycarbonate. This rational approach not only enabled to develop a comprehensive understanding of the functional properties of hard coatings, but also allowed to deduce design rules for the development of advanced hard coatings.

In this regards, a microscopic mechanism of the thermal oxidation of $\text{Ti}_{0.5}\text{Al}_{0.5}\text{N}$ was developed, which is characterized by the formation of a multi-layered surface oxide consisting of an intermediary oxynitridic growth region covered by a nitrogen-doped top oxide layer. This model was shown not only to be able to explain the surface chemistry of $\text{Ti}_{0.5}\text{Al}_{0.5}\text{N}$ after deposition and exposure to atmosphere, which is relevant for understanding its interfacial behaviour, but to be also transferrable to other hard coating systems such as $\text{V}_{0.5}\text{Al}_{0.5}\text{N}$ and $\text{Cr}_{0.8}\text{Al}_{0.2}\text{N}$.

Complementary to the thermal oxidation, the fundamentals of the corrosion behaviour of $\text{Ti}_{0.5}\text{Al}_{0.5}\text{N}$ were investigated by studying the interfacial anodic and cathodic reactions in aqueous solution. The derived microscopic model of the electrochemical oxidation revealed that in contrast to the thermal oxidation an enhanced oxidation occurs and a highly defective and non-protective surface oxide is formed of which the reactivity is governed by Ti(III) surface states. It follows that an oxidative treatment of $\text{Ti}_{0.5}\text{Al}_{0.5}\text{N}$ directly after deposition to form a dense surface oxide layer appears to be promising to mitigate the corrosion of the hard coating and the related accumulation of degraded polymer as encountered during plastics injection moulding. The comparative analysis of both oxidation mechanisms further highlighted that the reactive inward migration of oxygen and the related intermediary formation of an oxynitridic growth region ultimately define the surface chemistry in both cases and are of central relevance also for other hard coatings such as VAlN and CrAlN. This underlines that the herein developed models of oxidation may be also applicable to other hard coating systems.

Based on the thorough analysis of the surface chemistry, it could be shown that the simple exposure of molten polycarbonate to the surface of the $\text{Ti}_{0.5}\text{Al}_{0.5}\text{N}$ hard coating not causes an accelerated interfacial degradation, but results into a restructuring of the polycarbonate as a consequence of the strong adsorption. This highlights that the accelerated degradation and interfacial accumulation of polycarbonate observed in practice may be rather explained by the presence of the shear-field and related reactive intermediates or by the superimposed corrosion. In contrast, the experience that non-alloyed steel surfaces show a poor performance in polymer moulding could be validated and explained by an interfacial catalytic degradation, which results into the formation of cross-linked products including cyclic anhydrides, aromatic esters and char.

The correlation of the surface chemistry of $Ti_{0.5}Al_{0.5}N$ with the force interactions with polycarbonate showed that the van der Waals forces decrease non-linearly with the degree of surface oxidation of $Ti_{0.5}Al_{0.5}N$ due to the high polarizability of the oxynitridic growth region. Moreover, the Ti(IV) ion present in the surface top oxide layer was found to increase the van der Waals interactions in comparison to the Al(III) ion again due to a related higher polarizability. Consequently, the design rule could be deduced that the van der Waals interactions can be minimized by the formation of an Al_2O_3 cover layer. In this regards, a new method was developed to predict van der Waals interactions between surfaces by electron spectroscopy in order to facilitate the tailoring of these interactions. The in-depth analysis of the overall adhesion force showed that beside van der Waals forces additional acid-base interactions need to be considered and may even dominate the overall adhesion when oxygen-bearing functional groups such as COOH are present in the surface of the polymer. This finding indicates that the adhesive phenomena encountered in injection moulding are affected by the chemical degradation of the polymer.

Finally, it is noted that especially the REELS based approach for the calculation of Hamaker coefficients by Lifshitz theory as presented in publication IV is a highly promising approach to analyse van der Waals forces with relevance far beyond the field of injection moulding. Future studies should therefore harness the high potential of this unique method: for example, the deduction of three-dimensional van der Waals potential volumes above single-crystalline surfaces should be tractable, because the required REELS spectra are almost unaffected by channelling effects. Moreover, it is possible for the first time to include non-local effects into the calculation of Hamaker coefficients based on real optical data, which allows to investigate the limits of the continuum theory. Finally, this method represents an important step towards a purely spectroscopic prediction of interaction potentials, because the important d^{-6} -term of the Lennard-Jones potential can be accurately estimated.

7 List of abbreviations

AGC	Automated Gain Control
AFM	Atomic Force Microscope
AM	Amplitude Modulation
CFM	Chemical Force Microscopy
CVD	Chemical Vapour Deposition
dcMS	direct current Magnetron Sputtering
DFS	Dynamic Force Spectroscopy
EAL	Effective Attenuation Length
FM	Frequency Modulation
HiPIMS	High Power Impuls Magnetron Sputtering
HPPMS	High Power Pulsed Magnetron Sputtering
IMFP	Inelastic Mean Free Path
ISS	Ion Scattering Spectroscopy
LEIS	Low Energy Ion Scattering
PLL	Phase-Locked Loop
PSD	Position Sensitive Device
REELS	Reflection Electron Energy Loss Spectroscopy
SMFS	Single-Molecule Force Spectroscopy
UHV	Ultra-High Vacuum
VUV	Vacuum Ultra Violet
XPS	X-Ray Photoelectron Spectroscopy

8 Bibliography

1. Attia, U. M., Marson, S. & Alcock, J. R. Micro-injection moulding of polymer microfluidic devices. *Microfluid. Nanofluidics* **7**, 1 (2009).
2. Bobzin, K., Nickel, R., Bagcivan, N. & Manz, F. D. PVD—Coatings in Injection Molding Machines for Processing Optical Polymers. *Plasma Process. Polym.* **4**, S144–S149 (2007).
3. Bobzin, K. *et al.* Injection molding of products with functional surfaces by micro-structured, PVD coated injection molds. *Prod. Eng.* **5**, 415–422 (2011).
4. Bienk, E. J. & Mikkelsen, N. J. Application of advanced surface treatment technologies in the modern plastics moulding industry. *Wear* **207**, 6–9 (1997).
5. Saha, B. *et al.* A review on the importance of surface coating of micro/nano-mold in micro/nano-molding processes. *J. Micromechanics Microengineering* **26**, 013002 (2016).
6. Bobzin, K. *et al.* (Cr,Al)N/(Cr,Al)ON Oxy-nitride Coatings deposited by Hybrid dcMS/HPPMS for Plastics Processing Applications. *Surf. Coat. Technol.* **308**, 394–403 (2016).
7. PalDey, S. & Deevi, S. C. Single layer and multilayer wear resistant coatings of (Ti,Al)N: a review. *Mater. Sci. Eng. A* **342**, 58–79 (2003).
8. Musil, J. Hard and superhard nanocomposite coatings. *Surf. Coat. Technol.* **125**, 322–330 (2000).
9. Kim, H. C. & Alford, T. L. Investigation on diffusion barrier properties of reactive sputter deposited TiAl_xNyOz thin films for Cu metallization. *Thin Solid Films* **449**, 6–11 (2004).
10. Rebouta, L. *et al.* Optical characterization of TiAlN/TiAlON/SiO₂ absorber for solar selective applications. *Surf. Coat. Technol.* **211**, 41–44 (2012).
11. Anders, A. A review comparing cathodic arcs and high power impulse magnetron sputtering (HiPIMS). *Surf. Coat. Technol.* **257**, 308–325 (2014).
12. Martin, P. J. & Bendavid, A. Review of the filtered vacuum arc process and materials deposition. *Thin Solid Films* **394**, 1–14 (2001).
13. Sarakinos, K., Alami, J. & Konstantinidis, S. High power pulsed magnetron sputtering: A review on scientific and engineering state of the art. *Surf. Coat. Technol.* **204**, 1661–1684 (2010).
14. Samuelsson, M. *et al.* On the film density using high power impulse magnetron sputtering. *Surf. Coat. Technol.* **205**, 591–596 (2010).
15. Kouznetsov, V., Macák, K., Schneider, J. M., Helmersson, U. & Petrov, I. A novel pulsed magnetron sputter technique utilizing very high target power densities. *Surf. Coat. Technol.* **122**, 290–293 (1999).
16. Ehiasarian, A. P., Wen, J. G. & Petrov, I. Interface microstructure engineering by high power impulse magnetron sputtering for the enhancement of adhesion. *J. Appl. Phys.* **101**, 054301 (2007).
17. Lundin, D. & Sarakinos, K. An introduction to thin film processing using high-power impulse magnetron sputtering. *J. Mater. Res.* **27**, 780–792 (2012).
18. Gudmundsson, J. T., Brenning, N., Lundin, D. & Helmersson, U. High power impulse magnetron sputtering discharge. *J. Vac. Sci. Technol. A* **30**, 030801 (2012).
19. Greczynski, G. *et al.* A review of metal-ion-flux-controlled growth of metastable TiAlN by HIPIMS/DCMS co-sputtering. *Surf. Coat. Technol.* **257**, 15–25 (2014).
20. Anders, A. Tutorial: Reactive high power impulse magnetron sputtering (R-HiPIMS). *J. Appl. Phys.* **121**, 171101 (2017).
21. Ohring, M. *Materials Science of Thin Films: Deposition and Structure*. (Academic Press, 2002).
22. Barbee, T. W., Holmes, W. H., Keith, D. L., Pyzyna, M. K. & Ilonca, G. Synthesis of amorphous niobium-nickel alloys by vapor quenching. *Thin Solid Films* **45**, 591–599 (1977).
23. Anders, A. A structure zone diagram including plasma-based deposition and ion etching. *Thin Solid Films* **518**, 4087–4090 (2010).
24. Joelsson, T., Hörling, A., Birch, J. & Hultman, L. Single-crystal Ti₂AlN thin films. *Appl. Phys. Lett.* **86**, 111913 (2005).
25. Carter, G. Influence of thermal spikes on preferred grain orientation in ion-assisted deposition. *Phys. Rev. B* **62**, 8376–8390 (2000).

26. Tholander, C., Alling, B., Tasnádi, F., Greene, J. E. & Hultman, L. Effect of Al substitution on Ti, Al, and N adatom dynamics on TiN(001), (011), and (111) surfaces. *Surf. Sci.* **630**, 28–40 (2014).
27. Abrikosov, I. A. *et al.* Phase Stability and Elasticity of TiAlN. *Materials* **4**, 1599–1618 (2011).
28. Alling, B. *et al.* Mixing and decomposition thermodynamics of c-Ti_{1-x}Al_xN from first-principles calculations. *Phys. Rev. B* **75**, 045123 (2007).
29. Alling, B., Karimi, A. & Abrikosov, I. A. Electronic origin of the isostructural decomposition in cubic M_{1-x}Al_xN (M=Ti, Cr, Sc, Hf): A first-principles study. *Surf. Coat. Technol.* **203**, 883–886 (2008).
30. Chen, L., Paulitsch, J., Du, Y. & Mayrhofer, P. H. Thermal stability and oxidation resistance of Ti–Al–N coatings. *Surf. Coat. Technol.* **206**, 2954–2960 (2012).
31. Endrino, J. L. *et al.* Spectral evidence of spinodal decomposition, phase transformation and molecular nitrogen formation in supersaturated TiAlN films upon annealing. *Acta Mater.* **59**, 6287–6296 (2011).
32. Gago, R., Redondo-Cubero, A., Endrino, J. L., Jiménez, I. & Shevchenko, N. Aluminum incorporation in Ti_{1-x}Al_xN films studied by x-ray absorption near-edge structure. *J. Appl. Phys.* **105**, 113521 (2009).
33. Holec, D., Rovere, F., Mayrhofer, P. H. & Barna, P. B. Pressure-dependent stability of cubic and wurtzite phases within the TiN–AlN and CrN–AlN systems. *Scr. Mater.* **62**, 349–352 (2010).
34. Holec, D. *et al.* Phase stability and alloy-related trends in Ti–Al–N, Zr–Al–N and Hf–Al–N systems from first principles. *Surf. Coat. Technol.* **206**, 1698–1704 (2011).
35. Mayrhofer, P. H. *et al.* Self-organized nanostructures in the Ti–Al–N system. *Appl. Phys. Lett.* **83**, 2049–2051 (2003).
36. Rachbauer, R., Stergar, E., Massl, S., Moser, M. & Mayrhofer, P. H. Three-dimensional atom probe investigations of Ti–Al–N thin films. *Scr. Mater.* **61**, 725–728 (2009).
37. Rachbauer, R., Massl, S., Stergar, E., Felfer, P. & Mayrhofer, P. H. Atom probe specimen preparation and 3D interfacial study of Ti–Al–N thin films. *Surf. Coat. Technol.* **204**, 1811–1816 (2010).
38. Rogström, L. *et al.* Strain evolution during spinodal decomposition of TiAlN thin films. *Thin Solid Films* **520**, 5542–5549 (2012).
39. Schalk, N., Mitterer, C., Keckes, J., Penoy, M. & Michotte, C. Influence of residual stresses and grain size on the spinodal decomposition of metastable Ti_{1-x}Al_xN coatings. *Surf. Coat. Technol.* **209**, 190–196 (2012).
40. Vogtenhuber-Pawelczak, D., Herzig, P. & Klíma, J. A theoretical investigation of titanium aluminium nitrides, (Ti, Al)N: Electronic structure and chemical bonding. *Z. Für Phys. B Condens. Matter* **84**, 211–219 (1991).
41. Wüstefeld, C. *et al.* Decomposition kinetics in Ti_{1-x}Al_xN coatings as studied by in-situ X-ray diffraction during annealing. *Surf. Coat. Technol.* **206**, 1727–1734 (2011).
42. Baben, M. to, Raumann, L., Music, D. & Schneider, J. M. Origin of the nitrogen over- and understoichiometry in Ti_{0.5}Al_{0.5}N thin films. *J. Phys. Condens. Matter* **24**, 155401 (2012).
43. Baben, M. to *et al.* Unprecedented thermal stability of inherently metastable titanium aluminum nitride by point defect engineering. *Mater. Res. Lett.* **0**, 1–12 (2016).
44. Rotert, S. J., Music, D., Baben, M. to & Schneider, J. M. Theoretical study of elastic properties and phase stability of M_{0.5}Al_{0.5}N_{1-x}O_x (M = Sc, Ti, V, Cr). *J. Appl. Phys.* **113**, 083512 (2013).
45. Seifert, H. J., Kussmaul, A. & Aldinger, F. Phase equilibria and diffusion paths in the Ti–Al–O–N system. *J. Alloys Compd.* **317–318**, 19–25 (2001).
46. Baben, M. to, Raumann, L. & Schneider, J. M. Phase stability and elastic properties of titanium aluminum oxynitride studied by ab initio calculations. *J. Phys. Appl. Phys.* **46**, 084002 (2013).
47. Hans, M. *et al.* Effect of oxygen incorporation on the structure and elasticity of Ti–Al–O–N coatings synthesized by cathodic arc and high power pulsed magnetron sputtering. *J. Appl. Phys.* **116**, 093515 (2014).
48. Adibi, F. *et al.* Defect structure and phase transitions in epitaxial metastable cubic Ti_{0.5}Al_{0.5}N alloys grown on MgO(001) by ultra-high-vacuum magnetron sputter deposition. *J. Appl. Phys.* **69**, 6437–6450 (1991).

49. Wahlström, U. *et al.* Crystal growth and microstructure of polycrystalline Ti_{1-x}Al_xN alloy films deposited by ultra-high-vacuum dual-target magnetron sputtering. *Thin Solid Films* **235**, 62–70 (1993).
50. Alling, B. *et al.* Mixing and decomposition thermodynamics of c-Ti_{1-x}Al_xN from first-principles calculations. *Phys. Rev. B* **75**, 045123 (2007).
51. Alling, B., Karimi, A. & Abrikosov, I. A. Electronic origin of the isostructural decomposition in cubic M_{1-x}Al_xN (M=Ti, Cr, Sc, Hf): A first-principles study. *Surf. Coat. Technol.* **203**, 883–886 (2008).
52. Alling, B., Karimi, A., Hultman, L. & Abrikosov, I. A. First-principles study of the effect of nitrogen vacancies on the decomposition pattern in cubic Ti_{1-x}Al_xN_{1-y}. *Appl. Phys. Lett.* **92**, 071903 (2008).
53. Vogtenhuber-Pawelczak, D., Herzig, P. & Klíma, J. A theoretical investigation of titanium aluminium nitrides, (Ti, Al)N: Electronic structure and chemical bonding. *Z. Für Phys. B Condens. Matter* **84**, 211–219 (1991).
54. Rotert, S. J., Music, D., Baben, M. to & Schneider, J. M. Theoretical study of elastic properties and phase stability of M_{0.5}Al_{0.5}N_{1-x}O_x (M = Sc, Ti, V, Cr). *J. Appl. Phys.* **113**, 083512 (2013).
55. Milošev, I., Strehblow, H.-H. & Navinšek, B. Comparison of TiN, ZrN and CrN hard nitride coatings: Electrochemical and thermal oxidation. *Thin Solid Films* **303**, 246–254 (1997).
56. Tillmann W. *et al.* The detachment behavior of polycarbonate on thin films above the glass transition temperature. *Polym. Eng. Sci.* **56**, 786–797 (2016).
57. Bobzin, K. *et al.* Enhanced replication ratio of injection molded plastic parts by using an innovative combination of laser-structuring and PVD coating. *Surf. Coat. Technol.* **332**, 474–483 (2017).
58. Music, D. *et al.* Polypropylene–MAIN (M = Ti, Cr) interface interactions. *Surf. Sci.* **606**, 986–989 (2012).
59. Didier, F. & Jupille, J. The van der Waals contribution to the adhesion energy at metal-oxide interfaces. *Surf. Sci.* **314**, 378–384 (1994).
60. Martin, M. & Fromm, E. Low-temperature oxidation of metal surfaces. *J. Alloys Compd.* **258**, 7–16 (1997).
61. Cabrera, N. & Mott, N. F. Theory of the oxidation of metals. *Rep. Prog. Phys.* **12**, 163 (1949).
62. Fehlner, F. P. & Mott, N. F. Low-temperature oxidation. *Oxid. Met.* **2**, 59–99 (1970).
63. Lawless, K. R. The oxidation of metals. *Rep. Prog. Phys.* **37**, 231 (1974).
64. Fromhold, A. T. *Theory of Metal Oxidation. Vol. 1: Fundamentals.* (North Holland Publishing Co., 1976).
65. Atkinson, A. Transport processes during the growth of oxide films at elevated temperature. *Rev. Mod. Phys.* **57**, 437–470 (1985).
66. Bailey, J. M. & Ritchie, I. M. Metal oxidation: An electrochemical perspective. *Oxid. Met.* **30**, 405–418 (1988).
67. Fromhold Jr., A. T. Plasma oxidation. *Thin Solid Films* **95**, 297–308 (1982).
68. Besenbacher, F. & Nørskov, J. K. Oxygen chemisorption on metal surfaces: General trends for Cu, Ni and Ag. *Prog. Surf. Sci.* **44**, 5–66 (1993).
69. Lohrengel, M. M. Thin anodic oxide layers on aluminium and other valve metals: high field regime. *Mater. Sci. Eng. R Rep.* **11**, 243–294 (1993).
70. Schultze, J. W. & Lohrengel, M. M. Stability, reactivity and breakdown of passive films. Problems of recent and future research. *Electrochimica Acta* **45**, 2499–2513 (2000).
71. Kirchheim, R. Growth kinetics of passive films. *Electrochimica Acta* **32**, 1619–1629 (1987).
72. Schmuki, P. From Bacon to barriers: a review on the passivity of metals and alloys. *J. Solid State Electrochem.* **6**, 145–164 (2002).
73. Macdonald, D. D. The history of the Point Defect Model for the passive state: A brief review of film growth aspects. *Electrochimica Acta* **56**, 1761–1772 (2011).
74. Macdonald, D. D. Passivity—the key to our metals-based civilization. *Pure Appl. Chem.* **71**, 951–978 (1999).
75. Macdonald, D. D. The Point Defect Model for the Passive State. *J. Electrochem. Soc.* **139**, 3434–3449 (1992).

76. Schultze, J. W., Lohrengel, M. M. & Ross, D. Nucleation and growth of anodic oxide films. *Electrochimica Acta* **28**, 973–984 (1983).
77. Macdonald, D. D., Biaggio, S. R. & Song, H. Steady-State Passive Films Interfacial Kinetic Effects and Diagnostic Criteria. *J. Electrochem. Soc.* **139**, 170–177 (1992).
78. Macdonald, D. D. Passivity: enabler of our metals based civilisation. *Corros. Eng. Sci. Technol.* **49**, 143–155 (2014).
79. Zhang, L., Macdonald, D. D., Sikora, E. & Sikora, J. On the Kinetics of Growth of Anodic Oxide Films. *J. Electrochem. Soc.* **145**, 898–905 (1998).
80. Wu, H. & Hebert, K. R. Electrochemical transients during the initial moments of anodic oxidation of aluminum. *Electrochimica Acta* **47**, 1373–1383 (2002).
81. Kendall, K. *Molecular Adhesion and Its Applications: The Sticky Universe*. (Springer US, 2001).
82. Fowkes, F. M. Role of acid-base interfacial bonding in adhesion. *J. Adhes. Sci. Technol.* **1**, 7–27 (1987).
83. Lang, N. D. & Kohn, W. Theory of Metal Surfaces: Charge Density and Surface Energy. *Phys. Rev. B* **1**, 4555–4568 (1970).
84. Lang, N. D. & Kohn, W. Theory of Metal Surfaces: Induced Surface Charge and Image Potential. *Phys. Rev. B* **7**, 3541–3550 (1973).
85. Gerlach, E. Equivalence of van der Waals Forces between Solids and the Surface-Plasmon Interaction. *Phys. Rev. B* **4**, 393–396 (1971).
86. Van Oss, C. J., Chaudhury, M. K. & Good, R. J. Interfacial Lifshitz-van der Waals and polar interactions in macroscopic systems. *Chem. Rev.* **88**, 927–941 (1988).
87. Suits, C. G. *The collected works of Irving Langmuir*. (Pergamnon Press, 1960).
88. Chaudhury, M. K. Interfacial interaction between low-energy surfaces. *Mater. Sci. Eng. R Rep.* **16**, 97–159 (1996).
89. Cwickel, D., Paz, Y. & Marmur, A. Contact angle measurement on rough surfaces: the missing link. *Surf. Innov.* **5**, 190–193 (2017).
90. Volpe, C. D. & Siboni, S. Use, Abuse, Misuse and Proper Use of Contact Angles: A Critical Review. *Rev. Adhes. Adhes.* **3**, 365–385 (2015).
91. Fowkes, F. M. Quantitative characterization of the acid-base properties of solvents, polymers, and inorganic surfaces. *J. Adhes. Sci. Technol.* **4**, 669–691 (1990).
92. Volpe, C. D. & Siboni, S. The Wilhelmy method: a critical and practical review. *Surf. Innov.* 1–13 (2017). doi:10.1680/jsuin.17.00059
93. Girifalco, L. A. & Good, R. J. A Theory for the Estimation of Surface and Interfacial Energies. I. Derivation and Application to Interfacial Tension. *J. Phys. Chem.* **61**, 904–909 (1957).
94. Good, R. J. & Hope, C. J. Test of Combining Rules for Intermolecular Distances. Potential Function Constants from Second Virial Coefficients. *J. Chem. Phys.* **55**, 111–116 (1971).
95. Fowkes, F. M. DETERMINATION OF INTERFACIAL TENSIONS, CONTACT ANGLES, AND DISPERSION FORCES IN SURFACES BY ASSUMING ADDITIVITY OF INTERMOLECULAR INTERACTIONS IN SURFACES. *J. Phys. Chem.* **66**, 382–382 (1962).
96. Fowkes, F. M. ATTRACTIVE FORCES AT INTERFACES. *Ind. Eng. Chem.* **56**, 40–52 (1964).
97. Volpe, C. D. & Siboni, S. Acid–base surface free energies of solids and the definition of scales in the Good–van Oss–Chaudhury theory. *J. Adhes. Sci. Technol.* **14**, 235–272 (2000).
98. Love, J. C., Estroff, L. A., Kriebel, J. K., Nuzzo, R. G. & Whitesides, G. M. Self-Assembled Monolayers of Thiolates on Metals as a Form of Nanotechnology. *Chem. Rev.* **105**, 1103–1170 (2005).
99. Bain, C. D. & Whitesides, G. M. Depth sensitivity of wetting: monolayers of .omega.-mercapto ethers on gold. *J. Am. Chem. Soc.* **110**, 5897–5898 (1988).
100. Bain, C. D. *et al.* Formation of monolayer films by the spontaneous assembly of organic thiols from solution onto gold. *J. Am. Chem. Soc.* **111**, 321–335 (1989).
101. Butt, H.-J., Cappella, B. & Kappl, M. Force measurements with the atomic force microscope: Technique, interpretation and applications. *Surf. Sci. Rep.* **59**, 1–152 (2005).
102. Sader, J. E. *et al.* A virtual instrument to standardise the calibration of atomic force microscope cantilevers. *Rev. Sci. Instrum.* **87**, 093711 (2016).

103. Frisbie, C. D., Rozsnyai, L. F., Noy, A., Wrighton, M. S. & Lieber, C. M. Functional Group Imaging by Chemical Force Microscopy. *Science* **265**, 2071–2074 (1994).
104. Clear, S. C. & Nealey, P. F. Chemical Force Microscopy Study of Adhesion and Friction between Surfaces Functionalized with Self-Assembled Monolayers and Immersed in Solvents. *J. Colloid Interface Sci.* **213**, 238–250 (1999).
105. Tormoen, G. W., Drelich, J. & Beach, E. R. Analysis of atomic force microscope pull-off forces for gold surfaces portraying nanoscale roughness and specific chemical functionality. *J. Adhes. Sci. Technol.* **18**, 1–17 (2004).
106. Skulason, H. & Frisbie, C. D. Detection of Discrete Interactions upon Rupture of Au Microcontacts to Self-Assembled Monolayers Terminated with $-S(CO)CH_3$ or $-SH$. *J. Am. Chem. Soc.* **122**, 9750–9760 (2000).
107. Skulason, H. & Frisbie, C. D. Contact Mechanics Modeling of Pull-Off Measurements: Effect of Solvent, Probe Radius, and Chemical Binding Probability on the Detection of Single-Bond Rupture Forces by Atomic Force Microscopy. *Anal. Chem.* **74**, 3096–3104 (2002).
108. Sturm, S., Bullerjahn, J. T. & Kroy, K. Intramolecular relaxation in dynamic force spectroscopy. *Eur. Phys. J. Spec. Top.* **223**, 3129–3144 (2014).
109. Bullerjahn, J. T., Sturm, S. & Kroy, K. Theory of rapid force spectroscopy. *Nat. Commun.* **5**, (2014).
110. Arya, G. Models for recovering the energy landscape of conformational transitions from single-molecule pulling experiments. *Mol. Simul.* **42**, 1102–1115 (2016).
111. Merkel, R., Nassoy, P., Leung, A., Ritchie, K. & Evans, E. Energy landscapes of receptor–ligand bonds explored with dynamic force spectroscopy. *Nature* **397**, 50–53 (1999).
112. Noy, A. Strength in Numbers: Probing and Understanding Intermolecular Bonding with Chemical Force Microscopy. *Scanning* **30**, 96–105 (2008).
113. Friddle, R. W., Podsiadlo, P., Artyukhin, A. B. & Noy, A. Near-Equilibrium Chemical Force Microscopy. *J. Phys. Chem. C* **112**, 4986–4990 (2008).
114. Evans, E. Probing the Relation Between Force—Lifetime—and Chemistry in Single Molecular Bonds. *Annu. Rev. Biophys. Biomol. Struct.* **30**, 105–128 (2001).
115. Noy, A. & Friddle, R. W. Practical single molecule force spectroscopy: How to determine fundamental thermodynamic parameters of intermolecular bonds with an atomic force microscope. *Methods* **60**, 142–150 (2013).
116. Mosebach, B., Ozkaya, B., Giner, I., Keller, A. & Grundmeier, G. Analysis of acid-base interactions at Al_2O_3 (11-20) interfaces by means of single molecule force spectroscopy. *Appl. Surf. Sci.* **420**, 296–302 (2017).
117. Hughes, M. L. & Dougan, L. The physics of pulling polyproteins: a review of single molecule force spectroscopy using the AFM to study protein unfolding. *Rep. Prog. Phys.* **79**, 076601 (2016).
118. Hummer, G. & Szabo, A. Free Energy Surfaces from Single-Molecule Force Spectroscopy. *Acc. Chem. Res.* **38**, 504–513 (2005).
119. Gupta, A. N. *et al.* Experimental validation of free-energy-landscape reconstruction from non-equilibrium single-molecule force spectroscopy measurements. *Nat. Phys.* **7**, 631–634 (2011).
120. Ducker, W. A., Senden, T. J. & Pashley, R. M. Direct measurement of colloidal forces using an atomic force microscope. *Nature* **353**, 239–241 (1991).
121. Kappl, M. & Butt, H.-J. The Colloidal Probe Technique and its Application to Adhesion Force Measurements. *Part. Part. Syst. Charact.* **19**, 129–143 (2002).
122. Rabinovich, Y. I., Singh, A., Hahn, M., Brown, S. & Moudgil, B. Kinetics of Liquid Annulus Formation and Capillary Forces. *Langmuir* **27**, 13514–13523 (2011).
123. Harrison, A. J., Corti, D. S. & Beaudoin, S. P. Capillary Forces in Nanoparticle Adhesion: A Review of AFM Methods. *Part. Sci. Technol.* **33**, 526–538 (2015).
124. Biggs, S. & Spinks, G. Atomic force microscopy investigation of the adhesion between a single polymer sphere and a flat surface. *J. Adhes. Sci. Technol.* **12**, 461–478 (1998).
125. Parker, J. L., Claesson, P. M. & Attard, P. Bubbles, cavities, and the long-ranged attraction between hydrophobic surfaces. *J. Phys. Chem.* **98**, 8468–8480 (1994).

126. Attard, P. Thermodynamic Analysis of Bridging Bubbles and a Quantitative Comparison with the Measured Hydrophobic Attraction. *Langmuir* **16**, 4455–4466 (2000).
127. Simonsen, A. C., Hansen, P. L. & Klösgen, B. Nanobubbles give evidence of incomplete wetting at a hydrophobic interface. *J. Colloid Interface Sci.* **273**, 291–299 (2004).
128. Hamaker, H. C. The London—van der Waals attraction between spherical particles. *Physica* **4**, 1058–1072 (1937).
129. Derjaguin. Untersuchung über die Reibung und Adhäsion. *IV Kolloid-Z* **69**, 55–164 (1934).
130. Dzyaloshinskii, I. E., Lifshitz, E. M. & Pitaevskii, L. P. GENERAL THEORY OF VAN DER WAALS' FORCES. *Sov. Phys. Uspekhi* **4**, 153 (1961).
131. Parsegian, V. A. *Van der Waals Forces: A Handbook for Biologists, Chemists, Engineers, and Physicists*. (Cambridge University Press, 2005).
132. French, R. H. Origins and Applications of London Dispersion Forces and Hamaker Constants in Ceramics. *J. Am. Ceram. Soc.* **83**, 2117–2146 (2000).
133. Casimir, H. B. G. & Polder, D. The Influence of Retardation on the London-van der Waals Forces. *Phys. Rev.* **73**, 360–372 (1948).
134. Israelachvili, J. N. *Intermolecular and Surface Forces*. (Academic Press, 2011).
135. Gusso, A. & Burnham, N. A. Investigation of the range of validity of the pairwise summation method applied to the calculation of the surface roughness correction to the van der Waals force. *Surf. Sci.* **651**, 28–40 (2016).
136. Heinrichs, J. Non-local effects in the macroscopic theory of Van der Waals and adhesive forces. *Solid State Commun.* **13**, 1595–1598 (1973).
137. Esquivel-Sirvent, R. & Schatz, G. C. Spatial Nonlocality in the Calculation of Hamaker Coefficients. *J. Phys. Chem. C* **116**, 420–424 (2012).
138. Sun, J., Huang, Y. & Gao, L. Nonlocal composite media in calculations of the Casimir force. *Phys. Rev. A* **89**, 012508 (2014).
139. Fowkes, F. M. *et al.* Acid–base complexes of polymers. *J. Polym. Sci. Polym. Chem. Ed.* **22**, 547–566 (1984).
140. Lee, L.-H. Hard—Soft Acid—Base (HSAB) Principle for Solid Adhesion and Surface Interactions. in *Fundamentals of Adhesion* (ed. Lee, L.-H.) 349–362 (Springer US, 1991).
141. Lee, L.-H. Molecular Bonding and Adhesion at Polymer-Metal Interphases. *J. Adhes.* **46**, 15–38 (1994).
142. Rühle, M., Evans, A. G., Hirth, J. P. & Ashby, M. F. *Metal–Ceramic Interfaces. Proceedings of an International Workshop*. (Pergamon Press, 1990).
143. Klopman, G. & Hudson, R. F. Polyelectronic perturbation treatment of chemical reactivity. *Theor. Chim. Acta* **8**, 165–174 (1967).
144. Pearson, R. G. Hard and Soft Acids and Bases. *J. Am. Chem. Soc.* **85**, 3533–3539 (1963).
145. Rose, J. H., Ferrante, J. & Smith, J. R. Universal Binding Energy Curves for Metals and Bimetallic Interfaces. *Phys. Rev. Lett.* **47**, 675–678 (1981).
146. Banerjea, A. & Smith, J. R. Origins of the universal binding-energy relation. *Phys. Rev. B* **37**, 6632–6645 (1988).
147. Ferrante, J. & Smith, J. R. Theory of the bimetallic interface. *Phys. Rev. B* **31**, 3427–3434 (1985).
148. Drago, R. S., Vogel, G. C. & Needham, T. E. Four-parameter equation for predicting enthalpies of adduct formation. *J. Am. Chem. Soc.* **93**, 6014–6026 (1971).
149. Fowkes, F. M., Riddle, F. L., Pastore, W. E. & Weber, A. A. Interfacial interactions between self-associated polar liquids and squalane used to test equations for solid—liquid interfacial interactions. *Colloids Surf.* **43**, 367–387 (1990).
150. Napolitano, S. & Sferrazza, M. How irreversible adsorption affects interfacial properties of polymers. *Adv. Colloid Interface Sci.* **247**, 172–177 (2017).
151. Butt, H. J. *et al.* Interphase of a Polymer at a Solid Interface. *Macromolecules* **47**, 8459–8465 (2014).
152. Fleer, G. J. *Polymers at Interfaces*.

153. Jones, R. A. L. & Richards, R. W. *Polymers at Surfaces and Interfaces*. (Cambridge University Press, 1999).
154. Sanchez, I. C. *Physics of Polymer Surfaces and Interfaces*. (Butterworth-Heinemann, 1992).
155. Simmons, D. S. An Emerging Unified View of Dynamic Interphases in Polymers. *Macromol. Chem. Phys.* **217**, 137–148 (2016).
156. Napolitano, S. & Wübbenhorst, M. The lifetime of the deviations from bulk behaviour in polymers confined at the nanoscale. *Nat. Commun.* **2**, 260 (2011).
157. Housmans, C., Sferrazza, M. & Napolitano, S. Kinetics of Irreversible Chain Adsorption. *Macromolecules* **47**, 3390–3393 (2014).
158. Frantz, P. & Granick, S. Infrared Dichroism, Chain Flattening, and the Bound Fraction Histogram in Adsorbed Poly(methyl methacrylate) Layers. *Macromolecules* **28**, 6915–6925 (1995).
159. Jiang, N., Shang, J., Di, X., Endoh, M. K. & Koga, T. Formation Mechanism of High-Density, Flattened Polymer Nanolayers Adsorbed on Planar Solids. *Macromolecules* **47**, 2682–2689 (2014).
160. Simavilla, D. N. *et al.* Mechanisms of Polymer Adsorption onto Solid Substrates. *ACS Macro Lett.* **6**, 975–979 (2017).
161. Virgiliis, A. D., Milchev, A., Rostiashvili, V. G. & Vilgis, T. A. Structure and dynamics of a polymer melt at an attractive surface. *Eur. Phys. J. E* **35**, 97 (2012).
162. Steckelmacher, W. Energy analysers for charged particle beams. *J. Phys. [E]* **6**, 1061 (1973).
163. Tanuma, S., Powell, C. J. & Penn, D. R. Calculations of electron inelastic mean free paths. V. Data for 14 organic compounds over the 50–2000 eV range. *Surf. Interface Anal.* **21**, 165–176 (1994).
164. Seah, M. P. Simple universal curve for the energy-dependent electron attenuation length for all materials. *Surf. Interface Anal.* **44**, 1353–1359 (2012).
165. Jablonski, A. Elastic scattering and quantification in AES and XPS. *Surf. Interface Anal.* **14**, 659–685 (1989).
166. Hofmann, S. *Auger- and X-Ray Photoelectron Spectroscopy in Materials Science*. (Springer, 2013).
167. Cumpson, P. J. Angle-resolved XPS and AES: Depth-resolution limits and a general comparison of properties of depth-profile reconstruction methods. *J. Electron Spectrosc. Relat. Phenom.* **73**, 25–52 (1995).
168. Hüfner, S. *Photoelectron Spectroscopy*. (Springer Berlin Heidelberg, 2003).
169. Anthony, M. T. & Seah, M. P. XPS: Energy calibration of electron spectrometers. 1—An absolute, traceable energy calibration and the provision of atomic reference line energies. *Surf. Interface Anal.* **6**, 95–106 (1984).
170. Bagus, P. S., Ilton, E. S. & Nelin, C. J. The interpretation of XPS spectra: Insights into materials properties. *Surf. Sci. Rep.* **68**, 273–304 (2013).
171. Fahlman, A. *et al.* Electron Spectroscopy and Chemical Binding. *Nature* **210**, 4 (1966).
172. Gelius, U. Binding Energies and Chemical Shifts in ESCA. *Phys. Scr.* **9**, 133 (1974).
173. Bagus, P. S., Illas, F., Pacchioni, G. & Parmigiani, F. Mechanisms responsible for chemical shifts of core-level binding energies and their relationship to chemical bonding. *J. Electron Spectrosc. Relat. Phenom.* **100**, 215–236 (1999).
174. Barr, T. L., Hoppe, E., Dugall, T., Shah, P. & Seal, S. XPS and bonding: when and why can relaxation effects be ignored. *J. Electron Spectrosc. Relat. Phenom.* **98–99**, 95–103 (1999).
175. Briggs, D. & Grant, J. T. *Surface analysis by Auger and x-ray photoelectron spectroscopy*. (IMPublications and SurfaceSpectra, 2003).
176. Tielsch, B. J. & Fulghum, J. E. Differential Charging in XPS. Part I: Demonstration of Lateral Charging in a Bulk Insulator Using Imaging XPS. *Surf. Interface Anal.* **24**, 422–427 (1996).
177. Biswas, C., Shukla, A. K., Banik, S., Ahire, V. K. & Barman, S. R. XPS and LEED study of Argon bombarded Al(111) surface. *Nucl. Instrum. Methods Phys. Res. Sect. B Beam Interact. Mater. At.* **212**, 297–302 (2003).
178. Watson, R. E., Herbst, J. F. & Wilkins, J. W. Core level shifts of rare-gas atoms implanted in the noble metals. *Phys. Rev. B* **14**, 18–25 (1976).

179. Grosvenor, A. P., Biesinger, M. C., Smart, R. S. C. & McIntyre, N. S. New interpretations of XPS spectra of nickel metal and oxides. *Surf. Sci.* **600**, 1771–1779 (2006).
180. Longe, P. & Bose, S. M. Strength of plasmon satellites in the valence band photoemission spectra of metals. *Solid State Commun.* **38**, 527–530 (1981).
181. Manne, R. Molecular Orbitals and Inner-Electron-Shell Chemical Shifts for Sulfur and Chlorine Oxy-anions. *J. Chem. Phys.* **46**, 4645–4651 (1967).
182. Hollander, J. M., Hendrickson, D. N. & Jolly, W. L. Nitrogen 1s Electron Binding Energies. Correlation with CNDO Charges. *J. Chem. Phys.* **49**, 3315–3316 (1968).
183. Basch, H. & Snyder, L. C. ESCA: chemical shifts of K-shell electron binding energies for first-row atoms in molecules. *Chem. Phys. Lett.* **3**, 333–336 (1969).
184. Lindberg, B. J. *et al.* Molecular Spectroscopy by Means of ESCA II. Sulfur compounds. Correlation of electron binding energy with structure. *Phys. Scr.* **1**, 286 (1970).
185. Gelius, U. *et al.* Molecular Spectroscopy by Means of ESCA III. Carbon compounds. *Phys. Scr.* **2**, 70 (1970).
186. Allison, D. A. *et al.* Molecular spectroscopy by means of ESCA: V. Boron compounds. *J. Electron Spectrosc. Relat. Phenom.* **1**, 269–283 (1972).
187. Cole, R. J., Matthew, J. A. D. & Weightman, P. Extra-atomic relaxation energy calculations using an extended potential model. *J. Electron Spectrosc. Relat. Phenom.* **72**, 255–259 (1995).
188. Bagus, P. S., Pacchioni, G., Sousa, C., Minerva, T. & Parmigiani, F. Chemical shifts of the core-level binding energies for the alkaline-earth oxides. *Chem. Phys. Lett.* **196**, 641–646 (1992).
189. Sousa, C., Minerva, T., Pacchioni, G., Bagus, P. S. & Parmigiani, F. Electrostatic and chemical bonding contributions to the cation core level binding energy shifts in MgO, CaO, SrO, BaO. A cluster model study. *J. Electron Spectrosc. Relat. Phenom.* **63**, 189–205 (1993).
190. Briggs, D. Surface Analysis of Polymers by XPS and Static SIMS. *Cambridge Core* (1998). Available at: [/core/books/surface-analysis-of-polymers-by-xps-and-static-sims/C2008EFA035292E66F8786BC31572110](https://doi.org/10.1017/C2008EFA035292E66F8786BC31572110). (Accessed: 12th February 2018)
191. Åberg, T. Theory of X-Ray Satellites. *Phys. Rev.* **156**, 35–41 (1967).
192. Hermsmeier, B. D. *et al.* Energy dependence of the outer core-level multiplet structures in atomic Mn and Mn-containing compounds. *Phys. Rev. B* **48**, 12425–12437 (1993).
193. Cox, P. A. Ionization energies of open-shell molecules in the frozen orbital approximation. *Mol. Phys.* **30**, 389–403 (1975).
194. Bagus, P. S., Illas, F. & Casanovas, J. The importance of 2s bonding contributions for the core level binding energies in organic compounds. *Chem. Phys. Lett.* **272**, 168–172 (1997).
195. Bagus, P. S., Illas, F., Casanovas, J. & Miguel Jiménez-Mateos, J. Novel mechanisms for core level shifts in organic compounds. *J. Electron Spectrosc. Relat. Phenom.* **83**, 151–158 (1997).
196. Schönhammer, K. & Gunnarsson, O. Many body effects in deep level spectroscopy from adsorbates. *Surf. Sci.* **89**, 575–587 (1979).
197. Bagus, P. S. & Illas, F. Decomposition of the chemisorption bond by constrained variations: Order of the variations and construction of the variational spaces. *J. Chem. Phys.* **96**, 8962–8970 (1992).
198. Anderson, P. W. Localized Magnetic States in Metals. *Phys. Rev.* **124**, 41–53 (1961).
199. von Niessen, W., Schirmer, J. & Cederbaum, L. S. Computational methods for the one-particle green's function. *Comput. Phys. Rep.* **1**, 57–125 (1984).
200. Jolly, W. L. & Hendrickson, D. N. Thermodynamic interpretation of chemical shifts in core-electron binding energies. *J. Am. Chem. Soc.* **92**, 1863–1871 (1970).
201. Gunnarsson, O. & Schönhammer, K. Electron spectroscopies for Ce compounds in the impurity model. *Phys. Rev. B* **28**, 4315–4341 (1983).
202. Moretti, G. The Wagner plot and the Auger parameter as tools to separate initial- and final-state contributions in X-ray photoemission spectroscopy. *Surf. Sci.* **618**, 3–11 (2013).
203. Grosvenor, A. P., Biesinger, M. C., Smart, R. S. C. & Gerson, A. R. The Influence of Final-State Effects on XPS Spectra from First-Row Transition-Metals. in *Hard X-ray Photoelectron Spectroscopy (HAXPES)* 217–262 (Springer, Cham, 2016).

204. Kotani, A. & Toyozawa, Y. Photoelectron Spectra of Core Electrons in Metals with an Incomplete Shell. *J. Phys. Soc. Jpn.* **37**, 912–919 (1974).
205. Gunnarsson, O. *et al.* Occupancy and hybridization of the f level in Ce compounds. *Phys. Rev. B* **28**, 7330–7333 (1983).
206. van Veenendaal, M. A. & Sawatzky, G. A. Nonlocal screening effects in 2p x-ray photoemission spectroscopy core-level line shapes of transition metal compounds. *Phys. Rev. Lett.* **70**, 2459–2462 (1993).
207. Altieri, S., Tjeng, L. H., Tanaka, A. & Sawatzky, G. A. Core-level x-ray photoemission on NiO in the impurity limit. *Phys. Rev. B* **61**, 13403–13409 (2000).
208. Mahan, G. D. Excitons in Metals: Infinite Hole Mass. *Phys. Rev.* **163**, 612–617 (1967).
209. NOZIÈRES, P. & DE DOMINICIS, C. T. Singularities in the X-Ray Absorption and Emission of Metals. III. One-Body Theory Exact Solution. *Phys. Rev.* **178**, 1097–1107 (1969).
210. Mahan, G. D. Collective excitations in x-ray spectra of metals. *Phys. Rev. B* **11**, 4814–4824 (1975).
211. Doniach, S. The birth of the DS lineshape. *J. Phys. Condens. Matter* **28**, 421005 (2016).
212. Doniach, S. & Sunjic, M. Many-electron singularity in X-ray photoemission and X-ray line spectra from metals. *J. Phys. C Solid State Phys.* **3**, 285 (1970).
213. Wertheim, G. K. & Citrin, P. H. Fermi surface excitations in X-ray photoemission line shapes from metals. in *Photoemission in Solids I* 197–236 (Springer, Berlin, Heidelberg, 1978).
214. Kotani, A. & Toyozawa, Y. Optical Spectra of Core Electrons in Metals with an Incomplete Shell. I. Analytic Features. *J. Phys. Soc. Jpn.* **35**, 1073–1081 (1973).
215. Kotani, A. & Toyozawa, Y. Optical Spectra of Core Electrons in Metals with an Incomplete Shell. II. Numerical Calculations of Overall Line Shapes. *J. Phys. Soc. Jpn.* **35**, 1082–1088 (1973).
216. Gunnarsson, O. & Schönhammer, K. Photoemission from Ce Compounds: Exact Model Calculation in the Limit of Large Degeneracy. *Phys. Rev. Lett.* **50**, 604–607 (1983).
217. Gunnarsson, O. & Schönhammer, K. Double occupancy of the f orbital in the Anderson model for Ce compounds. *Phys. Rev. B* **31**, 4815–4834 (1985).
218. Taguchi, M. *et al.* Bulk screening in core-level photoemission from Mott-Hubbard and charge-transfer systems. *Phys. Rev. B* **71**, 155102 (2005).
219. van Veenendaal, M. Competition between screening channels in core-level x-ray photoemission as a probe of changes in the ground-state properties of transition-metal compounds. *Phys. Rev. B* **74**, 085118 (2006).
220. Taguchi, M. & Panaccione, G. Depth-Dependence of Electron Screening, Charge Carriers and Correlation: Theory and Experiments. in *Hard X-ray Photoelectron Spectroscopy (HAXPES)* 197–216 (Springer, Cham, 2016).
221. Karis, O. *et al.* High-kinetic-energy photoemission spectroscopy of Ni at $1s$: 6-eV satellite at 4 eV. *Phys. Rev. B* **78**, 233105 (2008).
222. Fuggle, J. C. & Zolnierok, Z. The relationship between empty d-state density and XPS satellite intensities in nickel alloys. *Solid State Commun.* **38**, 799–802 (1981).
223. Porte, L., Roux, L. & Hanus, J. Vacancy effects in the x-ray photoelectron spectra of $\text{Ti}_{1-x}\text{N}_x$. *Phys. Rev. B* **28**, 3214–3224 (1983).
224. Fuggle, J. C., Campagna, M., Zolnierok, Z., Lässer, R. & Platau, A. Observation of a Relationship between Core-Level Line Shapes in Photoelectron Spectroscopy and the Localization of Screening Orbitals. *Phys. Rev. Lett.* **45**, 1597–1600 (1980).
225. Biesinger, M. C. *et al.* Quantitative chemical state XPS analysis of first row transition metals, oxides and hydroxides. *J. Phys. Conf. Ser.* **100**, 012025 (2008).
226. Tougaard, S. Algorithm for analysis of low-energy-resolution REELS; determination of inelastic electron scattering cross-sections and applications in quantitative XPS. *Surf. Sci.* **464**, 233–239 (2000).
227. Gupta, R. P. & Sen, S. K. Calculation of multiplet structure of core p-vacancy levels. *Phys. Rev. B* **10**, 71–77 (1974).

228. Gupta, R. P. & Sen, S. K. Calculation of multiplet structure of core p -vacancy levels. II. *Phys. Rev. B* **12**, 15–19 (1975).
229. Wagner, C. D. Chemical shifts of Auger lines, and the Auger parameter. *Faraday Discuss. Chem. Soc.* **60**, 291–300 (1975).
230. Wagner, C. D. & Joshi, A. The auger parameter, its utility and advantages: a review. *J. Electron Spectrosc. Relat. Phenom.* **47**, 283–313 (1988).
231. Snijders, P. C., Jeurgens, L. P. H. & Sloof, W. G. Structural ordering of ultra-thin, amorphous aluminium-oxide films. *Surf. Sci.* **589**, 98–105 (2005).
232. Végh, J. The Shirley background revised. *J. Electron Spectrosc. Relat. Phenom.* **151**, 159–164 (2006).
233. Tougaard, S. Practical algorithm for background subtraction. *Surf. Sci.* **216**, 343–360 (1989).
234. Seah, M. P., Gilmore, I. S. & Spencer, S. J. Background subtraction: II. General behaviour of REELS and the Tougaard universal cross section in the removal of backgrounds in AES and XPS. *Surf. Sci.* **461**, 1–15 (2000).
235. Seah, M. P., Gilmore, I. S. & Spencer, S. J. Quantitative AES IX and quantitative XPS II: Auger and x-ray photoelectron intensities and sensitivity factors from spectral digital databases reanalysed using a REELS database. *Surf. Interface Anal.* **31**, 778–795 (2001).
236. Simonsen, A. C., Yubero, F. & Tougaard, S. Quantitative model of electron energy loss in XPS. *Phys. Rev. B* **56**, 1612–1619 (1997).
237. Tougaard, S. & Yubero, F. QUEELS software package for calculation of surface effects in electron spectra. *Surf. Interface Anal.* **36**, 824–827 (2004).
238. Scofield, J. H. Hartree-Slater subshell photoionization cross-sections at 1254 and 1487 eV. *J. Electron Spectrosc. Relat. Phenom.* **8**, 129–137 (1976).
239. Reilman, R. F., Msezane, A. & Manson, S. T. Relative intensities in photoelectron spectroscopy of atoms and molecules. *J. Electron Spectrosc. Relat. Phenom.* **8**, 389–394 (1976).
240. Powell, C. J. & Jablonski, A. *NIST Electron Effective-Attenuation-Length Database*. (National Institute of Standards and Technology, Gaithersburg, MD, 2011).
241. Palmberg, P. W. *Anal. Chem.* **45**, 549A (1973).
242. Tougaard, S. Surface nanostructure determination by x-ray photoemission spectroscopy peak shape analysis. in **14**, 1415–1423 (AVS, 1996).
243. Hajati, S. & Tougaard, S. XPS for non-destructive depth profiling and 3D imaging of surface nanostructures. *Anal. Bioanal. Chem.* **396**, 2741–2755 (2010).
244. Greczynski, G. & Hultman, L. Self-consistent modelling of X-ray photoelectron spectra from air-exposed polycrystalline TiN thin films. *Appl. Surf. Sci.* **387**, 294–300 (2016).
245. Hofmann, S. Sputter-depth profiling for thin-film analysis. *Philos. Trans. R. Soc. Lond. Ser. Math. Phys. Eng. Sci.* **362**, 55–75 (2004).
246. Cumpson, P. J. Angle-resolved XPS and AES: Depth-resolution limits and a general comparison of properties of depth-profile reconstruction methods. *J. Electron Spectrosc. Relat. Phenom.* **73**, 25–52 (1995).
247. Powell, C. J. & Jablonski, A. Progress in quantitative surface analysis by X-ray photoelectron spectroscopy: Current status and perspectives. *J. Electron Spectrosc. Relat. Phenom.* **178–179**, 331–346 (2010).
248. Cumpson, P. J. The Thickogram: a method for easy film thickness measurement in XPS. *Surf. Interface Anal.* **29**, 403–406 (2000).
249. Taglauer, E. & Heiland, W. Surface analysis with low energy ion scattering. *Appl. Phys.* **9**, 261–275 (1976).
250. Niehus, H., Heiland, W. & Taglauer, E. Low-energy ion scattering at surfaces. *Surf. Sci. Rep.* **17**, 213–303 (1993).
251. Brongersma, H. H., Draxler, M., de Ridder, M. & Bauer, P. Surface composition analysis by low-energy ion scattering. *Surf. Sci. Rep.* **62**, 63–109 (2007).
252. Arnau, A. Charge states and energy loss of ions in solids. *Nucl. Instrum. Methods Phys. Res. Sect. B Beam Interact. Mater. At.* **93**, 195–202 (1994).

253. Brongersma, H. H., de Ridder, M., Gildenpennig, A. & Viitanen, M. M. Insight in the outside: materials science at the atomic level using LEIS. *J. Eur. Ceram. Soc.* **23**, 2761–2767 (2003).
254. Brongersma, H. H. *et al.* A round robin experiment of elemental sensitivity factors in low-energy ion scattering. *Nucl. Instrum. Methods Phys. Res. Sect. B Beam Interact. Mater. At.* **142**, 377–386 (1998).
255. Aono, M. & Souda, R. Quantitative Surface Atomic Structure Analysis by Low-Energy Ion Scattering Spectroscopy (ISS). *Jpn. J. Appl. Phys.* **24**, 1249 (1985).
256. Mikhailov, S. N. *et al.* Quantification in low-energy ion scattering: elemental sensitivity factors and charge exchange processes. *Nucl. Instrum. Methods Phys. Res. Sect. B Beam Interact. Mater. At.* **93**, 149–155 (1994).
257. Primetzhofer, D., Markin, S. N., Juaristi, J. I., Taglauer, E. & Bauer, P. LEIS: A reliable tool for surface composition analysis? *Nucl. Instrum. Methods Phys. Res. Sect. B Beam Interact. Mater. At.* **267**, 624–627 (2009).
258. Young, V. Y., Hoflund, G. B. & Miller, A. C. A model for analysis and quantification of ion scattering spectroscopy data. *Surf. Sci.* **235**, 60–66 (1990).
259. Veen, R. ter, Fartmann, M., Kersting, R. & Hagenhoff, B. Combining dynamic and static depth profiling in low energy ion scattering. *J. Vac. Sci. Technol. A* **31**, 01A113 (2013).
260. Wiesing, M., de los Arcos, T. & Grundmeier, G. The Thermal Oxidation of TiAlN High Power Pulsed Magnetron Sputtering Hard Coatings as Revealed by Combined Ion and Electron Spectroscopy. *Adv. Mater. Interfaces* 1600861 (2017). doi:10.1002/admi.201600861
261. Souda, R., Aono, M., Oshima, C., Otani, S. & Ishizawa, Y. Shadowing and focusing effects in the angular distributions of low-energy rare-gas ions scattered from solid surfaces. *Surf. Sci.* **179**, 199–208 (1987).
262. Sasaki, M., Scanlon, P. J., Ermolov, S. & Brongersma, H. H. Neutralization of He ions scattered from Ca surface. *Nucl. Instrum. Methods Phys. Res. Sect. B Beam Interact. Mater. At.* **190**, 127–130 (2002).
263. Hofmann, S. Sputter depth profile analysis of interfaces. *Rep. Prog. Phys.* **61**, 827 (1998).
264. Harrington, W. L., Honig, R. E., Goodman, A. M. & Williams, R. Low-energy ion-scattering spectrometry (ISS) of the SiO₂/Si interface. *Appl. Phys. Lett.* **27**, 644–645 (1975).
265. Aguzzoli, C. *et al.* Atomic transport and chemical reaction in TiN/Ti nanolayers on plasma nitrided steel. *Appl. Phys. A* **94**, 263–269 (2009).
266. Schwarz, P. U. D. & Hölscher, D. H. Dynamic Force Microscopy and Spectroscopy in Vacuum. in *Scanning Probe Microscopy* (eds. Kalinin, S. & Gruverman, A.) 506–533 (Springer New York, 2007).
267. Hölscher, H., Ebeling, D., Schmutz, J.-E., Schäfer, M. M. & Anczykowski, B. Dynamic Force Microscopy and Spectroscopy Using the Frequency-Modulation Technique in Air and Liquids. in *Scanning Probe Microscopy in Nanoscience and Nanotechnology* (ed. Bhushan, B.) 3–21 (Springer Berlin Heidelberg, 2010).
268. Baykara, M. Z. & Schwarz, U. D. 3D Force Field Spectroscopy. in *Noncontact Atomic Force Microscopy* (eds. Morita, S., Giessibl, F. J., Meyer, E. & Wiesendanger, R.) 9–28 (Springer International Publishing, 2015).
269. Schirmeisen, A., Hölscher, H. & Schwarz, U. D. Force Field Spectroscopy in Three Dimensions. in *Noncontact Atomic Force Microscopy* (eds. Morita, S., Giessibl, F. J. & Wiesendanger, R.) 95–119 (Springer Berlin Heidelberg, 2009).
270. Herruzo, E. T., Asakawa, H., Fukuma, T. & Garcia, R. Three-dimensional quantitative force maps in liquid with 10 piconewton, angstrom and sub-minute resolutions. *Nanoscale* **5**, 2678–2685 (2013).
271. Fukuma, T. Advanced Instrumentation of Frequency Modulation AFM for Subnanometer-Scale 2D/3D Measurements at Solid-Liquid Interfaces. in *Noncontact Atomic Force Microscopy* (eds. Morita, S., Giessibl, F. J., Meyer, E. & Wiesendanger, R.) 435–460 (Springer International Publishing, 2015).
272. Guggisberg, M. *et al.* Separation of interactions by noncontact force microscopy. *Phys. Rev. B* **61**, 11151–11155 (2000).

273. Schirmeisen, A., Weiner, D. & Fuchs, H. Measurements of metal–polymer adhesion properties with dynamic force spectroscopy. *Surf. Sci.* **545**, 155–162 (2003).
274. Albrecht, T. R., Grütter, P., Horne, D. & Rugar, D. Frequency modulation detection using high-Q cantilevers for enhanced force microscope sensitivity. *J. Appl. Phys.* **69**, 668–673 (1991).
275. Hölscher, H. *et al.* Measurement of conservative and dissipative tip-sample interaction forces with a dynamic force microscope using the frequency modulation technique. *Phys. Rev. B* **64**, 075402 (2001).
276. Gotsmann, B. & Fuchs, H. Dynamic AFM using the FM technique with constant excitation amplitude. *Appl. Surf. Sci.* **188**, 355–362 (2002).
277. Hölscher, H., Gotsmann, B. & Schirmeisen, A. Dynamic force spectroscopy using the frequency modulation technique with constant excitation. *Phys. Rev. B* **68**, 153401 (2003).
278. Anczykowski, B., Gotsmann, B., Fuchs, H., Cleveland, J. P. & Elings, V. B. How to measure energy dissipation in dynamic mode atomic force microscopy. *Appl. Surf. Sci.* **140**, 376–382 (1999).
279. Giessibl, F. J. Forces and frequency shifts in atomic-resolution dynamic-force microscopy. *Phys. Rev. B* **56**, 16010–16015 (1997).
280. Gotsmann, B., Seidel, C., Anczykowski, B. & Fuchs, H. Conservative and dissipative tip-sample interaction forces probed with dynamic AFM. *Phys. Rev. B* **60**, 11051–11061 (1999).
281. Sader, J. E. & Jarvis, S. P. Accurate formulas for interaction force and energy in frequency modulation force spectroscopy. *Appl. Phys. Lett.* **84**, 1801–1803 (2004).
282. Press, W. H., Teukolsky, S. A., Vetterling, W. T. & Flannery, B. P. *Numerical Recipes in C*. (Cambridge University Press, 1992).
283. Suzuki, K., Kobayashi, K., Labuda, A., Matsushige, K. & Yamada, H. Accurate formula for dissipative interaction in frequency modulation atomic force microscopy. *Appl. Phys. Lett.* **105**, 233105 (2014).
284. Simon, G. H., Heyde, M. & Rust, H.-P. Recipes for cantilever parameter determination in dynamic force spectroscopy: spring constant and amplitude. *Nanotechnology* **18**, 255503 (2007).
285. Bobzin, K. *et al.* (Cr,Al)N/(Cr,Al)ON Oxy-nitride Coatings deposited by Hybrid dcMS/HPPMS for Plastics Processing Applications. *Surf. Coat. Technol.* **308**, 394–403 (2016).
286. Bobzin, K. *et al.* A Contribution to explain the Mechanisms of Adhesive Wear in Plastics Processing by example of Polycarbonate. *Surf. Coat. Technol.* **332**, 464–473 (2017).